Frequency up-conversion of nonclassical states of light

Von der QUEST-Leibniz-Forschungsschule
der Gottfried Wilhelm Leibniz Universität Hannover
zur Erlangung des Grades

DOKTOR DER NATURWISSENSCHAFTEN
Dr. rer. nat.

genehmigte Dissertation
von

M.Sc. Christoph Baune

2016

Referent	Prof. Dr. rer. nat. Roman Schnabel Institut für Laserphysik und Zentrum für Optische Quantentechnologien Universität Hamburg
Korreferent	Prof. Dr. rer. nat. Karsten Danzmann Albert-Einstein-Institut, AEI Hannover: Max-Planck-Institut für Gravitationsphysik und Institut für Gravitationsphysik der Leibniz Universität Hannover
Tag der Promotion	22. Juni 2016

Kurzfassung

Nichtklassische Zustände des Lichts spielen eine wichtige Rolle in der modernen Quantenoptik. Ihre Anwendungen reichen von der Hochpräzisionsmesstechnik, wo Empfindlichkeitsgrenzen aufgrund von Quantenrauschen mithilfe sogenannter *gequetschter Zustände* überschritten werden können, bis hin zu langreichweitiger sicherer Kommunikation durch die Ausnutzung von *Verschränkung* zwischen Knoten eines Quantennetzwerkes, was heutzutage ein immer dringlicher werdender Wunsch von Firmen, Regierungen und Privatleuten ist. *Einzelne Photonen*, die als kleinste Anregungen eines elektromagnetischen Feldes bereits von grundlegendem Interesse sind, finden ebenfalls Anwendung im wachsenden Feld der Quanteninformation.

In dieser Arbeit demonstriere ich, dass stark gequetschte Zustände auch bei sichtbaren Lichtwellenlängen erzeugt werden können. Bisher war es lediglich möglich, dies bei infraroten Wellenlängen zu realisieren, da nach aktuellem Stand nur dort nichtlineare Kristalle verfügbar sind, die die benötigten optischen Eigenschaften aufweisen. Ich zeige, dass dieser Umstand umgangen werden kann, indem ursprünglich bei 1550 nm gequetschte Zustände mithilfe einer Summenfrequenzerzeugung in den sichtbaren Wellenlängenbereich zu 532 nm übertragen werden. In einer Erweiterung dieses Experiments wird ein Teil eines zwei-Moden-gequetschten Zustandes konvertiert, sodass Verschränkung zwischen zwei unterschiedlichen Wellenlängenbereichen erzeugt wird. Da diese Konversion an jedem Punkt eines möglichen Quantennetzwerkes stattfinden kann, erlaubt diese Methode die sehr effiziente Übertragung der Zustände im infraroten Bereich durch existierende Glasfasern sowie eine anschließende Weiterverarbeitung in Quantenspeichern, welche bei deutlich kürzeren Wellenlängen bevorzugt wird.

In dieser Arbeit werden außerdem experimentelle Untersuchungen zu Einzelphotonen unternommen. Unter Ausnutzung von zeitlichen Korrelationen in erzeugten Photonenpaaren können einzelne Photonen vorhergesagt werden. Ich zeige die Realisierung eines solchen Experimentes und die Rekonstruktion einer Quasi-Wahrscheinlichkeitsverteilung: Die Wignerfunktion des Zustandes weist negative Bereiche auf, was mit klassischen Zuständen nicht erklärbar ist und daher rein quantenmechanische Eigenschaften offenlegt. In einem weiteren Experiment werden einzelne Photonen zu kürzeren Wellenlängen konvertiert. Es wird erstmals gezeigt, dass im Konversionsprozess eine sogenannte *Quanten-Nichtgaußizität* erhalten bleibt, was ebenfalls ein starkes Kriterium für nichtklassische Eigenschaften ist.

Diese Arbeit zeigt, dass Frequenz-Hochkonversion die Erzeugung nichtklassischer Zustände bei sichtbaren Wellenlängen ermöglicht, wodurch Impulse für die Weiterentwicklung von Quantenmetrologie und Quanteninformation gegeben werden.

Schlüsselbegriffe: Frequenz-Hochkonversion, gequetschtes Licht, Verschränkung, Einzelphotonen, Quanten-Nichtgaußizität, negative Wignerfunktion

Abstract

Nonclassical states of light play a prominent role in quantum optics. Their applications range from high-precision metrology, where limits on measurement sensitivity due to quantum noise can be surpassed using so-called *squeezed states* of light, to long-distance secure communication, which can be facilitated by distributing nonclassical correlations between nodes of a quantum network using *entangled states* of light. *Single photons* are elementary excitations of an electromagnetic field, and are fundamentally interesting while also having various applications in the growing field of quantum information science. Nonclassical states of light thus hold interest for fundamental as well as practical reasons – they allow us to test the limits of quantum theory, but also allow the distribution of information with mathematically-proven security, which is of increasing interest to governments, companies and individuals.

In this thesis I demonstrate the generation of strongly squeezed states at visible wavelengths. Up to now, such states could only be generated at infrared wavelengths, since nonlinear crystals with appropriate properties for directly generating squeezed states at shorter wavelengths have not been found yet. A way of circumventing this is demonstrated via the frequency up-conversion of a squeezed state initially at 1550 nm. By means of sum-frequency generation the state's noise properties are transferred to a field at 532 nm. In an extension to this experiment, one part of a two-mode 1550 nm squeezed state is converted to 532 nm, to demonstrate entanglement between two distinct wavelength regimes. This demonstration is interesting for quantum networks: optical states can efficiently distribute entanglement over telecommunication fibers, and then be interfaced with matter-based nodes that generally operate at shorter wavelengths.

This thesis also presents experimental work on heralded single photon states. Temporal correlations of photon pairs are exploited to herald a single photon in one mode, and a quasi-probability distribution known as the Wigner function is experimentally reconstructed. The Wigner function includes negative values that cannot be explained classically, and thus signify the purely quantum mechanical properties of the state. These heralded photons are also up-converted to shorter wavelengths, and are for the first time shown to be *quantum non-Gaussian*, which is a strong criterion for nonclassicality.

The experiments in this thesis focus on the frequency up-conversion of nonclassical states of light. Both squeezed states and single photons are converted from infrared (telecommunication) to visible wavelengths, demonstrating a key technique for potential quantum technologies. The quantum properties of the up-converted states are rigorously characterized, and a number of benchmarks are demonstrated for the first time in this frequency regime.

Key words: Frequency up-conversion, squeezed light, entanglement, single photons, quantum non-Gaussianity, negative Wigner function

Contents

Kurzfassung iii

Abstract v

Glossary xi

1. Introduction 1

2. Theoretical background 5
- 2.1. Quantum optics basics 5
  - 2.1.1. The quantized electromagnetic field 5
  - 2.1.2. Phase-space representation – Wigner function 7
  - 2.1.3. Fock states 8
  - 2.1.4. Coherent states 10
  - 2.1.5. Squeezed states 11
  - 2.1.6. Nonclassical states 13
- 2.2. Balanced homodyne detection 14
- 2.3. Nonlinear optics 16
  - 2.3.1. Nonlinear polarization 16
  - 2.3.2. Three wave mixing 16
- 2.4. Frequency up-conversion of quantum states 21

3. Frequency up-conversion of squeezed vacuum states 25
- 3.1. Degenerate parametric down-conversion and squeezing 26
- 3.2. Experimental setup 27
  - 3.2.1. Laser source and second harmonic generation 27
  - 3.2.2. Non-degenerate optical parametric oscillator 29
  - 3.2.3. Second harmonic generation from 1550 to 775 nm 31
  - 3.2.4. Degenerate optical parametric amplifier 32
  - 3.2.5. Sum-frequency generation 32
  - 3.2.6. Balanced homodyne detector at 532 nm 35
- 3.3. Results 35
  - 3.3.1. Strongly squeezed vacuum states at 532 nm 35
  - 3.3.2. Sensitivity improvement of a Mach-Zehnder interferometer 36
- 3.4. Discussion and outlook 38

4. An unconditional entanglement interface for quantum networks 39
- 4.1. Generation of entanglement 40

4.2. Experimental setup 43
4.3. Measurement protocol and results 43
4.4. Discussion and outlook 46

5. Frequency up-conversion of single photon states **49**
5.1. Experimental setup 50
  5.1.1. SPDC 51
  5.1.2. Filter cavity 51
  5.1.3. Avalanche photo detectors (APDs) 52
  5.1.4. Data acquisition 53
5.2. Cavity enhanced spontaneous parametric down-conversion 54
  5.2.1. Temporal correlations of the SPDC output 54
  5.2.2. Temporal correlations with filtered signal mode 55
5.3. Results 56
  5.3.1. Two- and threefold coincidences 57
  5.3.2. Second order correlation function 58
5.4. Quantum non-Gaussianity 60
5.5. Extended analysis 64
  5.5.1. Dead time of APD-T 64
  5.5.2. Afterpulses 64
5.6. Discussion and outlook 65

6. Single photon state tomography **67**
6.1. Experimental setup 67
  6.1.1. Homodyne detector 68
  6.1.2. Trigger filtering 69
  6.1.3. Measurement protocol 70
6.2. Results 71
  6.2.1. Signal mode-function 71
  6.2.2. Segment noise 72
  6.2.3. Extracting quadrature values 72
  6.2.4. Reconstruction of the Wigner function 73
  6.2.5. Significance of negativity 76
6.3. Discussion and outlook 77

7. Summary and outlook **79**

A. Calculations **81**
A.1. Cavity input-output formalism 81
A.2. Mode filtering 83
A.3. Degenerate parametric down-conversion and squeezing 84
  A.3.1. OPA: Frequency-space solution 85
  A.3.2. The squeezing spectrum 86
  A.3.3. Additional frequency filter 88

A.4. Non-degenerate spontaneous parametric down-conversion 89
  A.4.1. SPDC: Frequency-space solution 90
  A.4.2. Temporal correlations of the SPDC output 91
  A.4.3. Temporal correlation with equal decay rates 93
  A.4.4. Temporal correlations with filtered signal mode 94
A.5. Maximum likelihood estimation of quantum states 95

B. Programs **101**
B.1. Filter cavities 101
B.2. APD power supply 102
B.3. Mathematica 105
B.4. python programs 110
  B.4.1. Data acquisition with an oscilloscope-PC interface 110
  B.4.2. Data conversion to hdf5 112
  B.4.3. Data size reduction 114
  B.4.4. Quantum non-Gaussianity verification 116
  B.4.5. Quantum state estimation 119
  B.4.6. Wigner function reconstruction 121
B.5. gnuplot programs 123
  B.5.1. Determine optical loss in squeezing measurements 123
  B.5.2. Correlations in two-mode squeezing 123

C. Contributions **125**

D. Material **127**

E. Fundings **129**

F. Acknowledgments **131**

G. Gallery **133**

Bibliography **135**

Curriculum vitae **143**

List of publications **144**

Glossary

APD avalanche photo diode.

BBS balanced beam splitter.

BHD balanced homodyne detector.

BS beam splitter.

CV continuous variable.

DBS dichroic beam splitter.

DV discrete variable.

FC filter cavity.

FWHM full width at half maximum.

HWHM half width at half maximum.

NTC negative temperature coefficient.

OPA optical parametric amplifier.

OPO optical parametric oscillator.

PPKTP periodically poled potassium titanyl phosphate.

QM quantum memory.

QNG quantum non-Gaussianity.

RR retro-reflector.

SFG sum-frequency generation.

SHG second harmonic generation.

SPDC spontaneous parametric down-conversion.

VBS variable beam splitter.

1. Introduction

Nonclassical states of light are states that cannot be described by means of classical statistics. Among them, squeezed and single photon states are the most prominent. Their unique intrinsic correlations and sometimes even counter-intuitive properties allow for a variety of applications in quantum metrology and quantum information. However, nonclassical states are very sensitive to optical loss and thus efficient techniques to generate, process and detect them are required.

Quantum metrology exploits nonclassical states to enhance the precision of measurement devices and in this context, squeezed vacuum states of light have proven to be a useful resource. The gravitational wave detector GEO600 located close to Hanover, Germany, routinely uses squeezed vacuum states of light to improve the devices measurement sensitivity [Gro13]. The Advanced LIGO detectors will also implement squeezed light sources to further increase their sensitivity, which is a major advance in the recently opened era of gravitational wave astronomy [LIG16].

Squeezed states of light are routinely generated at infrared wavelengths via spontaneous parametric down-conversion utilizing a second harmonic pump field [Ebe10, Meh11]. However, many measurement protocols require squeezed states at a variety of optical wavelengths to achieve increased sensitivity. For example, a proposal for DECIGO, a gravitational wave detector operating at 532 nm, has been made [Kaw06], and it would benefit from squeezed vacuum states at this wavelength. Beyond that, in saturation spectroscopy squeezed states are required at wavelengths close to optical transitions which are spread over the entire spectrum [Pol92]. In this thesis, I present an experiment where strongly squeezed states at 532 nm are generated by means of frequency up-conversion.

Nonclassical states are also necessary in quantum information. Today, messages to be transmitted over communication channels are commonly encrypted with protocols whose security is based on the difficulty of factorizing large numbers with classical computers in a reasonable amount of time. A quantum computer, once realized, is able to perform this task much faster and would thus create the need for a revolution in communication systems - at least when absolute security is required. Fortunately, quantum mechanics also provides features to restore the security and quantum communication is an extensively studied field: see [Gis02] and [Bra05, Wee12] for reviews on quantum information with discrete and continuous variables, respectively.

The distribution of quantum information encoded in light modes over long distances is challenging as the involved nonclassical states are sensitive to optical loss, which is small but unavoidable in telecommunication fibers. Unlike in classical communication, quantum information for cryptographic purposes cannot be noiselessly amplified due to the no-cloning theorem [Die82, Woo82]. However, so-called quantum repeaters [Bri98] allow to split a quantum communication channel at one or more nodes. By means of entanglement distillation and swapping [Bra05], it is then possible to entangle space-like separated nodes and the communication distance can be significantly increased.

Quantum repeaters are based on quantum memories where photons are reversibly mapped to atomic ensembles, molecular gases, solids, *et cetera* [Sim10, Hes16]. Thus, efficient light-matter interfaces between infrared wavelengths, where transmission through optical fibers is preferred, and optical modes of quantum memories play key roles in quantum communication research.

In this thesis, I present a proof-of-principle implementation of an interface for quantum communication tasks. Based on frequency up-conversion, nonclassical correlations are transferred from the telecommunication wavelength 1550 nm to 532 nm, which represents a possible operational regime where a quantum memory might be realized. A conceptual schematic of an elementary quantum link between two nodes of a quantum network using this interface is illustrated in Figure 1.1.

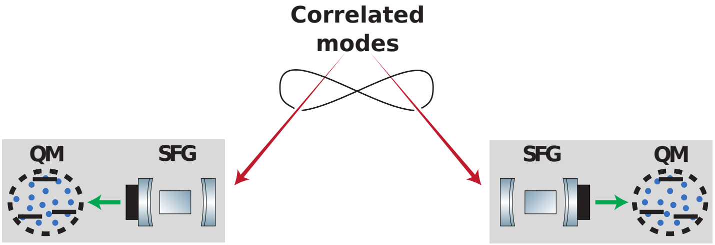

Figure 1.1.: Conceptual schematic of an elementary segment of a quantum network. Quantum correlations are established between two nodes of the network. Efficient transmission of light is achieved by operating at telecommunication wavelength, and the coupling to local quantum memories (QM) is enabled by frequency up-conversion based on sum-frequency generation (SFG) of the transmitted light beams.

A source emits two optical beams prepared at telecommunication wavelength in a quantum-correlated state, and each beam is sent to one node of the quantum network. To enable efficient interfacing with quantum memories, the transmitted light beams are frequency up-converted, and their quantum state is stored in quantum memories for further processing. This schematic can represent an elementary segment of a quantum repeater, where efficient transmission of light over short distances would be combined with local processing of stored quantum states. Quantum correlations can be established over much longer distances than possible without quantum repeaters.

In this thesis, squeezed and entangled states of light as well as single photons are frequency up-converted from 1550 nm to 532 nm. Furthermore, a state showing a negative Wigner function is realized at telecommunication wavelength. The results give new insights and impulses for nonclassical state generation for quantum metrology and quantum information research.

Outline of this thesis

The structure of this thesis is as follows:

- Chapter 2 reviews quantum optical concepts to make the thesis relatively self-contained for a reader familiar with basic quantum mechanics and to introduce my notations and normalizations. Furthermore, a brief introduction of the nonlinear optical effects that are most important in the experimental realization of this thesis is provided.
- Chapter 3 presents the experimental frequency up-conversion of squeezed vacuum states from 1550 to 532 nm.
- Chapter 4 demonstrates nonclassical correlations between widely separated wavelength regimes by means of frequency up-conversion of half of a two-mode squeezed state.
- Chapter 5 presents the frequency up-conversion of single photons. The up-converted photons are certified to be nonclassical utilizing a quantum non-Gaussianity criterion.
- Chapter 6 presents the realization of a negative Wigner function at the telecommunication wavelength of 1550 nm. The experimental preparation is assisted with frequency up-conversion of single photons heralding the state.
- Chapter 7 summarizes the results and gives an outlook.

2. Theoretical background

2.1. Quantum optics basics

The work presented in this thesis reveals phenomena that cannot be fully understood with a classical theory of light and a quantum mechanical treatment is necessary. This section covers theoretical basics of the quantized single mode electromagnetic field to provide tools that allow theoretical analyses, simulations and modeling of quantum mechanical effects. In every chapter these fundamentals are extended to the respective topic.

This section restricts to aspects that reappear in calculations throughout this thesis and I refer the reader to introductory textbooks of quantum optics for further reading, for example the textbook by Gerry and Knight [Ger05] and references therein. Unfortunately, different normalizations used by the various authors of many theses, journal articles and textbooks lead to slightly different formulae. Thus, another intention of this chapter is to get the reader used to the notation of physical entities that are used throughout this thesis.

Starting with the quantized harmonic oscillator, some prominent quantum states will be introduced, namely Fock or number states, coherent states and quadrature squeezed states. A phase space representation, the Wigner function, serves to visualize statistical properties of these states. The section will conclude with a discussion of nonclassicality.

2.1.1. The quantized electromagnetic field

Several experiments of the last century showed that light has both wave and particle properties. Interference, dispersion and polarization effects visualize the wave features while single photon detectors measure a light mode to be excited at very distinct times and reveal particle-like characteristics. The quantum optical basics presented here mainly follow the first chapters in Leonhardt's book [Leo05]. However, fundamental quantum mechanics can be found in many other textbooks. In the following a light field is described by the quantized electric field propagating in z-direction

$$\hat{E}(z,t) = \mathbf{u}^*(z,t)\hat{a} + \mathbf{u}(z,t)\hat{a}^\dagger\,, \tag{2.1}$$

where $\mathbf{u}(z,t) = \mathbf{u}_0 \exp[\mathrm{i}(z\mathbf{k} - \omega t)]$ with the polarization vector $\mathbf{u}_0$, wave vector $\mathbf{k}$ and angular frequency ω describes a plane wave. This plane wave is excited by the quantized amplitude $\hat{a}$. The hât above a physical entity depicts that it is a quantum mechanical operator while the superscripts * and † denote complex and hermitian conjugates, respectively.

The amplitude operators obey the bosonic commutation relation

$$[\hat{a}, \hat{a}^\dagger] = 1 \tag{2.2}$$

and with these, one can introduce the dimensionless quadrature operators

$$\begin{aligned} \hat{q} &= \frac{1}{\sqrt{2}}(\hat{a} + \hat{a}^\dagger)\,, \\ \hat{p} &= \frac{1}{\mathrm{i}\sqrt{2}}(\hat{a} - \hat{a}^\dagger)\,, \end{aligned} \tag{2.3}$$

which are hermitian operators with real eigenvalues.

They are motivated by the fact that they are proportional to the real and imaginary part of the quantized field amplitude

$$\hat{a} = \frac{1}{\sqrt{2}}(\hat{q} + \mathrm{i}\hat{p})\,. \tag{2.4}$$

The commutation relation between the quadrature operators is

$$[\hat{q}, \hat{p}] = \mathrm{i} \tag{2.5}$$

from which their Heisenberg uncertainty relation follows to be

$$\Delta\hat{q} \cdot \Delta\hat{p} \geq \frac{1}{2}\,. \tag{2.6}$$

Here, the standard deviation of an operator $\hat{A}$ is defined as

$$\Delta\hat{A} = \sqrt{\langle \hat{A}^2 \rangle - \langle \hat{A} \rangle^2} \tag{2.7}$$

where $\langle \cdot \rangle$ is the quantum mechanical expectation value. The Hamiltonian of the system in terms of the quadrature operators is

$$\mathbf{H} = \frac{1}{2}\hbar\omega(\hat{q}^2 + \hat{p}^2)\,. \tag{2.8}$$

Furthermore it is useful to introduce the generalized, phase rotated quadrature operator

$$\hat{q}_\theta = \frac{1}{\sqrt{2}}(\hat{a}\mathrm{e}^{-\mathrm{i}\theta} + \hat{a}^\dagger\mathrm{e}^{\mathrm{i}\theta}) = \hat{q}\cos\theta + \hat{p}\sin\theta\,. \tag{2.9}$$

The eigenstates of the quadrature operators are the so-called quadrature states and are defined as

$$\hat{q}|q\rangle = q|q\rangle, \quad \hat{p}|p\rangle = p|p\rangle\,. \tag{2.10}$$

One can change from one representation to the other via the Fourier transform

$$\begin{aligned} |q\rangle &= \frac{1}{\sqrt{2\pi}}\int_{-\infty}^{\infty} dp\, \mathrm{e}^{-\mathrm{i}qp}|p\rangle \\ |p\rangle &= \frac{1}{\sqrt{2\pi}}\int_{-\infty}^{\infty} dq\, \mathrm{e}^{+\mathrm{i}qp}|q\rangle \end{aligned} \tag{2.11}$$

and they are often used when one uses the quadrature wave functions

$$\psi(q) = \langle q|\psi\rangle, \quad \tilde{\psi}(p) = \langle p|\psi\rangle\,, \tag{2.12}$$

which are experimentally accessible using balanced homodyne detection. The absolute square of quadrature operators gives the probability distribution

$$P(q,p) = |\langle q_\theta|\psi\rangle|^2 \tag{2.13}$$

and describes the statistics of a measurement on $|\psi\rangle$.

2.1.2. Phase-space representation – Wigner function

In classical physics there is the phase-space distribution $P(q,p)$, which gives the probability of finding a pair of q and p values in their simultaneous measurement. The situation is different in quantum mechanics: It is due to Heisenberg's uncertainty principle Eq. (2.6) that one cannot measure position and momentum of the quantized harmonic oscillator simultaneously with arbitrary precision, for example. In this sense, a probability distribution in quantum physics seems not to make sense. However, we can measure probability distributions like Eq. (2.13) which allows us to develop the idea of a *quasi*probability distribution $W(q,p)$ that accounts for quantum features. The most popular one is called Wigner function which can most easily be defined using quantum states described in terms of the density matrix.

Given that a state is formed by an ensemble of quantum states $|\psi_i\rangle$, the state's density operator $\hat{\rho}$ is defined as

$$\hat{\rho} = \sum_i p_i|\psi_i\rangle\langle\psi_i|\,, \tag{2.14}$$

where p_i is the probability of finding the state in $|\psi_i\rangle$. If only one p_i is non-vanishing, the state is called a pure state, otherwise it is a mixed state. The density operator can be expressed in any other basis $\{|\phi_k\rangle\}$ using the relation

$$\hat{\rho} = \sum_{k,l} \rho_{kl}|\phi_k\rangle\langle\phi_l|\,, \quad \rho_{kl} = \langle\phi_k|\hat{\rho}|\phi_l\rangle\,. \tag{2.15}$$

The matrix ρ_{kl} is called density matrix.

Using the density operator, the Wigner function is then defined as [Leo05]

$$W(q,p) = \frac{1}{2\pi}\int_{-\infty}^{\infty} dx\, \mathrm{e}^{\mathrm{i}px} \left\langle q - \frac{x}{2}\middle|\hat{\rho}\middle|q + \frac{x}{2}\right\rangle\,. \tag{2.16}$$

The probability distribution of one quadrature, called marginal distribution, can be obtained by integration over the other, for example

$$P(q) = \int_{-\infty}^{\infty} dp\, W(q,p) = \langle q|\hat{\rho}|q\rangle\,. \tag{2.17}$$

In the following sections I will present some of the most popular quantum states and plot their Wigner function.

2.1.3. Fock states

Fock states $|n\rangle$ are also called number states as they are eigenstates of the photon number operator, which is defined as

$$\hat{n} = \hat{a}^\dagger \hat{a} \tag{2.18}$$

analogously to a classical modulus-squared amplitude. Its action on an eigenstate is

$$\hat{n}|n\rangle = n|n\rangle, \quad n \in \mathbb{N}\,. \tag{2.19}$$

Fock states have a defined (integer) photon number. Even though their theoretical description is rather easy, their experimental generation requires relatively complex techniques.

We can rewrite the Hamiltonian of the quantum mechanical harmonic oscillator by inserting Eq. (2.3) into Eq. (2.8) and using the commutation relation Eq. (2.2)

$$\mathbf{H} = \frac{1}{2}\hbar\omega(\hat{q}^2 + \hat{p}^2) = \hbar\omega(\hat{n} + \frac{1}{2})\,. \tag{2.20}$$

Thus the energy of the quantum mechanical harmonic oscillator can both be expressed in terms of continuous variables (the quadratures) and discrete numbers. So to speak, this is the wave-particle duality in a single equation.

The action of the operators $\hat{a}$ and $\hat{a}^\dagger$ is

$$\begin{aligned} \hat{a}|n\rangle &= \sqrt{n}|n-1\rangle\,, \\ \hat{a}^\dagger|n\rangle &= \sqrt{n+1}|n+1\rangle \end{aligned} \tag{2.21}$$

so that it becomes rather obvious why $\hat{a}$ and $\hat{a}^\dagger$ are commonly called annihilation and creation operator, respectively. They lower or increase the number of excitations in the state. A Fock state $|n\rangle$ - keeping a proper renormalization - can be expressed via n-times action of the creation operator to the Fock state $|0\rangle$

$$|n\rangle = \frac{\hat{a}^{\dagger n}}{\sqrt{n!}}|0\rangle\,. \tag{2.22}$$

According to Eq. (2.20), the so-called vacuum state $|0\rangle$ contains the energy $\hbar\omega/2$. This results in some interesting phenomena like the Casimir effect but is also reason for a limitation of measurement devices where vacuum fluctuations spoil their sensitivity.

Finally I note that the Fock states are complete and orthonormal

$$\begin{gathered} \sum_{n=0}^{\infty} |n\rangle\langle n| = 1 \\ \langle n|n'\rangle = \delta_{nn'} \end{gathered} \tag{2.23}$$

and form the most common Hilbert space basis in quantum optics, the Fock basis.

Even though the photon number of a Fock state is precisely determined, the standard deviation of the generalized quadrature is non-vanishing and phase independent

$$\Delta\hat{q}_\theta = \sqrt{\frac{1}{2}(2n+1)}\,. \tag{2.24}$$

Only the Fock state with no excitation $|n = 0\rangle$ is a minimum uncertainty state with $\Delta\hat{q}\Delta\hat{p} = \frac{1}{2}$.

If a state is given in the Fock basis $\hat{\rho} = \sum_{m,n} \rho_{mn}|m\rangle\langle n|$, its Wigner function is given by

$$\begin{aligned} W(q,p) &= \frac{1}{2\pi}\int_{-\infty}^{\infty} dx\, \mathrm{e}^{\mathrm{i}px}\langle q - x/2|\left[\sum_{m,n}\rho_{mn}|m\rangle\langle n|\right]|q + x/2\rangle \\ &= \sum_{m,n}\rho_{mn}W_{mn}(q,p)\,. \end{aligned} \tag{2.25}$$

The Wigner function element $W_{mn}(q,p)$ is given by [MN10]

$$\begin{aligned} W_{mn}(q,p) &= \frac{1}{2\pi}\int_{-\infty}^{\infty} dx\, \mathrm{e}^{\mathrm{i}px}\langle q - x/2|m\rangle\langle n|q + x/2\rangle \\ &= \frac{1}{\pi}\mathrm{e}^{-q^2-p^2}\cdot\begin{cases} 2^{m-n}(-1)^m(-q+\mathrm{i}p)^{m-n}\sqrt{\frac{n!}{m!}}L_n^{(m-n)}[2(q^2+p^2)] & \text{for } m \geq n \\ 2^{n-m}(-1)^n(-q+\mathrm{i}p)^{n-m}\sqrt{\frac{m!}{n!}}L_m^{(n-m)}[2(q^2+p^2)] & \text{for } m < n \end{cases}, \end{aligned} \tag{2.26}$$

where $L_k^{(l)}(x)$ are generalized Laguerre polynomials [Bro08]. The overlap between a Fock state and a quadrature eigenstate is [Leo05]

$$\langle n|q\rangle = \frac{\mathrm{e}^{-q^2/2}H_n(q)}{\sqrt{2^n n!\sqrt{\pi}}}\,, \tag{2.27}$$

where $H_n(x)$ is the nth Hermite polynomial [Bro08]. For a Fock state with $\hat{\rho} = |n\rangle\langle n|$ one finally obtains

$$W_n(q,p) = \frac{1}{\pi}\mathrm{e}^{-q^2-p^2}(-1)^n L_n^{(0)}[2(q^2+p^2)]\,, \tag{2.28}$$

which gives for the vacuum state $|0\rangle$

$$W_0(q,p) = \frac{1}{\pi}\mathrm{e}^{-q^2-p^2} \tag{2.29}$$

and for the single photon state $|1\rangle$

$$W_1(q,p) = \frac{1}{\pi}\mathrm{e}^{-q^2-p^2}(2q^2 - 2p^2 - 1)\,. \tag{2.30}$$

These two Wigner functions are plotted in Figure 2.1. The Wigner function of the vacuum is a simple Gaussian with variance $\frac{1}{2}$, while the single photon has negative values around the origin. This feature is a strong evidence of the state's nonclassical properties as I will discuss in Section 2.1.6.

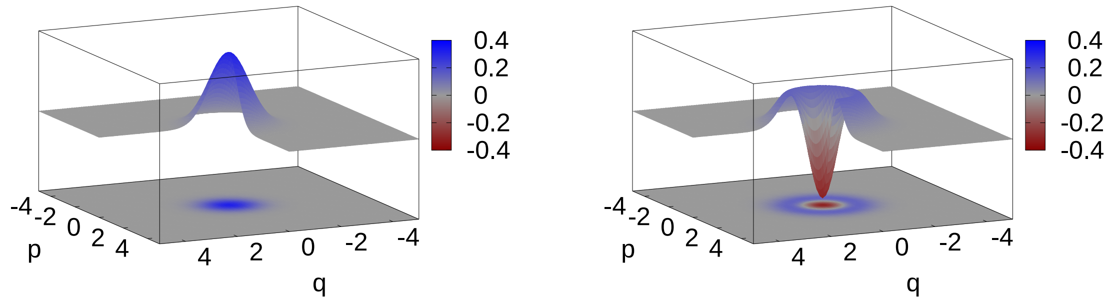

(a) Vacuum state $|0\rangle$.

(b) Single photon state $|1\rangle$.

Figure 2.1.: Wigner functions of the vacuum and single photon state. While the vacuum state is a simple Gaussian distribution, the single photon state has negative values around the origin. These are strong evidences for nonclassical properties.

2.1.4. Coherent states

Coherent states $|\alpha\rangle$ represent quantum states as they are produced by a high-quality laser and they are defined as eigenstates of the annihilation operator

$$\hat{a}|\alpha\rangle = \alpha|\alpha\rangle\,, \quad \alpha \in \mathbb{C}\,. \tag{2.31}$$

Any given state can be expressed in the coherent state basis

$$|\psi\rangle = \frac{1}{\pi}\int d^2\alpha\,|\alpha\rangle\langle\alpha|\psi\rangle \tag{2.32}$$

as they are a complete set of non-orthogonal basis vectors:

$$\frac{1}{\pi}\int d^2\alpha\,|\alpha\rangle\langle\alpha| = 1, \quad \langle\alpha|\alpha'\rangle = \mathrm{e}^{-|\alpha|^2/2+\alpha^*\alpha'-|\alpha'|^2/2}\,. \tag{2.33}$$

The coherent states can be expressed in the Fock state basis as

$$|\alpha\rangle = \mathrm{e}^{-|\alpha|^2/2}\sum_{n=0}^{\infty}\frac{\alpha^n}{\sqrt{n!}}|n\rangle\,. \tag{2.34}$$

The photon number distribution of a coherent state is therefore given as

$$p_\alpha(n) = |\langle n|\alpha\rangle|^2 = \frac{|\alpha|^{2n}}{n!}\mathrm{e}^{-|\alpha|^2}\,. \tag{2.35}$$

The quadrature variance of a coherent state is $(\Delta\hat{q}_\theta)^2 = \langle\alpha|\hat{q}_\theta^2|\alpha\rangle - \langle\alpha|\hat{q}_\theta|\alpha\rangle^2 = \frac{1}{2}$. Like the vacuum state, a coherent state is a minimum uncertainty state as

$$\Delta\hat{q}\cdot\Delta\hat{p} = \frac{1}{2}\,. \tag{2.36}$$

The Wigner function of a coherent state is given by

$$W_\alpha(q,p) = \frac{1}{\pi}\mathrm{e}^{-(q-q_0)^2-(p-p_0)^2}\,, \quad \alpha = \frac{1}{\sqrt{2}}(q_0 + \mathrm{i}p_0) \tag{2.37}$$

and is plotted in Figure 2.2. A coherent state has the same noise properties as a vacuum state except that it is shifted (displaced) from the origin.

The expectation values for the quadratures are the respective displacement from the origin given a complex amplitude $\alpha = \frac{1}{\sqrt{2}}(q_0 + \mathrm{i}p_0)$:

$$\langle\hat{q}\rangle_\alpha = q_0\,, \quad \langle p\rangle_\alpha = p_0\,. \tag{2.38}$$

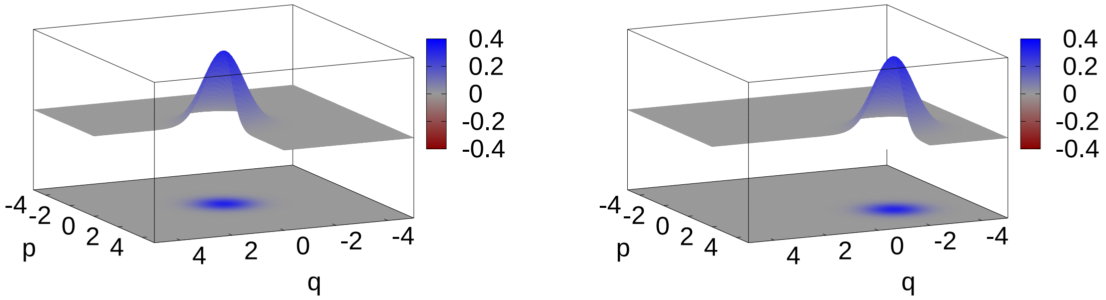

(a) Vacuum state $|0\rangle$.

(b) Coherent state $|\alpha\rangle$.

Figure 2.2.: Wigner functions of the vacuum and coherent state with $\alpha = \frac{1}{\sqrt{2}}(2\mathrm{i} - 2)$. Both states are minimum uncertainty states with the same noise properties. The coherent state is a displaced vacuum state.

2.1.5. Squeezed states

In the two previous sections the vacuum and coherent states were found to be minimum uncertainty states with $\Delta\hat{q}\Delta\hat{p} = \frac{1}{2}$. However, this equation does not mean that both standard deviations must be equal $\Delta\hat{q} = \Delta\hat{p} = \frac{1}{\sqrt{2}}$. Heisenberg's uncertainty relation is still fulfilled when the noise in one quadrature is smaller than $\frac{1}{\sqrt{2}}$ while the orthogonal quadrature shows a correspondingly higher noise, of course. A state with these properties is called a (quadrature) squeezed state.

A squeezed state is formally described by the unitary squeezing operator [Dru81, Wal94]

$$\hat{S}(\zeta) = \mathrm{e}^{\frac{1}{2}(\zeta\hat{a}^{\dagger 2} - \zeta^*\hat{a}^2)}\,, \tag{2.39}$$

where $\zeta = r\mathrm{e}^{-\mathrm{i}\phi}$ ($r \in \mathbb{R}^+$) is a complex number. One can show that the annihilation and creation operator of the light field are transformed like

$$\begin{aligned} \hat{S}^\dagger(\zeta)\hat{a}\hat{S}(\zeta) &= \hat{a}\cosh(r) + \hat{a}^\dagger\mathrm{e}^{-\mathrm{i}\phi}\sinh(r)\,, \\ \hat{S}^\dagger(\zeta)\hat{a}^\dagger\hat{S}(\zeta) &= \hat{a}^\dagger\cosh(r) + \hat{a}\mathrm{e}^{\mathrm{i}\phi}\sinh(r)\,. \end{aligned} \tag{2.40}$$

A generalized quadrature operator is then transformed like

$$\hat{S}^{\dagger}(\zeta)\hat{q}_{\theta}\hat{S}(\zeta) = \hat{q}_{\theta}\cosh(r) + \hat{q}_{-\phi-\theta}\sinh(r)\,. \tag{2.41}$$

The effect of squeezing becomes obvious when one looks at the orthogonal quadratures $\hat{q}_{\theta'}$ and $\hat{q}_{\theta''}$ with the phases $\theta' = -\frac{\phi}{2}$ and $\theta'' = \theta' + \frac{\pi}{2}$:

$$\begin{aligned} \hat{S}^{\dagger}(\zeta)\hat{q}_{\theta'}\hat{S}(\zeta) &= \hat{q}_{\theta'}\mathrm{e}^{+r}\,, \\ \hat{S}^{\dagger}(\zeta)\hat{q}_{\theta''}\hat{S}(\zeta) &= \hat{q}_{\theta''}\mathrm{e}^{-r}\,. \end{aligned} \tag{2.42}$$

This implies that the variance is increased (anti-squeezed) at the phase θ' and decreased (squeezed) at phase θ'':

$$\Delta^2\hat{S}^{\dagger}\hat{q}_{\theta'}\hat{S} = \mathrm{e}^{+2r}\Delta^2\hat{q}_{\theta'}\,, \quad \Delta^2\hat{S}^{\dagger}\hat{q}_{\theta''}\hat{S} = \mathrm{e}^{-2r}\Delta^2\hat{q}_{\theta''} \tag{2.43}$$

The variance of a vacuum state is $\Delta^2\hat{q} = \langle 0|\hat{q}^2|0\rangle - \langle 0|\hat{q}|0\rangle^2 = \frac{1}{2}$. A vacuum that is squeezed in q-direction (choose ϕ such that $\theta'' = 0$, i.e. $\phi = \pi$) has reduced variance along the q-axis and increased noise along the p-axis

$$\Delta^2\hat{q} = \frac{1}{2}\mathrm{e}^{-2r}\,, \quad \Delta^2\hat{p} = \frac{1}{2}\mathrm{e}^{+2r}\,. \tag{2.44}$$

Even though the variance along one axis drops below the vacuum noise, Heisenberg's uncertainty relation is still valid and a pure squeezed vacuum state stays a minimum uncertainty state

$$\Delta\hat{q}\cdot\Delta\hat{p} = \frac{1}{2}\,. \tag{2.45}$$

The Wigner function of a squeezed vacuum state is shown in Figure 2.3. The noise along one axis is reduced while it is increased along the orthogonal one. The formula for a Wigner function of a vacuum state squeezed in the q-quadrature ($\zeta = -r$) is

$$W_r(q,p) = \frac{1}{\pi}\exp(-\mathrm{e}^{2r}q^2 - \mathrm{e}^{-2r}p^2)\,. \tag{2.46}$$

The squeezing operator has quadratic terms of the creation operator which means that two photons are generated at the same time. This is reflected in the photon number distribution of a squeezed vacuum state [Scu97]

$$p(n) = \begin{cases} 0\,, & n \text{ odd} \\ \frac{n!}{(n/2)!^2}\frac{1}{\cosh(r)}\left(\frac{1}{2}\tanh(r)\right)^n & n \text{ even} \end{cases}\,. \tag{2.47}$$

The probability of finding an odd number of photons in a pure squeezed vacuum state is zero. The mean photon number of a squeezed vacuum is not zero, but $\langle\hat{n}\rangle = \sinh^2(r)$.

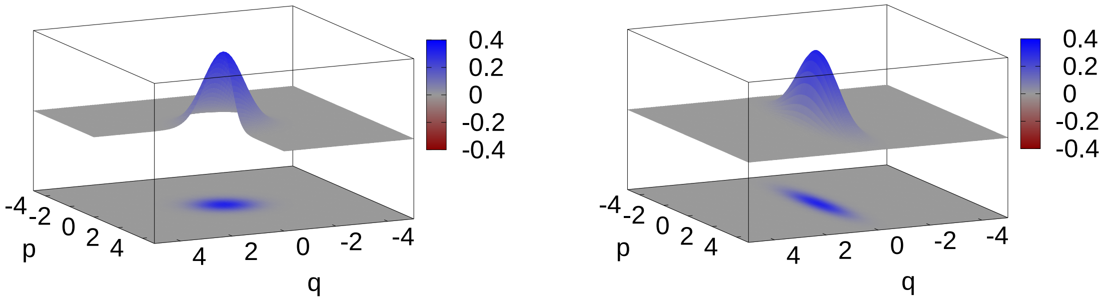

(a) Vacuum state $|0\rangle$.

(b) Squeezed vacuum state $\hat{S}(\zeta = -0.75)|0\rangle$.

Figure 2.3.: Wigner functions of the vacuum and squeezed vacuum state with $\zeta = -0.75$, i.e. $r = 0.75$, $\phi = \pi$. The noise of the squeezed state drops below the vacuum noise in one quadrature at the cost of higher noise in the orthogonal one.

2.1.6. Nonclassical states

All states of light can be expressed in the Fock basis, which is a consequence of the quantization of the electromagnetic field. It therefore seems an oxymoron to speak of classical states of light. However, due to the correspondence principle, there must be some formalism that represents the analogue of a classical harmonic oscillator. It was Erwin Schrödinger in 1926 who showed that states we know as coherent states today do the job [Sch26]. However, in the first place it seemed "bizarre" to him that superpositions of quantum mechanical eigenfunctions lead to the description of a classical system.

In 1963, Roy Glauber's famous paper on coherent states of light was published [Gla63]. Glauber found that the coherent states best describe classical light fields on a quantum mechanical basis. He also introduced the so-called P-function, which is a weight function for a state in the basis of coherent states

$$\hat{\rho} = \int d^2\alpha \, P(\alpha) \, |\alpha\rangle\langle\alpha| \, . \tag{2.48}$$

For a (pure) coherent state, $P(\alpha)$ is a δ-function, for a thermal state it is a Gaussian distribution. However, for many other states the P-function can be very ill-behaved: it can have negative values or strong singularities like derivatives of δ-functions. The P-function is then no longer a probability distribution. For example, a Fock state $|n\rangle$ contains a $2n$-order derivative of a δ-function [Ger05], for a squeezed vacuum state the order of derivatives is ∞ [Kie11]. These states and all states that cannot be described by a well-behaved P-function are *nonclassical.*

Nonclassical states are a resource in today's quantum technology research. When experimenters generate these state they obviously need tools to verify the nonclassicality. Due to the already mathematically challenging properties of the P-function, direct reconstruction of this distribution is impossible [Kie11]. Throughout this thesis I will make use of different criteria certifying nonclassicality:

1. Negative Wigner function: It is always possible to reconstruct the Wigner function of a state and negative values of this quasi-probability distribution clearly illustrate nonclassicality.

2. Quantum non-Gaussianity: The nonclassical properties of optical states are very sensitive to losses. If, for instance, a single photon state $|1\rangle$ is mixed with more than 50% of a vacuum state, its Wigner function does not show negative values anymore. However, it is still possible to certify strongly nonclassical properties with a criterion called quantum non-Gaussianity (QNG) [Fil11]. A state showing QNG cannot be expressed as a convex mixture of Gaussian states for which higher order nonlinearities are required. A more detailed presentation of this criterion is given in Chapter 5.

3. Nonclassical noise suppression: Squeezed states possess a positive (Gaussian) Wigner function. Nonetheless, their P-function is mathematically ill-behaved and nonclassical features become evident when analyzing the states' noise properties. Squeezed states have noise below the vacuum level in one quadrature at the cost of higher noise in the orthogonal quadrature.

These criteria are not the only measures of nonclassicality, of course. Especially when analyzing single photon sources there exists a variety of tools to analyze the states like anti-correlation parameters [Gra86] or the second order correlation function $g^{(2)}$. I will restrict the analysis to measures that are easy to understand, quite straightforward to apply and strong evidence for nonclassicality of quantum states.

2.2. Balanced homodyne detection

In Section 2.1.1 I have introduced the dimensionless quadrature operators $\hat{q}$ and $\hat{p}$ and the generalized quadrature operator

$$\hat{q}_\theta = \frac{1}{\sqrt{2}}(\hat{a}\mathrm{e}^{-\mathrm{i}\theta} + \hat{a}^\dagger \mathrm{e}^{\mathrm{i}\theta}) = \hat{q}\cos\theta + \hat{p}\sin\theta\,. \tag{2.49}$$

This can be made accessible experimentally by the method of balanced homodyne detection which I will introduce here.

In balanced homodyne detection the signal field of interest is overlapped with a local oscillator at a 50:50 (balanced) beam splitter. In the continuous wave case the local oscillator is a strong coherent light field with the same optical frequency as the signal field. In its optical path there is a phase shifter to set the relative phase ψ between the signal and the local oscillator.

A schematic of a balanced homodyne detector (BHD) is shown in Figure 2.4. The signal field enters the beam splitter in port a, the local oscillator in port b. The output ports c and d are recorded with photo detectors whose signals are subtracted and analyzed at a spectrum analyzer or oscilloscope.

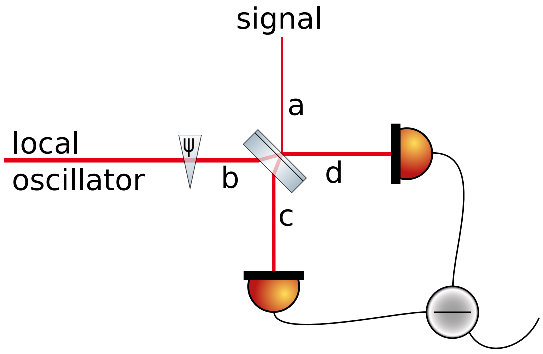

Figure 2.4.: Schematic of a balanced homodyne detector (BHD). A signal field is overlapped with a local oscillator field at a 50:50 beam splitter. The two output ports of the BHD are recorded with two photo detectors and electronically subtracted.

The output ports of the beam splitter read

$$\begin{aligned} \hat{c} &= \frac{1}{\sqrt{2}}(\hat{a} + \mathrm{i}\hat{b})\,, \\ \hat{d} &= \frac{1}{\sqrt{2}}(\hat{b} + \mathrm{i}\hat{a})\,. \end{aligned} \tag{2.50}$$

The photo currents $I_c \propto \langle \hat{c}^\dagger \hat{c} \rangle$ and $I_d \propto \langle \hat{d}^\dagger \hat{d} \rangle$ are subtracted. The difference signal reads

$$\begin{aligned} I_c - I_d &\propto \langle \hat{c}^\dagger \hat{c} - \hat{d}^\dagger \hat{d} \rangle \\ &= \mathrm{i}\langle \hat{a}^\dagger \hat{b} - \hat{a}\hat{b}^\dagger \rangle\,. \end{aligned} \tag{2.51}$$

Mode b is a strong field reaching the classical limit so that $\hat{b} = \beta \mathrm{e}^{-\mathrm{i}\omega t}$ with $\beta = |\beta|\mathrm{e}^{-\mathrm{i}\psi}$. We then get

$$I_c - I_d \propto |\beta| \langle \hat{a}\mathrm{e}^{\mathrm{i}\omega t}\mathrm{e}^{-\mathrm{i}\theta} + \hat{a}^\dagger \mathrm{e}^{-\mathrm{i}\omega t}\mathrm{e}^{\mathrm{i}\theta} \rangle\,, \tag{2.52}$$

where $\theta = \psi + \frac{\pi}{2}$. The signal field has the same frequency as the local oscillator and we can write $\hat{a} = \hat{a}_0 \mathrm{e}^{-\mathrm{i}\omega t}$. Using the generalized quadrature operator

$$\hat{q}_\theta = \frac{1}{\sqrt{2}} \left(\hat{a}_0 \mathrm{e}^{-\mathrm{i}\theta} + \hat{a}_0^\dagger \mathrm{e}^{\mathrm{i}\theta} \right) \tag{2.53}$$

we can write the photo detector difference as

$$I_c - I_d \propto \sqrt{2}|\beta| \langle \hat{q}_\theta \rangle\,. \tag{2.54}$$

The output of a BHD is the quadrature amplitude of the signal field, amplified by the local oscillator amplitude. When the signal port is blocked, the BHD measures vacuum fluctuations which are usually used as a reference for subsequent measurements. If the signal input is a squeezed vacuum state for instance, the noise drops significantly below the vacuum reference and reveals the nonclassical properties of the field. By scanning the relative phase between the signal and local oscillator field, one can continuously access the different quadratures of the signal. A balanced homodyne detector is also often used to perform a full tomography of a quantum state to reconstruct its Wigner function.

2.3. Nonlinear optics

Nonlinear optics is present in basically every quantum optics laboratory and fundamentally important for the generation of nonclassical states. In this section I will briefly introduce the basic processes that are relevant in the experimental realization of this thesis. The classical treatment basically follows the book by Boyd [Boy03] and plane waves are assumed (for deviations from this assumption and consequences see [Las07], e.g.).

2.3.1. Nonlinear polarization

The description of nonlinear processes is done via the dipole moment per unit volume, called the polarization P. The power series of P in terms of the electric field E reads

$$P(t) = \epsilon_0 \left(\chi^{(1)} E(t) + \chi^{(2)} E^2(t) + \chi^{(3)} E^3(t) + \dots\right) . \tag{2.55}$$

The first term describes the linear response of the system like the refractive properties of a material. Nonlinear optics starts with the second term. The nonlinear polarizations are proportional to the nonlinear susceptibilities of second ($\chi^{(2)}$) and third ($\chi^{(3)}$) order. In practice, these higher order susceptibilities are much smaller than the first order susceptibility $\chi^{(1)}$. This means that nonlinear optical phenomena require strong electric fields to become measurable.

2.3.2. Three wave mixing

Let a light field consist of two fields with (angular) frequency ω_1 and ω_2 so that

$$E(t) = E_1 \mathrm{e}^{-\mathrm{i}\omega_1 t} + E_2 \mathrm{e}^{-\mathrm{i}\omega_2 t} . \tag{2.56}$$

When this is inserted into the power series of the polarization Eq. (2.55), the nonlinear polarization of second order is given by

$$P^{(2)}(t) = \epsilon_0 \chi^{(2)} [E_1^2 \mathrm{e}^{-2\mathrm{i}\omega_1 t} + E_2^2 \mathrm{e}^{-2\mathrm{i}\omega_2 t} + 2E_1E_2 \mathrm{e}^{-\mathrm{i}(\omega_1+\omega_2)t} + 2E_1E_2 \mathrm{e}^{-\mathrm{i}(\omega_1-\omega_2)t}] . \tag{2.57}$$

Terms with $2\omega_j$ ($j = 1;2$) describe the generation of the second harmonic fields of E_j, while ($\omega_1 \pm \omega_2$) are the result of sum- and difference-frequency generation. By choosing appropriate phase matching conditions, one individual term can dominate the others that are suppressed. This way it is possible to run a system in sum- or difference-frequency generation mode only.

Sum-frequency generation

In sum-frequency generation the energy of two input fields adds up, generating a new field with a higher optical frequency. Let's assume that a nonlinear crystal is pumped with a field with frequency ω_2 and its amplitude is approximately constant along the crystal axis, i.e. $\frac{dE_2}{dz} = 0$ where z is the direction of the interaction. The sum-frequency generation happens, when a photon with frequency ω_1 combines with a pump photon. A new, high-energy photon is generated, $\omega_1 + \omega_2 = \omega_3$. Following Boyd [Boy03], the coupled equations of motion for the process are

$$\frac{dE_1}{dz} = K_1 E_3 \mathrm{e}^{-\mathrm{i}\Delta k z}\,, \tag{2.58}$$

$$\frac{dE_3}{dz} = K_3 E_1 \mathrm{e}^{+\mathrm{i}\Delta k z}\,, \tag{2.59}$$

where E_j ($j \in \{1, 2, 3\}$) are the amplitudes of the fields with frequency ω_j. The wave vectors for the fields are k_j and $\Delta k = k_1 + k_2 - k_3$ is the wave vector mismatch which will be discussed a little later. The complex constants K_j are defined as

$$K_1 = \frac{\mathrm{i}\omega_1^2 \chi^{(2)}}{k_1 c^2} E_2^*, \quad K_3 = \frac{\mathrm{i}\omega_3^2 \chi^{(2)}}{k_3 c^2} E_2\,. \tag{2.60}$$

The solutions of the coupled differential equations is formally given by

$$E_1(z) = (F\mathrm{e}^{\mathrm{i}gz} + G\mathrm{e}^{-\mathrm{i}gz})\mathrm{e}^{-\mathrm{i}\Delta k z/2}\,, \tag{2.61}$$

$$E_3(z) = (C\mathrm{e}^{\mathrm{i}gz} + D\mathrm{e}^{-\mathrm{i}gz})\mathrm{e}^{+\mathrm{i}\Delta k z/2}\,, \tag{2.62}$$

and shows oscillatory behavior. The coefficients C, D, F and G are to be determined from boundary conditions. Inserting the solution into Eq. (2.58) gives

$$\begin{aligned}&(\mathrm{i}gF\mathrm{e}^{\mathrm{i}gz} - \mathrm{i}gG\mathrm{e}^{-\mathrm{i}gz})\mathrm{e}^{-\mathrm{i}\Delta k z/2} - \frac{1}{2}\mathrm{i}\Delta k(F\mathrm{e}^{\mathrm{i}gz} + G\mathrm{e}^{-\mathrm{i}gz})\mathrm{e}^{-\mathrm{i}\Delta k z/2}\\ &= (K_1 C\mathrm{e}^{\mathrm{i}gz} + K_1 D\mathrm{e}^{-\mathrm{i}gz})\mathrm{e}^{-\mathrm{i}\Delta k z/2}\end{aligned} \tag{2.63}$$

and

$$\begin{aligned}&(\mathrm{i}gC\mathrm{e}^{\mathrm{i}gz} - \mathrm{i}gD\mathrm{e}^{-\mathrm{i}gz})\mathrm{e}^{+\mathrm{i}\Delta k z/2} + \frac{1}{2}\mathrm{i}\Delta k(C\mathrm{e}^{\mathrm{i}gz} + D\mathrm{e}^{-\mathrm{i}gz})\mathrm{e}^{+\mathrm{i}\Delta k z/2}\\ &= (K_3 F\mathrm{e}^{\mathrm{i}gz} + K_3 G\mathrm{e}^{-\mathrm{i}gz})\mathrm{e}^{+\mathrm{i}\Delta k z/2}\,.\end{aligned} \tag{2.64}$$

These relations have to be fulfilled by the terms varying with $\mathrm{e}^{+\mathrm{i}gz}$ and $\mathrm{e}^{-\mathrm{i}gz}$ separately so that one obtains a set of linear equations

$$\begin{pmatrix} \mathrm{i}(g - \frac{1}{2}\Delta k) & -K_1 \\ -K_3 & \mathrm{i}(g + \frac{1}{2}\Delta k) \end{pmatrix} \begin{pmatrix} F \\ C \end{pmatrix} = 0\,. \tag{2.65}$$

A solution exists if the determinant of the matrix vanishes, i.e.

$$g^2 = -K_1 K_3 + \frac{1}{4}\Delta k^2 \tag{2.66}$$

and with the definition $\kappa^2 = -K_1 K_3$ we can write

$$g = \sqrt{\kappa^2 + \frac{1}{4}\Delta k^2}\,. \tag{2.67}$$

Assuming that there is no field with frequency ω_3 at the input ($E_3(0) = 0$) and knowing the strength of $E_1(0)$, we can determine the coefficients

$$\begin{aligned} C = -D \;&=\; -\frac{\mathrm{i}}{2}\frac{K_3}{g}E_1(0)\,, \\ F &= \frac{1}{2}E_1(0) + \frac{1}{4}\frac{\Delta k}{g}E_1(0)\,, \\ G &= \frac{1}{2}E_1(0) - \frac{1}{4}\frac{\Delta k}{g}E_1(0)\,. \end{aligned} \tag{2.68}$$

With this the amplitudes of the fields evolve as

$$E_1(z) = \left(E_1(0)\cos(gz) + \frac{\mathrm{i}\Delta k}{2g}E_1(0)\sin(gz)\right)\mathrm{e}^{-\mathrm{i}\Delta k z/2}\,, \tag{2.69}$$

$$E_3(z) = \frac{K_3}{g}E_1(0)\sin(gz)\mathrm{e}^{\mathrm{i}\Delta k z/2} \tag{2.70}$$

and the intensity of the generated field is proportional to

$$|E_3(z)|^2 = |E_1(0)|^2\frac{|K_3|^2}{g^2}\sin^2(gz)\,. \tag{2.71}$$

If the wave vector mismatch Δk is zero, g is minimal and the intensity of the generated field is maximized. For an increasing wave vector mismatch, the maximum achievable intensity of the generated field decreases but is obtained at an earlier point. This behavior is illustrated in Figure 2.5. A special case of sum-frequency generation is when $\omega_1 = \omega_2$ and therefore $\omega_3 = 2\omega_1$. This is called second harmonic generation (SHG).

Difference-frequency generation

In difference frequency generation two photons at frequencies ω_3 and ω_1 combine to a new photon at their difference frequency $\omega_2 = \omega_3 - \omega_1$. We assume that the field at frequency ω_3 is constant throughout the process so that $\frac{dE_3}{dz} = 0$. The coupled equations for the other two amplitudes read

$$\begin{aligned} \frac{dE_1}{dz} &= \frac{\mathrm{i}\omega_1^2\chi^{(2)}}{k_1 c^2}E_3 E_2^* \mathrm{e}^{\mathrm{i}\Delta k z}\,, \\ \frac{dE_2}{dz} &= \frac{\mathrm{i}\omega_2^2\chi^{(2)}}{k_2 c^2}E_3 E_1^* \mathrm{e}^{\mathrm{i}\Delta k z}\,, \end{aligned} \tag{2.72}$$

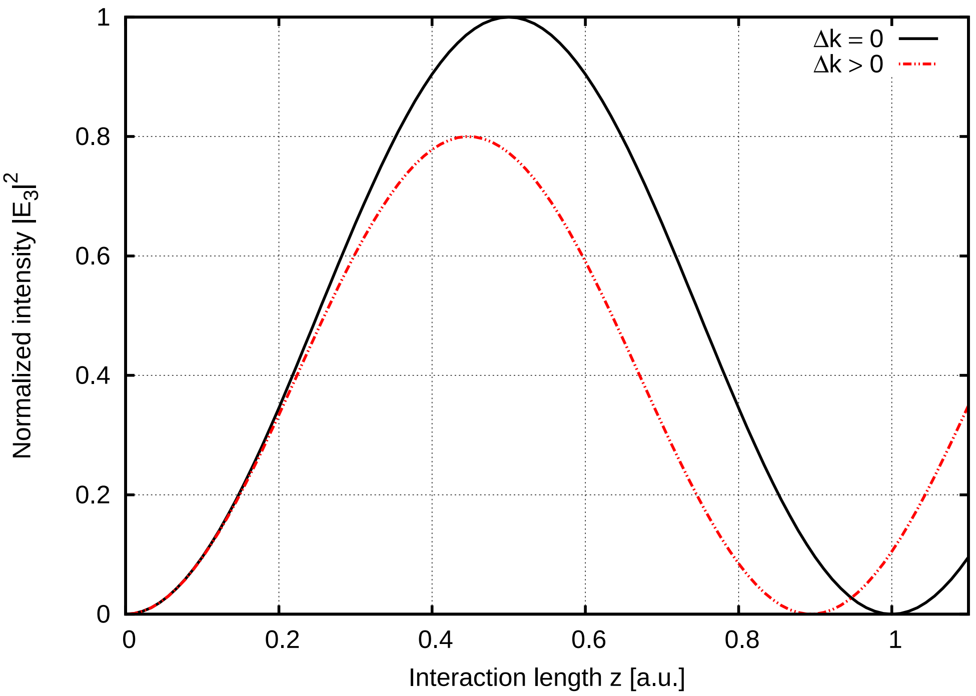

Figure 2.5.: The sum-frequency intensity $|E_3|^2$ as a function of the interaction length and two different phase mismatches Δk assuming plane waves. Maximum intensity can be obtained for zero phase mismatch and a certain interaction length. After this point the generated field gets converted back to the field at frequency ω_1 [Bau11, Sam12].

and have the solution

$$\begin{aligned} E_1(z) &= \left[E_1(0)\left(\cosh(gz) - \frac{\mathrm{i}\Delta k}{2g}\sinh(gz)\right) + \frac{\kappa_1}{g}E_2^*(0)\sinh(gz)\right]\mathrm{e}^{\mathrm{i}\Delta kz/2}\,, \\ E_2(z) &= \left[E_2(0)\left(\cosh(gz) - \frac{\mathrm{i}\Delta k}{2g}\sinh(gz)\right) + \frac{\kappa_2}{g}E_1^*(0)\sinh(gz)\right]\mathrm{e}^{\mathrm{i}\Delta kz/2}\,, \end{aligned} \tag{2.73}$$

where

$$g = \sqrt{K_1K_2^* - \frac{1}{4}\Delta k^2} \quad \text{and} \quad K_j = \frac{\mathrm{i}\omega_j^2\chi^{(2)}E_3}{k_jc^2}\,. \tag{2.74}$$

With constant pump power (frequency ω_3) and optimal[1] phase matching $\Delta k = 0$ the low frequency fields are amplified. The generated field at ω_2 stimulates the generation of the field at ω_1 and vice versa. The process is also called parametric amplification.

---

[1] Plane waves are assumed here. In a full treatment with Gaussian beams, slight modifications have to be taken into account [Las07]

Optical parametric oscillator (OPO)

An optical parametric oscillator is a device where parametric amplification is enhanced by embedding the nonlinear medium in an optical resonator and driving the system above the so-called oscillation threshold. This is the point where the pump field is so strong that the internal amplification is higher than the round trip losses of the resonator. The OPO then starts acting as a laser and when operated far above the oscillation threshold it emits coherent beams at the frequencies ω_1 and ω_2. Vacuum fluctuations initialize the process and no seed field besides the pump field is required as input to the system. Only resonance conditions of the cavity and phase matching determines what the output frequencies are. One could imagine that these are many parameters and an OPO is a rather complex system. It has to be stabilized very carefully to handle longitudinal mode hops and cluster jumps, both changing the output frequencies significantly. I will not treat the OPO with all its properties here and refer the reader to the detailed analysis of Eckhardt [Eck91]. An experimental study of the OPO as the fundamental light source used throughout this thesis can be found in my master thesis [Bau11] and in the doctoral theses of Aiko Samblowski [Sam12] and Christina Vollmer [Vol14a].

Despite the complexity of an OPO, I will briefly describe the basic mechanisms using a classical treatment. As mentioned before, the oscillation starts when a threshold condition is fulfilled, that is when the amplification of the fields at ω_1 and ω_2 exceeds the round trip loss. Round trip losses are absorption, scattering or simply the transmission through the resonator's outcoupling mirror that has a reflectivity of $R_{1|2}$ for the fields at $\omega_{1|2}$. The incoupling mirror is assumed to have perfect reflectivity for both frequencies and the system is not a cavity for the pump field. Using the solutions for the difference frequency generation Eq. (2.73) and $\Delta k = 0$ for simplicity we get

$$\begin{aligned} E_1(0) &= \left[E_1(0)\cosh(gL) + \frac{\kappa_1}{g}E_2^*(0)\sinh(gL)\right](1-l_1)\,, \\ E_2^*(0) &= \left[E_2^*(0)\cosh(gL) + \frac{\kappa_2^*}{g}E_1(0)\sinh(gL)\right](1-l_2)\,, \end{aligned} \tag{2.75}$$

where $l_j = 1 - R_j \mathrm{e}^{-\beta_j L}$ ($j = \mathrm{in}, \mathrm{out}$) is the fraction of power that gets lost internally ($\beta_{1|2}$ are the loss coefficients) or due to transmission through the outcoupling mirror. The two equations can be solved to provide the threshold condition

$$\cosh(gL) > 1 + \frac{l_1 l_2}{2 - l_1 - l_2}\,, \tag{2.76}$$

which simplifies for $l_j \ll 1$ as one can approximate $\cosh(x) = 1 + \frac{1}{2}x^2$:

$$g^2L^2 > l_1 l_2\,. \tag{2.77}$$

The factor g^2 is dependent on the pump power which is proportional to $|E_3|^2$ so that the threshold condition is usually given in terms of the pump power.

By replacing g with $g\,\mathrm{sinc}(\Delta kL/2)$, the analysis can be easily generalized to non-perfect phase matching. As a result one obtains a gain profile depending on the phase mismatch Δk in which oscillations can appear. Another condition is that both fields have to be simultaneously resonant which is non-trivial for $\omega_1 \neq \omega_2$. Oscillations do not necessarily appear for $\Delta k = 0$. Far above the threshold for one pair of frequencies ω_1 and ω_2, other pairs might fulfill the threshold condition as well, making the system run in a multi-frequency mode. Beyond that, tiny changes in the resonance conditions or phase mismatch may lead the system to "jump" to another frequency pair. This effect may be wanted as the output frequencies can be tuned in a quite wide range. However, stable control of phase matching and resonance conditions is required to maintain the oscillation at a specific frequency pair once it is set to a preferred operational point. Especially in the experiments presented in this thesis the performance of subsequent systems strongly depend on the output frequencies of the OPO.

An optical parametric oscillator below threshold is called optical parametric amplifier (OPA). Below threshold, the pump power is not high enough to lead to parametric oscillation. However, optical fields are generated which are not coherent fields but photon pairs with sub-Poissonian statistics; always two photons at ω_1 and ω_2 at a time. In this thesis an OPA is used to generate photon pairs at well separated optical frequencies. The degenerate case $\omega_1 = \omega_2$ is also very interesting: it is the resource of squeezed vacuum states. Both, the degenerate and non-degenerate OPA are working horses of uncountable quantum optics experiments and developed to standard tools in quantum information science and quantum metrology. I will present a quantum mechanical treatment of these systems in following chapters.

2.4. Frequency up-conversion of quantum states

In the previous sections I introduced the concept of sum-frequency generation with classical optics. Here, I will present a quantum mechanical treatment of the process and show that quantum states can be frequency up-converted. I closely follow the description by Prem Kumar [Kum90], who also demonstrated quantum up-conversion for the first time in the early 1990s [Hua92].

We have seen that in sum-frequency generation two photons with frequency ω_1 and ω_2 can combine to a new photon at frequency $\omega_3 = \omega_1 + \omega_2$. The effective Hamiltonian for this process is

$$\mathbf{H}'_{\text{eff}} = \mathrm{i}\hbar\zeta'(\hat{a}_1\hat{a}_2\hat{a}_3^\dagger - \hat{a}_1^\dagger\hat{a}_2^\dagger\hat{a}_3)\,, \tag{2.78}$$

where the coupling constant ζ' describes the nonlinear optical interaction and is proportional to the nonlinear susceptibility $\chi^{(2)}$. In the following we assume that the field at frequency ω_2 is a strong pump field so that it is assumed not to be affected by the process and remains undepleted. The Hamiltonian then reduces to

$$\mathbf{H}_{\text{eff}} = \mathrm{i}\hbar\zeta(\hat{a}_1\hat{a}_3^\dagger - \hat{a}_1^\dagger\hat{a}_3)\,, \tag{2.79}$$

where $\zeta = \zeta'\langle\hat{a}_2\rangle$. In the interaction picture one obtains the Heisenberg equations of motion for the operators $\hat{a}_1$ and $\hat{a}_3$

$$\begin{aligned}\frac{d\hat{a}_1}{dt} &= \frac{\mathrm{i}}{\hbar}[\mathbf{H}_{\text{eff}}, \hat{a}_1] \\ &= \frac{\mathrm{i}}{\hbar}\mathrm{i}\hbar\zeta[\hat{a}_1\hat{a}_3^\dagger - \hat{a}_1^\dagger\hat{a}_3, \hat{a}_1] \\ &= -\zeta\left(\hat{a}_1\underbrace{[\hat{a}_3^\dagger, \hat{a}_1]}_{0} + \underbrace{[\hat{a}_1, \hat{a}_1]}_{0}\hat{a}_3^\dagger - \hat{a}_1^\dagger\underbrace{[\hat{a}_3, \hat{a}_1]}_{0} - \underbrace{[\hat{a}_1^\dagger, \hat{a}_1]}_{-1}\hat{a}_3\right) \\ &= -\zeta\hat{a}_3\,,\end{aligned} \tag{2.80}$$

$$\begin{aligned}\frac{d\hat{a}_3}{dt} &= \frac{\mathrm{i}}{\hbar}[\mathbf{H}_{\text{eff}}, \hat{a}_3] \\ &= \frac{\mathrm{i}}{\hbar}\mathrm{i}\hbar\zeta[\hat{a}_1\hat{a}_3^\dagger - \hat{a}_1^\dagger\hat{a}_3, \hat{a}_3] \\ &= -\zeta\left(\hat{a}_1\underbrace{[\hat{a}_3^\dagger, \hat{a}_3]}_{-1} + \underbrace{[\hat{a}_1, \hat{a}_3]}_{0}\hat{a}_3^\dagger - \hat{a}_1^\dagger\underbrace{[\hat{a}_3, \hat{a}_3]}_{0} - \underbrace{[\hat{a}_1^\dagger, \hat{a}_3]}_{0}\hat{a}_3\right) \\ &= \zeta\hat{a}_1\,.\end{aligned} \tag{2.81}$$

These coupled differential equations have the solution

$$\begin{aligned}\hat{a}_1(t) &= \hat{a}_1(0)\cos(\zeta t) - \hat{a}_3(0)\sin(\zeta t) \\ \hat{a}_3(t) &= \hat{a}_3(0)\cos(\zeta t) + \hat{a}_1(0)\sin(\zeta t)\,.\end{aligned} \tag{2.82}$$

At times $t = \frac{\pi}{2\zeta}$ we have full conversion as

$$\hat{a}_1(t = \frac{\pi}{2\zeta}) = -\hat{a}_3(0) \quad \text{and} \quad \hat{a}_3(t = \frac{\pi}{2\zeta}) = \hat{a}_1(0)\,. \tag{2.83}$$

The time of full conversion depends on the pump power which is proportional to the squared pump amplitude $P_2 \propto \langle\hat{a}_2\rangle^2$.

During the process all quantum properties are maintained. Given that a state is prepared as $|\Psi\rangle = |\psi\rangle_1|\phi\rangle_3$, the expectation values are $\langle\hat{f}_1\rangle := \langle\Psi|\hat{f}_1(\hat{a}_1)|\Psi\rangle$ and $\langle\hat{f}_3\rangle := \langle\Psi|\hat{f}_3(\hat{a}_3)|\Psi\rangle$. The functions $\hat{f}_1$ and $\hat{f}_3$ depend on $\hat{a}_1$ and $\hat{a}_3$. For $t = 0$ the quantum properties are described by the individual states $|\psi\rangle_1$ and $|\phi\rangle_3$ as

$$\begin{aligned}\langle\hat{f}_1\rangle_{t=0} &= {}_1\langle\psi|\hat{f}_1(\hat{a}_1(0))|\psi\rangle_1\,, \\ \langle\hat{f}_3\rangle_{t=0} &= {}_3\langle\phi|\hat{f}_3(\hat{a}_3(0))|\phi\rangle_3\,.\end{aligned} \tag{2.84}$$

At $t = \frac{\pi}{2\zeta}$ these properties are in the other mode as

$$\begin{aligned}\langle\hat{f}_1\rangle_{t=\frac{\pi}{2\zeta}} &= {}_3\langle\phi|\hat{f}_1(-\hat{a}_3(0))|\phi\rangle_3\,, \\ \langle\hat{f}_3\rangle_{t=\frac{\pi}{2\zeta}} &= {}_1\langle\psi|\hat{f}_3(\hat{a}_1(0))|\psi\rangle_1\,.\end{aligned} \tag{2.85}$$

The process of quantum up-conversion is illustrated in Figure 2.6. In this thesis the signal is converted from the infrared wavelength 1550 nm into the visible spectrum at 532 nm while using a strong pump field at 810 nm.

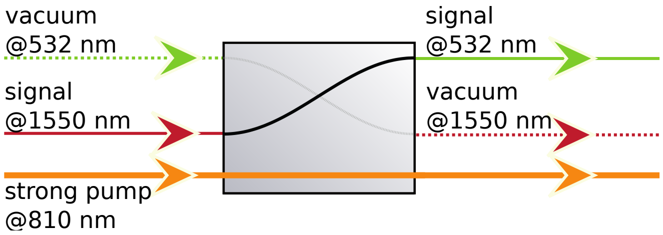

Figure 2.6.: Illustration of quantum up-conversion. A signal field at 1550 nm is converted to 532 nm using a strong pump field which is assumed not to be affected by the process. The illustration was first published in [Vol14b].

Phase noise

The assumption that the field at ω_2 (810 nm) is just driving the conversion process and its properties are not affecting the up-converted state is valid only if the classical noise is negligible. If the pump field's phase ϕ_p (defined as the difference phase between the pump field and the input signal) is included in the treatment, the coupling constant ζ can be written as $\zeta = |\zeta|\mathrm{e}^{\mathrm{i}\phi_p}$. The evolutions of the operators are then given by

$$\begin{aligned}\hat{a}_1(t) &= \hat{a}_1(0)\cos(|\zeta|t) - \hat{a}_3(0)\frac{\zeta^*}{|\zeta|}\sin(|\zeta|t)\\ \hat{a}_3(t) &= \hat{a}_3(0)\cos(|\zeta|t) + \hat{a}_1(0)\frac{\zeta}{|\zeta|}\sin(|\zeta|t)\,.\end{aligned} \tag{2.86}$$

After the time $t = \pi/2\zeta$ the state is transferred from $\hat{a}_1$ to $\hat{a}_3$ and the pump field's phase is imprinted on the up-converted state:

$$\hat{a}_2\left(\frac{\pi}{2\zeta}\right) = \hat{a}_1(0)\mathrm{e}^{\mathrm{i}\phi_p}\,. \tag{2.87}$$

If the pump phase fluctuates also the up-converted state's phase fluctuates. This is critical if the states are phase sensitive as squeezed states are for example. A stable pump phase is therefore required.

3. Frequency up-conversion of squeezed vacuum states

C. Baune, J. Gniesmer, A. Schönbeck, C. E. Vollmer, J. Fiurášek, and R. Schnabel
Strongly squeezed states at 532 nm based on frequency up-conversion
Optics Express **23**, 16035 (2015)

Squeezed vacuum states of light are an important resource in modern quantum metrology. For example, the recent detection of gravitational waves opened a new era of astronomy [LIG16], and it is foreseeable that besides the detector GEO600 close to Hanover, Germany [Gro13] also the aLIGO detectors in the USA will apply squeezed states for further sensitivity improvements. The generation of squeezed vacuum states is very well established in the infrared wavelength regime and a shot noise suppression of more than 12.3 dB was demonstrated at 1064 and 1550 nm [Ebe10, Meh11]. However, squeezed states of light are required at a variety of optical wavelengths.

The standard method for the generation of squeezed vacuum states of light – parametric down-conversion utilizing a second harmonic pump field – cannot be applied at short wavelengths. Up to today, no nonlinear materials are available showing low optical absorption and sufficiently high nonlinear susceptibilities for ultraviolet fields that would be required as pump fields. These fields lead to disturbing effects like blue light induced infrared absorption (BLIIRA) [Mab94] or photo-refractive damage. Alternative approaches to produce squeezed states at visible wavelengths are based on four-wave-mixing [Slu85], self-phase modulation [Ber91] or second-harmonic generation [Tsu95]. None of these processes has shown to enable the generation of squeezed vacuum states with a reasonably high nonclassical noise suppression.

The most promising approach to obtain squeezed states at short wavelengths is their generation at infrared wavelengths and subsequent frequency up-conversion. By mixing a squeezed vacuum field at infrared wavelengths with an intense pump field, the nonclassical noise properties can be transferred to a field with a much higher optical frequency, i.e. shorter wavelength. This chapter presents an experiment following this approach, which was initiated during the doctoral theses of Aiko Samblowski [Sam12] and Christina Vollmer [Vol14a], who both supervised me during my master thesis [Bau11]. First results were published in *Physical Review Letters* **112** where we showed a nonclassical noise suppression of 1.5 dB below the vacuum reference [Vol14b]. In my work presented in the following the squeezing strength could be significantly increased, and a nonclassical noise suppression of 5.5 dB below the shot noise is demonstrated.

In Section 3.1 theoretical formulae for squeezed vacuum states that are subject to frequency up-conversion are given. The experimental setup is explained in detail in

Section 3.2. After that the measurement results are presented as well as a demonstration of the applicability of the up-converted states in a proof-of-principle quantum metrology setup (Section 3.3). The chapter concludes with a discussion and an outlook.

3.1. Degenerate parametric down-conversion and squeezing

The degenerate optical parametric amplifier (OPA) is the common resource of squeezed vacuum states of light. It generally consists of an optical cavity and a non-linear optical medium inside which is driven with a second harmonic pump field. In the degenerate down-conversion process one pump photon decays into two photons. By applying a balanced homodyne detection (BHD) scheme, cf. Section 2.2, different quadratures of the light field can be analyzed. If the phase of the BHD is set appropriately, squeezed noise statistics are revealed while anti-squeezed statistics are measured in the orthogonal quadrature.

The output spectra of an OPA for the two extremal quadratures are given by

$$\begin{aligned} S^{+}(\omega) &= \frac{1}{2} + \eta \frac{2\gamma|\varepsilon|}{\lambda^2 + \omega^2}\,, \\ S^{-}(\omega) &= \frac{1}{2} - \eta \frac{2\gamma|\varepsilon|}{\mu^2 + \omega^2}\,, \end{aligned} \tag{3.1}$$

where ω is the sideband (angular) frequency, γ is the leakage rate of the cavity, and the pump parameter ε is proportional to the pump field amplitude. The state is detected with an efficiency η, that includes propagation losses and a finite detection efficiency of the BHD. Furthermore, I used the abbreviations $\lambda = \gamma - |\varepsilon|$ and $\mu = \gamma + |\varepsilon|$. A detailed derivation of the power spectrum is given in the appendix, Section A.3.

The spectrum mentioned above directly describes the output of an OPA. However, during the process of frequency up-conversion the state passes another cavity that introduces additional frequency filtering. The output spectrum is then given by

$$\begin{aligned} S^{+}_{\text{fil}}(\omega) &= \frac{1}{2} + \eta \frac{\kappa^2}{\kappa^2 + \omega^2} \frac{2\gamma|\varepsilon|}{\lambda^2 + \omega^2}\,, \\ S^{-}_{\text{fil}}(\omega) &= \frac{1}{2} - \eta \frac{\kappa^2}{\kappa^2 + \omega^2} \frac{2\gamma|\varepsilon|}{\mu^2 + \omega^2}\,, \end{aligned} \tag{3.2}$$

where κ is the decay rate of the additional sum-frequency generation cavity.

In Figure 3.1 the power spectrum is shown for a squeezed and anti-squeezed quadrature, both with and without an additional frequency filter. The degree of squeezing degrades for increasing sideband frequencies. A larger cavity decay rate γ (γ/π is FWHM) would increase the bandwidth of the squeezed states at the cost of the need for a higher pump parameter ε. Thus, if the pump power is limited as it is in the experiment presented below, a compromise has to be found. The same argument holds for the bandwidth of the frequency up-conversion cavity; if its bandwidth κ was increased,

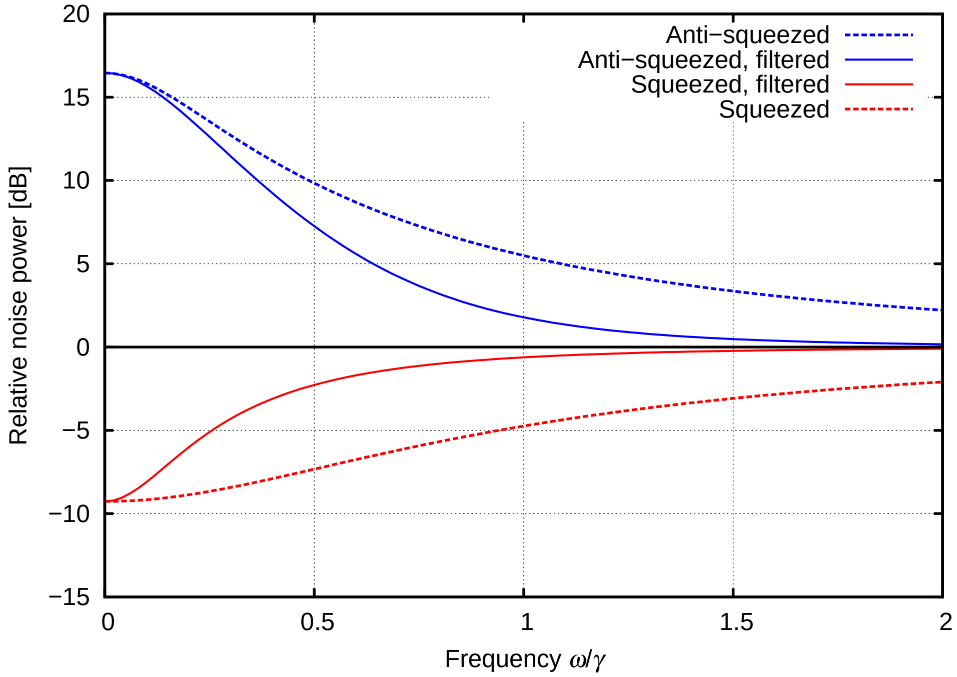

Figure 3.1.: Logarithmic power spectrum of an OPA with and without additional frequency filtering relative to the vacuum reference. The power spectrum of the (anti-)squeezed quadrature is shown in red (blue). The dashed lines represent states without additional filtering, while the solid lines are states that passed an additional frequency filter with $\kappa = 0.5\gamma$. Other parameters are $\eta = 0.9$, $|\varepsilon| = 0.75\gamma$.

the squeezing would be stronger at higher frequencies, but a higher pump power would be needed to achieve the same conversion efficiency since the intra-cavity buildup is necessary to achieve a sufficiently strong nonlinearity [Sam14].

3.2. Experimental setup

The experimental setup is illustrated in Figure 3.2. I will briefly introduce the main components in the following.

3.2.1. Laser source and second harmonic generation

The laser driving the whole experiment is a neodymium-doped Yttrium Aluminum Garnet (Nd:YAG) solid state laser (*Mephisto* by InnoLight) providing up to 2.1 W of light at a wavelength of 1064 nm (crystal temperature 25.74°C, injection current 2.3 A). The laser is optically decoupled from subsequent optics with an optical isolator (not shown in the figure).

The 1064 nm light is frequency doubled in a second harmonic generation (SHG) cavity

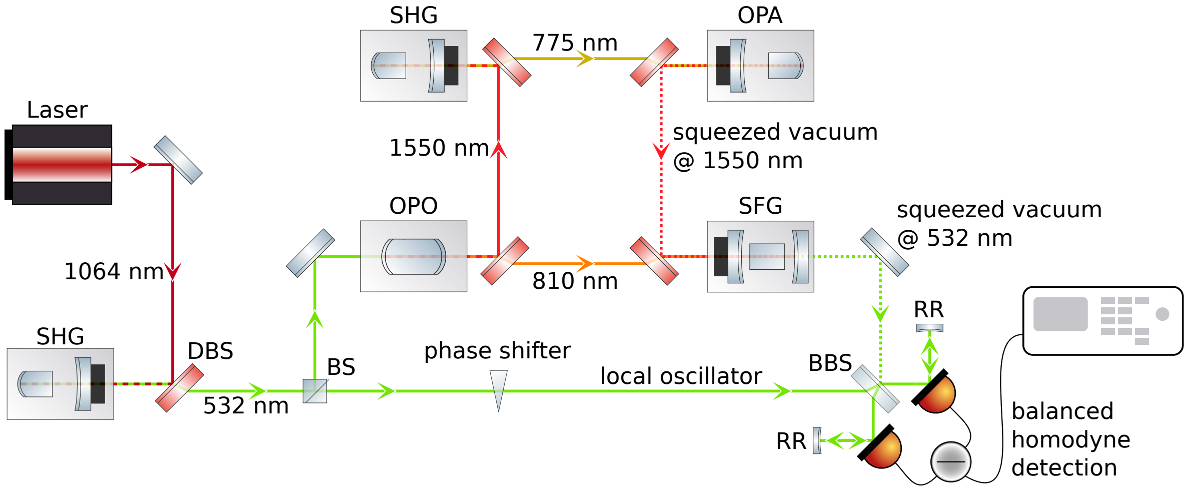

Figure 3.2.: Schematic of the experimental setup involving five nonlinear optical processes. A 1064 nm laser beam is frequency doubled in a second harmonic generation (SHG) cavity. The resulting 532 nm beam with a power of about 1 W was split at a beam splitter (BS). Bright 810 and 1550 nm fields were produced via cavity-assisted non-degenerate optical parametric oscillation (OPO). The 1550 nm field is converted to 775 nm in another SHG. Squeezed vacuum states (illustrated by dashed lines) at 1550 nm were produced in a degenerate optical parametric amplification cavity (OPA) and up-converted in the sum-frequency generation cavity (SFG) to 532 nm. All cavities are decoupled from each other with optical isolators (not shown). The local oscillator for homodyne detection was provided by the second output port of the BS to ensure frequency stability with the up-converted state. DBS: dichroic beam splitter, BBS: balanced beam splitter, RR: retro-reflector.

consisting of a 7% doped MgO:LiNbO$_3$ crystal embedded in an oven for temperature stabilization. The back surface of the crystal is curved (radius of curvature: 8 mm) and highly reflective for both the fundamental field (1064 nm) and the second harmonic field (532 nm). The outcoupling mirror has a radius of curvature of 20 mm and a reflectivity of $R = 90\%$ for 1064 nm and $R < 4\%$ for 532 nm. The mirror is placed symmetrically with respect to the crystal's optical axis, leading to a stable cavity with a waist of about 25 µm. Length control is performed utilizing the Pound-Drever-Hall (PDH) technique [Bla01] with a (de-)modulation frequency of 15 MHz, and the crystal is actively temperature stabilized to a temperature of about 67°C. At this point the maximum output power was achieved.

The second harmonic light is subsequently filtered in a three mirror resonator (not shown in the Figure) to suppress technical noise and provide a clean TEM$_{00}$ spatial mode. This resonator is also actively stabilized using the PDH technique (29.5 MHz). The cavity's length is actuated with a piezo and a Peltier element, that are glued to one of the mirrors and the spacer, respectively. Up to 1 W of laser power at 532 nm is measured directly after the filter resonator.

The green light is split up at a variable beam splitter consisting of a half-wave plate and a polarizing beam splitter cube. The transmitted part is used as local oscillator for homodyne detection while the reflected part serves as the pump field for the non-degenerate OPO.

3.2.2. Non-degenerate optical parametric oscillator

A non-degenerate optical parametric oscillator (OPO) provides both the pump for the sum-frequency generation cavity (810 nm) and the SHG (1550 nm, required for squeezed state generation). It is a 8.9 mm long periodically poled potassium titanyl phosphate (PPKTP) crystal with two mirrors directly coated onto two curved surfaces (8 mm radii of curvature). The reflectivities for 810 and 1550 nm are $R = 99.9\%$ at the incoupling mirror and $R = 94\%$ at the outcoupling mirror. Thereby a monolithic cavity is built for the two generated infrared fields. The device is driven with 1 W of light at 532 nm for which only the outcoupling mirror is highly reflective and the incoupling mirror is anti-reflective.

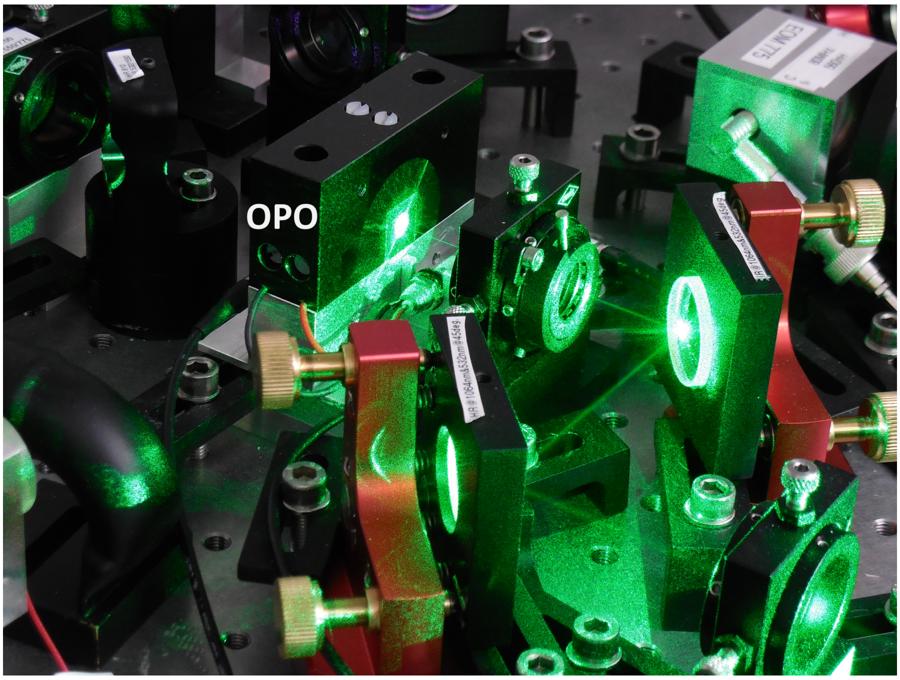

Figure 3.3.: The optical parametric oscillator (OPO). The nonlinear crystal is embedded in temperature stabilized housing (black plastic) and pumped with about 1 W of light at 532 nm.

Active temperature control of the crystal ensures stable resonance conditions for the two generated fields as well as phase matching. This is of great importance as tiny variations of the temperature change the output wavelengths quite significantly. Despite its simple architecture, the OPO's behavior is complex, and so-called (small) mode hops and (larger) cluster jumps occur when the temperature is changed. These features have been extensively studied theoretically [Eck91] and the OPO used throughout this thesis shows a behavior as shown in Figure 3.4.

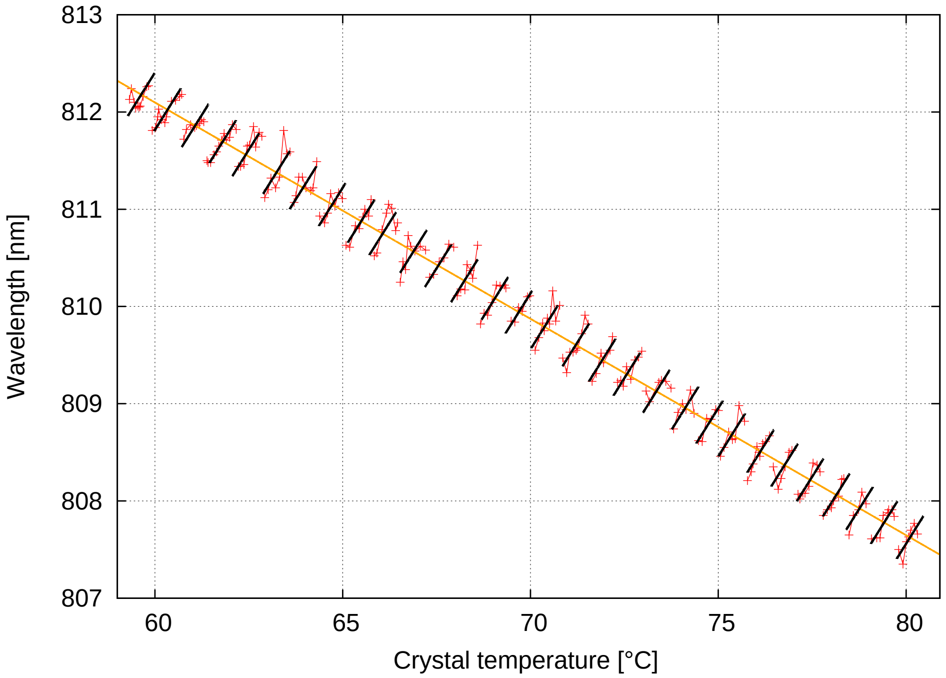

Figure 3.4.: Dependence of the OPO's output wavelength on a variation of the crystal's temperature. An increasing temperature at first leads to a slight increase in the wavelength around 810 nm (small mode hops) while the general trend has negative slope (large cluster jumps). For details also see [Bau11, Vol14a, Sam12]. Plot created by Aiko Samblowski.

An increasing temperature at first leads to a slight increase in the wavelength around 810 nm (small mode hops) while the general trend has negative slope (large cluster jumps). Due to energy conservation, the opposite behavior is true for the twin beam of about 1550 nm, of course. More details on the occurence and origin of the mode hops and cluster jumps can be found in [Bau11, Vol14a].

The operation point was chosen such that the NTC element directly attached to the crystal showed a value of about 16 kΩ corresponding to a temperature of 67°C. The efficiencies of three subsequent nonlinear optical cavities strongly depend on the output wavelengths of the OPO and this operation point was found to be optimal. As mentioned before, the temperature stabilization has to be very reliable and tiny variations can lead to significant changes of the output wavelengths such that the subsequent experiment does not work efficiently enough. However, once a stable operation point is achieved, the cover of the optical table and an air conditioning system in the laboratory help to suppress air and temperature fluctuations around the OPO. Continuous operation for hours is then possible and powers of about 210 and 110 mW are measured at 810 and 1550 nm, respectively.

3.2.3. Second harmonic generation from 1550 to 775 nm

The 1550 nm output of the OPO was used to pump a second harmonic generation (SHG) cavity to provide a 775 nm field. This SHG consists of a PPKTP crystal with one planar and anti-reflectively coated surface. The second surface is curved (radius of curvature 12 mm) and highly reflective for 1550 nm and 775 nm. The coupling mirror has an inner radius of curvature of 25 mm and reflectivities of 85% for 1550 nm and 97.5% for 775 nm. This way the cavity is doubly resonant for both the fundamental and second harmonic field and the conversion efficiency is much higher for low pump powers, which was limiting the available pump power in the previous experiment [Vol14b]. Furthermore a doubly resonant SHG allows to use the 775 nm field for length stabilization via the PDH technique. Therefore, a phase modulation (21.6 MHz) is imprinted on the fundamental field, which is then also converted to the second harmonic field. It is advantageous to use the second harmonic field for length stabilization of doubly resonant SHGs. When demodulating the fundamental field, the error signal shows unwanted deformations directly on resonance, since there the conversion efficiency is highest and most of the light is converted to 775 nm - and so is the phase modulation. The doubly resonant SHG was built during the Master thesis of Petrissa Zell [Zel14].

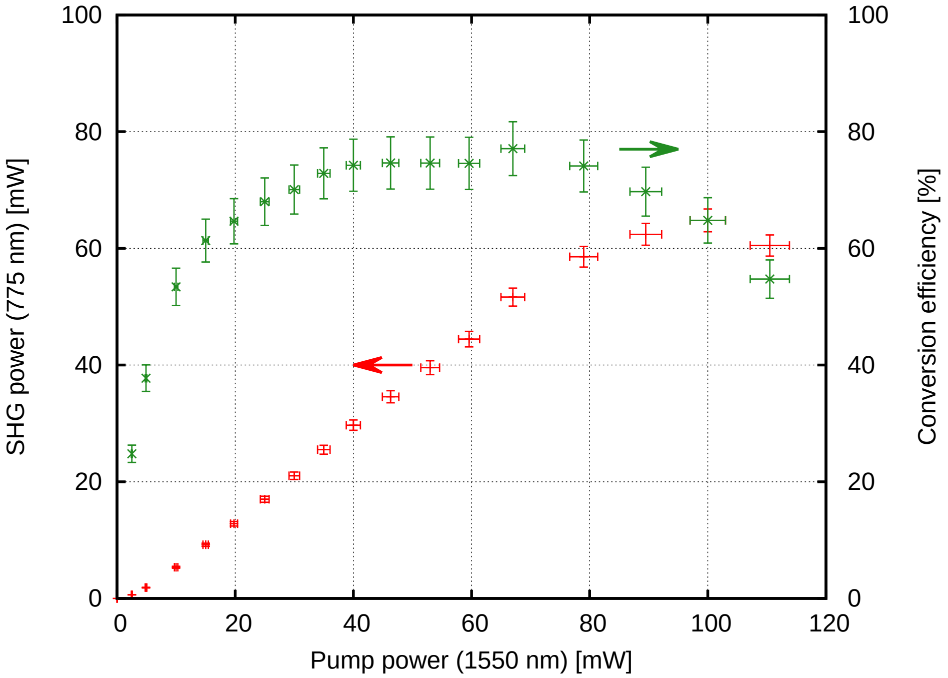

Figure 3.5.: Performance of the SHG converting 1550 nm to 775 nm at an operation point of the OPO, where the SHG performs best. The red points represent the measured output power at 775 nm with respect to the pump power at 1550 nm. The green points are the inferred conversion effciency. The maximum conversion efficiency of 75% was achieved at a pump power around 60 mW.

An exemplary plot of the performance of the SHG is shown in Figure 3.5. The conversion efficiency of about 75% is achieved at a pump power of 60 mW. For higher pump powers the second harmonic light is partially back converted to 1550 nm and the conversion efficiency decreases. Note that this measurement is taken at an OPO operation point for which the SHG performed best (NTC element at the OPO showed 16.52 kΩ), which is not the operation point for which all components together show best performance.

3.2.4. Degenerate optical parametric amplifier

The light at 775 nm generated in the SHG is used to pump a degenerate optical parametric amplifier (OPA) that produces squeezed vacuum states of light at 1550 nm. The OPA is set up exactly as the SHG with the same mirrors and was also built during the Master thesis of Petrissa Zell [Zel14].

A doubly resonant OPA has the advantage that length stabilization can be performed using the phase modulation on the pump field. Therefore, no control field is required. The pump field reflected off the coupling mirror is demodulated with the same frequency as the SHG is locked with. In single photon experiments one usually must not have a control field, as single photon detectors do not resolve sideband frequencies and any coherent field copropagating with the squeezed field would spoil the whole measurement.

The performance of the OPA was analyzed by setting up an auxiliary balanced homodyne detector (BHD) directly after the squeezed light source (not shown in Figure 3.2). The local oscillator for this BHD was provided by a small tap-off of 1550 nm light in front of the SHG. In Figure 3.6 a dark noise corrected power spectrum of the squeezed field at 1550 nm relative to a vacuum reference is shown on the left hand side. A theoretical model according to Eq. (3.1) is fitted to the data and yields a cavity parameter of $\gamma = 2\pi \cdot 60\,\mathrm{MHz}$.

On the right hand side of Figure 3.6 a zero span measurement at a sideband frequency of 5 MHz is shown. The homodyne phase was either held to measure the squeezed and anti-squeezed quadrature or scanned continuously. Up to -8.8 dB of nonclassical noise suppression with corresponding anti-squeezing of +17.9 dB are demonstrated (correction for electronic dark noise would lead to a squeezing value of -9.5 dB). Note that these measurements were performed with different homodyne detector electronics that were either optimized to measure a broadband power spectrum or at a single sideband frequency. Furthermore, when the zero span measurement was performed, the operation point of the OPO was different to when the spectrum was measured and the homodyne visibility was slightly better. This explains why the squeezing and anti-squeezing values differ in these two measurements.

3.2.5. Sum-frequency generation

The sum-frequency generation (SFG) cavity is the core component of the experiment. In this nonlinear optical cavity quantum states are up-converted from 1550 to 532 nm. It consists of a PPKTP crystal with two anti-reflectivity coated surfaces and two coupling

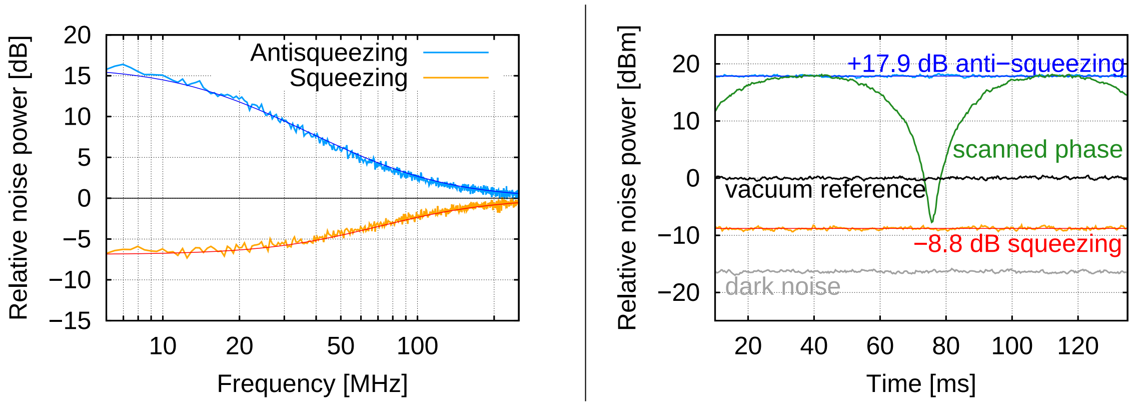

Figure 3.6.: Measurement of the squeezed vacuum states at 1550 nm. *left:* Power spectrum of the squeezed (orange) and anti-squeezed (cyan) quadrature noise normalized to the vacuum noise reference is shown. It was recorded with a resolution bandwidth of 1 MHz. The dark noise was subtracted from the data to allow for a comparison with a theoretical model (red and blue) leading to a cavity parameter of $\gamma = 2\pi \cdot 60\,\text{MHz}$ and $|\varepsilon| = 0.75\gamma$. *right:* Zero-span measurement at a Fourier frequency of 5 MHz without corrections for dark noise, recorded with a resolution bandwidth of 300 kHz. A continuous phase scan of the signal quadrature is shown in green.

mirrors. The incoupling mirror has a high reflectivity coating for 532 nm ($R > 99.9\%$), a reflectivity of 97% for 810 nm and a reflectivity of 91% for 1550 nm. The outcoupling mirror has an anti-reflectivity coating for 532 nm ($R < 0.1\%$) and a high reflective coating for 810 and 1550 nm ($R > 99.9\%$). An overview of all reflectivities and a photograph of the SFG is shown in Figure 3.7.

The SFG was characterized by using a weak coherent field at 1550 nm and converting it to 532 nm while varying the pump power at 810 nm. The input and output powers were compared and the conversion efficiency can be calculated with [Sam14]

$$\eta = \frac{532 \cdot P_{532}}{1550 \cdot P_{1550}} \,. \tag{3.3}$$

A maximum conversion efficiency of 90.2% was achieved at a pump power of about 140 mW. Figure 3.8 shows the conversion efficiency depending on the pump power. For the maximum conversion efficiency, a certain pump power is required as it drives the process. However, if the pump power is too high, the up-converted field gets back-converted to 1550 nm and the conversion efficiency decreases. Note that the conversion efficiency strongly depends on the phase matching of the three wavelengths involved [Bau11, Sam12]. It is crucial to find the optimal operation point of the OPO, that produces the light fields required for the up-conversion.

The SFG is stabilized via the Pound-Drever-Hall technique using a 24 MHz phase modulation on the 810 nm pump field.

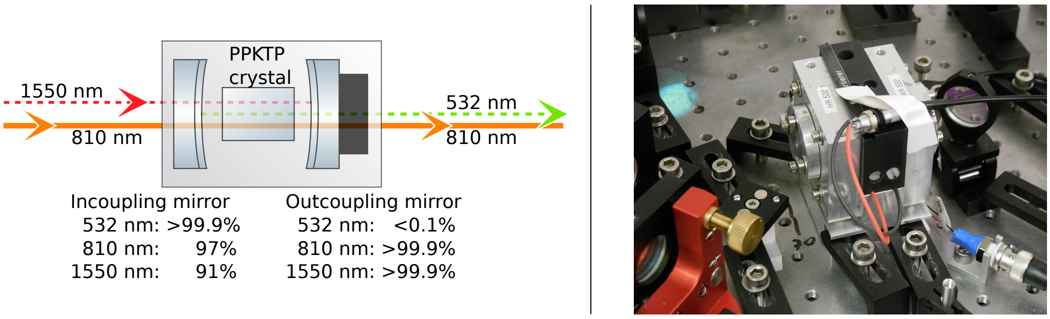
PPKTP
crystal
1550 nm
810 nm
532 nm
810 nm
Incoupling mirror
532 nm: >99.9%
810 nm: 97%
1550 nm: 91%
Outcoupling mirror
532 nm: <0.1%
810 nm: >99.9%
1550 nm: >99.9%

Figure 3.7.: The sum-frequency generator. *left:* The mirror reflectivities of the in- and outcoupling mirrors for all wavelengths involved. *right:* Photograph of the device. The PPKTP crystal is placed inside an oven which is actively temperature stabilized. The connector on the top is the power cord for the corresponding Peltier element. The in- and outcoupling mirrors are placed in the aluminum spacers. The outcoupling mirror is placed on a piezo-electric transducer to scan the cavity's length.

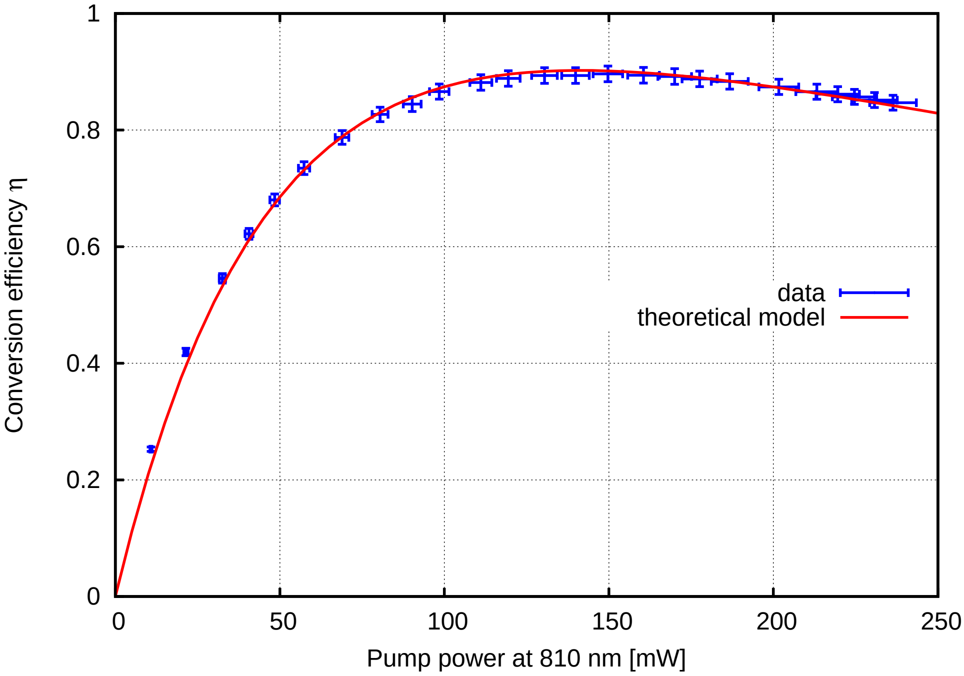

Figure 3.8.: Conversion efficiency of the sum-frequency generator depending on the pump power at 810 nm. The maximum conversion efficiency of about 90% was achieved at a pump power of 140 mW.

3.2.6. Balanced homodyne detector at 532 nm

An efficient balanced homodyne detector at 532 nm requires special approaches as there are no photo diodes commercially available that have a quantum efficiency comparable to those available for infrared wavelengths, for example. In his Bachelor thesis, Hendrik Weißbrich analyzed several commercially available photo diodes [Wei14]. The photo diodes S5973-02 from Hamamatsu, from which we removed the protective glass window to reduce reflections, performed best. Furthermore, the light was prepared to be p-polarized and the photo diodes were tilted horizontally to get closer to the Brewster angle. The angle of about 45 degree was found to be optimal. Small highly reflective concave mirrors with a radius of curvature of 25 mm were used as retro-reflectors, and re-focused the light that was not absorbed by the photo diode material, back onto the chip. An overall detection efficiency of about 90% was achieved with this technique. The retro-reflectors (RR) are also illustrated in Figure 3.2 and a photograph of the homodyne detector electronics built into the experiment is shown in Figure 3.9.

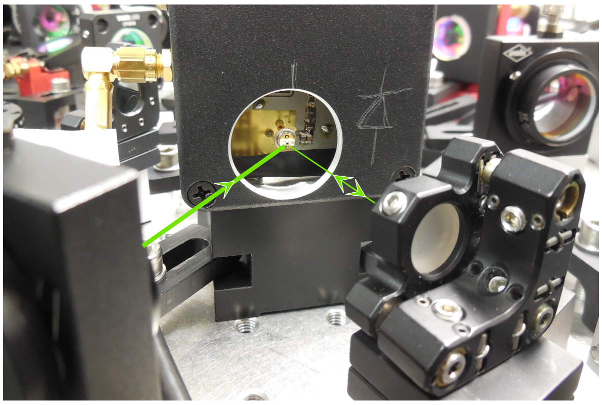

Figure 3.9.: Photograph of the homodyne detector at 532 nm. The photo diodes (S5973-02 from Hamamatsu) are tilted and, as illustrated by the green lines, the reflected light is re-focused onto the chip to increase the overall detection efficiency to about 90%.

3.3. Results

In this thesis squeezed vacuum states are efficiently up-converted from 1550 to 532 nm. The up-converted states are injected into a table-top Mach-Zehnder interferometer to perform a complementarily proof-of-principle demonstration of their use in quantum metrology.

3.3.1. Strongly squeezed vacuum states at 532 nm

The measurement results of a frequency up-converted squeezed vacuum state are shown in Figure 3.10. A power spectrum of the squeezed states at 532 nm relative to a vacuum state reference is shown on the left hand side. It was recorded with a resolution bandwidth (RBW) of 100 kHz and the data are corrected for dark noise of the detector to allow for a comparison with a theoretical model. The spikes at 21.6 and 26 MHz are electronic pick-up in the dark noise of the detector, caused by modulation frequencies used for cavity length stabilization of SHG, OPA and SFG. The theoretical fit is obtained using Eq. (3.2) with the previously determined cavity decay rate of the OPA $\gamma = 2\pi \cdot 60\,\mathrm{MHz}$, a pump parameter $|\varepsilon| = 0.85\gamma$ and the decay rate of the sum-frequency generation cavity $\kappa_{\mathrm{SFG}} = 2\pi \cdot 34\,\mathrm{MHz}$, causing additional frequency filtering.

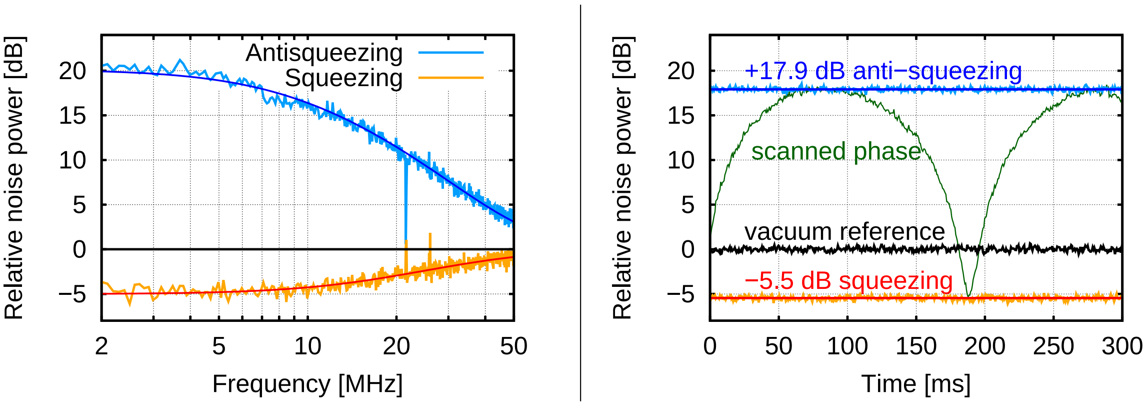

Figure 3.10.: Measurement of the up-converted squeezed vacuum states at 532 nm. *left:* Dark noise corrected power spectrum of the squeezed (orange) and anti-squeezed (cyan) quadrature noise normalized to the vacuum noise reference, as well as a theoretical model (red and blue). *right:* Zero-span measurement at a Fourier frequency of 5 MHz without corrections for dark noise, together with a continuous phase scan of the signal quadrature (green).

A zero-span measurement at a sideband frequency of 5 MHz is shown on the right hand side. Here, the RBW is 300 kHz and the dark noise is not subtracted from the data. A nonclassical noise suppression of 5.5 dB below shot noise is demonstrated, being – to the best of my knowledge – the highest value of squeezing at visible wavelengths achieved to date. The corresponding anti-squeezing was 18 dB above the vacuum reference. A total optical loss of 27% was deduced from this measurement originating from limited up-conversion and detection efficiencies (10% loss each), non-perfect mode-matchings (2.5% optical loss), limited visibility on the balanced homodyne detector (2% loss) and propagation losses (5% loss, mainly induced by an optical isolator in the path between OPA and SFG).

3.3.2. Sensitivity improvement of a Mach-Zehnder interferometer

The results presented in the previous section strongly verify that coherence properties are maintained during the up-conversion process. However, to demonstrate the applicability of frequency up-conversion in quantum metrology, the up-converted squeezed vacuum is used to enhance the sensitivity of a phase measurement device at 532 nm.

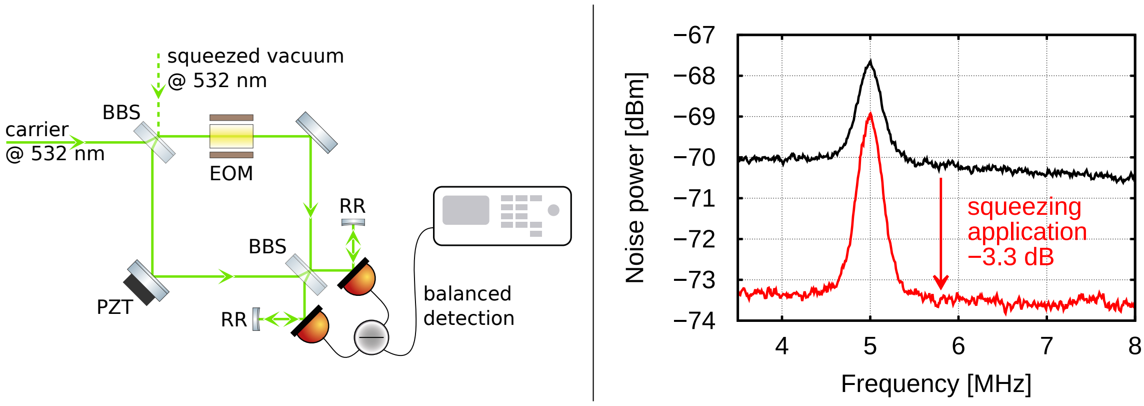

Figure 3.11.: Squeezed light enhanced Mach-Zehnder interferometer. *left:* Schematic of the setup. The carrier at 532 nm and the up-converted squeezed vacuum were the inputs of the interferometer, that consisted of two highly reflective mirrors and two balanced beam splitters (BBS). The two output ports were subtracted and analyzed with a balanced detector (interferometer locked to mid-fringe). An electro-optic modulator (EOM) in one of the interferometer arms generated a phase modulation at 5 MHz. *right:* Spectrum of the balanced detector. The modulation peak is clearly visible. When the up-converted squeezing was applied, the noise floor dropped and the signal-to-noise ratio improved. The resolution and video bandwidth were 300 kHz and 300 Hz, respectively, and no dark noise subtraction was performed. PZT: piezo-electric transducer to lock the interferometer, RR: retro-reflector.

The local oscillator at 532 nm of the balanced homodyne detector from the previous experiment is used as carrier field in a Mach-Zehnder interferometer and coupled through one input port. The second input is the squeezed vacuum field. An electro-optical modulator in one arm of the interferometer generated an artificial phase signal, whose signal-to-noise ratio is analyzed at the output of the interferometer. The output ports are balanced by locking the overall phase of the interferometer to mid-fringe and the photo current of the two detectors is subtracted. As before, reflected light is re-focused onto the detector's chips using retro-reflectors. A schematic of the setup is shown on the left hand side in Figure 3.11. On the right hand side of this figure, two measurements with the second interferometer port blocked (black trace) and open (red) are shown. When the up-converted squeezed vacuum enters the interferometer, the noise floor drops by about 3.3 dB, as indicated by the red arrow and the signal is emphasized. The noise reduction is equivalent to a 2.1-fold power increase which means a $\sqrt{2.1} = 1.46$ fold increase of phase sensitivity or signal-to-noise ratio.

A lower conversion efficiency (80%) and additional optics (including the EOM) increased the optical loss, which degraded the observable squeezing from 5.5 dB to 3.3 dB. The lower conversion efficiency was mainly caused by a degraded mode shape of the 810 nm pump beam, possibly caused by a dust particle on the NOPO crystal's surface to which the access is difficult. However, this result reaches the regime of practical usefulness in shot noise limited experiments. The measured quantum enhancement is comparable to large state-of-the-art squeezed light interferometers at infrared wavelengths like GEO600 [Gro13].

3.4. Discussion and outlook

In this experiment, squeezed vacuum states of light were successfully up-converted from 1550 to 532 nm and showed a nonclassical noise reduction of 5.5 dB below shot noise. To the best of my knowledge, the results represent the strongest ever achieved squeezing at visible wavelengths. Their usefulness in quantum metrology was demonstrated in a proof-of-principle experiment by exploiting the states in a table-top Mach-Zehnder interferometer.

In the experiment presented here, the optical setup was almost completely rebuilt aiming for a higher squeezing factor in the up-converted field compared to the experiment presented in [Vol14a, Vol14b]. The challenge of low pump powers in previous experiments was overcome here by using doubly resonant SHG and OPA. The homodyne detector at 532 nm was also re-designed. By removing the protective windows of the photo diodes, tilting them horizontally closer to the Brewster angle and re-focusing reflected light back onto the chip, the detection efficiency was increased to about 90%.

The up-conversion of squeezed vacuum states requires phase matching of four nonlinear optical cavities. Finding (and maintaining) an operation point where all these devices work satisfyingly is difficult and very time consuming. Furthermore, this operation point is not necessarily the point where all nonlinear optical cavities are at their peak performance and thus compromises have to be found. This problem could possibly be circumvented by amplifying the 1550 nm pump field for the SHG with a fiber amplifier to ensure that enough pump power for the OPA is always available to produce strongly squeezed states. In this case, only the OPO and SFG would have to be adjusted to provide a high up-conversion efficiency.

The main loss sources are still the limited up-conversion efficiency and the detection efficiency. The up-conversion efficiency could possibly be increased by optimizing the cavity design. A SFG consisting of a nonlinear cavity where one mirror is directly coated onto one side of the crystal would reduce the number of anti-reflective coatings inside the cavity, and therefore the losses. The detection efficiency can only be increased by using customized photo diodes with a quantum efficiency closer to unity for 532 nm. Currently no such photo diodes are available commercially. However, with these improvements, even higher squeezing values would be possible.

In conclusion, the frequency up-conversion of squeezed states enables quantum enhanced metrology at short wavelengths. It may develop into a standard tool in quantum optics laboratories whenever these states are required at wavelengths where their direct generation is daunting or impossible.

4. An unconditional entanglement interface for quantum networks

C. Baune, J. Gniesmer, S. Kocsis, C. E. Vollmer, P. Zell, J. Fiurášek,
and R. Schnabel
Unconditional entanglement interface for quantum networks
Physical Review A **93**, 010302 (2016)

Broadband two-mode squeezed vacuum states of light represent fundamental resources for continuous variable (CV) quantum information processing [Bra05]. Established fiber-optic technology offers relatively high transmission efficiency for wavelengths in the telecommunication band around 1550 nm, where scattering and absorption rates leading to photon loss are minimal. However, a true quantum information network would incorporate a number of nodes, where quantum states could be stored and even processed [Bri98]. These nodes could generally take the form of single atoms [Rit12], atomic ensembles [Jen11, Rei11], or solid-state systems [Ber13, Zho15]. This implies that the reversible mapping of quantum states between optical and material modes will necessarily be ubiquitous in quantum networks.

Almost all current quantum memories operate at visible wavelengths so that an efficient interface between entangled optical modes at telecommunication and visible wavelengths is a key capability to demonstrate. Previous work has demonstrated the interface between telecommunication and visible wavelengths with entangled photon pairs [Tan05], and storage in a quantum memory of single photons up-converted from telecom to visible wavelength has been reported [Mar14]. There have been several demonstrations of quantum memories for CV states [Jul04, App08, Hon08, Jen11, Hos11, Hed10] and the classical benchmark for memory fidelity has been experimentally surpassed using displaced two-mode squeezed states [Jen11].

It has been previously demonstrated that CV entanglement can span optical frequencies one octave apart [Gro08]. However, no "on the fly" wavelength conversion has yet been achieved. First attempts to verify entanglement between 1550 and 532 nm were performed in the doctoral thesis of Christina Vollmer [Vol14a] and the Master thesis of Petrissa Zell [Zel14]. Their experiment suffered from a limited squeezing strength and optical losses so that only about 3 dB of correlations could be measured.

In this chapter, the generation of a broadband two-mode squeezed vacuum state is demonstrated and one-half of this state is frequency up-converted from 1550 to 532 nm. I characterize the correlations between the two modes and verify that the up-conversion preserves the modes' broadband entanglement with 5.5 dB below the classical limit.

In Section 4.1 a theoretical analysis of the generation of two-mode squeezed states is given. After that the experimental setup and the measurement protocol will be explained in Section 4.2. In Section 4.3 the results are presented and an entanglement criterion developed by Duan *et al.* [Dua00] is applied to the data.

4.1. Generation of entanglement

Entanglement can be generated by mixing two squeezed vacua at a balanced beam splitter. The squeezing operators of two modes $\hat{a}$ and $\hat{b}$ are given by (cf. Section 2.1.5)

$$\hat{S}(\zeta) = \mathrm{e}^{\frac{1}{2}(\zeta\hat{a}^{\dagger 2} - \zeta^* \hat{a}^2)} \quad \text{and} \quad \hat{S}(\chi) = \mathrm{e}^{\frac{1}{2}(\zeta\hat{b}^{\dagger 2} - \zeta^* \hat{b}^2)}\,, \tag{4.1}$$

with $\zeta = r\,\mathrm{e}^{-\mathrm{i}\phi}$ and $\chi = s\,\mathrm{e}^{-\mathrm{i}\theta}$. The squeezing operation results in transformed modes

$$\begin{aligned} \hat{a}_r &= S^\dagger(\zeta)\,\hat{a}\,S(\zeta) = \hat{a}\cosh(r) - \hat{a}^\dagger \mathrm{e}^{-\mathrm{i}\phi}\sinh(r)\,, \\ \hat{b}_s &= S^\dagger(\chi)\,\hat{b}\,S(\chi) = \hat{b}\cosh(s) - \hat{b}^\dagger \mathrm{e}^{-\mathrm{i}\theta}\sinh(s)\,. \end{aligned} \tag{4.2}$$

These two squeezed modes are mixed at a balanced beam splitter.

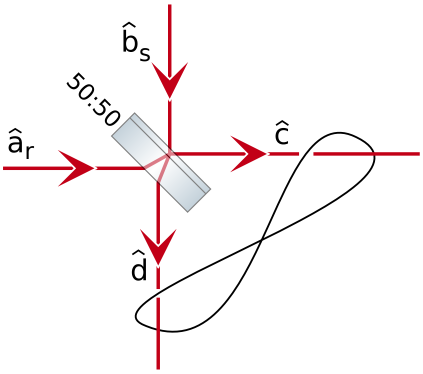

Figure 4.1.: Input and output modes of a balanced beam splitter with two input modes $\hat{a}_r$ and $\hat{b}_s$ to generate two-mode squeezing. The indices denote the respective squeezing parameter r and s. The output modes $\hat{c}$ and $\hat{d}$ are entangled which is indicated by the loop.

A schematic of this beam splitter with the modes involved is shown in Figure 4.1 and the input-output relations are given by [Wal94]

$$\begin{pmatrix} \hat{c} \\ \hat{d} \end{pmatrix} = \frac{1}{\sqrt{2}} \begin{pmatrix} 1 & -1 \\ 1 & 1 \end{pmatrix} \begin{pmatrix} \hat{a}_r \\ \hat{b}_s \end{pmatrix} \,. \tag{4.3}$$

Inserting the equations for the squeezed modes and using the relations $\cosh(x) = \frac{1}{2}(\mathrm{e}^x + \mathrm{e}^{-x})$ and $\sinh(x) = \frac{1}{2}(\mathrm{e}^x - \mathrm{e}^{-x})$ results in

$$\begin{pmatrix} \hat{c} \\ \hat{d} \end{pmatrix} = \frac{1}{2\sqrt{2}} \begin{pmatrix} \hat{a}(\mathrm{e}^r + \mathrm{e}^{-r}) - \hat{a}^\dagger \mathrm{e}^{-\mathrm{i}\phi}(\mathrm{e}^r - \mathrm{e}^{-r}) - \hat{b}(\mathrm{e}^s + \mathrm{e}^{-s}) + \hat{b}^\dagger \mathrm{e}^{-\mathrm{i}\theta}(\mathrm{e}^s - \mathrm{e}^{-s}) \\ \hat{a}(\mathrm{e}^r + \mathrm{e}^{-r}) - \hat{a}^\dagger \mathrm{e}^{-\mathrm{i}\phi}(\mathrm{e}^r - \mathrm{e}^{-r}) + \hat{b}(\mathrm{e}^s + \mathrm{e}^{-s}) - \hat{b}^\dagger \mathrm{e}^{-\mathrm{i}\theta}(\mathrm{e}^s - \mathrm{e}^{-s}) \end{pmatrix} \,. \tag{4.4}$$

Now I assume that the two input fields are orthogonally squeezed. Mode $\hat{a}_r$ is squeezed along the $\hat{p}$-quadrature ($\phi = 0$) and mode $\hat{b}_s$ along the $\hat{q}$-quadrature ($\theta = \pi$), cf. Section 2.1.5. The output modes then reduce to

$$\begin{pmatrix} \hat{c} \\ \hat{d} \end{pmatrix} = \frac{1}{2\sqrt{2}} \begin{pmatrix} \hat{a}(\mathrm{e}^r + \mathrm{e}^{-r}) - \hat{a}^\dagger(\mathrm{e}^r - \mathrm{e}^{-r}) - \hat{b}(\mathrm{e}^s + \mathrm{e}^{-s}) - \hat{b}^\dagger(\mathrm{e}^s - \mathrm{e}^{-s}) \\ \hat{a}(\mathrm{e}^r + \mathrm{e}^{-r}) - \hat{a}^\dagger(\mathrm{e}^r - \mathrm{e}^{-r}) + \hat{b}(\mathrm{e}^s + \mathrm{e}^{-s}) + \hat{b}^\dagger(\mathrm{e}^s - \mathrm{e}^{-s}) \end{pmatrix} . \tag{4.5}$$

The quadrature operators of the output modes are then given as

$$\begin{aligned} \hat{q}_c &= \frac{1}{\sqrt{2}}(\hat{c} + \hat{c}^\dagger) \\ &= \frac{1}{2}\left[(\hat{a}_r + \hat{a}_r^\dagger)\mathrm{e}^{-r} - (\hat{b}_s + \hat{b}_s^\dagger)\mathrm{e}^{s}\right] \\ &= \frac{1}{\sqrt{2}}\left[\hat{q}_a\mathrm{e}^{-r} - \hat{q}_b\mathrm{e}^{s}\right] , \\ \hat{p}_c &= \frac{1}{\mathrm{i}\sqrt{2}}(\hat{c} - \hat{c}^\dagger) = \frac{1}{\sqrt{2}}\left[\hat{p}_a\mathrm{e}^{r} - \hat{p}_b\mathrm{e}^{-s}\right] , \\ \hat{q}_d &= \frac{1}{\sqrt{2}}(\hat{d} + \hat{d}^\dagger) = \frac{1}{\sqrt{2}}\left[\hat{q}_a\mathrm{e}^{-r} + \hat{q}_b\mathrm{e}^{s}\right] , \\ \hat{p}_d &= \frac{1}{\mathrm{i}\sqrt{2}}(\hat{d} - \hat{d}^\dagger) = \frac{1}{\sqrt{2}}\left[\hat{p}_a\mathrm{e}^{r} + \hat{p}_b\mathrm{e}^{-s}\right] . \end{aligned} \tag{4.6}$$

Both modes $\hat{c}$ and $\hat{d}$ are measured via balanced homodyne detection and both signals are combined electronically. It is then possible to analyze their sum and difference, and thus reveal nonclassical correlations. Therefore the detector measuring mode $\hat{c}$ is first locked to an angle where its $\hat{q}$-quadrature is detected and it is added to a scanned quadrature of the detector measuring the d-mode. After inserting the output quadrature operators, the variance of the sum signal reads

$$\begin{aligned} \Delta^2\left[\hat{q}_c + \hat{q}_{\varphi,d}\right] =& \Delta^2\left[\hat{q}_c + \cos\varphi\,\hat{q}_d + \sin\varphi\,\hat{p}_d\right] \\ =& \frac{1}{2}\Delta^2\left[\hat{q}_a\mathrm{e}^{-r}(1+\cos\varphi) - \hat{q}_b\mathrm{e}^{s}(1-\cos\varphi) + \sin\varphi\,\hat{p}_a\mathrm{e}^{r} + \sin\varphi\,\hat{p}_b\mathrm{e}^{-s}\right] . \end{aligned} \tag{4.7}$$

The input quadratures $\hat{q}_a$, $\hat{p}_a$, $\hat{q}_b$ and $\hat{p}_b$ are mutually independent so that the total variance reduces to a sum of the individual ones and it reads

$$\Delta^2\left[\hat{q}_c + \hat{q}_{\varphi,d}\right] = \frac{1}{4}\left[\mathrm{e}^{-2r}\left(1+\cos\varphi\right)^2 - \mathrm{e}^{2s}\left(1-\cos\varphi\right)^2 + \sin^2\varphi\,\mathrm{e}^{2r} + \sin^2\varphi\,\mathrm{e}^{-2s}\right] . \tag{4.8}$$

Similarly, the variance of the difference of a locked $\hat{p}_c$ and a scanned $\hat{p}_{\varphi,d}$ quadrature is

$$\Delta^2\left[\hat{p}_c - \hat{p}_{\varphi,d}\right] = \frac{1}{4}\left[\mathrm{e}^{2r}\left(1-\cos\varphi\right)^2 - \mathrm{e}^{-2s}\left(1+\cos\varphi\right)^2 + \sin^2\varphi\,\mathrm{e}^{-2r} + \sin^2\varphi\,\mathrm{e}^{2s}\right] . \tag{4.9}$$

In the case where both input fields are squeezed vacua, i.e. $r > 0$ and $s > 0$, the resulting state is called *s-class entangled* [DiG07, Ebe13]. However, an entangled state is also obtained when $r > 0$ and $s = 0$, so one input mode is just vacuum. We will call these states *v-class entangled* [DiG07, Ebe11] and produce them in the experiment presented in the following.

In Figure 4.2 an example plot of the two variances as calculated above are shown, with $s = 0$. The other parameters are chosen approximately as they appear in the experiment ($r = 2.1$) and optical losses are taken into account (efficiency $\eta = 0.73$).

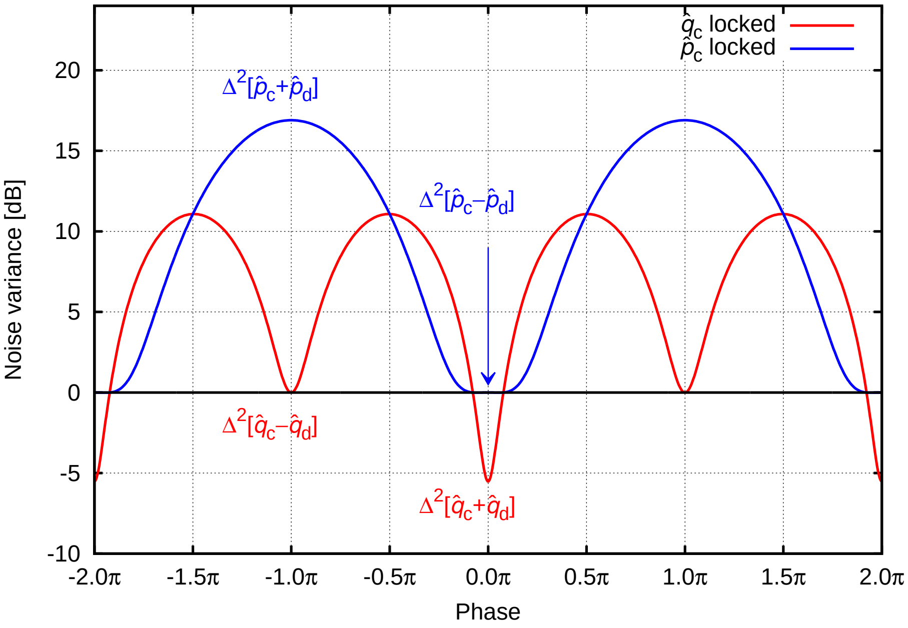

Figure 4.2.: Correlations and anti-correlations of the two modes after the beam splitter. The anti-squeezed statistics cancel out when $\hat{p}_c - \hat{p}_d$ is measured and reveal the full anti-squeezing of mode a when $\hat{p}_c + \hat{p}_d$ is measured. In the setting where $\hat{q}_c - \hat{q}_d$ is measured, the variance drops to the vacuum level as the squeezed statistics are canceled out. Finally, the full nonclassical correlations are revealed when $\hat{q}_c + \hat{q}_d$ is measured.

The variance of the two combined phase quadratures reaches maximum variance when they are added and drops to the vacuum level when they are subtracted. This can be understood as follows: one input state is squeezed in the amplitude quadrature and correspondingly anti-squeezed in the phase quadrature. The phase relation between the two output states is such that the full anti-correlation is recovered when adding the two phase quadratures, while they cancel out – and drop to the vacuum level – when subtracting.

The variance of the sum of the two amplitude quadratures, on the other hand, reveals the full correlations and the noise drops below the vacuum. When subtracting the two amplitude quadratures, the squeezing properties cancel out – and give vacuum. In all intermediate combinations, the fixed amplitude quadrature of mode c is mixed with varying portions of the phase quadrature contributions, which is anti-squeezed, and the noise levels rise.

4.2. Experimental setup

The experimental setup for the generation of entanglement of two widely separated wavelengths is shown in Figure 4.3.

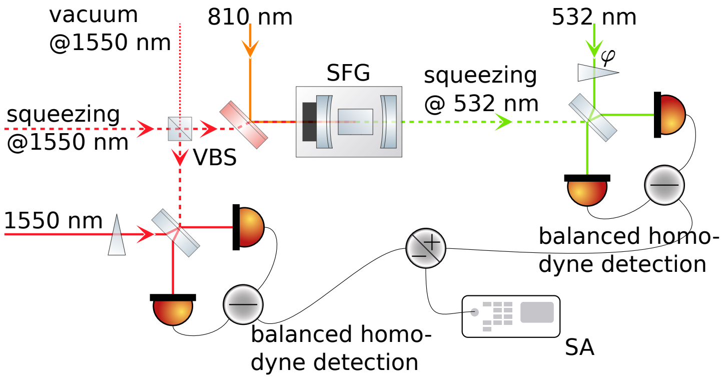

Figure 4.3.: Illustration of the experimental setup. Squeezed vacuum states of continuous-wave light at 1550 nm are produced in the OPA described in detail in Section 3, and split up at a variable beam splitter. One part is directly sent to a balanced homodyne detection (BHD) while the other mode is up-converted to 532 nm and also detected in a BHD. The electronic sum and difference of the BHD signals is recorded by a spectrum analyzer (SA). VBS: variable beam splitter.

In the same way as described in the previous chapter, squeezed vacuum states of light are generated at 1550 nm. These states are mixed with vacuum on a variable beam splitter (VBS) to produce v-class entangled states in the outputs of the beam splitter. One mode is directly sent to a balanced homodyne detector at 1550 nm, using a small portion of the bright 1550 nm light produced by the OPO (cf. Section 3.2) as local oscillator. The other output mode of the beam splitter is sent to the SFG and up-converted to 532 nm. The same balanced homodyne detector at 532 nm is used as in the experiment for up-conversion of squeezed vacuum states. The VBS was tuned such that the two modes at 1550 and 532 nm are symmetric, i.e. they suffer the same amount of optical loss, and therefore the same nonclassical noise suppression is measured by the two homodyne detectors. Both homodyne signals are subsequently added or subtracted in a passive electronic addition/subtraction box, and the resulting signal is recorded by a spectrum analyzer.

4.3. Measurement protocol and results

The measurement was performed by keeping the measured quadrature of the 1550 nm mode constant and continuously scanning the readout quadrature of the 532 nm mode. Assuming that the field entering the VBS is squeezed in the $\hat{q}$ quadrature, I observe a behavior of the resulting signal as theoretically predicted in Section 4.1. The experimental data are shown in Figure 4.4.

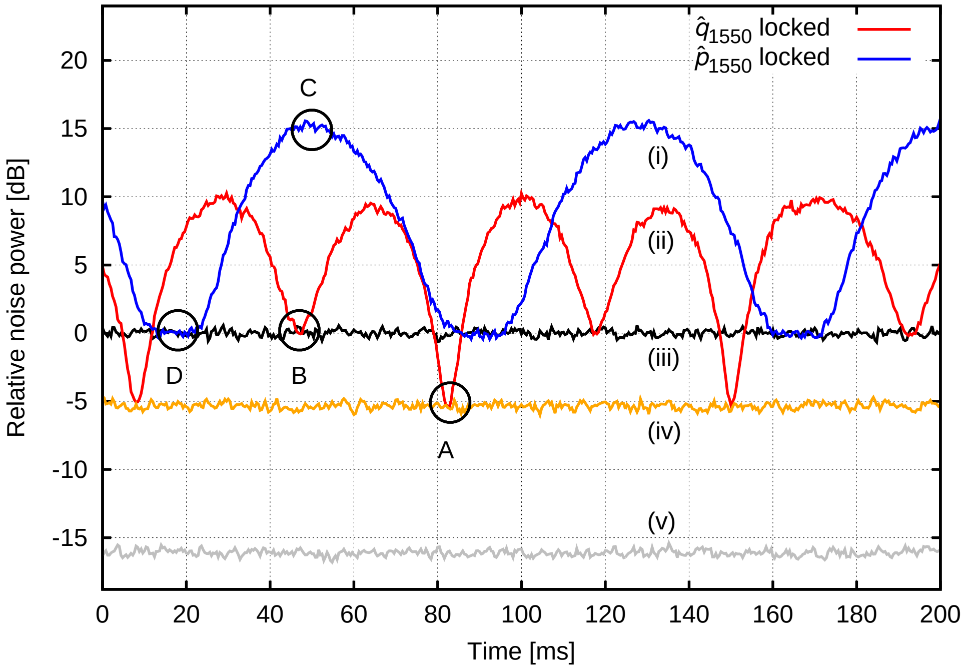

Figure 4.4.: Characterization of the unconditional quantum interface. Shown is the sum of the two BHD signals at 5 MHz sideband frequency. While the phase φ of the BHD at 532 nm was continuously scanned, the phase of the BHD at 1550 nm was set to measure the squeezed amplitude quadrature $\hat{q}_{1550}$ (ii, red trace) or anti-squeezed $\hat{p}_{1550}$ quadrature (i, blue). The four extremal points represent the following measurement settings: A: $\Delta^2[\hat{q}_{1550} + \hat{q}_{532}]$, B: $\Delta^2[\hat{q}_{1550} - \hat{q}_{532}]$, C: $\Delta^2[\hat{p}_{1550} + \hat{p}_{532}]$, D: $\Delta^2[\hat{p}_{1550} - \hat{p}_{532}]$. The orange trace (iv) was recorded when the 532 nm phase was also fixed, revealing stable nonclassical correlations about 5.5 dB below the vacuum level (iii, black). Note that the traces were recorded successively, and there is no actual meaning in the relative positions along the x-axis of the minima and maxima. None of the traces is corrected for our detection scheme's dark noise (v, gray).

When the phase of the BHD at 1550 nm is set to measure the $\hat{p}_{1550}$ quadrature – while the phase of the detector at 532 nm is continuously scanned – one obtains the blue trace. The full anti-correlations are revealed when the phase of the BHD at 532 nm is such that it measures the $\hat{p}_{532}$ quadrature and the two BHD signals are summed up (point C in Figure 4.4). However, when one subtracts the two signals, the noise drops to the vacuum level (point D). This behavior is predicted by the simple theoretical model presented in Section 4.1. Note that the electronic signals are always summed. Hence, the difference signal is obtained when the phase of one homodyne detector is shifted by 180° with respect to the setting when measuring the sum.

The red trace is obtained when the phase of the BHD at 1550 nm is set to measure the $\hat{q}_{1550}$ quadrature. If a phase relation between the two modes is reached such that the second BHD measures the $\hat{q}_{532}$ quadrature, and the two homodyne signals are subtracted from each other, the noise drops to the vacuum level (point B). The most interesting condition is when both detectors measure $\hat{q}$ and the signals are summed up (point A): The noise drops significantly below the shot noise level and reveals nonclassical correlations between the widely separated wavelengths 532 and 1550 nm.

To analyze the spectral properties of the correlations, the frequency dependence of the sum signal was measured and is shown in Figure 4.5. The phase of the 1550 nm field was set to measure the squeezed (red trace) or anti-squeezed (blue trace) quadrature while the 532 nm phase was set to measure the minimum noise in the sum signal. A correlation strength of more than 3 dB below the vacuum noise is measured up to a sideband frequency of about 20 MHz, limited by the SFG linewidth and the bandwidth of the detector electronics.

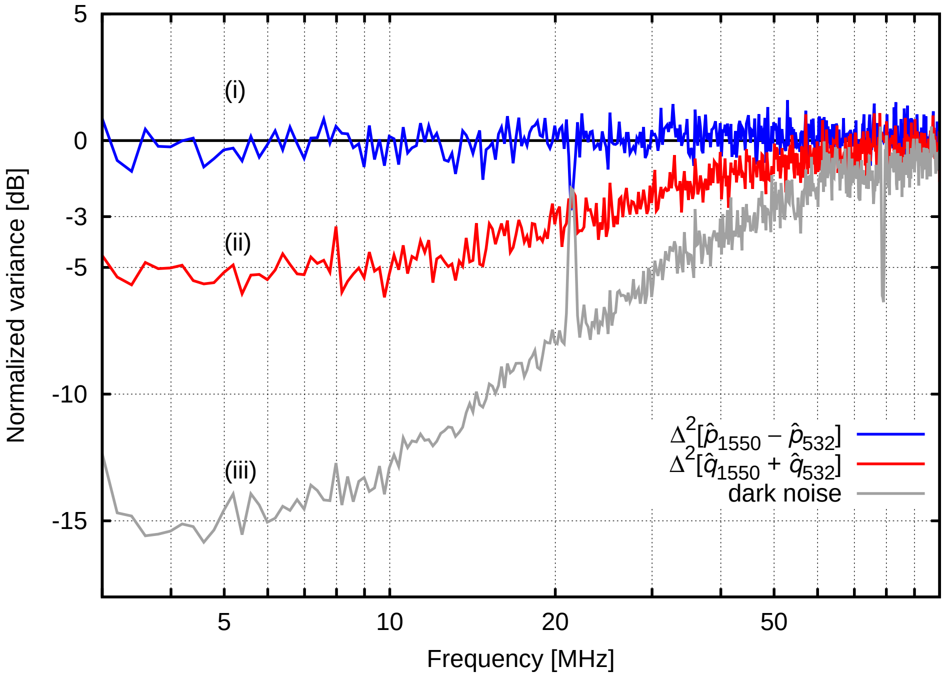

Figure 4.5.: Spectral characterization of the entanglement interface. Trace (i) shows the spectrum when $\Delta^2[\hat{p}_{1550} - \hat{p}_{532}]$ is detected, corresponding to point D from Figure 4.4. Trace (ii) shows the spectrum for $\Delta^2[\hat{q}_{1550} + \hat{q}_{532}]$, corresponding to point A from Figure 4.4. Normalized variance values below zero, the vacuum reference, signify nonclassical correlations. The bottom trace (iii) shows the dark noise of our balanced homodyne detectors.

Criterion by Duan et al.

The entanglement of two light beams at 532 nm and 1550 nm can be conveniently characterized by the quantity $\mathcal{I}$, introduced by Duan *et al.* [Dua00],

$$\mathcal{I} = \Delta^2[\hat{q}_{1550} + \hat{q}_{532}] + \Delta^2[\hat{p}_{1550} - \hat{p}_{532}], \tag{4.10}$$

where $\hat{q}_\lambda$ and $\hat{p}_\lambda$ denote the amplitude and phase quadratures, respectively, of an optical beam at wavelength λ. The quadrature variances are normalized such that $\Delta^2[\hat{q}] = \Delta^2[\hat{p}] = \frac{1}{2}$ for vacuum, and $\mathcal{I} < 2$ certifies sufficiently the presence of entanglement of the two beams [Dua00]. The variances of linear combinations of quadratures appearing in Eq. (4.10) characterize correlations between individual modes of a two-mode quantum state. A simple theoretical model yields

$$\begin{aligned} \Delta^2[\hat{q}_{1550} + \hat{q}_{532}] &= 1 - \left(\frac{1}{2} - V_-\right)(t\tau_{532} + r\tau_{1550})^2 , \\ \Delta^2[\hat{p}_{1550} - \hat{p}_{532}] &= 1 + \left(V_+ - \frac{1}{2}\right)(t\tau_{532} - r\tau_{1550})^2 . \end{aligned} \tag{4.11}$$

Here V_- and V_+ denote the variances of squeezed and anti-squeezed quadratures of the input state to the VBS. The amplitude transmittance and reflectance of the VBS are denoted by t and r, respectively. The effective overall amplitude transmittances of the two output modes of the VBS, including final detection efficiencies in each of the BHDs, are denoted as τ_{532} and τ_{1550}.

In the experiment, the variable beam splitter is tuned such that the anti-squeezed noise is fully canceled in the difference of the phase quadrature amplitudes $\hat{p}_{1550} - \hat{p}_{532}$. This is achieved when $t\tau_{532} = r\tau_{1550}$, and in this case the variance of the difference in phase quadratures reaches the vacuum noise level, $\Delta^2[\hat{p}_{1550} - \hat{p}_{532}] = 1$, see point D in Figure 4.4. Within the error bars of the experiment, this setting also provides the strongest Gaussian entanglement as quantified by $\mathcal{I}$. Indeed, it follows from Eq. (4.11) that, for this setting, entanglement is certified and $\mathcal{I} < 2$ whenever the input state is squeezed and $V_- < \frac{1}{2}$. A more detailed theoretical analysis, however, reveals that the minimum value of $\mathcal{I}$ is attained at a marginally different beam splitter tuning [Wag14]. In our experiment, the variable beam splitter sent a larger fraction of the squeezed input state to the entanglement interface to compensate for the non-perfect SFG conversion efficiency, as well as the non-perfect quantum efficiency of the photo diodes at 532 nm, both of which were approximately 90%. In contrast, the mode at 1550 nm has less downstream loss, on the order of 12%, dominated by the visibility of the balanced homodyne detector.

The measured correlations of -5.5 dB in the first measurement and 0 dB in the second yield a value of $\mathcal{I} = 1.28$, which significantly beats the classical limit of 2.

4.4. Discussion and outlook

In this chapter, I presented an entanglement-preserving interface for multi-color quantum optical networks. The results demonstrate frequency up-conversion of half of an entangled two-mode state. As a proof-of-principle, I up-converted one part of a two-mode squeezed state from the near-infrared to the green spectrum, producing CV entanglement between continuous-wave light fields at 1550 and 532 nm. Up to 5.5 dB of nonclassical correlations with a bandwidth of about 20 MHz were maintained during the conversion process.

The demonstrated entanglement interface in combination with quantum memories operating at visible wavelengths represents a promising and flexible alternative to direct quantum storage of photons at telecommunication wavelengths [Jin15, Sag15]. With minimal modifications, the setup could be easily matched to any frequency single-mode CV quantum memory having a bandwidth in the MHz regime [Sim10]. The optical bandwidth can be varied by changing the mirror reflectivities of the squeezed light source and up-conversion cavities. The optical frequency of the up-converted states can easily be changed by varying the frequency of the pump field. These capabilities are necessary to achieve high efficiency when interfacing an optical entanglement source with a quantum memory.

Entanglement was generated in the experiment by sending a squeezed vacuum state to a beam splitter, and mixing it with a vacuum state. The maximum strength of correlations between the output modes is limited in this method, but it was still sufficient for a proof-of-principle demonstration. Generating two-mode entanglement that is not limited in this way, in the original sense meant by Einstein, Podolsky and Rosen [Ein35], only requires mixing of two squeezed vacuum fields on a beam splitter. Such a fully controlled source of EPR entanglement [Rei89] has previously been demonstrated [Ebe13]. Integrating it with the up-conversion set-up is technically more involved but straightforward in principle.

The storage of optical states in quantum memories is a key technology in setting up long-distance quantum networks [San11]. Multi-mode quantum memories are also being investigated, particularly to achieve reasonable long-distance data transfer rates when they are used as quantum repeaters [Afz09, Sin14]. Frequency multi-mode operation has recently been demonstrated with quantum memories based on atomic frequency combs (AFC) in rare-earth ion doped materials, and in principle these quantum memories could have a total accessible bandwidth in the range of hundreds of GHz [Sin14, Sag15]. The total bandwidth of the states used in the presented approach can be multiplexed [Hag10] to take advantage of a large section of a multi-mode storage capacity. In this sense a larger bandwidth implies a larger frequency space in which to encode distinct modes, and a nonclassical noise suppression of more than 3 dB over a bandwidth exceeding a GHz has been achieved at 1550 nm [Ast13].

Another promising application that could take advantage of the interface is for continuous-variable quantum computing in atomic memories using time-frequency entangled quantum modes [Hum14]. The proposal is based on the cluster-state quantum computing approach, which requires a large resource state with multi-mode entanglement. A squeezed vacuum field such as the one I characterized has a broad sideband spectrum that could be used for encoding these time-frequency quantum modes. I consider this work to be an important building block for future multi-color quantum networks, which may further include continuous as well as discrete variable concepts.

5. Frequency up-conversion of single photon states

C. Baune, A. Schönbeck, A. Samblowski, J. Fiurášek, and R. Schnabel
Quantum non-Gaussianity of frequency up-converted single photons
Optics Express **22**, 22808 (2014)

J. Fiurášek, C. Baune, A. Schönbeck, and R. Schnabel
Analysis of counting measurements on narrowband frequency up-converted single photons and the influence of heralding detector dead time
Physical Review A **91**, 013829 (2015)

Single photon states are optical states with the minimal non-zero excitation of a mode and are not only of fundamental interest. Quantum information processing with single photons or discrete variables (DV) in general has the advantage that the fidelity of operations can reach almost unity [Gis02, O'B09]. In 1991, A. K. Ekert proposed to use correlated photon pairs for quantum cryptography [Eke91] and nowadays many quantum information protocols employ DV states, although they require post-selection which decreases the success rate, e.g. see [Pan12] for a review. Single photons can be used in quantum key distribution to allow for longer transmission channels than faint coherent states [Lou05], especially when they are used together with quantum repeaters [Bri98, San11].

Distant nodes of a network can be connected by transmission through existing telecommunication fibers and intermediate processing in quantum repeaters. However, the preferred optical wavelengths for these two tasks usually differ significantly. While optical fibers have lowest absorption in the near infrared regime, quantum memories are usually operated at much shorter wavelengths [Hes16].

The frequency up-conversion of single photons can play an important role in a quantum communication network, as it allows to connect different subsystems of a quantum communication network. In this chapter the frequency up-conversion of single photons is demonstrated. Therefore, photon pairs at 810 and 1550 nm are generated via spontaneous parametric down-conversion. The detections of 810 nm photons herald the existence of 1550 nm photons which are subsequently up-converted to 532 nm. The up-converted photons are shown to be not expressible by mixtures of Gaussian states. This so-called quantum non-Gaussianity has recently been identified as a sufficient criterion for secure quantum communication [Las16].

This chapter starts with presenting the experimental setup in Section 5.1, where I also describe the basic tools for the data acquisition and analysis. A theoretical description of the single photon source based on spontaneous parametric down-conversion is given in Section 5.2. In Section 5.3 the experimental data is analyzed with respect to temporal correlations between trigger and signal photons and different criteria for nonclassicality are applied. The quantum non-Gaussianity criterion is applied to the data in Section 5.4. A short overview on a deeper analysis of the experimental data, performed mainly by Jaromír Fiurášek, is added in Section 5.5.

5.1. Experimental setup

The experimental setup for the up-conversion of single photons is shown in Figure 5.1.

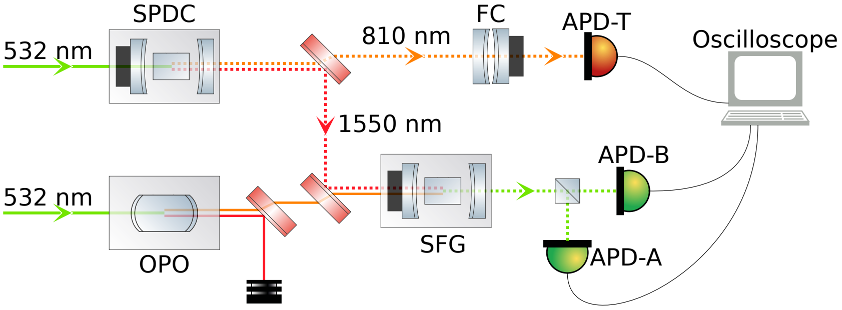

Figure 5.1.: Experimental setup for the up-conversion of single photons. A 532 nm field pumps two optical parametric oscillators. One is operated above threshold (OPO), the other one below threshold (SPDC). In the latter, photon pairs at 810 and 1550 nm are produced via spontaneous parametric down-conversion. The 810 nm photons are filtered and used to herald 1550 nm photons, which are subsequently up-converted to 532 nm using a strong 810 nm pump field generated in the OPO. The up-converted photons are analyzed in a Hanbury Brown and Twiss setup. See the main text for more details.

An optical parametric oscillator is operated above threshold and generates strong fields at 1550 and 810 nm, where the latter is used as pump field for the sum-frequency generation cavity (SFG). The SFG and the generation of the 532 nm pump field for the OPO is described in detail earlier (cf. Chapter 3).

Photon pairs are generated in another OPO, which is operated below threshold by using just a few Milliwatts of 532 nm pump power. The intra-cavity gain is not high enough to compensate for the cavity mirrors' decay rate and losses so that the oscillation does not start (cf. Section 2.3.2). Instead, in spontaneous parametric down-conversion (SPDC) photon pairs are generated and split at a dichroic beam splitter. The 810 nm photons pass a filter cavity (FC, see below) and are detected with the avalanche photo detector APD-T. As the photons at 810 and 1550 nm are correlated in their arrival time (cf. Section 5.2), the event of a photo detection at APD-T heralds the existence of a correlated photon at 1550 nm, which is subsequently up-converted to 532 nm in the SFG. Consequently, the 810 nm photons are used to trigger the data acquisition of the up-converted states that are analyzed in a Hanbury Brown and Twiss setup [Han56] using two APDs (APD-A and -B).

5.1.1. SPDC

The single photon source based on spontaneous parametric down-conversion (SPDC) consists of a periodically poled potassium titanyl phosphate (PPKTP) crystal which is anti-reflective coated on its two end surfaces. The crystal is embedded in an optical cavity with mirror reflectivities similar to those of the OPO (cf. Section 3.2.2). A piezo electric transducer is mounted to one of the cavity mirrors. Thereby the cavity can be scanned by applying a voltage to the piezo and it is easier to mode match the optical fields to the cavity.

The cavity decay rates can be determined using Pound-Drever-Hall error signals [Bla01]. In the Pound-Drever-Hall technique a phase modulation is applied to a light field which is mode matched to the optical cavity. The reflected light is detected by a photo diode and the photo current is demodulated, and information on the behavior of the sidebands inside the cavity can be extracted. This technique is used for the stabilization of cavities as it generates a zero crossing exactly on resonance when demodulated with the correct phase, and can be used as error signal for a control loop. When the demodulation phase is exactly 90° off this point, the error signal has maxima and minima exactly the modulation frequency away from the center of the carrier field's Airy peak. They can therefore be used as frequency markers [Brü10] to determine the width of the Airy pattern. Thereby the cavity decay rates of the SPDC cavity can be determined, which are crucial parameters for further analyses. In Figure 5.2 this is shown for the 810 and 1550 nm field using a 90 MHz modulation frequency. A full width at half maximum (FWHM) of 34 MHz and 17 MHz is inferred for 810 and 1550 nm, respectively. (As already mentioned earlier, the cavity decay rate γ is connected to the half width at half maximum via $\frac{\gamma}{2\pi}$ =HWHM, so that $\frac{\gamma}{\pi}$ =FWHM.) The linewidth at 810 nm is larger than at 1550 nm because of higher optical absorption at 810 nm in the crystal itself and deviations in the reflectivities of the mirrors, which are specified to $96 \pm 0.5\%$.

5.1.2. Filter cavity

The SPDC cavity emits photon pairs at 810 and 1550 nm in many free spectral ranges (FSRs). However, only very distinct modes at 1550 nm are up-converted to 532 nm as they have to match the resonance condition of the sum-frequency generation cavity. On the other hand, the avalanche photo detector (APD) measuring the 810 nm does not discriminate between photons from several FSRs, so that an APD event will herald the existence of a 1550 nm but not necessarily of an up-converted 532 nm photon. To avoid this, the 810 nm path has to be spectrally filtered to avoid this effect.

A filter cavity is designed which has a large FSR to suppress as many modes as possible and a linewidth that is not too small to cause the correlations to smooth out (cf. Section 5.2.2). A *Finesse* [Fre14] file is written, using the cavity parameters of the SPDC as determined before. It can be found in the appendix (B.1). The FSR of the

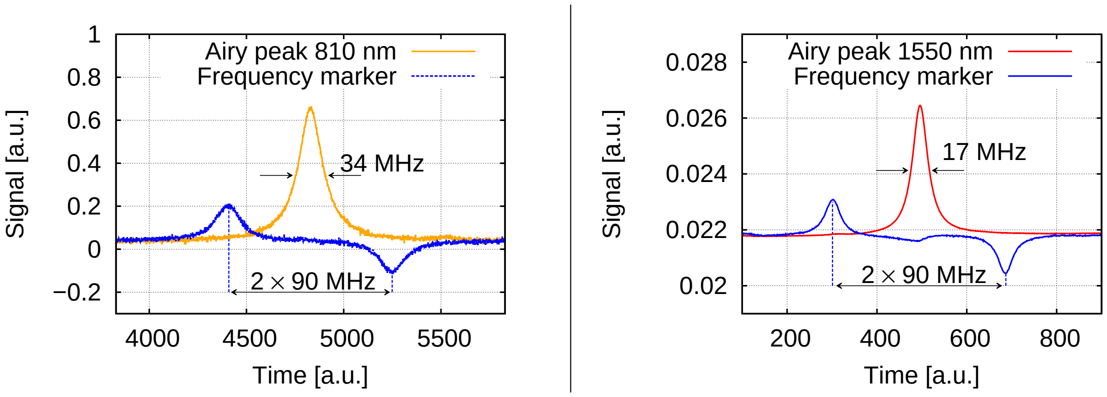

Figure 5.2.: Determining the cavity decay rates of the SPDC using a 90 MHz modulation/demodulation technique at 810 (*left*) and 1550 nm (*right*). The markers set by the modulation frequency (blue) are compared to the Airy patterns of the scanned cavity. Cavity decay rates of γ/π=34 MHz and γ/π=17 MHz are inferred for the fields at 810 and 1550 nm, respectively.

designed filter cavity is 60 GHz while its FWHM is 190 MHz. A CAD drawing of the filter cavity (provided by Axel Schönbeck) and the simulated filtering is shown in Figure 5.3. It consists of an aluminum spacer where two mirrors with 99% reflectivity are mounted to form a cavity with a 2.5 mm air gap in between. One of the mirrors is attached to a piezo electric transducer to enable scanning of the cavity. In the experiment, the cavity is held on resonance by hand, which was easily possible due to the compact and thus intrinsically stable setup of the cavity and using the count rate of APD-A as a monitor.

5.1.3. Avalanche photo detectors (APDs)

In the experiment three APDs are used. APD-T at 810 nm is used to herald the existence of a photon in the correlated 1550 nm mode. This mode is up-converted to 532 nm where it is analyzed in a Hanbury Brown and Twiss setup using APD-A and APD-B. The APD-T is made by PerkinElmer (model *SPCM-AQRH-13-FC*) with a fiber connector in front of the active surface. It has a nominal quantum efficiency of 60% at 810 nm and a dark count rate of about 250 ct/s. The dead time is measured to be 29±0.5 ns. APD-A and -B are from Laser Components (model *Count-250B*), also equipped with a fiber connector. The quantum efficiency is about 70% at 532 nm and the dark count rate is measured to be below 50 ct/s. The dead time is about 50 ns.

To analyze optical modes, they are mode-matched to standard optical fibers, which have a custom made opaque flexible aluminum shield so that no ambient light could enter the fibers and cause false events on the APDs. All coupling efficiencies are above 80%.

The power supplies for the APDs are equipped with a special protection circuit. Whenever the APD count rate increases, the electrical power consumption increases as well. The current ran through a high power shunt resistor and the voltage at the input of

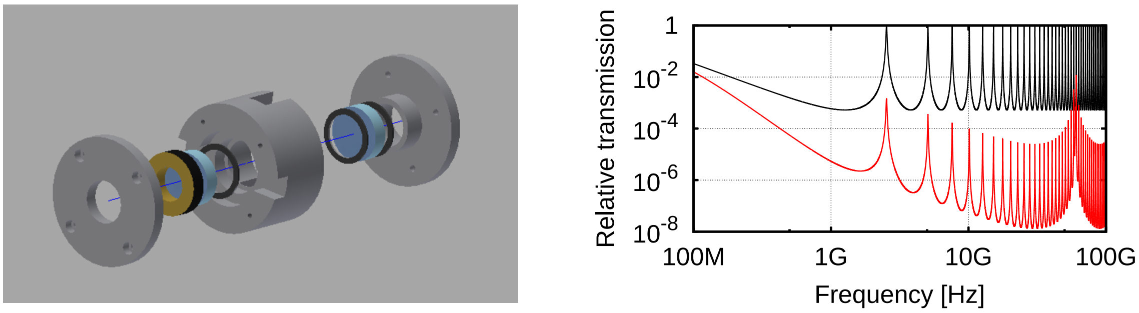

Figure 5.3.: The cavity to filter the signal mode. *left:* CAD drawing of the filter cavity done by Axel Schönbeck. The aluminum spacer held two mirrors at a distance of about 2.5 mm. *right:* The simulated mode spectrum of the SPDC cavity and the subsequent filter cavity are shown in black and red, respectively. The first significant disturbing mode appeared only at around 70 GHz.

the resistor is compared to the voltage at the output. If this difference voltage exceeds a particular value, a relay is triggered and shuts down the power supply. Additionally, an optical shutter is driven with this circuit and it blocks the optical path in case of a too high count rate. Thereby the APDs are protected from too strong optical fields. These may occur, if the SPDC is accidentally set to an operation point where too many photons are produced or if it is driven above oscillation threshold. A schematic of the APD power supply is presented in the appendix (Section B.2).

All APDs are on-off-detectors and not number resolving. This means that they indicate an event whenever they measure *something*. Even if there are two (or more) photons impinging on the detector, they generate just one electronic pulse of the same height as if only one photon is measured. In the following I will denote every APD event a *click*.

5.1.4. Data acquisition

The data acquisition is performed with an oscilloscope (AGILENT *DSO 7014B*). All three time series of the APDs with a duration of 2 ms are recorded simultaneously with a sample rate of 2 GSa/s. This is done 2000 times so that in each measurement run 4 s of data are available containing about 10^5 to 10^6 trigger events (depending on the gain parameter ε). Each time series is directly transferred as binary data to a PC via the local LAN network utilizing the *VISA* protocol in a *python* environment (*PyVISA*). The programm codes for interfacing the oscilloscope with the PC, all settings and the loops for data acquisition are given in Section B.4.1.

The binary data are converted to hdf5-files, which can be processed efficiently by *python*. In a final pre-processing step the data are “shrinked”, i.e. the hdf5-files are scanned and only actual events are kept and given an integer time-tag. Thereby the size of the data files is considerably reduced and further data analysis can be performed in reasonable time. The programs for data conversion and shrinking are also presented in the appendix (Sections B.4.2 and B.4.3).

5.2. Cavity enhanced spontaneous parametric down-conversion

The treatment of the spontaneous parametric down-conversion cavity (SPDC) is similar to the degenerate OPA of Chapter 3 with one difference: the two correlated photons generated in the down-conversion process do not have the same frequency. This leads to the fact, that generally these two fields have different decay rates γ_+ and γ_-. The two indices denote the upper and lower sideband which have the frequencies ω_+ and ω_-. Of course, energy conservation must hold so that $\omega_+ + \omega_- = \omega_\mathrm{p}$. In the experiment performed in this thesis, ω_+ corresponds to the field that has the wavelength of approximately 810 nm, ω_- is the frequency of the field with the telecommunication wavelength 1550 nm and the pump field is the 532 nm field (ω_p).

5.2.1. Temporal correlations of the SPDC output

In the experiment, non-degenerate output modes of the SPDC are spatially separated by a dichroic beam splitter. A photon in one of these modes (at 810 nm) heralds the existence of a photon in the other mode (1550 nm). The setup is sketched in Figure (5.4).

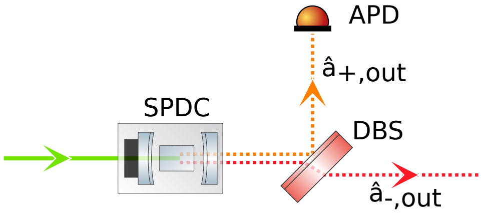

Figure 5.4.: Schematic of the heralded single photon source. The detection of a photon in the $\hat{a}_{+,\mathrm{out}}$ mode (810 nm) heralds the existence of a photon in the $\hat{a}_{-,\mathrm{out}}$ mode (1550 nm). The detection is performed by an avalanche photo diode (APD) and the spatial separation of the two output modes of the SPDC takes place on a dichroic beam splitter (DBS).

The temporal correlation function of the two modes is given by

$$\Gamma(\tau) = \langle \hat{a}^\dagger_{+,\mathrm{out}}(t)\hat{a}^\dagger_{-,\mathrm{out}}(t+\tau)\hat{a}_{-,\mathrm{out}}(t+\tau)\hat{a}_{+,\mathrm{out}}(t)\rangle \,, \tag{5.1}$$

where $\hat{a}_{\pm,\mathrm{out}}$ are the mode operators for the trigger (+) and signal (-) field.

The mode operators can be calculated following a cavity input-output formalism. A detailed calculation is given in the appendix, Section A.4 with the resulting temporal correlation function

$$\begin{aligned}\Gamma(\tau) = &\left[\frac{\varepsilon\gamma}{2}\left(\frac{1}{\lambda}\mathrm{e}^{-\lambda|\tau|} + \frac{1}{\mu}\mathrm{e}^{-\mu|\tau|}\right)\right]^2 \\ &+ \left[\frac{|\varepsilon|^2\gamma}{\gamma^2 - |\varepsilon|^2}\right]^2 + \left[\frac{\varepsilon\gamma}{2}\left(\frac{1}{\lambda}\mathrm{e}^{-\lambda|\tau|} - \frac{1}{\mu}\mathrm{e}^{-\mu|\tau|}\right)\right]^2 .\end{aligned} \tag{5.2}$$

Here, τ is the time delay between two subsequent detections of a trigger and a signal photon, ε is the gain parameter, γ is the cavity decay rate of the SPDC, and $\lambda = \gamma - |\varepsilon|$, $\mu = \gamma + |\varepsilon|$. The oscillation threshold is given for $|\varepsilon| = \gamma$.

To the best of my knowledge, this full temporal correlation function hasn't been mentioned elsewhere before as usually a low-gain-approximation is used. However, this approximation very well covers the interesting features: the second term of Eq. (5.2) is a time independent offset while the third term is much smaller than the first one. Especially in the low-gain-limit with $|\varepsilon| \ll \gamma$ (i.e. $\lambda \approx \mu$) it becomes negligible. The shape of the correlation function is thus approximated very well by the first term of Eq. (5.2) since the experiment is operated with low gain $|\varepsilon| \ll \gamma$, see also the appendix A.4.3. I will continue all calculations with the first term only.

5.2.2. Temporal correlations with filtered signal mode

In the experiment, the two fields generated via non-degenerate down-conversion experience different transfer functions. An asymmetry is caused by frequency filtering of the signal mode by up-conversion in a sum-frequency generation cavity with a relatively small linewidth. Unequal decay rates in the generation process of the two down-converted fields have a similar effect. Here, I will pool these two effects (that actually are present in the experiment) by letting one of the modes (the 1550 nm field, $\hat{a}_-$) be transmitted through one cavity with the decay rate κ. A schematic of the propagation of the two modes and the cavities involved is shown in Figure 5.5.

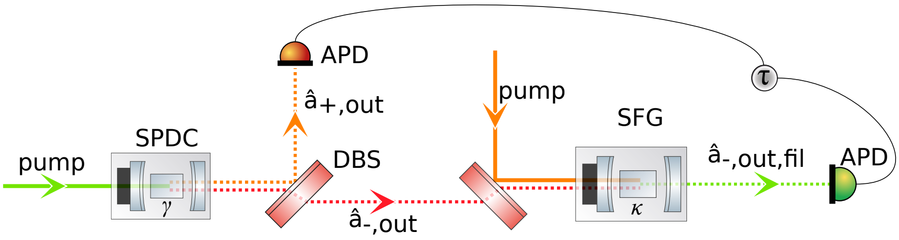

Figure 5.5.: Schematic of the heralded single photon source and subsequent frequency up-conversion of the signal mode in a sum-frequency generation cavity (SFG). The SFG is a cavity with decay rate κ so that the signal mode experiences additional frequency filtering. The correlations between the trigger and the up-converted signal mode are analyzed by measuring the time delay τ between clicks of the illustrated APDs.

The $\hat{a}_{-,\mathrm{out}}$ mode is frequency up-converted in the sum-frequency generation cavity (SFG) and detected with an APD. The time correlations between a click at this detector and the trigger detector is given by

$$\Gamma_{\text{filtered}}(\tau) = \begin{cases} \left[\frac{\gamma\varepsilon\kappa}{2}\left(\frac{\mathrm{e}^{\mu\tau}}{\mu(\kappa+\mu)} + \frac{\mathrm{e}^{\lambda\tau}}{\lambda(\kappa+\lambda)}\right)\right]^2 & , \tau < 0 \\ \left[\frac{\gamma\varepsilon\kappa}{2}\left(\frac{\mathrm{e}^{-\mu\tau}}{\mu(\kappa-\mu)} + \frac{\mathrm{e}^{-\lambda\tau}}{\lambda(\kappa-\lambda)} - \frac{2\mathrm{e}^{-\kappa\tau}}{(\kappa+\mu)(\kappa-\mu)} - \frac{2\mathrm{e}^{-\kappa\tau}}{(\kappa+\lambda)(\kappa-\lambda)}\right)\right]^2 & , \tau \geq 0\,. \end{cases} \tag{5.3}$$

In Figure 5.6 the effect of filtering is shown.

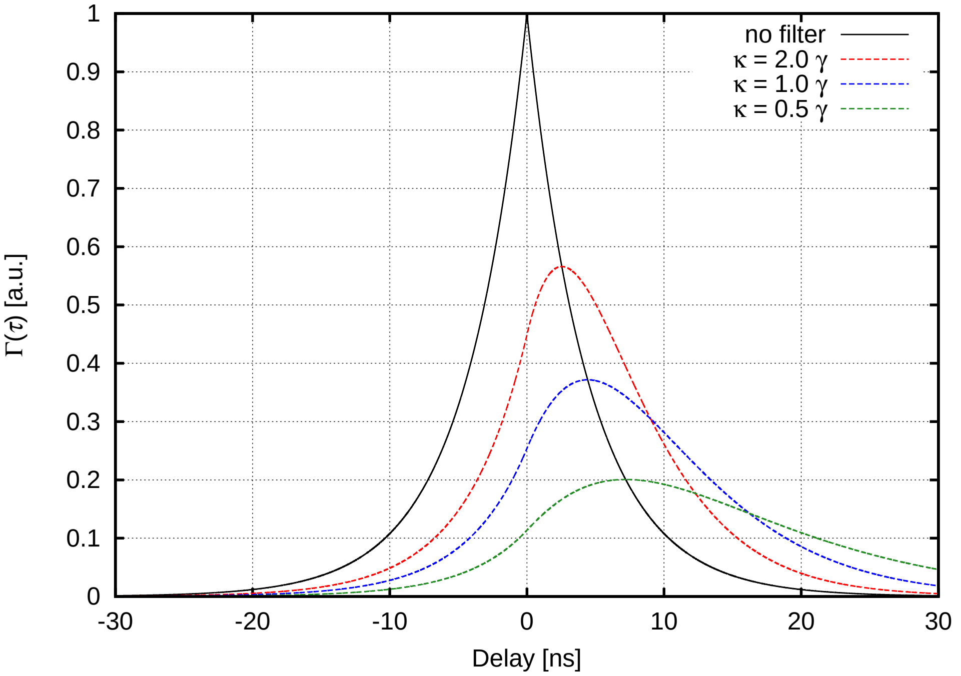

Figure 5.6.: Effect of extra-filtering of the signal mode $\hat{a}_-(t)$. The smaller the decay rate κ of the extra filter, the more the correlations between trigger and signal smooth out. Parameters are $\gamma = \pi{\cdot}35\,\mathrm{MHz}$, $\varepsilon = \gamma/10$.

In case of no additional frequency filtering ($\kappa = \infty$), the correlations between the trigger and signal photon are approximated by a double exponential decay. However, the smaller the decay rate κ of the SFG, the more the signal photons are delayed and the correlations smooth out. This effect will be clearly visible in the experimental data.

5.3. Results

In the first step of the data analysis, the correlations between the trigger events and the signal photons at 532 nm are analyzed. In further steps, the probabilities of vacuum, single photons and higher photon contributions are determined, which enable the application of criteria of nonclassicality.

5.3.1. Two- and threefold coincidences

The SPDC cavity is characterized by analyzing two- and threefold coincidences of the three detectors. A two-fold coincidence is an event, where APD-T and APD-A or APD-T and APD-B click within a certain time window. These coincidences are described by the correlation function developed in Section 5.2. An event where all three detectors click is called three-fold coincidence and is generally unwanted as it means that there are more than one photon in the 532 nm mode.

The counting statistics of APD-A and -B triggered on APD-T are shown in Figure 5.7 for a pump parameter $\varepsilon = 0.07\gamma$, i.e. the pump amplitude is at 7% of the oscillation threshold. The temporal profile of the up-converted photons clearly shows the smoothed out exponential decay predicted by Eq. (5.3). The theoretical curve was obtained by using a decay rate of $\gamma = \pi \cdot 31\,\text{MHz}$ and an extra filtering effect of the signal mode with $\kappa = 1.4\gamma$. As already briefly discussed in Section 5.2, this filtering of the signal mode is caused by asymmetric decay rates of the SPDC cavity and the transmission of the signal through the up-conversion cavity. The FC introduces negligible frequency filtering to the trigger mode due to its relatively large linewidth (190 MHz). In this graph, three-fold coincidence events do not show any significant contribution to the statistics.

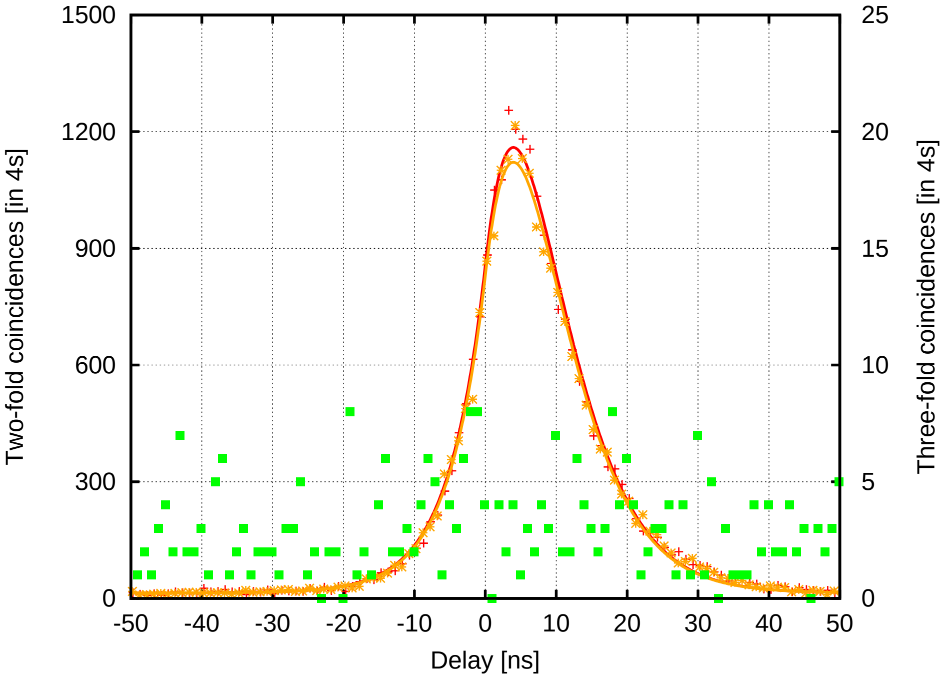

Figure 5.7.: Histogram of the two-fold coincidence detections at APD-T and APD-A (red), and APD-T and APD-B (yellow) with theoretical curves ($\gamma = \pi \cdot 31\,\text{MHz}$, $\kappa = 1.4\gamma$, $\varepsilon = 0.07\gamma$). The delay for the three-fold coincidences of APD-T, APD-A and APD-B (green points, right y-axis) is defined as the time between counts at APD-A and -B given that the trigger APD-T detected a photon (within a 100 ns time window).

When the pump power for SPDC is higher, the probability of generating more than one photon pair within the same coherence time increases. In Figure 5.8 the counting statistics are shown for measurements with $\varepsilon = 0.11\gamma$ and $\varepsilon = 0.19\gamma$. The three-fold coincidences indicated by the green circles now significantly contribute to the counting statistics.

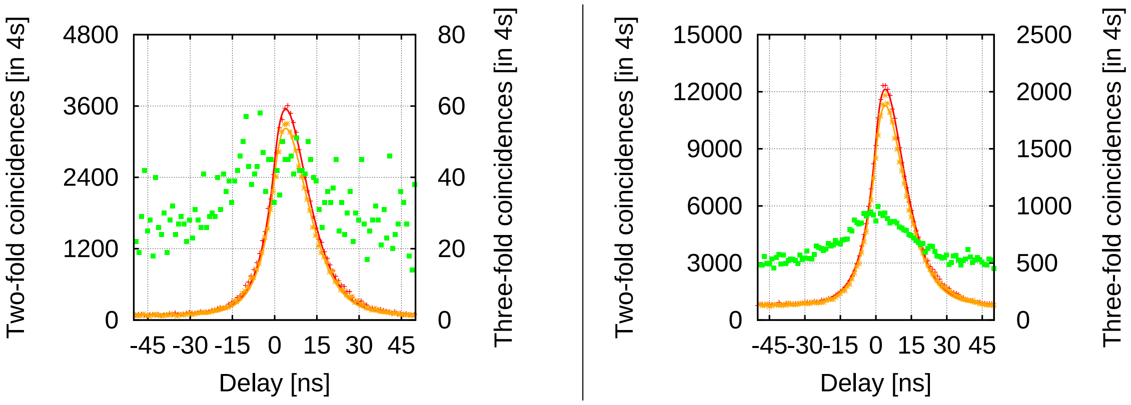

Figure 5.8.: Histogram of the two- and threefold coincidences, as in Figure 5.7 with the only difference being that $\varepsilon = 0.11\gamma$ (*left*) and $\varepsilon = 0.19\gamma$ (*right*). The three-fold coincidences significantly contribute to the statistics.

5.3.2. Second order correlation function

Nonclassicality of a state can be certified by a $g^{(2)}$ parameter which is defined as [Ger05]

$$g^{(2)}(0) = \frac{\langle \hat{a}^\dagger \hat{a}^\dagger \hat{a} \hat{a} \rangle}{\langle \hat{a}^\dagger \hat{a} \rangle^2} . \tag{5.4}$$

Whenever $g^{(2)}(0) < 1$, the state has sub-Poissonian photon number statistics, which is evidence for nonclassicality. (For a coherent state $g^{(2)}(0) = 1$.) In a photon counting experiment like the one presented here, the generated state can be very well approximated by $\rho = p_0|0\rangle\langle 0| + p_1|1\rangle\langle 1| + (1 - p_0 - p_1)|2\rangle\langle 2|$, where p_0 is the probability of measuring vacuum and p_1 the single photon probability. With these probabilities the $g^{(2)}(0)$ value can be calculated as [Jež11]

$$g^{(2)}(0) = \frac{2(1 - p_0 - p_1)}{[2(1 - p_0 - p_1) + p_1]^2} = \frac{2(1 - p_0 - p_1)}{[2(1 - p_0) - p_1]^2} . \tag{5.5}$$

The numerator is twice the probability that both detectors click simultaneously. The factor of two results in the fact that the signal is split up at a 50:50 beam splitter, and when there are two photons in the mode they can split with 50% probability or both go to just one APD that cannot distinguish if there is only one or more photons. The two-(or more) photon probability is thus twice the value determined directly from the measured rate. The denominator is the probability of one detector clicking. It clicks with twice the probability of measuring two photons (same argumentation as before) plus the probability of detecting a single photon. This holds for both APDs and the square arises from the definition of $g^{(2)}(0)$, i.e. Eq. (5.4).

All events at APD-A and -B should coincide with a click at APD-T as only then one can be sure that an actual signal is measured. Ambient light, stray light or some other uncorrelated photons would result in a classical counting statistic. Therefore, with a click of APD-T a time window – symmetric about this event – is opened and whenever APD-A or APD-B clicks within this window (or both), a counter is increased. The counters for two-fold coincidences of APD-T with APD-A or -B are denoted R_{1A} and R_{1B} and the counter for three-fold coincidences is R_2. The total number of trigger events is R_0. The probability for a vacuum state is then

$$p_0 = 1 - \frac{R_{1A} + R_{1B} + R_2}{R_0} \,. \tag{5.6}$$

The number of single events is bounded from below by

$$p_1 > \frac{R_{1A} + R_{1B}}{R_0} - \frac{T^2 + (1-T)^2}{2T(1-T)} \frac{R_2}{R_0} \,, \tag{5.7}$$

where T is the beam splitter ratio in the Hanbury Brown and Twiss setup, $T = R_{1A}/(R_{1A} + R_{1B})$, see [Jež11] for details.

The rates R_x strongly depend on the size of the coincidence window. An illustration on how the coincidence window is set is shown in Figure 5.9. Obviously, if it is chosen too small, not all photons at 532 nm are taken into account as they are spread over some finite time as it can be seen from Figure 5.7 or Eq. (5.3). The total number of events

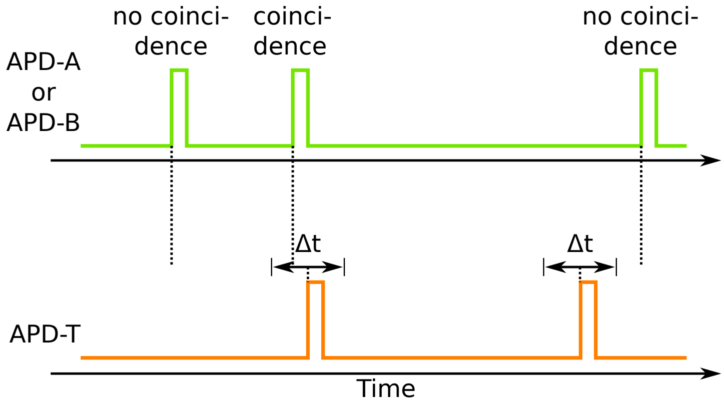

Figure 5.9.: The coincidence window is a time frame symmetric about a click at APD-T. If a click happens within this time window at APD-A or APD-B, this click is accepted as a coincidence. When the window is chosen too small, less coincidences are measured and the vacuum probability is overestimated. However, if the window is too large, uncorrelated photons or background noise is considered a coincidence, which reduces the single photon probability.

decreases and so does the statistical significance. However, when the chosen window is too large, uncorrelated photons are measured and three-fold coincidences become more and more likely, reducing the single photon content of the state. The optimum value can be found by varying the coincidence window in post-processing, as the data acquisition allows access to the full time series of all events.

In Figure 5.10 the $g^{(2)}(0)$ value is plotted against the size of the coincidence window. The error bars are obtained by assuming Poissonian counting statistics and corresponding error propagation. In Poissonian counting statistics the standard deviation of a measured rate is given by $\Delta R = \sqrt{R}$.

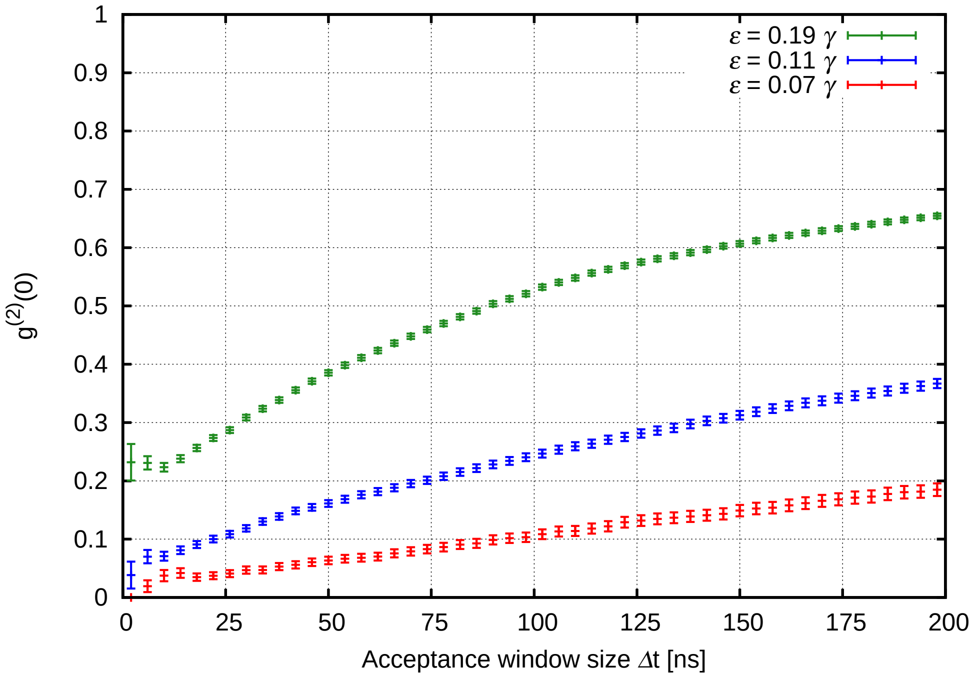

Figure 5.10.: Experimentally determined $g^{(2)}(0)$ value according to Eq. (5.5). The lower the gain parameter ε, the lower the $g^{(2)}(0)$ value, which is below 0.05 for $\varepsilon = 0.07\gamma$ and coincidence windows smaller than 34 ns.

For small parametric gain ($\varepsilon = 0.07\gamma$), the $g^{(2)}(0)$ value reaches values smaller than 0.05 for coincidence windows smaller than 34 ns. Larger windows lead to three-fold coincidences caused by noise and the single photon probability decreases. If the pump power of the SPDC and thus the parametric gain ε is increased, the contribution of higher numbers of photons in the state increases. This leads to a higher rate of three-fold coincidences and a reduction of the single photon contribution.

5.4. Quantum non-Gaussianity

The sub-Poissonian statistics indicated by a $g^{(2)}(0)$ smaller than unity are a strong signature for the nonclassicality of the states. An even stronger feature of nonclassicality is a negative Wigner function, the hallmark of single-photon states [Lvo01]. However, due to mixture with vacuum, the negativity of such states decreases, or even vanishes, when losses exceed 50 %. Nevertheless, it is still possible to certify a quantum non-Gaussianity (QNG) of the state. Recently it has been shown, that QNG is a sufficient condition for the security of a discrete-variable quantum key distribution scheme [Las16]. QNG is thus a useful feature for quantum information tasks. The measured probabilities p_0 and p_1 can be used to analyze whether the up-converted states ρ are quantum non-Gaussian or not. The QNG criterion has been used in a variety of experiments to characterize single photon sources [Jež11, Jež12, Pre14].

The property of QNG was originally proposed by R. Filip and L. Mišta [Fil11] and I will briefly sketch their idea here. Let $\mathcal{G}$ be the set of all Gaussian states and mixtures thereof. Any state ρ which is not in $\mathcal{G}$ is defined to be quantum non-Gaussian. This criterion identifies QNG states using a simple and experimentally feasible criterion based on photon number probabilities. For a given (measured) vacuum probability p_0 a maximum single-photon probability p_1 achievable by a Gaussian state can be calculated. If the measured p_1 is higher, then $\rho \notin \mathcal{G}$.

The boundary values for p_0 and p_1 for still forming a state in $\mathcal{G}$ is given by [Jež11]

$$\begin{aligned} p_0 &= \frac{\exp\left[d\left(\tanh r - 1\right)\right]}{\cosh r}, \\ p_1 &= \frac{d\exp\left[d\left(\tanh r - 1\right)\right]}{\cosh^3 r}, \end{aligned} \tag{5.8}$$

where $d = (e^{4r} - 1)/4$ and $r = -\frac{1}{2}\ln(1 - \frac{4\varepsilon/\gamma}{(1+\varepsilon/\gamma)^2}) \overset{\varepsilon\ll\gamma}{\approx} 2\varepsilon/\gamma$ is the squeezing parameter. In Figure 5.11 the area of states that can be described by mixtures of Gaussian states is shown in red. The border of this area is specified by Eq. (5.8). All states that lie beyond this border are quantum non-Gaussian (green area).

The witness of QNG is defined as $W = p_1 + ap_0 - W_G(a)$, where $a < 1$ is a parameter specifying the witness and $W_G(a)$ represents the maximum of $p_1 + ap_0$ achievable by Gaussian states for a given a. Assuming Poissonian statistics of the measured coincidences, the statistical error of the witness can be determined and one can express the witness in numbers of standard deviations ΔW. A positive witness certifies QNG of the state, even though in general it can be a mixed state with a positive Wigner function. It has been shown that the QNG criterion is very robust against optical losses [Str14], possibly qualifying it to become a standard tool in single photon state characterization.

The experimental result is shown in Figure 5.12. In the plot the witness of QNG, W, is shown for measurements with three different gain parameters ε, dependent on the coincidence window size Δt. Also shown is W in numbers of standard deviations, ΔW. For each ε and Δt, the parameter a of the QNG witness W was optimized such as to maximize $W/\Delta W$. If the witness is positive, then $\rho \notin \mathcal{G}$. The program for the calculation of the witness is given in the appendix, Section B.4.4.

For low gain $\varepsilon = 0.07\gamma$, the witness of QNG was positive for all coincidence windows smaller than 300 ns, reaching a maximum of 16 standard deviations around Δt=34 ns. For higher gain, the multiphoton contribution increases, which lowers the witness. For

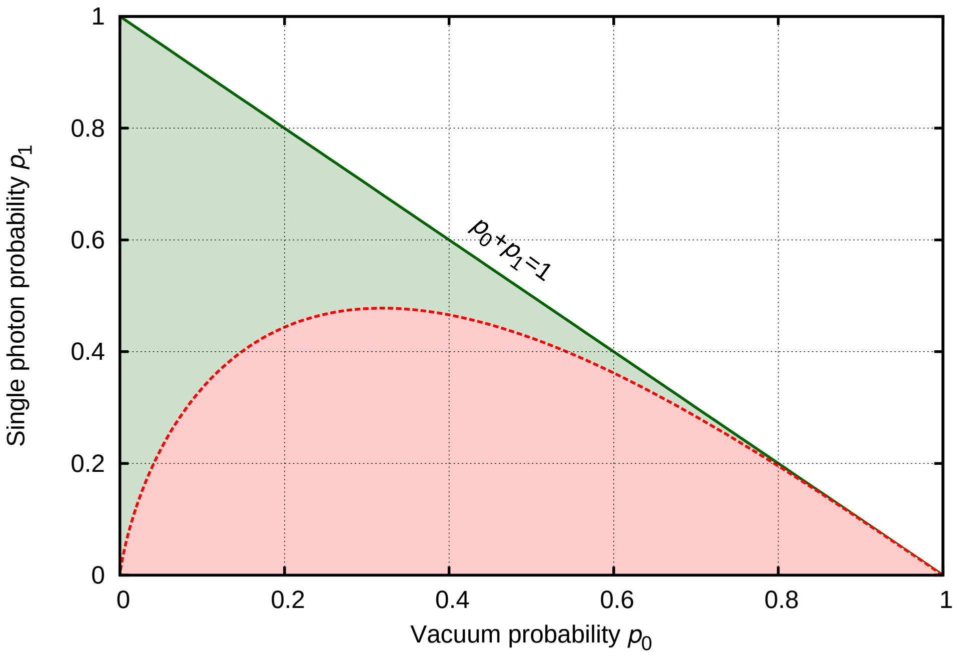

Figure 5.11.: Quantum non-Gaussianity. For every vacuum probability p_0 a maximum single photon probability p_1 can be calculated so that the pair still forms a Gaussian state. All these pairs lie on the red-dashed line. Every pair below this curve can be described as a mixture of Gaussian states lying in the area called $\mathcal{G}$ (red area). However, every pair above this line describes a state $\rho \notin \mathcal{G}$ and is quantum non-Gaussian (green area). The green diagonal is the border of physically allowed states.

$\varepsilon = 0.11\gamma$ and $\Delta t \geq 120\,\mathrm{ns}$ the witness is negative, indicating that the state could possibly be expressed as a convex mixture of Gaussian states. For even higher gain ($\varepsilon = 0.19\gamma$) the witness of QNG is never positive. Since the mode approaches thermal statistics [Yur87], higher photon number contributions show up and background noise increases.

The maximum achievable witness can be calculated by applying the following model. I assume an initial two-mode squeezed vacuum state, produced by the SPDC and characterized by the pump parameter ε. Both modes propagate through lossy channels with transmittances η_S (signal) and η_T (trigger) that account for all imperfections of the setup, i.e. quantum efficiency of the APDs, limited up-conversion efficiencies or other optical losses. The highest value of W_{max} is achieved in the weak squeezing limit ($\varepsilon \rightarrow 0$), where higher photon numbers become negligible and the single photon probability is simply given by the signal detection efficiency η_S, $p_1 = \eta_S$, and $p_0 = 1 - \eta_S$. In the present experiment, this efficiency is bounded from below by $\eta_S = 0.2$, which yields a maximum witness $W_{\mathrm{max}} = 0.00486$. Evaluating the experimental data, the maximum witness that is achieved is $W_{\mathrm{exp}} = 0.00315$, when $\varepsilon = 0.07\gamma$. As this reduction was most likely caused by dark counts and background noise, that were not included in the model, the exper-

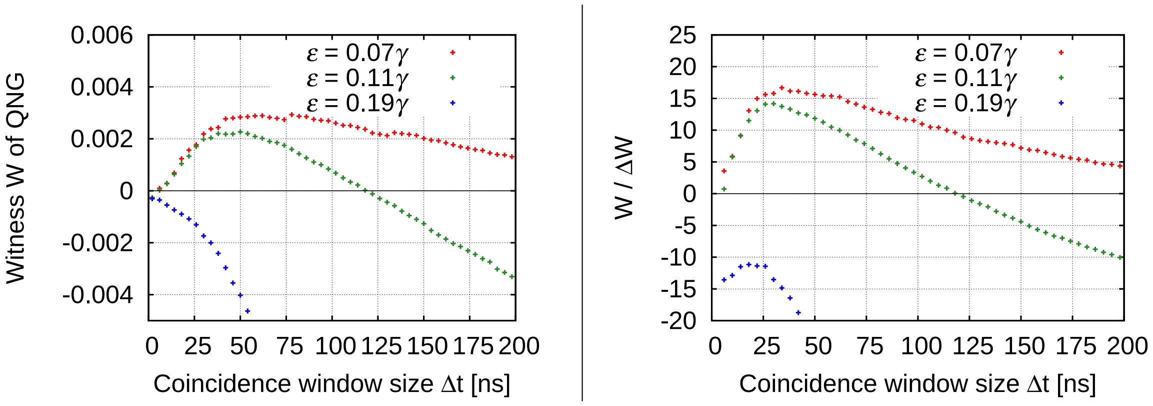

Figure 5.12.: Witness of quantum non-Gaussianity (QNG) of the frequency up-converted single photons. *left:* The witness depending on the coincidence window size for three different gain parameters ε. The witness is the highest for the smallest $\varepsilon = 0.07\gamma$ and at a particular coincidence window size. For higher gain and for a too long coincidence window, the witness becomes negative at some point as too many uncorrelated events are considered a coincidence. If $\varepsilon = 0.19\gamma$, no quantum non-Gaussianity can be witnessed for any coincidence window size. *right:* The witness in numbers of standard deviations with a maximum significance of more than 16 standard deviations at $\Delta t = 34\,\mathrm{ns}$ and for $\varepsilon = 0.07\gamma$.

imental data are in good agreement with the theoretical predictions. Furthermore, the experiment is not performed exactly in the weak squeezing limit. At least the gain had to be $\varepsilon = 0.07\gamma$ to achieve sufficiently high probability of conditional generation of the single photon state and to accumulate enough data during the experiment.

5.5. Extended analysis

Initiated by Jaromír Fiurášek, the experimental data were analyzed to reveal more subtle features. These studies base on a full multi-mode description of the SPDC output and discretized time slots. The results are presented in a second publication related to this experiment [Fiu15].

The theoretical framework and analyses were provided by Jaromír Fiurášek. The manuscript is self consistent and I refrain from reciting everything at this point. However, our experimental data and results from some additional measurements are used and I will briefly present the main results in the following.

5.5.1. Dead time of APD-T

The dead time t_D denotes a time interval after a click of an APD during which this detector is blind and cannot detect any photons. This means that if APD-T clicks at time t_0, the detector did not detect any photons in the time interval $[-t_D, t_0]$, because otherwise it would be blind and could not have detected a photon at time t_0. A click of the trigger detector thus excludes the possibility of a trigger event at the particular preceding time interval. The fact that the trigger detector did not register any photons in the time interval $[-t_D, t_0]$ implies that the idler beam was projected onto vacuum in this time interval. The intrinsic quantum correlations between signal and idler photons consequently also reduce the multi-photon contributions in the signal beam and the value of the quantum non-Gaussianity witness increases.

5.5.2. Afterpulses

Avalanche photo diodes also show the effect of afterpulsing, i.e. a spurious event occurs some time after an actual click. The effect originates in the electronics of the device when the electron avalanche is not completely quenched after a click. It occurs with some probability (typically 1%) and decays exponentially with a time constant of a few ns. The measured distribution of the detector APD-T is shown in Figure 5.13, where also the dead time of 29 ns is clearly visible. It was measured by simply detecting an attenuated coherent field, where photons are not time-correlated to each other ($g^{(2)}(\tau) = 1$ for all τ). For a period of $t_D = 29\,\mathrm{ns}$ no subsequent clicks are detected as expected, as this is the dead time of the APD. Directly after the dead time, one measures an increased probability for a subsequent photon, which is due to the afterpulsing effect. This probability decreases exponentially with a time constant of 28 ns. After about 100 ns, no afterpulses occur anymore and only *real* photons are measured.

The afterpulses are not of optical origin. One expects that their exclusion from the data analysis would further increase the single photon contribution, as they pretend a trigger event that has no correlated signal photon. In Figure 5.14, the QNG witness is shown dependent on a certain minimum “waiting time” t_{min}. This is the time before a click at APD-T that had to be passed without any other click. By introducing t_{min} one

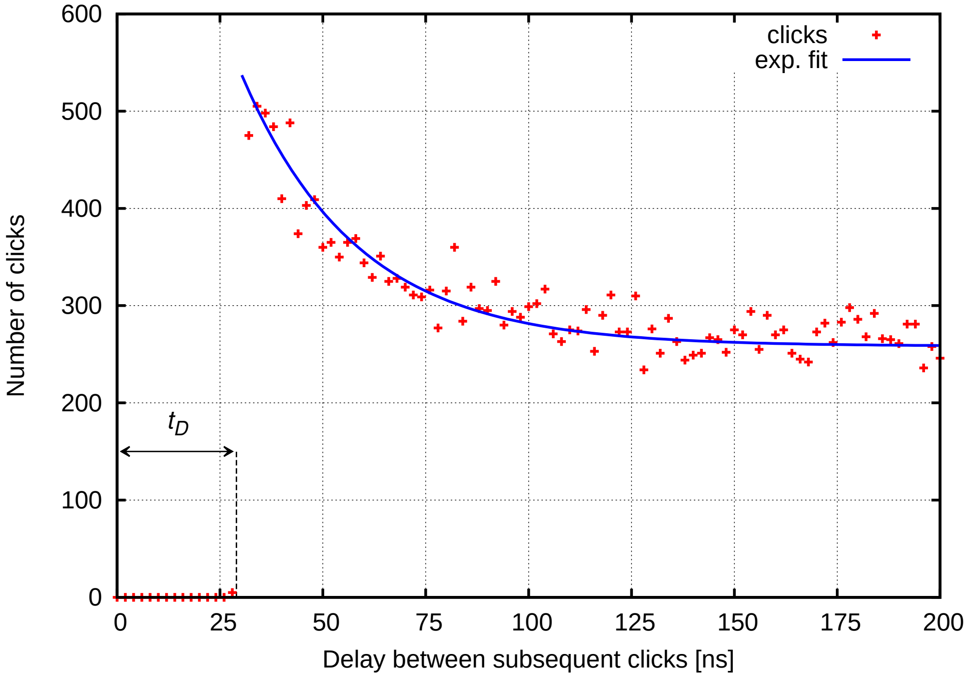

Figure 5.13.: Statistics on the occurrence of about 10^6 clicks at APD-T. A coherent state is measured so that in an ideal detector no preferred or neglected delays should be visible. However, in the first 29 ns the detector is blind due to the dead time t_D. After this time afterpulses originating from the electronics of the APD cause the count rate to increase. The afterpulse probability follows an exponential decay with a time constant of 28 ns.

can exclude that the current click is not caused by afterpulsing. The plot shows that the QNG witness actually increases if afterpulses are excluded from the analysis.

5.6. Discussion and outlook

The experiment presented here was the first discrete variable experiment realized in the working group of Professor Roman Schnabel. Many optics, electronics and programs to control the experiment and to acquire and analyze the data were designed and built from scratch. I expect and hope that many of the presented calculations, ideas, simulations, circuit boards and programs will be used in future experiments. The most relevant ones can be found in the appendix.

I presented the generation of heralded single photons generated by spontaneous parametric down-conversion. The single photons at the telecom wavelength of 1550 nm were subsequently up-converted to 532 nm and analyzed in a Hanbury Brown and Twiss setup. A $g^{(2)}(0)$ value smaller than 0.05 was demonstrated.

To the best of my knowledge, for the first time frequency up-converted states are demonstrated to show quantum non-Gaussianity. An up-converted heralded single pho-

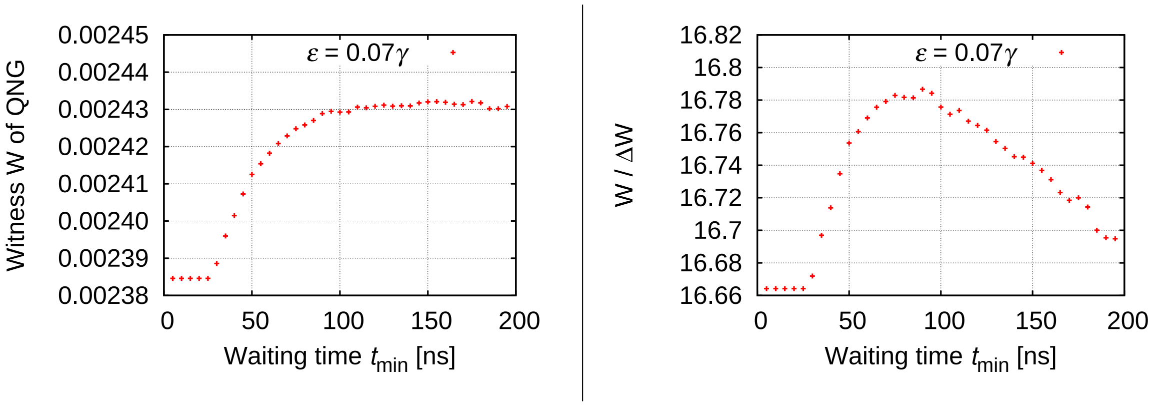

Figure 5.14.: *left:* Witness of QNG dependent on a minimum waiting time t_{min}. A trigger click is only accepted, when t_{min} has passed after a preceding click. Thereby false (i.e. uncorrelated) clicks caused by afterpulses can be excluded that reduce the single photon probability of the up-converted state. *right:* The witness in numbers of standard deviations. For increasing t_{min} the total number of accepted clicks reduces so that the standard deviation increases causing the points on the right side to drop. The pump parameter is $\varepsilon = 0.07\gamma$ and the coincidence window was fixed at $\Delta t = 34\,\mathrm{ns}$.

ton state was witnessed to be quantum non-Gaussian with more than 16 standard deviations. This strong measure of nonclassicality is a sufficient condition for the security in discrete variable quantum key distribution. Thus, the frequency up-conversion of single photons may evolve into a useful tool in quantum information science.

6. Single photon state tomography

Quantum computers solve certain problems much faster than ordinary computers. The Gottesman-Knill theorem states that a wide class of systems can be efficiently simulated with classical methods [Got99, Bar02]. Only when states with a negative Wigner function are used, a quantum computer outperforms its classical counterpart [Mar12]. One of the examples of states with a negative Wigner function is the single photon state and the generation of these kind of states is realized in the experiment presented in this chapter. Another goal of this experiment is to establish a hybrid quantum state generation scheme, i.e. the combination of discrete (e.g. single photons) and continuous (e.g. squeezed states) variable techniques, in the telecommunication wavelength regime around 1550 nm.

Squeezed vacuum states consist of photon pairs in a very good approximation when the pump power is low (and so is the squeezing strength) and no higher order pairs occur. If this state is sent to a high reflection beam splitter and a photon is detected in transmission, the state in reflection is projected into a single photon state [Dak97, Møl06]. This way, single photons can be conditionally prepared (heralded) and subsequently analyzed via quantum state tomography. In the experiment presented here, the detection of the heralding photon is assisted by on-the-fly frequency up-conversion to 532 nm to take advantage of low noise silicon avalanche photo detectors.

Previous works at other wavelengths have demonstrated negative Wigner functions both with pulsed and continuous wave setups [Lvo01, NN07]. Very helpful to realize the experiment were thus the PhD theses of Jonas Schou Neergaard-Nielsen [NN08] and Bo Melholt Nielsen [MN10] and the main ideas can also be found there.

In Section 6.1 the experimental setup and the main components for data acquisition are introduced. Many components could be adapted from the experiment on up-conversion of single photons, cf. Section 5, so that only components that are specific for this experiment are presented. The data processing and the results are presented in Section 6.2, followed by an outlook.

6.1. Experimental setup

The experimental setup for the single photon tomography is shown in Figure 6.1. Squeezed states of light at 1550 nm are generated in an optical parametric amplifier (OPA). The OPA is described in detail in Section 3.2.4. A small fraction of this state (about 0.5%) is subtracted from this state and the remaining state is analyzed via balanced homodyne detection (BHD). The subtracted mode is up-converted to 532 nm in the sum-frequency generation cavity (SFG), cf. Section 3.2.5. After passing a filter cavity (FC) the up-

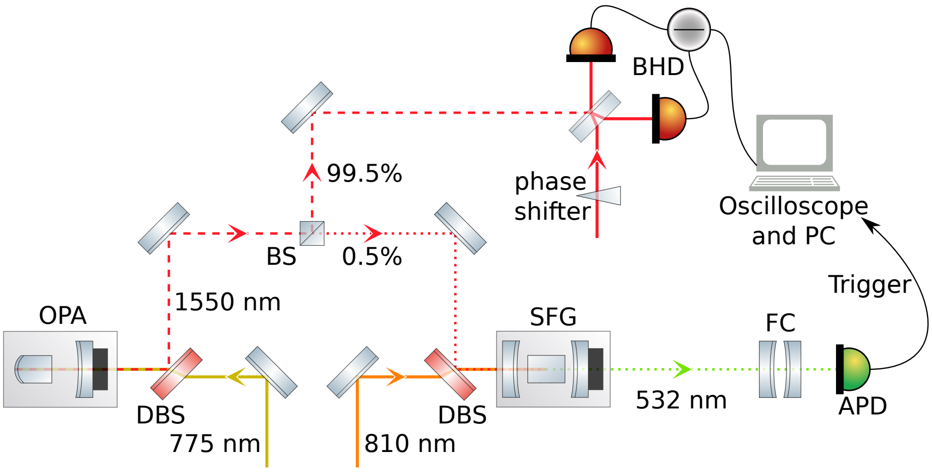

Figure 6.1.: Experimental setup for the Fock state tomography. Squeezed states of light at 1550 nm are generated in an optical parametric amplification cavity (OPA) using a pump field at 775 nm. A small fraction (0.5%) is subtracted from this state and up-converted to 532 nm in a sum-frequency generation cavity (SFG) using a pump field at 810 nm. The up-converted state passes a filter cavity (FC) and is detected with an avalanche photo detector (APD). The remaining state at 1550 nm is analyzed with a balanced homodyne detector (BHD). The electronic signal is acquired with an oscilloscope that is triggered by APD events. The data is directly transferred to a PC. DBS: dichroic beam splitter; BS: beam splitter.

converted mode is detected with an avalanche photo detector (APD). Every click of this detector triggers an oscilloscope, which records the BHD signal. The recorded raw data are directly transferred to a PC.

The frequency up-conversion of the trigger photons from 1550 to 532 nm is done to enable the use of commercially available, low noise and easy-to-use silicon APDs that are not responsive for infrared wavelengths. APDs for 1550 nm based on InGaAs chips or superconducting sensors would require cooling up to cryogenic temperatures to achieve comparable detection efficiencies and noise performance [Had09].

6.1.1. Homodyne detector

The analysis of the signal state is performed via optical homodyne tomography [Lvo09] which requires a balanced homodyne detection scheme. The electronics of the detector have to be fast enough to be capable of resolving as much as possible of the spectral properties of the state. As the OPA has a linewidth of 120 MHz (FWHM), the detector needs to have at least the same bandwidth as otherwise the effective efficiency of detecting the state would decrease [Kum12]. Moritz Mehmet and Stefan Ast designed, built and used a homodyne detector for gigahertz applications and kindly provided a device for my purposes. A short description of the design can be found in the doctoral thesis of Stefan Ast [Ast15]. The electronic circuit was modified for the use with photo diodes with a larger active area which makes them easier to align. Their internal capacitance is higher which reduces the bandwidth of the detector that remains sufficient though. A spectrum of the detector's dark noise and a vacuum reference is shown in Figure 6.2. The detector has a flat response and a dark noise clearance of more than 15 dB up to 200 MHz, disturbed just by electronic pick-up peaks in the dark noise of unknown origin at 100 and 120 MHz.

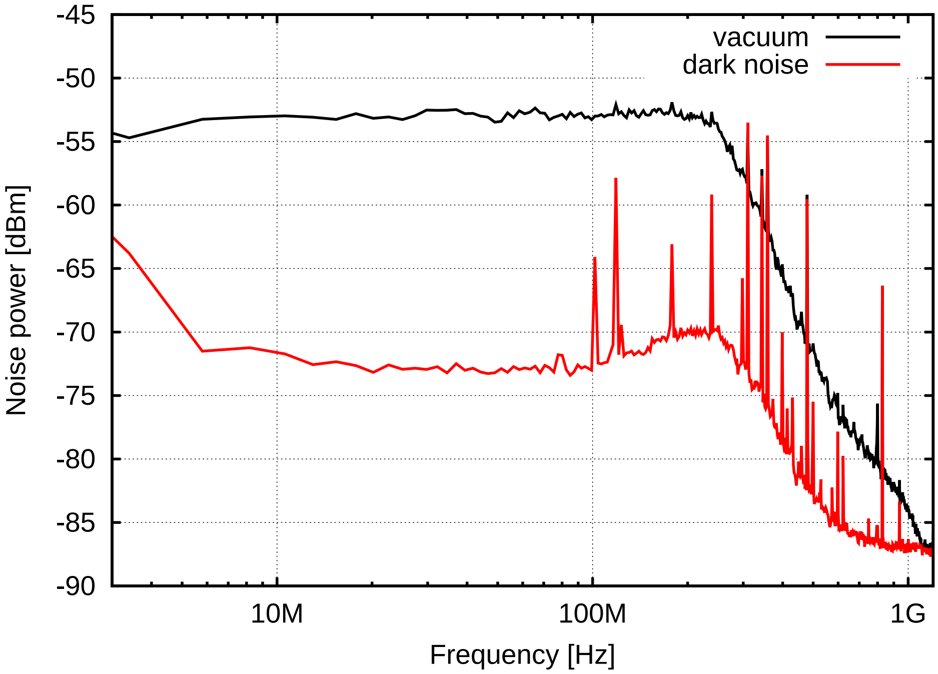

Figure 6.2.: Power spectrum of the fast homodyne detector. The vacuum reference is more than 15 dB above the dark noise of the detector up to a frequency of 200 MHz except two peaks caused by electronic pick-up. The vacuum reference was recorded with a local oscillator power of about 10 mW and the signal port blocked.

6.1.2. Trigger filtering

The generation of single photons is performed by splitting a squeezed vacuum state at an unbalanced beam splitter. Since squeezed vacuum consists of photon pairs, detecting a single photon in one mode, the other mode is conditionally projected into a photon subtracted state. The photon pairs are not only generated in the fundamental mode of the OPA but in many free spectral ranges symmetric about the central wavelength (1550 nm). The state tomography of the heralded state is performed by the balanced homodyne detector (BHD) that has a bandwidth sufficiently large to resolve the spectral properties of the fundamental mode but much narrower than the free spectral range of the OPA. Thus, only the fundamental mode can be analyzed by the BHD. However, the single photon detection module used for heralding the state of interest does not discriminate photons from different free spectral ranges and just clicks whenever there is a photon – whatever its precise frequency is. Hence, most of the time it would be triggered by photons which cannot be detected by the BHD. This effect would show up as optical loss. Therefore, proper frequency filtering of the trigger mode has to be provided so that the single photon detector only clicks when there is a photon that would also be seen by the BHD.

The filtering of the trigger mode is performed in two steps. In the first stage the mode is frequency up-converted to 532 nm with the sum-frequency generator (SFG) as used in the experiments presented earlier. The SFG cavity is doubly resonant for two wavelengths (810 and 1550 nm) that are not multiples of each other. Therefore, if fields of about these wavelengths are simultaneously resonant, neighboring free spectral ranges are not. Furthermore, the phase matching condition is optimal for only few pairs of signal and pump wavelength and the up-conversion efficiency is much lower for others. The second filter stage was implemented with a short linear optical filter cavity (FC). This cavity consists of two half-inch mirrors with a nominal reflectivity of 99% and a spacing of 3.2 mm yielding a linewidth (FWHM) of 150 MHz and a free spectral range of 47 GHz. The mechanical design was adapted and slightly modified from the one presented in Section 5.1.2. Note that in the experiment presented here, the up-converted mode at 532 nm is filtered while in that of Chapter 5 the 810 nm mode was subject to filtering. In Figure 6.3 the mode spectrum of the OPA as well as the mode spectra after passing the SFG and the filter cavity are shown. Note that the up-conversion efficiency is assumed to be unity for the whole spectrum, which is not realistic, but otherwise too complicated to include into the simulation. Realistically, the SFG suppresses the higher free spectral ranges of the OPA even more so the plot is an upper bound for the resulting mode spectrum.

6.1.3. Measurement protocol

The data acquisition is performed with an oscilloscope (Agilent *DSO 7014B*) that is controlled with a python program via the VISA protocol. The program is a slightly modified version of the one presented in detail in Section 5.1.4. The oscilloscope is triggered with clicks from the APD and samples data with 2 GSa/s. In a first step 10^4 traces (called segments in the following) are recorded with the signal port of the balanced homodyne detector blocked to obtain a vacuum reference. Each recorded segment consists of 10^3 data points representing 250 ns of data before and after each trigger event and is directly transferred to the PC. After recording the vacuum, the signal port is opened and $5 \cdot 10^4$ segments are recorded while the filter cavity is hold on resonance by hand using a frequency counter as monitor. The drifts of the quasi-monolithic filter cavity are slow so that this is easily possible for hours. The stored binary data is converted into hdf5 files and subject to the data processing and analysis.

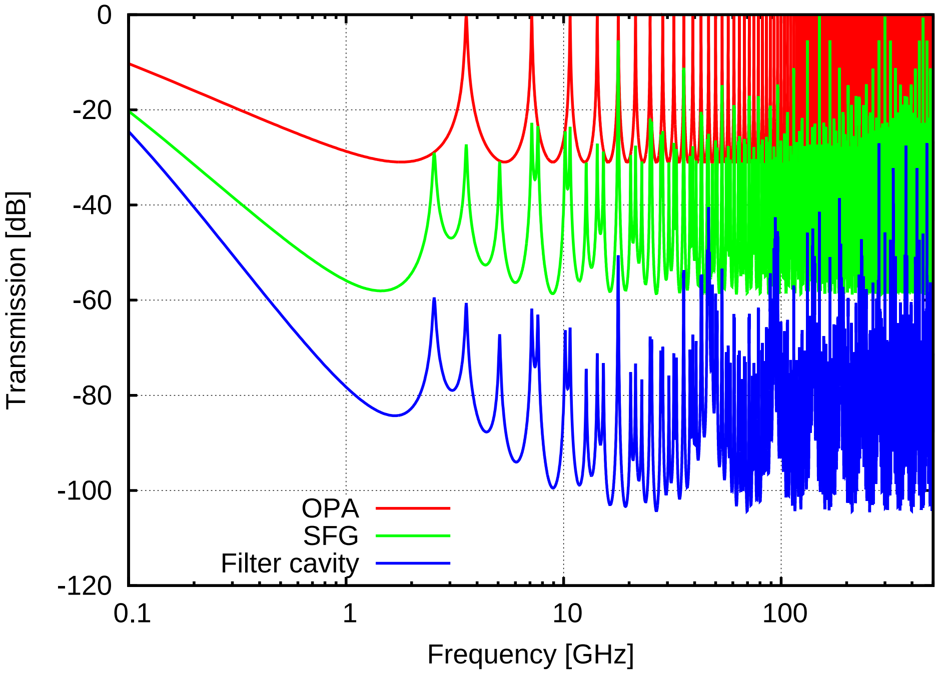

Figure 6.3.: Simulation of the filter effect of the SFG and the additional filter cavity. The red trace shows the mode spectrum of the OPA with a free spectral range of 3.6 GHz. The green and blue trace show the mode spectrum after the transmission of the SFG and the filter cavity, respectively. Up to a sideband frequency of about 250 GHz the resulting suppression of higher free spectral ranges is better that -30 dB.

6.2. Results

6.2.1. Signal mode-function

The acquisition of data is always triggered by a detection of a photon in the frequency up-converted mode. These photons at 532 nm are correlated with the photons at 1550 nm that are reflected at the beam splitter and which are analyzed in the BHD. The temporal correlation function is

$$\Gamma_{\text{filtered}}(\tau) = \begin{cases} \left[\frac{\gamma\varepsilon\kappa}{2}\left(\frac{\mathrm{e}^{\mu\tau}}{\mu(\kappa-\mu)} + \frac{\mathrm{e}^{\lambda\tau}}{\lambda(\kappa-\lambda)} - \frac{2\mathrm{e}^{\kappa\tau}}{(\kappa+\mu)(\kappa-\mu)} - \frac{2\mathrm{e}^{\kappa\tau}}{(\kappa+\lambda)(\kappa-\lambda)}\right)\right]^2 & , \tau < 0 \\ \left[\frac{\gamma\varepsilon\kappa}{2}\left(\frac{\mathrm{e}^{-\mu\tau}}{\mu(\kappa+\mu)} + \frac{\mathrm{e}^{-\lambda\tau}}{\lambda(\kappa+\lambda)}\right)\right]^2 & , \tau \geq 0\,, \end{cases} \tag{6.1}$$

where τ is the delay between the trigger and the signal photon, $\gamma = \pi \cdot 120\,\text{MHz}$ is the OPA's decay rate, $\varepsilon \ll \gamma$ is the gain parameter, $\kappa = \pi \cdot 68\,\text{MHz}$ is the combined decay rate of the frequency filter in the trigger path[1] and $\lambda = \gamma - \varepsilon$, $\mu = \gamma + \varepsilon$.

---

[1] The SFG decay rate $\kappa_{\text{SFG}} = \pi \cdot 68\,\text{MHz}$ (cf. Section 3.3.1) is dominant over the FC decay rate $\kappa_{\text{FC}} = \pi \cdot 150\,\text{MHz}$ so that $\kappa \approx \kappa_{\text{SFG}}$. The narrower the linewidth of a cavity, the stronger the filter effect.

For details please refer to Chapter A.4, where the calculation is explicitly performed. The only difference is that there the *signal* mode is subject to additional frequency filtering compared to filtering of the *trigger* mode here. Note that the trigger filtered correlation function is related to the signal filtered function shown in Eq. (5.3) via the transformation $\tau \rightarrow -\tau$.

6.2.2. Segment noise

It is initially unknown at which points in time the signal is contained in the segments because of finite response times of the photo detectors and electronic delays. However, one can make use of the fact, that the variance of a Fock state is higher than that of a vacuum state, $\Delta\hat{q}_\theta = \sqrt{(2n+1)/2}$. To "find" the photon I calculate the so-called segment noise which is the variance of individual points in a segment across all segments. In each segment the data at the same position in the segment is taken and the variance across the selected points is calculated. For points that are "far" away from the trigger event, the variance is just at the vacuum level, while for points close to the trigger, the variance rises and peaks at a particular point. This point is not exactly at the trigger time (i.e. $\tau = 0$) but slightly earlier, because the APDs have a finite response time and other delays (optically or electronically) shift the signal. The segment noise is shown in Figure 6.4 with the trigger filtered correlation function Eq. (6.1) fitted to the data. The fitting gives the parameters $\gamma = \pi \cdot 120\,\mathrm{MHz}$, $\kappa = \pi \cdot 68\,\mathrm{MHz}$, $\varepsilon = 0.1\gamma$, which are in a very good agreement with previously determined values (except the uncritical ε), cf. Chapter 3. The curve is shifted from $\tau = 0$ by 10 ns. This shift is caused by various electronic delays in the detection scheme.

6.2.3. Extracting quadrature values

In the next step of the data analysis quadrature values are obtained. Each segment is post-processed by multiplying the signal mode-function $f_\mathrm{s}(\tau)$ to the raw data, which is given by the square root of the temporal correlation function

$$f_\mathrm{s}(\tau) = \sqrt{\Gamma_\mathrm{filtered}(\tau)}\,. \tag{6.2}$$

This way the parts of the segment containing the signal are emphasized and the others are neglected.

In Figure 6.5 a segment and the signal mode-function as well as a data stream after multiplying the mode-function to the segment is shown.

A quadrature value is obtained by integrating the segment data after multiplication of the signal mode-function. Each segment therefore results in one single quadrature value. The result as well as a vacuum reference, is shown in Figure 6.6 where the quadrature values are normalized to give $\Delta^2 q_\mathrm{vac} = \frac{1}{2}$.

The quadrature values are shown in a histogram in Figure 6.7, where a Gaussian distribution with variance $\Delta^2 q = \frac{1}{2}$ is fitted to the data of the vacuum reference. The plot is scaled to obtain a (normalized) probability distribution. The red dots represent

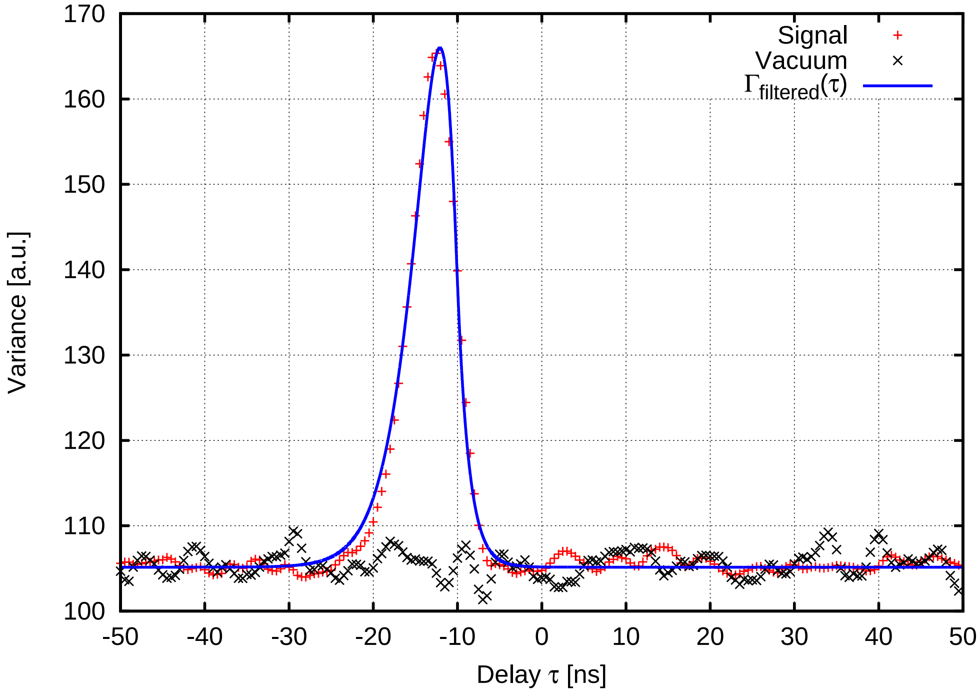

Figure 6.4.: Pointwise variance of all recorded segments. With the signal beam blocked, the variance is constant for all times (black). If the signal port of the BHD is open, the variance of the segments peaks around a particular time (red). The trigger filtered correlation function Eq. (6.1) is fitted to the data (blue).

the histogram of the quadrature data of the signal. The model that is fitted to this data is obtained by a mixture of Fock states. Fock states $|n\rangle$ with $n \in [0, 5]$ are assumed to be present in the signal. The probability distribution is then given by a weighted sum of marginal distributions

$$P(q) = \sum_{n=0}^{5} p_n \int_{-\infty}^{\infty} dp\, W_n(q,p)\,, \tag{6.3}$$

where p_n is the probability of state $|n\rangle$ and $W_n(q,p)$ is given by Eq. (2.28). The fit yields the probabilities $p_0 = 0.39$, $p_1 = 0.57$, $p_2 = 0$, $p_3 = 0.03$, $p_4 = 0$, $p_5 = 0.01$.

6.2.4. Reconstruction of the Wigner function

The reconstruction of the Wigner function is the final step of the data analysis. Therefore, the maximum likelihood estimation algorithm is applied to the quadrature values. An introduction to the maximum likelihood estimation algorithm can be found in Section A.5. The result of the (phase randomized) algorithm is a density matrix in Fock

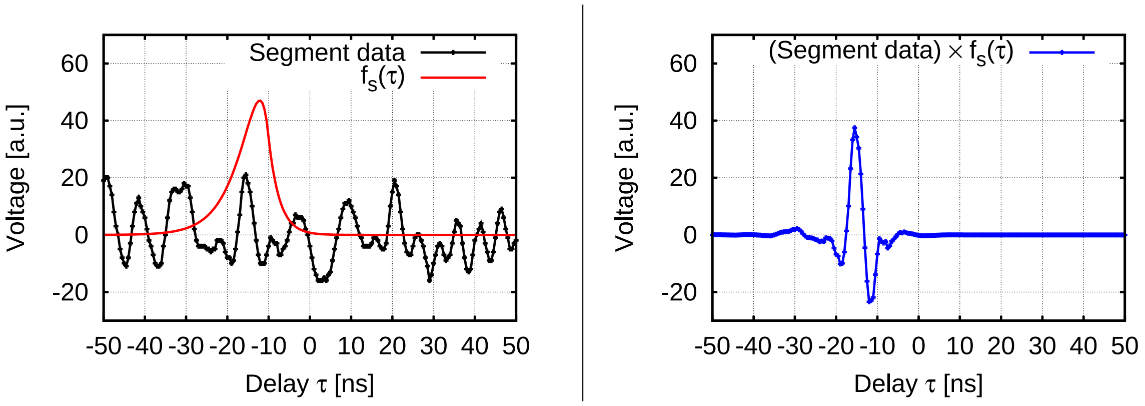

Figure 6.5.: Segment noise of the recorded data and mode function. *left:* The segment data as recorded by the oscilloscope and the signal mode-function. The mode-function is obtained from the fit of the segment noise as shown in Fig. 6.4. *right:* The segment after multiplying the mode-function to the data.

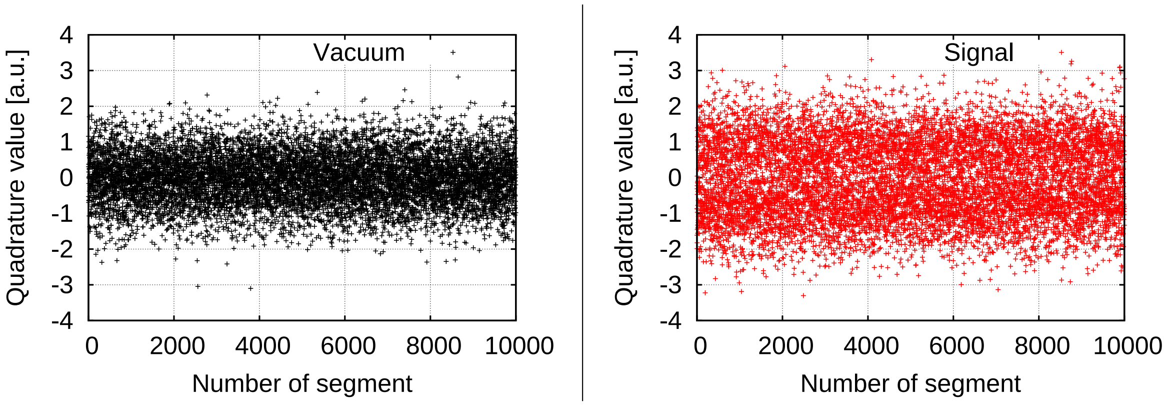

Figure 6.6.: Quadrature values obtained from multiplication of the signal mode-function to the segment data and integrating the result. *left:* Vacuum reference scaled to a variance of $\frac{1}{2}$. *right:* Quadrature values for the signal scaled with the same factor.

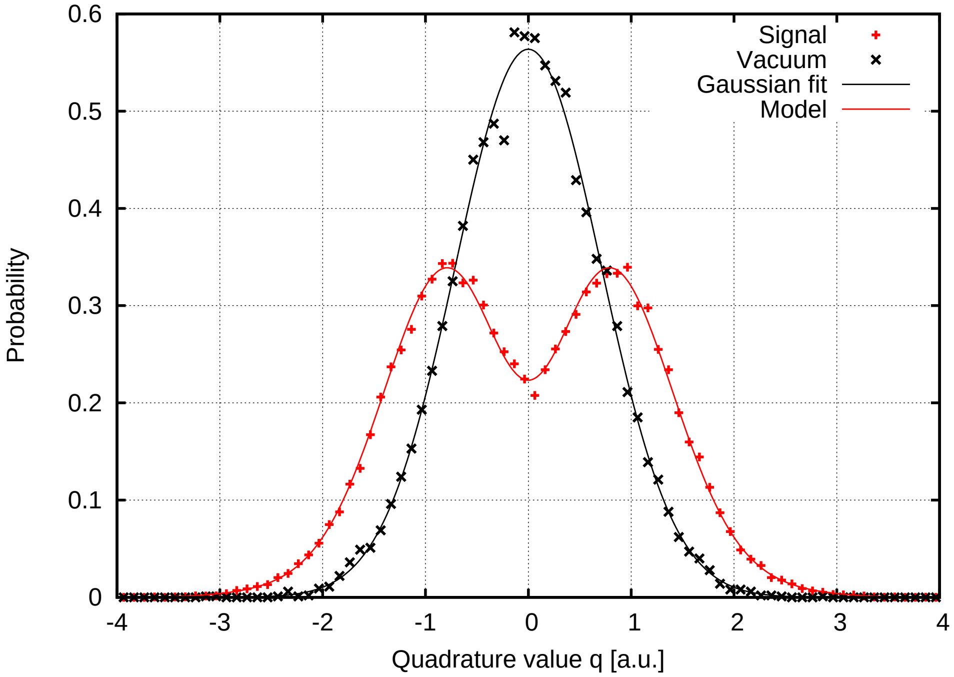

Figure 6.7.: Normalized histogram and probability distribution of the quadrature values of Figure 6.6. The data of the vacuum reference is compared to a Gaussian distribution with variance 1/2. The red dots are the distribution of quadrature values for the signal state and the dip of the probability around the origin is clearly visible which is characteristic for a single photon state. The solid red curve is a model for a state with $p_0 = 0.39$, $p_1 = 0.57$, $p_2 = 0$, $p_3 = 0.03$, $p_4 = 0$, $p_5 = 0.01$ where p_n is the probability of Fock state $|n\rangle$ in the signal.

basis:

$$\tilde{\rho} = \begin{pmatrix} 0.392 & 0 & 0 & 0 & 0 & 0 \\ 0 & 0.572 & 0 & 0 & 0 & 0 \\ 0 & 0 & 0.003 & 0 & 0 & 0 \\ 0 & 0 & 0 & 0.028 & 0 & 0 \\ 0 & 0 & 0 & 0 & 0.004 & 0 \\ 0 & 0 & 0 & 0 & 0 & 0.001 \end{pmatrix}. \tag{6.4}$$

The density matrix has the probabilities p_n on its diagonal, $n \in [0, 5]$. These very well agree with the values already obtained from a fit of the marginal distribution. The relatively high vacuum contribution $p_0 = 0.392$ is caused by false trigger events, who originate in dark counts of APD and improper trigger filtering, and optical losses in the signal path. The signal could be detected with an efficiency of about 80%, which includes propagation losses, limited detection efficiency of the homodyne detector and the beam splitter to tap off a small part for the trigger path. This efficiency was inferred with an auxiliary squeezing/anti-squeezing measurement when the OPA was operated with much more parametric gain. The vacuum contribution can be further reduced by setting up another filter cavity in the trigger path. This is, however, connected to much more experimental effort as then two filter cavities have to be held on resonance for hours and elaborate locking techniques are required.

With the density matrix $\tilde{\rho}$ the Wigner function can be reconstructed using the mathematical tools as given in Section 2.1.3. The reconstructed Wigner function is shown in Figure 6.8 as well as a slice through its center in Figure 6.9. The Wigner function clearly shows negative values around the origin, with a maximum negativity of -0.063.

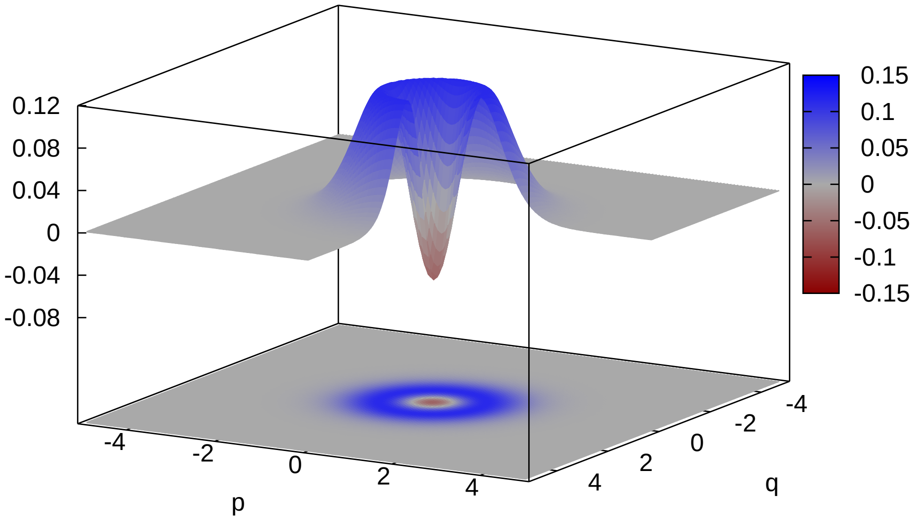

Figure 6.8.: Reconstructed Wigner function by maximum likelihood estimation. Around the origin, the Wigner function has negative values down to -0.063±0.004.

6.2.5. Significance of negativity

A Wigner function having negative values is a strong statement for having a nonclassical state. To get a statistical predicate on the negativity of the Wigner function of the states, a bootstrap algorithm was applied to the data and the reconstruction algorithm is repeated with the new data set. By randomly combining quadrature values (with repetition) of the data set, a new data set is formed. For every iteration of this procedure, the origin of the Wigner function has a different value and a mean value as well as a standard deviation can be calculated. A plot of this mean value with its standard deviation dependent on the number of bootstrap iterations is shown in Figure 6.10. It can be seen that both the mean value and standard deviation converge to $W(0,0) = -0.063 \pm 0.004$. The Wigner function is witnessed to be negative with more than 15 standard deviations.

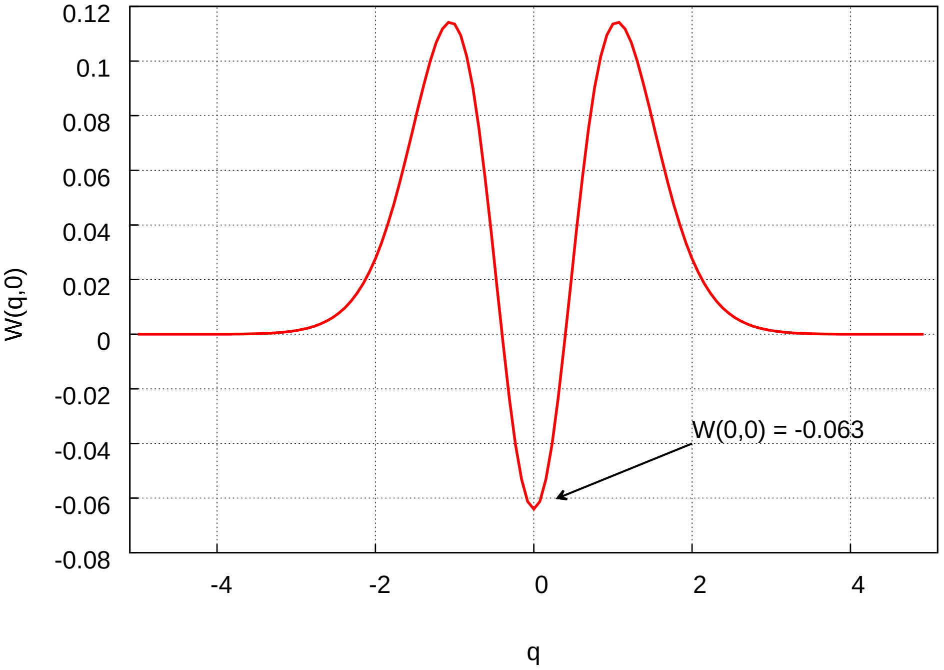

Figure 6.9.: A slice through the center of the Wigner function presented in Figure 6.8 to emphasize the negativity.

6.3. Discussion and outlook

Single photons are generated by weakly pumping a optical parametric amplifier and subtracting a small portion of the resulting weakly squeezed state at a low transmission beam splitter. The subtracted mode is frequency up-converted to 532 nm and detected on an APD. Any click of this detector projects the remaining state at 1550 nm into a single photon state which is analyzed via (phase randomized) optical quantum state tomography. The reconstructed Wigner function shows negative values around its origin with $W(0,0) = -0.063 \pm 0.004$, which is a very strong criterion for nonclassicality.

To the best of my knowledge, a state showing a negative Wigner function is prepared at the telecommunication wavelength 1550 nm for the first time. This result may find applications in quantum computing or quantum communication. Beyond that, this experiment is the first realization of discrete-continuous variable (hybrid) experiment in the working group of Roman Schnabel. The experimental requirements, simulations, data acquisition protocols and the data analysis were developed from scratch. I assume that many of the programs and techniques may be re-used in future experiments.

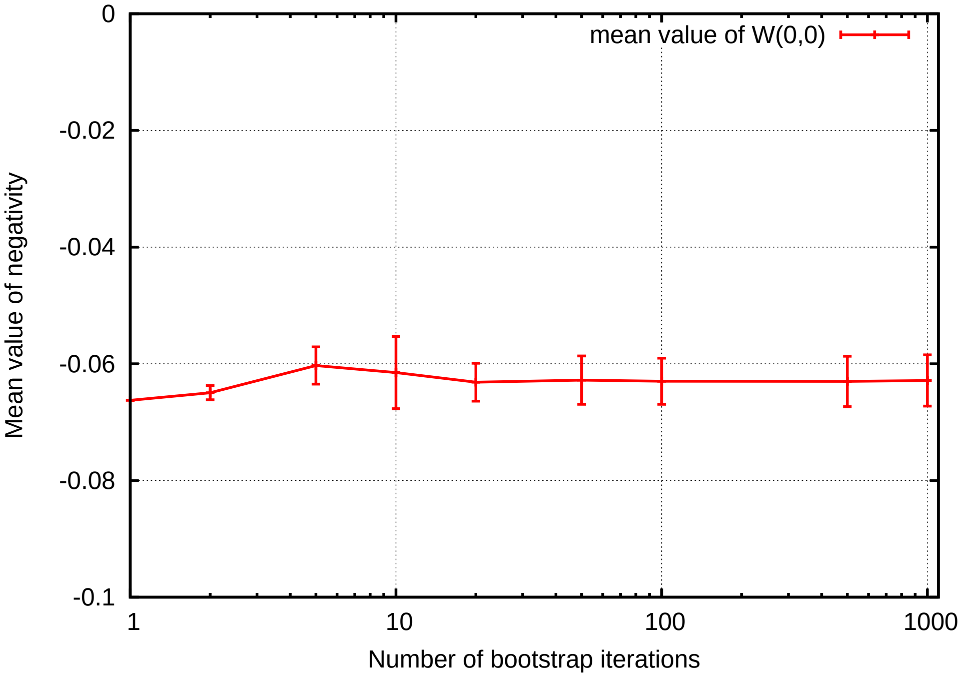

Figure 6.10.: Origin of the reconstructed Wigner function $W(0,0)$ versus the number of bootstrap iterations with inferred error bars. The negativity converges to $W(0,0) = -0.063 \pm 0.004$.

7. Summary and outlook

Frequency up-conversion of nonclassical states opens up new possibilities in quantum metrology and quantum information processing. The direct generation of squeezed states at 532 nm via parametric down-conversion is daunting as an intense ultra-violet pump field would be required and no nonlinear crystals are available with satisfying optical properties in this wavelength regime. In this thesis, I demonstrate the up-conversion of nonclassical states of light from 1550 nm to 532 nm. Squeezed vacuum states are initially generated at 1550 nm and subsequently up-converted to 532 nm by means of sum-frequency generation with a 810 nm pump field. A nonclassical noise suppression of 5.5 dB below the shot noise level was shown. In a subsequent proof-of-principle experiment, the up-converted squeezed states were used to enhance the signal-to-noise ratio of a table-top Mach Zehnder interferometer.

Frequency up-conversion furthermore has the potential to develop into a standard tool in quantum communication, as it allows bridging the gap between widely separated wavelength regimes. The generation and analysis of squeezed and entangled states has previously been established at 1550 nm, where optical fibers show low absorption enabling long distance transmission. However, quantum memories are part of many quantum information protocols and usually operate at much shorter wavelengths. An on-the-fly frequency up-conversion allows for both long distance transmission of optical states and their storage in quantum memories. I show the realization of a scheme to interface two widely separated wavelength regimes. By frequency up-conversion of one part of a two-mode squeezed state, strong nonclassical correlations of 5.5 dB below a vacuum reference are certified between two modes at 1550 nm and 532 nm.

Single photons have been used in many previous experiments, both to probe fundamental issues in quantum theory, and to investigate and develop future quantum technologies. The frequency up-conversion of single photons is also presented in this thesis. Spontaneous parametric down-conversion is used to produce photon pairs at 1550 and 810 nm where the latter herald single photons at 1550 nm that are then frequency up-converted to 532 nm and analyzed in a Hanbury Brown and Twiss setup. For the first time, frequency up-converted single photons are shown to be quantum non-Gaussian with more than 16 standard deviations. Quantum non-Gaussianity certifies that a state is not expressible as mixtures of coherent states, and is a sufficient condition for secure quantum communication.

Probably the most characteristic feature of single photons is negativity of the Wigner function, which is a quasi-probability distribution. This feature is discriminatory for nonclassical states and enables particular quantum information protocols. To the best of my knowledge, the first experimental realization of a heralded single photon source at 1550 nm with subsequent quantum state tomography is presented in this thesis. The prepared state is certified to have a Wigner function with a value of -0.063 at its origin with a significance of the negativity of more than 15 standard deviations. During the preparation, frequency up-conversion is employed to enable the use of easy-to-handle silicon avalanche photo detectors.

Future research on the frequency up-conversion of nonclassical states may focus on interfacing optical quantum networks with quantum memories. The storage of optical states in quantum memories is a key technology in setting up long-distance quantum networks. The transmission of states through optical fibers is well established at 1550 nm and the next step would be to map these states to atomic transition frequencies. Exploiting the flexibility of the approach, different nodes in a quantum network could have different operational frequencies, and all be interfaced with 1550 nm, simply by designing specific SFG cavities at each site.

The sum-frequency generation technique presented in this thesis is a versatile tool. With minimal modifications, the current setup could be easily matched to a quantum memory having a bandwidth in the MHz regime. The optical bandwidth can be varied by changing the mirror reflectivities of the squeezed light source and up-conversion cavities. The optical frequency of the up-converted states can easily be changed by varying the frequency of the pump field using acousto- or electro-optical modulators. These capabilities are necessary to achieve high efficiency when integrating an optical source of nonclassical states with a quantum memory.

Frequency up-conversion of nonclassical states of light is a powerful technique for quantum state engineering and thus the results of this thesis give new impulses for quantum metrology and quantum information research.

A. Calculations

A.1. Cavity input-output formalism

In this section I will review the basic formalism for the description of input and output modes of optical cavities. Based on this, the properties of degenerate and non-degenerate optical parametric oscillators below threshold will be developed in the corresponding chapters. The treatment basically follows the textbooks of Walls and Milburn [Wal94], Gardiner and Zoller [Gar91] with some issues from Scully and Zubairy [Scu97].

An internal mode $\hat{a}$ of an optical cavity is considered to interact with external modes $\hat{b}$, whereby the interaction strength κ is small compared to the frequency of the external modes. This allows for the rotating wave approximation, where counter rotating terms disappear from the equations of motion (for a brief overview of its validity see [Fuj13]). The intracavity modes obey the bosonic commutation relation $[\hat{a}, \hat{a}^\dagger] = 1$ and the external modes – closely separated in frequency – satisfy $[\hat{b}(\omega), \hat{b}^\dagger(\omega')] = \delta(\omega - \omega')$.

The interaction energy is given by the Hamiltonian

$$\mathbf{H}_{\text{int}} = \mathrm{i}\hbar\kappa \int d\omega \big[\hat{b}(\omega)\hat{a}^\dagger - \hat{a}\hat{b}^\dagger(\omega)\big] \,, \tag{A.1}$$

where κ is the coupling rate, assumed to be independent of frequency about the central frequency (i.e. cavity resonance frequency). This assumption is called the first Markov approximation and incorporates that the external modes are *memoryless* [Scu97]. This is well justified in quantum optical systems as the interaction time of the system with the bath (in the order of 1/MHz) is much longer than the correlation times inside the bath (1/THz). After the interaction, the bath gets back to its initial state quasi-instantaneously. The equation of motion for the external modes then is a first order differential equation

$$\frac{d\hat{b}(\omega)}{dt} = -\frac{\mathrm{i}}{\hbar}[\hat{b}(\omega), \mathbf{H}] = \kappa \int d\omega' \delta(\omega - \omega')\hat{a} - \mathrm{i}\omega\hat{b}(\omega) = \kappa\hat{a} - \mathrm{i}\omega\hat{b}(\omega) \,, \tag{A.2}$$

where the total Hamiltonian $\mathbf{H}$ is the sum of the system Hamiltonian $\mathbf{H}_{\text{sys}}$ describing the dynamics of the cavity modes $\hat{a}$, the interaction of the system with the environment $\mathbf{H}_{\text{int}}$ and the free Hamiltonian for the external modes $\mathbf{H}_{\text{env}} = \hbar\omega\hat{b}^\dagger\hat{b}$. This differential equation can be solved with standard methods[1]. This is done for two time intervals:

---

[1] This first order differential equation is of the type $\dot{y} + c(t)y = r(t)$ with initial condition $y(t_0) = y_0$. The solution reads $y(t) = \mathrm{e}^{-C(t)} \int_{t_0}^{t} dt'\, r(t')\, \mathrm{e}^{C(t')} + y_0\, \mathrm{e}^{-C(t)}$, where $C(t) = \int_{t_0}^{t} dt'\, c(t')$.

$t_0 < t$ which is the input and $t_1 > t$, the output.

$$\begin{aligned}\hat{b}(\omega) &= \mathrm{e}^{-\mathrm{i}\omega(t-t_0)}\int_{t_0}^{t} dt'\,\kappa\hat{a}(t')\mathrm{e}^{\mathrm{i}\omega(t'-t_0)} + \mathrm{e}^{-\mathrm{i}\omega(t-t_0)}\hat{b}_0(\omega)\\ &= \kappa\int_{t_0}^{t} dt'\,\hat{a}(t')\mathrm{e}^{-\mathrm{i}\omega(t-t')} + \hat{b}_0(\omega)\mathrm{e}^{-\mathrm{i}\omega(t-t_0)},\end{aligned} \tag{A.3}$$

$$\begin{aligned}\hat{b}(\omega) &= \mathrm{e}^{-\mathrm{i}\omega(t-t_1)}\int_{t_1}^{t} dt'\,\kappa\hat{a}(t')\mathrm{e}^{\mathrm{i}\omega(t'-t_1)} + \mathrm{e}^{-\mathrm{i}\omega(t-t_1)}\hat{b}_1(\omega)\\ &= -\kappa\int_{t}^{t_1} dt'\,\hat{a}(t')\mathrm{e}^{-\mathrm{i}\omega(t-t')} + \hat{b}_1(\omega)\mathrm{e}^{-\mathrm{i}\omega(t-t_1)},\end{aligned} \tag{A.4}$$

where $\hat{b}_i(\omega)$ is $\hat{b}(\omega)$ at $t = t_i$. The cavity mode operator obeys the equation

$$\frac{d\hat{a}}{dt} = -\frac{\mathrm{i}}{\hbar}[\hat{a},\mathbf{H}] = -\frac{\mathrm{i}}{\hbar}[\hat{a},\mathbf{H}_{\mathrm{sys}}] - \kappa\int_{-\infty}^{\infty} d\omega\,\hat{b}(\omega)\,. \tag{A.5}$$

Inserting the solution with initial conditions leads to

$$\begin{aligned}\frac{d\hat{a}}{dt} &= -\frac{\mathrm{i}}{\hbar}[\hat{a},\mathbf{H}_{\mathrm{sys}}] - \kappa^2\int_{-\infty}^{\infty} d\omega\int_{t_0}^{t} dt'\,\hat{a}(t')\mathrm{e}^{-\mathrm{i}\omega(t-t')} + \sqrt{2\pi}\kappa\,\hat{a}_{\mathrm{in}}(t)\\ &= -\frac{\mathrm{i}}{\hbar}[\hat{a},\mathbf{H}_{\mathrm{sys}}] - 2\pi\kappa^2\int_{t_0}^{t} dt'\,\hat{a}(t')\delta(t-t') + \sqrt{2\pi}\kappa\,\hat{a}_{\mathrm{in}}(t)\end{aligned} \tag{A.6}$$

where the input field operator is defined as

$$\hat{a}_{\mathrm{in}}(t) = \frac{-1}{\sqrt{2\pi}}\int_{-\infty}^{\infty} d\omega\,\hat{b}_0(\omega)\mathrm{e}^{-\mathrm{i}\omega(t-t_0)}\,. \tag{A.7}$$

It obeys the commutation relation

$$\begin{aligned}[\hat{a}_{\mathrm{in}}(t),\hat{a}_{\mathrm{in}}^{\dagger}(t')] &= \frac{1}{2\pi}\int d\omega\int d\omega'[\hat{b}_0(\omega),\hat{b}_0^{\dagger}(\omega')]\mathrm{e}^{-\mathrm{i}\omega(t-t_0)}\mathrm{e}^{+\mathrm{i}\omega'(t'-t_0)}\\ &= \frac{1}{2\pi}\int d\omega\int d\omega'\delta(\omega-\omega')\mathrm{e}^{-\mathrm{i}\omega(t-t_0)}\mathrm{e}^{+\mathrm{i}\omega'(t'-t_0)}\\ &= \frac{1}{2\pi}\int d\omega\mathrm{e}^{-\mathrm{i}\omega(t-t')}\\ &= \delta(t-t')\,.\end{aligned} \tag{A.8}$$

After defining $\kappa^2 = \gamma/\pi$ and using[2] $\int_{t_0}^{t} dt'\,\hat{a}(t')\delta(t-t') = \frac{1}{2}\hat{a}(t)$ we obtain

$$\frac{d\hat{a}(t)}{dt} = -\frac{\mathrm{i}}{\hbar}[\hat{a}(t),\mathbf{H}_{\mathrm{sys}}] - \gamma\hat{a}(t) + \sqrt{2\gamma}\hat{a}_{\mathrm{in}}\,. \tag{A.9}$$

---

[2] If a function $f(t)$ smoothly tends to zero for $t \to \pm\infty$ the following is true:

$$\int_{-\infty}^{\infty} dt'\,f(t')\delta(t-t') = f(t) \curvearrowright \int_{t_0}^{t_1} dt'\,f(t')\delta(t-t') \approx f(t)$$

$$\int_{t_0}^{t} dt'\,f(t')\delta(t-t') \approx \int_{t}^{t_1} dt'\,f(t')\delta(t-t') \approx \frac{1}{2}f(t)$$

In terms of an experimentalist, $\frac{\gamma}{2\pi}$ is the half width at half maximum (HWHM) of the cavity, measured in Hertz. If the solution for the final conditions ($t_1 > t$) is inserted in Eq. (A.6), the equation reads

$$\frac{d\hat{a}(t)}{dt} = -\frac{\mathrm{i}}{\hbar}[\hat{a}(t), \mathbf{H}_{\mathrm{sys}}] + \gamma\hat{a}(t) - \sqrt{2\gamma}\hat{a}_{\mathrm{out}}\,, \tag{A.10}$$

where the output field operator is defined as

$$\hat{a}_{\mathrm{out}}(t) = \frac{1}{\sqrt{2\pi}}\int_{-\infty}^{\infty} d\omega\,\hat{b}_1(\omega)\mathrm{e}^{-\mathrm{i}\omega(t-t_1)}\,. \tag{A.11}$$

Subtraction of one solution from the other leads to a relation between the input and output fields,

$$\hat{a}_{\mathrm{in}}(t) + \hat{a}_{\mathrm{out}}(t) = \sqrt{2\gamma}\hat{a}(t)\,. \tag{A.12}$$

A schematic of the system is depicted in Figure A.1.

Note that the extension to a system where also the second mirror has some transmittivity (two-sided cavity) is straightforward [Wal94]. However, most systems that were investigated throughout this thesis could all be well explained in the one-sided formalism.

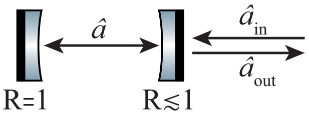

Figure A.1.: Schematic of the investigated system. The (one-sided) cavity consists of one perfectly reflecting mirror and one coupling mirror, through which the system interacts with the environment. See the text for the definition of the input and output operators $\hat{a}_{in}$ and $\hat{a}_{out}$.

A.2. Mode filtering

A mode experiencing an additional filter with decay rate κ is transformed as

$$\hat{a}_{\mathrm{fil}}(t) = \int_{-\infty}^{t} dy\,\kappa e^{-\kappa(t-y)}\hat{a}(y) \tag{A.13}$$

in the time domain which is a through pass Lorentzian filter in the frequency domain:

$$\tilde{a}_{\mathrm{fil}}(\omega) = \frac{\kappa}{\kappa - i\omega}\tilde{a}(\omega)\,. \tag{A.14}$$

This relation is derived here.

The Fourier and inverse Fourier transforms of a mode are given by

$$\begin{aligned} \tilde{a}(\omega) &= \frac{1}{\sqrt{2\pi}} \int_{-\infty}^{\infty} dt\, e^{i\omega t} \hat{a}(t) \\ \hat{a}(t) &= \frac{1}{\sqrt{2\pi}} \int_{-\infty}^{\infty} d\omega\, e^{-i\omega t} \tilde{a}(\omega) \end{aligned} \tag{A.15}$$

I now replace the time domain operators in Eq. (A.13) by their Fourier transforms, change the order of integration on the right side and solve analytically:

$$\begin{aligned} \frac{1}{\sqrt{2\pi}} \int_{-\infty}^{\infty} d\omega\, e^{-i\omega t} \tilde{a}_{\text{fil}}(\omega) &= \int_{-\infty}^{t} dy\, \kappa e^{-\kappa(t-y)} \frac{1}{\sqrt{2\pi}} \int_{-\infty}^{\infty} d\omega\, e^{-i\omega y} \tilde{a}(\omega) \\ &= \frac{1}{\sqrt{2\pi}} \int_{-\infty}^{\infty} d\omega\, \tilde{a}(\omega) \kappa e^{-\kappa t} \int_{-\infty}^{t} dy\, e^{y(\kappa - i\omega)} \\ &= \frac{1}{\sqrt{2\pi}} \int_{-\infty}^{\infty} d\omega\, \tilde{a}(\omega) \kappa e^{-\kappa t} \frac{1}{\kappa - i\omega} e^{t(\kappa - i\omega)} \\ &= \frac{1}{\sqrt{2\pi}} \int_{-\infty}^{\infty} d\omega\, e^{-i\omega t} \frac{\kappa}{\kappa - i\omega} \tilde{a}(\omega) \end{aligned} \tag{A.16}$$

By comparison of the left and right side we see that the Fourier transform of the filtered mode is the same as the Fourier transform of the unfiltered mode with the prefactor $\frac{\kappa}{\kappa - i\omega}$:

$$\tilde{a}_{\text{fil}}(\omega) = \frac{\kappa}{\kappa - i\omega} \tilde{a}(\omega)\,. \tag{A.17}$$

A.3. Degenerate parametric down-conversion and squeezing

The degenerate optical parametric amplifier (OPA) is the common resource of squeezed vacuum states of light. It generally consists of two partially reflecting mirrors (with leakage rates γ_1 and γ_2) and a non-linear optical medium between them. The device is driven with a pump field with frequency $\omega_{\text{p}} = 2\omega_0$. In the degenerate down-conversion process one pump photon decays into two photons which are correlated and make up the squeezed noise statistics.

The Hamiltonian is given by

$$\mathbf{H} = \underbrace{\mathbf{H}_{\text{free}} + \mathbf{H}_{\text{int}}}_{\mathbf{H}_{\text{sys}}} + \mathbf{H}_{\text{bath}}\,, \tag{A.18}$$

where the system's free Hamiltonian is given by

$$\mathbf{H}_{\text{free}} = \hbar\omega_0 \hat{a}^\dagger \hat{a}\,, \tag{A.19}$$

and the interaction is described by

$$\mathbf{H}_{\text{int}} = \frac{\mathrm{i}\hbar}{2} \left(\varepsilon \mathrm{e}^{-\mathrm{i}\omega_{\text{p}} t} \hat{a}^{\dagger 2} - \varepsilon^* \mathrm{e}^{\mathrm{i}\omega_{\text{p}} t} \hat{a}^2 \right)\,, \tag{A.20}$$

where $\varepsilon = |\varepsilon|\mathrm{e}^{-\mathrm{i}\phi}$ is proportional to the pump amplitude. This entity is treated classically because the pump usually is very strong compared to the fundamental field and therefore assumed not to be depleted by the down-conversion process. $\mathbf{H}_{\text{bath}}$ is the Hamiltonian for the external modes, coupling into the cavity through the mirrors. See Section A.1 for details.

For simplicity and to demonstrate the general dynamics of an OPA, we assume the cavity to be one-sided: one mirror is perfect ($\gamma_2 = 0$), the other one partially reflecting ($\gamma_1 = \gamma$). Following the cavity input-output formalism introduced in Section A.1 the equation of motion is

$$\frac{d\hat{a}(t)}{dt} = -\frac{\mathrm{i}}{\hbar}[\hat{a}(t), \mathbf{H}_{\text{sys}}] - \gamma\hat{a}(t) + \sqrt{2\gamma}\hat{a}_{\text{in}}(t)\,. \tag{A.21}$$

After expanding the commutator[3] and going into the rotating frame ($\hat{a} \to \hat{a}\mathrm{e}^{-\mathrm{i}\omega_0 t}$) we end up with

$$\frac{d\hat{a}(t)}{dt} = \varepsilon\hat{a}^\dagger(t) - \gamma\hat{a}(t) + \sqrt{2\gamma}\hat{a}_{\text{in}}(t)\,. \tag{A.22}$$

A.3.1. OPA: Frequency-space solution

The equation of motion for the OPA, Eq. (A.22), can conveniently be solved using the Fourier transforms

$$\begin{aligned} \hat{a}(t) &= \frac{1}{\sqrt{2\pi}}\int_{-\infty}^{\infty} d\omega\, \mathrm{e}^{-\mathrm{i}\omega t}\tilde{a}(\omega)\,, \\ \hat{a}^\dagger(t) &= \frac{1}{\sqrt{2\pi}}\int_{-\infty}^{\infty} d\omega\, \mathrm{e}^{+\mathrm{i}\omega t}\tilde{a}^\dagger(\omega) \\ &= \frac{1}{\sqrt{2\pi}}\int_{-\infty}^{\infty} d\omega\, \mathrm{e}^{-\mathrm{i}\omega t}\tilde{a}^\dagger(-\omega)\,. \end{aligned} \tag{A.23}$$

The resulting equation reads

$$\begin{aligned} \frac{d}{dt}\frac{1}{\sqrt{2\pi}}\int_{-\infty}^{\infty} d\omega\, \mathrm{e}^{-\mathrm{i}\omega t}\tilde{a}(\omega) =& \varepsilon\frac{1}{\sqrt{2\pi}}\int_{-\infty}^{\infty} d\omega\, \mathrm{e}^{-\mathrm{i}\omega t}\tilde{a}^\dagger(-\omega) - \gamma\frac{1}{\sqrt{2\pi}}\int_{-\infty}^{\infty} d\omega\, \mathrm{e}^{-\mathrm{i}\omega t}\tilde{a}(\omega) \\ &+ \sqrt{2\gamma}\frac{1}{\sqrt{2\pi}}\int_{-\infty}^{\infty} d\omega\, \mathrm{e}^{-\mathrm{i}\omega t}\tilde{a}_{\text{in}}(\omega)\,. \end{aligned} \tag{A.24}$$

After performing the differentiation the integrals can be “crossed out” and the equation can be simplified to

$$(\gamma - \mathrm{i}\omega)\,\tilde{a}(\omega) = \varepsilon\tilde{a}^\dagger(-\omega) + \sqrt{2\gamma}\tilde{a}_{\text{in}}(\omega)\,. \tag{A.25}$$

The corresponding hermitian conjugate is

$$\begin{aligned} (\gamma + \mathrm{i}\omega)\,\tilde{a}^\dagger(\omega) &= \varepsilon^*\tilde{a}(-\omega) + \sqrt{2\gamma}\tilde{a}^\dagger_{\text{in}}(\omega)\,, \\ (\gamma - \mathrm{i}\omega)\,\tilde{a}^\dagger(-\omega) &= \varepsilon^*\tilde{a}(\omega) + \sqrt{2\gamma}\tilde{a}^\dagger_{\text{in}}(-\omega) \end{aligned} \tag{A.26}$$

---

[3] $-\frac{\mathrm{i}}{\hbar}[\hat{a}, \frac{\mathrm{i}\hbar}{2}\left(\varepsilon\hat{a}^{\dagger 2} - \varepsilon^*\hat{a}^2\right)] = \frac{\varepsilon}{2}\left(\hat{a}^\dagger[\hat{a},\hat{a}^\dagger] + [\hat{a},\hat{a}^\dagger]\hat{a}^\dagger\right) = \varepsilon\hat{a}^\dagger$

where in the second line we transformed $\omega \to -\omega$. Now we insert Eq. (A.26) into Eq. (A.25) and obtain

$$\begin{aligned}
(\gamma - \mathrm{i}\omega)\tilde{a}(\omega) &= \varepsilon \left(\frac{\varepsilon^* \tilde{a}(\omega) + \sqrt{2\gamma}\tilde{a}_{\mathrm{in}}^\dagger(-\omega)}{\gamma - \mathrm{i}\omega} \right) + \sqrt{2\gamma}\hat{a}_{\mathrm{in}} \,, \\
\left((\gamma - \mathrm{i}\omega)^2 - |\varepsilon|^2 \right) \tilde{a}(\omega) &= \varepsilon \sqrt{2\gamma}\tilde{a}^\dagger(-\omega) + (\gamma - \mathrm{i}\omega)\sqrt{2\gamma}\tilde{a}_{\mathrm{in}}(\omega) \,, \qquad (A.27) \\
\tilde{a}(\omega) &= \frac{\varepsilon\sqrt{2\gamma}\tilde{a}_{\mathrm{in}}^\dagger(-\omega) + (\gamma - \mathrm{i}\omega)\sqrt{2\gamma}\tilde{a}_{\mathrm{in}}(\omega)}{(\gamma - \mathrm{i}\omega)^2 - |\varepsilon|^2} \,.
\end{aligned}$$

Recalling the result of Section A.1, that also holds for the Fourier transformed operators, $\tilde{a}_{\mathrm{in}} + \tilde{a}_{\mathrm{out}} = \sqrt{2\gamma}\tilde{a}$, the outgoing field is

$$\begin{aligned}
\tilde{a}_{\mathrm{out}}(\omega) &= \frac{\varepsilon 2\gamma}{(\gamma - \mathrm{i}\omega)^2 - |\varepsilon|^2}\tilde{a}_{\mathrm{in}}^\dagger(-\omega) + \left(2\gamma \frac{\gamma - \mathrm{i}\omega}{(\gamma - \mathrm{i}\omega)^2 - |\varepsilon|^2} - 1 \right) \tilde{a}_{\mathrm{in}}(\omega) \\
&= \frac{\varepsilon 2\gamma}{(\gamma - \mathrm{i}\omega)^2 - |\varepsilon|^2}\tilde{a}_{\mathrm{in}}^\dagger(-\omega) + \frac{\gamma^2 + \omega^2 + |\varepsilon|^2}{(\gamma - \mathrm{i}\omega)^2 - |\varepsilon|^2}\tilde{a}_{\mathrm{in}}(\omega) \,, \qquad (A.28) \\
\tilde{a}_{\mathrm{out}}^\dagger(-\omega) &= \frac{\varepsilon^* 2\gamma}{(\gamma - \mathrm{i}\omega)^2 - |\varepsilon|^2}\tilde{a}_{\mathrm{in}}(\omega) + \frac{\gamma^2 + \omega^2 + |\varepsilon|^2}{(\gamma - \mathrm{i}\omega)^2 - |\varepsilon|^2}\tilde{a}_{\mathrm{in}}^\dagger(-\omega) \,.
\end{aligned}$$

A.3.2. The squeezing spectrum

The spectral density or power spectrum of the outgoing field is defined as

$$: S_\theta(\omega) := \int_{-\infty}^{\infty} d\omega' \langle :\, \tilde{q}_{\theta,\mathrm{out}}(\omega), \tilde{q}_{\theta,\mathrm{out}}(\omega') \,: \rangle \,, \qquad (A.29)$$

where : : denotes normal ordering and $\hat{q}_{\theta,\mathrm{out}}(\omega)$ are generalized quadrature operators:

$$\tilde{q}_{\theta,\mathrm{out}}(\omega) = \frac{1}{\sqrt{2}} \left(\tilde{a}_{\mathrm{out}}(\omega) \mathrm{e}^{-\mathrm{i}\theta} + \tilde{a}_{\mathrm{out}}^\dagger(\omega)\mathrm{e}^{i\theta} \right) \,. \qquad (A.30)$$

Thus, we get

$$\begin{aligned}
\langle \tilde{q}_{\theta,\mathrm{out}}(\omega), \tilde{q}_{\theta,\mathrm{out}}(\omega') \rangle =& \frac{1}{2} \big[\langle \tilde{a}_{\mathrm{out}}(\omega), \tilde{a}_{\mathrm{out}}(\omega') \rangle \mathrm{e}^{-2\mathrm{i}\theta} + \langle \tilde{a}_{\mathrm{out}}(\omega), \tilde{a}_{\mathrm{out}}^\dagger(\omega') \rangle \qquad (A.31) \\
&+ \langle \tilde{a}_{\mathrm{out}}^\dagger(\omega), \tilde{a}_{\mathrm{out}}(\omega') \rangle + \langle \tilde{a}_{\mathrm{out}}^\dagger(\omega), \tilde{a}_{\mathrm{out}}^\dagger(\omega') \rangle \mathrm{e}^{2\mathrm{i}\theta} \big] \,.
\end{aligned}$$

We need to calculate the second order moments[4] of the outgoing field given in Eq. (A.28). The input field $\tilde{a}_{\mathrm{in}}(\omega)$ is assumed to be in the vacuum state so that the only non-vanishing term is the one containing the anti-normally ordered moment $\langle \tilde{a}_{\mathrm{in}}(\omega), \tilde{a}_{\mathrm{in}}^\dagger(\omega') \rangle = \delta(\omega - \omega')$.

---

[4] Throughout this thesis we will only deal with states of zero mean field amplitude. Therefore, the second order moments $\langle A, B \rangle = \langle AB \rangle - \langle A \rangle \langle B \rangle$ reduce to $\langle A, B \rangle = \langle AB \rangle$.

We obtain

$$\begin{aligned}\langle\tilde{a}_{\text{out}}(\omega),\tilde{a}_{\text{out}}(\omega')\rangle =&\frac{\gamma^2+|\varepsilon|+\omega^2}{(\gamma-\mathrm{i}\omega)^2-|\varepsilon|^2}\,\frac{2\gamma\varepsilon}{(\gamma-\mathrm{i}\omega')^2-|\varepsilon|^2}\langle\tilde{a}_{\text{in}}(\omega),\tilde{a}^\dagger_{\text{in}}(-\omega')\rangle\\ =&\frac{\gamma^2+|\varepsilon|+\omega^2}{(\gamma-\mathrm{i}\omega)^2-|\varepsilon|^2}\,\frac{2\gamma\varepsilon}{(\gamma+\mathrm{i}\omega)^2-|\varepsilon|^2}\delta(\omega+\omega')\\ =&\gamma|\varepsilon|\mathrm{e}^{-\mathrm{i}\phi}\left(\frac{1}{(\gamma-|\varepsilon|)^2+\omega^2}+\frac{1}{(\gamma+|\varepsilon|)^2+\omega^2}\right)\delta(\omega+\omega')\,,\\ \langle\tilde{a}^\dagger_{\text{out}}(\omega),\tilde{a}_{\text{out}}(\omega')\rangle =&\frac{2\gamma\varepsilon^*}{(\gamma+\mathrm{i}\omega)^2-|\varepsilon|^2}\,\frac{2\gamma\varepsilon}{(\gamma-\mathrm{i}\omega')^2-|\varepsilon|^2}\langle\tilde{a}_{\text{in}}(-\omega),\tilde{a}^\dagger_{\text{in}}(-\omega')\rangle\\ =&\frac{2\gamma\varepsilon^*}{(\gamma+\mathrm{i}\omega)^2-|\varepsilon|^2}\,\frac{2\gamma\varepsilon}{(\gamma-\mathrm{i}\omega)^2-|\varepsilon|^2}\delta(\omega-\omega')\\ =&\gamma|\varepsilon|\left(\frac{1}{(\gamma-|\varepsilon|)^2+\omega^2}-\frac{1}{(\gamma+|\varepsilon|)^2+\omega^2}\right)\delta(\omega-\omega')\,.\end{aligned}\tag{A.32}$$

One can see that $\langle\tilde{a}^\dagger_{\text{out}}(\omega),\tilde{a}_{\text{out}}(\omega')\rangle=\langle\tilde{a}^\dagger_{\text{out}}(\omega'),\tilde{a}_{\text{out}}(\omega)\rangle$ $\big($while remembering that $\delta(-x)=\delta(x)\big)$. The missing second order moments can be obtained by

$$\begin{aligned}\langle\tilde{a}_{\text{out}}(\omega),\tilde{a}^\dagger_{\text{out}}(\omega')\rangle&=\langle\tilde{a}^\dagger_{\text{out}}(\omega'),\tilde{a}_{\text{out}}(\omega)\rangle+\delta(\omega-\omega')\,,\\ \langle\tilde{a}^\dagger_{\text{out}}(\omega),\tilde{a}^\dagger_{\text{out}}(\omega')\rangle&=\langle\tilde{a}_{\text{out}}(\omega),\tilde{a}_{\text{out}}(\omega')\rangle^\dagger\,.\end{aligned}\tag{A.33}$$

The quadrature moments are

$$\begin{aligned}\langle\tilde{q}_{\theta,\text{out}}(\omega),\tilde{q}_{\theta,\text{out}}(\omega')\rangle =&\frac{1}{2}\big[|\langle\tilde{a}_{\text{out}}(\omega),\tilde{a}_{\text{out}}(\omega')\rangle|\big(\mathrm{e}^{-\mathrm{i}(2\theta+\phi)}+\mathrm{e}^{\mathrm{i}(2\theta+\phi)}\big)\\ &+2\langle\tilde{a}^\dagger_{\text{out}}(\omega),\tilde{a}_{\text{out}}(\omega')\rangle+\delta(\omega-\omega')\big]\\ =&|\langle\tilde{a}_{\text{out}}(\omega),\tilde{a}_{\text{out}}(\omega')\rangle|\cos(2\theta+\phi)+\langle\tilde{a}^\dagger_{\text{out}}(\omega),\tilde{a}_{\text{out}}(\omega')\rangle+\frac{1}{2}\delta(\omega-\omega')\\ =&\langle:\tilde{q}_{\theta,\text{out}}(\omega),\tilde{q}_{\theta,\text{out}}(\omega'):\rangle+\frac{1}{2}\delta(\omega-\omega')\,.\end{aligned}\tag{A.34}$$

The normal ordered quadrature correlations can be obtained by simply inserting the quantities of Eq. (A.32) while introducing the abbreviations $\lambda=\gamma-|\varepsilon|$ and $\mu=\gamma+|\varepsilon|$

$$\begin{aligned}\langle:\tilde{q}_{\theta,\text{out}}(\omega),\tilde{q}_{\theta,\text{out}}(\omega'):\rangle =&\gamma|\varepsilon|\left(\frac{1}{\lambda^2+\omega^2}+\frac{1}{\mu^2+\omega^2}\right)\cos(2\theta+\phi)\delta(\omega+\omega')\\ &+\gamma|\varepsilon|\left(\frac{1}{\lambda^2+\omega^2}-\frac{1}{\mu^2+\omega^2}\right)\delta(\omega-\omega')\,.\end{aligned}\tag{A.35}$$

Integration over ω' gives the power spectrum [Wal94]

$$:S_\theta(\omega):=\gamma|\varepsilon|\left(\frac{\cos(2\theta+\phi)+1}{\lambda^2+\omega^2}+\frac{\cos(2\theta+\phi)-1}{\mu^2+\omega^2}\right)\,.\tag{A.36}$$

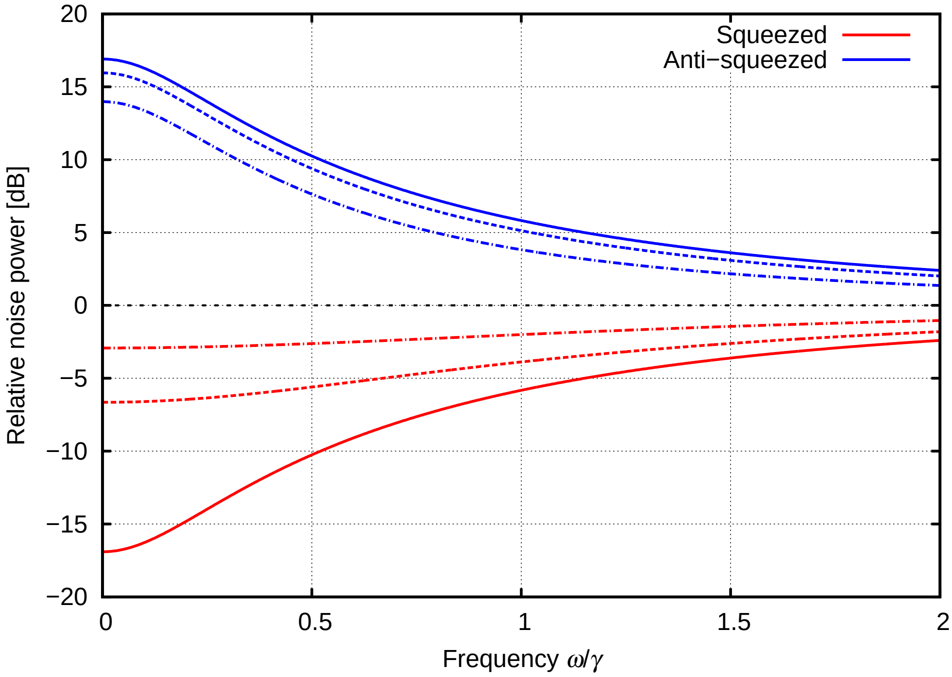

Figure A.2.: Logarithmic power spectrum for the squeezed ($S^-(\omega)$, red) and anti-squeezed ($S^+(\omega)$, blue) quadrature with a fixed pump strength of $|\varepsilon| = 0.75\,\gamma$ and different detection efficiencies (solid: $\eta = 1$, dashed: $\eta = 0.8$, dot-dashed: $\eta = 0.5$).

If we take a finite detection efficiency η into account and remember that the vacuum level is $\frac{1}{2}$, the spectrum is

$$S_\theta(\omega) = \eta : S_\theta(\omega) : + \frac{1}{2}\,. \tag{A.37}$$

The two extremal power spectra reflecting the anti-squeezed and squeezed quadrature read

$$\begin{aligned} S^+(\omega) &= S_{\theta=-\frac{\phi}{2}}(\omega) = \frac{1}{2} + \eta\frac{2\gamma|\varepsilon|}{\lambda^2+\omega^2} \\ S^-(\omega) &= S_{\theta=\frac{\pi-\phi}{2}}(\omega) = \frac{1}{2} - \eta\frac{2\gamma|\varepsilon|}{\mu^2+\omega^2}\,, \end{aligned} \tag{A.38}$$

and this is the result given in Eq. (3.1). In Figure A.2 the variances normalized to the vacuum level are shown, with different detection efficiencies.

A.3.3. Additional frequency filter

The spectrum derived in the previous section describes the output of an OPA directly. However, during the process of frequency up-conversion the state passes through another cavity that introduces additional frequency filtering. This effect will be treated in the following.

A mode experiencing an additional filter with decay rate κ is transformed as

$$\hat{a}_{\text{fil}}(t) = \int_{-\infty}^{t} dz\, \kappa e^{-\kappa(t-z)} \hat{a}(z) \tag{A.39}$$

in the time domain which is a through-pass Lorentzian filter in the frequency domain (see Section A.2):

$$\tilde{a}_{\text{fil}}(\omega) = \frac{\kappa}{\kappa - \mathrm{i}\omega} \tilde{a}(\omega) \,. \tag{A.40}$$

Using this relation one can rewrite Eq. (A.34) to obtain the filtered quadrature moments

$$\begin{aligned}\langle \tilde{q}_{\theta,\text{out,fil}}(\omega), \tilde{q}_{\theta,\text{out,fil}}(\omega')\rangle =& |\langle \tilde{a}_{\text{out,fil}}(\omega), \tilde{a}_{\text{out,fil}}(\omega')\rangle| \cos(2\theta + \phi) \\ &+ \langle \tilde{a}^{\dagger}_{\text{out,fil}}(\omega), \tilde{a}_{\text{out,fil}}(\omega')\rangle + \frac{1}{2}\delta(\omega - \omega') \\ =& \left| \frac{\kappa}{\kappa - \mathrm{i}\omega} \frac{\kappa}{\kappa - \mathrm{i}\omega} \right| |\langle \tilde{a}_{\text{out}}(\omega), \tilde{a}_{\text{out}}(\omega')\rangle| \cos(2\theta + \phi) \\ &+ \frac{\kappa}{\kappa + \mathrm{i}\omega} \frac{\kappa}{\kappa - \mathrm{i}\omega} \langle \tilde{a}^{\dagger}_{\text{out}}(\omega), \tilde{a}_{\text{out}}(\omega')\rangle + \frac{1}{2}\delta(\omega - \omega') \\ =& \frac{\kappa^2}{\kappa^2 + \omega^2} \langle :\tilde{q}_{\theta,\text{out}}(\omega), \tilde{q}_{\theta,\text{out}}(\omega') :\rangle + \frac{1}{2}\delta(\omega - \omega') \,.\end{aligned} \tag{A.41}$$

Using Eq. (A.35) and integrating over ω' gives the filtered power spectrum and the spectra for the anti-squeezed and squeezed quadrature read

$$\begin{aligned} S^{+}_{\text{fil}}(\omega) &= \frac{1}{2} + \eta \frac{\kappa^2}{\kappa^2 + \omega^2} \frac{2\gamma|\varepsilon|}{\lambda^2 + \omega^2} \,, \\ S^{-}_{\text{fil}}(\omega) &= \frac{1}{2} - \eta \frac{\kappa^2}{\kappa^2 + \omega^2} \frac{2\gamma|\varepsilon|}{\mu^2 + \omega^2} \,, \end{aligned} \tag{A.42}$$

and this is the result given in Eq. (3.2).

A.4. Non-degenerate spontaneous parametric down-conversion

Here, the temporal correlations for the SPDC source of Chapter 5 will be calculated based on the cavity input-output formalism, Section A.1.

The Hamiltonian of the system under investigation is

$$\mathbf{H}_{\text{sys}} = \hbar\omega_{+}\hat{a}^{\dagger}_{+}\hat{a}_{+} + \hbar\omega_{-}\hat{a}^{\dagger}_{-}\hat{a}_{-} + \mathrm{i}\hbar\left(\varepsilon \mathrm{e}^{-\mathrm{i}\omega_{\text{p}}t}\hat{a}^{\dagger}_{+}\hat{a}^{\dagger}_{-} - \varepsilon^{*}\mathrm{e}^{\mathrm{i}\omega_{\text{p}}t}\hat{a}_{+}\hat{a}_{-}\right) \tag{A.43}$$

with the pump parameter ε that is proportional to the pump field amplitude. Following the cavity input-output formalism, the corresponding Heisenberg equations of motion read

$$\frac{d\hat{a}_{\pm}(t)}{dt} = -\frac{\mathrm{i}}{\hbar}\left[\hat{a}_{\pm}(t), \mathbf{H}_{\text{sys}}\right] - \gamma_{\pm}\hat{a}_{\pm}(t) + \sqrt{2\gamma_{\pm}}\hat{a}_{\pm,\text{in}}(t) \,. \tag{A.44}$$

After transforming into the rotating frame ($\hat{a}_\pm \to \hat{a}_\pm \mathrm{e}^{-\mathrm{i}\omega_\pm t}$) we get

$$\frac{d\hat{a}_\pm(t)}{dt} - \mathrm{i}\omega_\pm \hat{a}_\pm(t) = -\frac{\mathrm{i}}{\hbar}\left[\hbar\omega_\pm \hat{a}_\pm(t) + \mathrm{i}\hbar\varepsilon \hat{a}^\dagger_\mp(t)\right] - \gamma_\pm \hat{a}_\pm(t) + \sqrt{2\gamma_\pm}\,\hat{a}_{\pm,\mathrm{in}}(t) \tag{A.45}$$

and

$$\frac{d\hat{a}_\pm(t)}{dt} = \varepsilon \hat{a}^\dagger_\mp(t) - \gamma_\pm \hat{a}_\pm(t) + \sqrt{2\gamma_\pm}\,\hat{a}_{\pm,\mathrm{in}}(t)\,. \tag{A.46}$$

A.4.1. SPDC: Frequency-space solution

Following the same procedure as in the treatment of the OPA, we replace the operators of Eq. (A.46) by their fourier transforms (marked with a tilde $\tilde{a}$)

$$\begin{aligned} \hat{a}_\pm(t) &= \frac{1}{\sqrt{2\pi}}\int_{-\infty}^{\infty} d\omega\, e^{-\mathrm{i}\omega t}\tilde{a}_\pm(\omega) \\ \hat{a}^\dagger_\pm(t) &= \frac{1}{\sqrt{2\pi}}\int_{-\infty}^{\infty} d\omega\, e^{+\mathrm{i}\omega t}\tilde{a}^\dagger_\pm(\omega) \\ &= \frac{1}{\sqrt{2\pi}}\int_{-\infty}^{\infty} d\omega\, e^{-\mathrm{i}\omega t}\tilde{a}^\dagger_\pm(-\omega)\,. \end{aligned} \tag{A.47}$$

The equation of motion is then given by

$$(\gamma_\pm - \mathrm{i}\omega)\tilde{a}_\pm(\omega) = \varepsilon \tilde{a}^\dagger_\mp(-\omega) + \sqrt{2\gamma_\mp}\,\tilde{a}_{\pm,\mathrm{in}}(\omega) \tag{A.48}$$

and the corresponding hermitian conjugate is (where we additionally transform $\omega \to -\omega$ and swap the indices)

$$(\gamma_\mp - \mathrm{i}\omega)\tilde{a}^\dagger_\mp(-\omega) = \varepsilon \tilde{a}_\pm(\omega) + \sqrt{2\gamma_\pm}\,\tilde{a}^\dagger_{\mp,\mathrm{in}}(-\omega)\,. \tag{A.49}$$

As we want to express the intra-cavity field operators in terms of input field operators, we insert Eq. (A.49) into Eq. (A.48) and obtain

$$\tilde{a}_\pm(\omega) = \frac{\varepsilon\sqrt{2\gamma_\mp}}{(\gamma_\pm - \mathrm{i}\omega)(\gamma_\mp - \mathrm{i}\omega) - |\varepsilon|^2}\tilde{a}^\dagger_{\mp,\mathrm{in}}(-\omega) + \frac{\sqrt{2\gamma_\pm}(\gamma_\mp - \mathrm{i}\omega)}{(\gamma_\pm - \mathrm{i}\omega)(\gamma_\mp - \mathrm{i}\omega) - |\varepsilon|^2}\tilde{a}_{\pm,\mathrm{in}}(\omega)\,. \tag{A.50}$$

As developed in Section A.1, the relation between intra-cavity, input and output fields is

$$\tilde{a}_{\pm,\mathrm{in}} + \tilde{a}_{\pm,\mathrm{out}} = \sqrt{2\gamma_\pm}\,\tilde{a}_\pm \tag{A.51}$$

so that the output fields read

$$
\begin{aligned}
\tilde{a}_{\pm,\mathrm{out}}(\omega) =& \frac{2\varepsilon\sqrt{\gamma_+\gamma_-}}{(\gamma_+ - \mathrm{i}\omega)(\gamma_- - \mathrm{i}\omega) - |\varepsilon|^2}\tilde{a}^\dagger_{\mp,\mathrm{in}}(-\omega) \\
&+ \left(\frac{2\gamma_\pm(\gamma_\mp - \mathrm{i}\omega)}{(\gamma_\pm - \mathrm{i}\omega)(\gamma_\mp - \mathrm{i}\omega) - |\varepsilon|^2} - 1\right)\tilde{a}_{\pm,\mathrm{in}}(\omega) \\
=& A(\omega)\tilde{a}^\dagger_{\pm,\mathrm{in}}(-\omega) + B_\pm(\omega)\tilde{a}_{\pm,\mathrm{in}}(\omega)\,, \\
\tilde{a}^\dagger_{\pm,\mathrm{out}}(-\omega) =& \frac{2\varepsilon\sqrt{\gamma_+\gamma_-}}{(\gamma_+ - \mathrm{i}\omega)(\gamma_- - \mathrm{i}\omega) - |\varepsilon|^2}\tilde{a}_{\mp,\mathrm{in}}(\omega) \\
&+ \left(\frac{2\gamma_\pm(\gamma_\mp - \mathrm{i}\omega)}{(\gamma_\pm - \mathrm{i}\omega)(\gamma_\mp - \mathrm{i}\omega) - |\varepsilon|^2} - 1\right)\tilde{a}^\dagger_{\pm,\mathrm{in}}(-\omega) \\
=& A(\omega)\tilde{a}_{\pm,\mathrm{in}}(\omega) + B_\pm(\omega)\tilde{a}^\dagger_{\pm,\mathrm{in}}(-\omega)\,,
\end{aligned}
\tag{A.52}
$$

with the notations

$$
A(\omega) = \frac{2\varepsilon\sqrt{\gamma_+\gamma_-}}{(\gamma_+ - \mathrm{i}\omega)(\gamma_- - \mathrm{i}\omega) - |\varepsilon|^2}\,,\; B_\pm(\omega) = \frac{\gamma_+\gamma_- \pm \mathrm{i}\omega(\gamma_+ - \gamma_-) + \omega^2 + |\varepsilon|^2}{(\gamma_+ - \mathrm{i}\omega)(\gamma_- - \mathrm{i}\omega) - |\varepsilon|^2}\,. \tag{A.53}
$$

A.4.2. Temporal correlations of the SPDC output

In the experiment, non-degenerate output modes of the SPDC are spatially separated by a dichroic beam splitter. A photon in one of these modes (at 810 nm) heralds the existence of a photon in the other mode (1550 nm).

The temporal correlation function of the two modes is given by [Lu00]

$$
\Gamma(\tau) = \langle E^-_{\mathrm{trigger}}(t)E^-_{\mathrm{signal}}(t+\tau)E^+_{\mathrm{signal}}(t+\tau)E^+_{\mathrm{trigger}}(t)\rangle\,, \tag{A.54}
$$

where

$$
\begin{aligned}
E^-_{\mathrm{trigger}}(t) &= \hat{a}^\dagger_{+,\mathrm{out}}(t) = \frac{1}{\sqrt{2\pi}}\int_{-\infty}^{\infty} d\omega\, \mathrm{e}^{-\mathrm{i}\omega t}\tilde{a}^\dagger_{+,\mathrm{out}}(-\omega)\,, \\
E^-_{\mathrm{signal}}(t) &= \hat{a}^\dagger_{-,\mathrm{out}}(t) = \frac{1}{\sqrt{2\pi}}\int_{-\infty}^{\infty} d\omega\, \mathrm{e}^{-\mathrm{i}\omega t}\tilde{a}^\dagger_{-,\mathrm{out}}(-\omega)\,, \\
E^+_{\mathrm{signal}}(t) &= \hat{a}_{-,\mathrm{out}}(t) = \frac{1}{\sqrt{2\pi}}\int_{-\infty}^{\infty} d\omega\, \mathrm{e}^{-\mathrm{i}\omega t}\tilde{a}_{-,\mathrm{out}}(\omega)\,, \\
E^+_{\mathrm{trigger}}(t) &= \hat{a}_{+,\mathrm{out}}(t) = \frac{1}{\sqrt{2\pi}}\int_{-\infty}^{\infty} d\omega\, \mathrm{e}^{-\mathrm{i}\omega t}\tilde{a}_{+,\mathrm{out}}(\omega)
\end{aligned}
\tag{A.55}
$$

and, as calculated in the previous section,

$$
\begin{aligned}
\tilde{a}_{+,\mathrm{out}}(\omega) =& A(\omega)\tilde{a}^\dagger_{-,\mathrm{in}}(-\omega) + B_+(\omega)\tilde{a}_{+,\mathrm{in}}(\omega)\,, \\
\tilde{a}^\dagger_{+,\mathrm{out}}(-\omega) =& A(\omega)\tilde{a}_{-,\mathrm{in}}(\omega) + B_+(\omega)\tilde{a}^\dagger_{+,\mathrm{in}}(-\omega)\,, \\
\tilde{a}_{-,\mathrm{out}}(\omega) =& A(\omega)\tilde{a}^\dagger_{+,\mathrm{in}}(-\omega) + B_-(\omega)\tilde{a}_{-,\mathrm{in}}(\omega)\,, \\
\tilde{a}^\dagger_{-,\mathrm{out}}(-\omega) =& A(\omega)\tilde{a}_{+,\mathrm{in}}(\omega) + B_-(\omega)\tilde{a}^\dagger_{-,\mathrm{in}}(-\omega)\,.
\end{aligned}
\tag{A.56}
$$

The temporal correlation function can then be written as

$$\begin{aligned}
\Gamma(\tau) =& \frac{1}{4\pi^2}\int_{-\infty}^{\infty} d\omega\, d\omega'\, d\omega''\, d\omega'''\; \mathrm{e}^{-\mathrm{i}(\omega+\omega'+\omega''+\omega''')t}\mathrm{e}^{-\mathrm{i}(\omega'+\omega'')\tau} \\
& \langle \tilde{a}^{\dagger}_{+,\mathrm{out}}(-\omega)\tilde{a}^{\dagger}_{-,\mathrm{out}}(-\omega')\tilde{a}_{-,\mathrm{out}}(\omega'')\tilde{a}_{+,\mathrm{out}}(\omega''')\rangle \\
=& \frac{1}{4\pi^2}\int_{-\infty}^{\infty} d\omega\, d\omega'\, d\omega''\, d\omega'''\; \mathrm{e}^{-\mathrm{i}(\omega+\omega'+\omega''+\omega''')t}\mathrm{e}^{-\mathrm{i}(\omega'+\omega'')\tau} \\
& \langle [A(\omega)\tilde{a}_{-,\mathrm{in}}(\omega) + B_{+}(\omega)\tilde{a}^{\dagger}_{+,\mathrm{in}}(-\omega)][A(\omega')\tilde{a}_{+,\mathrm{in}}(\omega') + B_{-}(\omega')\tilde{a}^{\dagger}_{-,\mathrm{in}}(-\omega')] \\
& \times [A(\omega'')\tilde{a}^{\dagger}_{+,\mathrm{in}}(-\omega'') + B_{-}(\omega'')\tilde{a}_{-,\mathrm{in}}(\omega'')][A(\omega''')\tilde{a}^{\dagger}_{-,\mathrm{in}}(-\omega''') + B_{+}(\omega''')\tilde{a}_{+,\mathrm{in}}(\omega''')]\rangle\,.
\end{aligned} \tag{A.57}$$

There are only two moments that do not vanish - those that have two creation and two annihilation operators and where no creation operator is on the very left and no annihilation operator on the very right. An annihilation operator acting on a vacuum ket or a creation operator acting on a vacuum bra gives a zero. The two surviving moments can be simplified by repeatedly applying the commutation relation $[\tilde{a}(\omega), \tilde{a}^{\dagger}(-\omega')] = \delta(\omega + \omega')$. The non-vanishing moments are

$$\begin{aligned}
\langle \tilde{a}_{-,\mathrm{in}}(\omega)\tilde{a}^{\dagger}_{-,\mathrm{in}}(-\omega')\tilde{a}_{+,\mathrm{in}}(\omega'')\tilde{a}^{\dagger}_{+,\mathrm{in}}(-\omega''')\rangle &= \delta(\omega+\omega')\delta(\omega''+\omega''') \\
\langle \tilde{a}_{-,\mathrm{in}}(\omega)\tilde{a}_{+,\mathrm{in}}(\omega')\tilde{a}^{\dagger}_{+,\mathrm{in}}(-\omega'')\tilde{a}^{\dagger}_{-,\mathrm{in}}(-\omega''')\rangle &= \delta(\omega+\omega''')\delta(\omega'+\omega'') + \delta(\omega+\omega'')\delta(\omega'+\omega''')
\end{aligned} \tag{A.58}$$

The correlation function can be further simplified:

$$\begin{aligned}
\Gamma(\tau) =& \frac{1}{4\pi^2}\int_{-\infty}^{\infty} d\omega\, d\omega'\, d\omega''\, d\omega'''\; \mathrm{e}^{-\mathrm{i}(\omega+\omega'+\omega''+\omega''')t}\mathrm{e}^{-\mathrm{i}(\omega'+\omega'')\tau} \\
& \big[A(\omega)B_{-}(\omega')B_{-}(\omega'')A(\omega''')\delta(\omega+\omega')\delta(\omega''+\omega''') \\
& \quad + A(\omega)A(\omega')A(\omega'')A(\omega''')\delta(\omega+\omega''')\delta(\omega'+\omega'') \\
& \quad + A(\omega)A(\omega')A(\omega'')A(\omega''')\delta(\omega+\omega'')\delta(\omega'+\omega''')\big] \\
=& \frac{1}{4\pi^2}\int_{-\infty}^{\infty} d\omega'\, d\omega''\; \mathrm{e}^{-\mathrm{i}(\omega'+\omega'')\tau}A(-\omega')B_{-}(\omega')B_{-}(\omega'')A(-\omega'') \\
& + \frac{1}{4\pi^2}\int_{-\infty}^{\infty} d\omega\, d\omega'\; A(\omega)A(\omega')A(-\omega')A(-\omega) \\
& + \frac{1}{4\pi^2}\int_{-\infty}^{\infty} d\omega'\, d\omega''\; \mathrm{e}^{-\mathrm{i}(\omega'+\omega'')\tau}A(-\omega'')A(\omega')A(\omega'')A(-\omega') \\
=& \left[\frac{1}{2\pi}\int_{-\infty}^{\infty} d\omega\; \mathrm{e}^{-\mathrm{i}\omega\tau}A(-\omega)B_{-}(\omega)\right]^2 \\
& + \left[\frac{1}{2\pi}\int_{-\infty}^{\infty} d\omega\; A(-\omega)A(\omega)\right]^2 + \left[\frac{1}{2\pi}\int_{-\infty}^{\infty} d\omega\; \mathrm{e}^{-\mathrm{i}\omega\tau}A(-\omega)A(\omega)\right]^2 .
\end{aligned} \tag{A.59}$$

A.4.3. Temporal correlation with equal decay rates

Let us now assume equal decay rates for the two generated modes $\gamma_+ = \gamma_- = \gamma$. Then the two coefficients $A(-\omega)$ and $B(\omega)$ reduce to

$$\begin{aligned} A(-\omega) =& \frac{2\varepsilon\gamma}{(\gamma+\mathrm{i}\omega)^2 - |\varepsilon|^2} \, , \\ B(\omega) =& \frac{\gamma^2+\omega^2+|\varepsilon|^2}{(\gamma-\mathrm{i}\omega)^2 - |\varepsilon|^2} \, . \end{aligned} \tag{A.60}$$

To evaluate the temporal correlation function, I first need the following two factors:

$$\begin{aligned} A(-\omega)B(\omega) =& \frac{2\gamma\varepsilon(\gamma^2+\omega^2+|\varepsilon|^2)}{[(\gamma+\mathrm{i}\omega)^2-|\varepsilon|^2]\,[(\gamma-\mathrm{i}\omega)^2-|\varepsilon|^2]} \\ =& \gamma\varepsilon \frac{2(\gamma^2+\omega^2+|\varepsilon|^2)}{\gamma^4+\omega^4+|\varepsilon|^4+2\gamma^2\omega^2-2\gamma^2|\varepsilon|^2+2\omega^2|\varepsilon|^2} \\ =& \gamma\varepsilon\left(\frac{1}{\lambda^2+\omega^2}+\frac{1}{\mu^2+\omega^2}\right) \end{aligned} \tag{A.61}$$

with the abbreviations

$$\begin{aligned} \lambda &= \gamma - |\varepsilon| \, , \\ \mu &= \gamma + |\varepsilon| \, . \end{aligned} \tag{A.62}$$

In the same way I obtain

$$\begin{aligned} A(\omega)A(-\omega) =& \frac{2\varepsilon\gamma}{(\gamma+\mathrm{i}\omega)^2-|\varepsilon|^2}\frac{2\varepsilon\gamma}{(\gamma-\mathrm{i}\omega)^2-|\varepsilon|^2} \\ =& \gamma\varepsilon\left(\frac{1}{\lambda^2+\omega^2}-\frac{1}{\mu^2+\omega^2}\right) \, . \end{aligned} \tag{A.63}$$

The integrals in the temporal correlation function are analytically solvable and I obtain

$$\frac{1}{2\pi}\int_{-\infty}^{\infty} d\omega\, \mathrm{e}^{-\mathrm{i}\omega\tau} A(-\omega)B(\omega) = \frac{\varepsilon\gamma}{2}\left(\frac{1}{\lambda}\mathrm{e}^{-\lambda|\tau|}+\frac{1}{\mu}\mathrm{e}^{-\mu|\tau|}\right) \, , \tag{A.64}$$

$$\frac{1}{2\pi}\int_{-\infty}^{\infty} d\omega\, A(-\omega)A(\omega) = \frac{|\varepsilon|^2\gamma}{\gamma^2-|\varepsilon|^2} \, , \tag{A.65}$$

$$\frac{1}{2\pi}\int_{-\infty}^{\infty} d\omega\, \mathrm{e}^{-\mathrm{i}\omega\tau} A(-\omega)A(\omega) = \frac{\varepsilon\gamma}{2}\left(\frac{1}{\lambda}\mathrm{e}^{-\lambda|\tau|}-\frac{1}{\mu}\mathrm{e}^{-\mu|\tau|}\right) \, . \tag{A.66}$$

The temporal correlation function finally reads

$$\begin{aligned} \Gamma(\tau) = & \left[\frac{\varepsilon\gamma}{2}\left(\frac{1}{\lambda}\mathrm{e}^{-\lambda|\tau|}+\frac{1}{\mu}\mathrm{e}^{-\mu|\tau|}\right)\right]^2 \\ & + \left[\frac{|\varepsilon|^2\gamma}{\gamma^2-|\varepsilon|^2}\right]^2 + \left[\frac{\varepsilon\gamma}{2}\left(\frac{1}{\lambda}\mathrm{e}^{-\lambda|\tau|}-\frac{1}{\mu}\mathrm{e}^{-\mu|\tau|}\right)\right]^2 \, , \end{aligned} \tag{A.67}$$

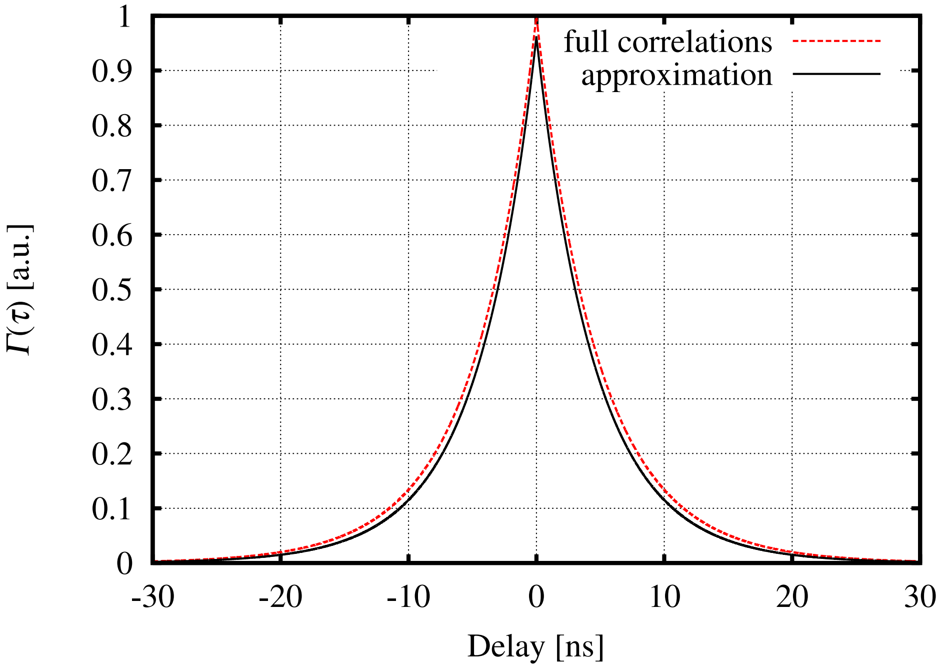

Figure A.3.: Temporal correlations of the output of a non-degenerate OPA far below threshold (red dashed). The temporal correlations are very well approximated by the first term of Eq. A.67 only (black curve, the constant offset is subtracted). Parameters are $\gamma = 2\pi \cdot 18\,\mathrm{MHz}$, $\varepsilon = 0.2\gamma$. Note that $\varepsilon = 0.2\gamma$ is the highest value used in the experiment. For lower values of ε, the approximation is even better.

and this is the result given in Eq. (5.2). A graph of the full correlations is shown in Figure A.3, where only the constant offset is subtracted.

The correlations are very well approximated by the first term of Eq. (A.67) only and all following calculations are continued with the approximation.

A.4.4. Temporal correlations with filtered signal mode

In the experiment, the two down-converted optical fields experience different transfer functions. This asymmetry is caused by frequency filtering of the signal mode by up-conversion in a sum-frequency generation cavity with a relatively small linewidth. Unequal decay rates in the generation process of the two down-converted fields have a similar effect. Here, I will pool these two effects (that actually are present in the experiment) by letting one of the modes (the 1550 nm field, $\hat{a}_-$) be transmitted through one cavity with the decay rate κ.

The modes experiencing an additional frequency filter are transformed via

$$\hat{a}_-(t) \to \hat{a}_-(t') = \int_{-\infty}^{t'} dz\, \kappa \mathrm{e}^{-\kappa(t'-z)} \hat{a}_-(z)\,. \tag{A.68}$$

The temporal correlations (Eq. (A.54)) transform like

$$
\begin{aligned}
\Gamma_{\text{filtered}}(\tau) \approx & \left\langle \kappa^2 \int_{-\infty}^{t+\tau} dz\, dz'\, \mathrm{e}^{-\kappa(t+\tau-z)} \mathrm{e}^{-\kappa(t+\tau-z')} \tilde{a}^{\dagger}_{+,\text{out}}(t) \tilde{a}^{\dagger}_{-,\text{out}}(z) \tilde{a}_{-,\text{out}}(z') \tilde{a}_{+,\text{out}}(t) \right\rangle \\
= & \kappa^2 \int_{-\infty}^{\tau} dz\, dz'\, \mathrm{e}^{-\kappa(\tau-z)} \mathrm{e}^{-\kappa(\tau-z')} \left\langle \tilde{a}^{\dagger}_{+,\text{out}}(t) \tilde{a}^{\dagger}_{-,\text{out}}(t+z) \tilde{a}_{-,\text{out}}(t+z') \tilde{a}_{+,\text{out}}(t) \right\rangle \\
= & \kappa^2 \int_{-\infty}^{\tau} dz\, dz'\, \mathrm{e}^{-\kappa(\tau-z)} \mathrm{e}^{-\kappa(\tau-z')} \\
& \cdot \frac{1}{4\pi^2} \int_{-\infty}^{\infty} d\omega' d\omega''\, \mathrm{e}^{-\mathrm{i}\omega' z} \mathrm{e}^{-\mathrm{i}\omega'' z'} \left[A(-\omega') B_-(\omega') B_-(\omega'') A(-\omega'') \right] \\
= & \left[\frac{\varepsilon\gamma\kappa}{2} \int_{-\infty}^{\tau} dz\, \mathrm{e}^{-\kappa(\tau-z)} \left(\frac{1}{\lambda} \mathrm{e}^{-\lambda|z|} + \frac{1}{\mu} \mathrm{e}^{-\mu|z|} \right) \right]^2 ,
\end{aligned}
\tag{A.69}
$$

where I omitted the negligible constant offset and the minor contributions, i.e. the second and third term of Eq. (A.67). The integration is analytically solvable and the signal-filtered correlation function reads

$$
\Gamma_{\text{filtered}}(\tau) = \begin{cases} \left[\frac{\gamma\varepsilon\kappa}{2} \left(\frac{\mathrm{e}^{\mu\tau}}{\mu(\kappa+\mu)} + \frac{\mathrm{e}^{\lambda\tau}}{\lambda(\kappa+\lambda)} \right) \right]^2 & , \tau < 0 \\ \left[\frac{\gamma\varepsilon\kappa}{2} \left(\frac{\mathrm{e}^{-\mu\tau}}{\mu(\kappa-\mu)} + \frac{\mathrm{e}^{-\lambda\tau}}{\lambda(\kappa-\lambda)} - \frac{2\mathrm{e}^{-\kappa\tau}}{(\kappa+\mu)(\kappa-\mu)} - \frac{2\mathrm{e}^{-\kappa\tau}}{(\kappa+\lambda)(\kappa-\lambda)} \right) \right]^2 & , \tau \geq 0 , \end{cases}
\tag{A.70}
$$

and this is the result given in Eq. (5.3).

A.5. Maximum likelihood estimation of quantum states

The scope of quantum state reconstruction is to find the state $\hat{\rho}$. A quantum state is a closed system that does not interact with the environment – until it is measured. In the positive operator-valued measure (POVM) framework, a measurement of a quantum state is fully described by a POVM $\{\hat{\Pi}_l\}$, which is a set of POVM elements $\hat{\Pi}_l$. This framework is sufficient and well suited, when the quantum state after the measurement is not of particular interest but only the measurement outcomes, or, as we deal with quantum mechanics, the outcome statistics. The probability that an apparatus responds with outcome $\hat{\Pi}_l$ when measuring a quantum state ρ_m is

$$
p_{lm} = \mathrm{Tr}[\hat{\Pi}_l \hat{\rho}_m] \, . \tag{A.71}
$$

The POVM elements are positive-semidefinite and decompose the unit operator

$$
\hat{\Pi}_l \geq 0 \, , \quad \sum_{l=1}^{k} \hat{\Pi}_l = \mathbf{1} \, . \tag{A.72}
$$

These properties ensure that $p_{lm} \geq 0$ and that something must be the outcome for a (large enough) k, which is the number of possible measurement outcomes[5]. The trace operation in Eq. (A.71) is a summation so that it can also be written as

$$p_{lm} = \sum_{i,j} \left(\hat{\Pi}_l\right)_{i,j} \hat{\rho}_{m,ij} \,, \tag{A.73}$$

which is just a set of linear equations like

$$\mathbf{M}\vec{\rho} = \vec{p} \,. \tag{A.74}$$

For an invertible matrix $\mathbf{M}$ this set can be easily solved. This is called direct quantum state reconstruction (for example via the inverse Radon transform) and involves no *a priori* restrictions. Thus, during the reconstruction algorithms, unphysical features like negative diagonal elements of the state $\hat{\rho}$ may occur, causing ripples in the reconstructed Wigner function. A different approach is traced by *maximum likelihood estimation*. This technique always maintains a physically plausible density matrix and results in a $\hat{\rho}$ that is most likely to be the cause of the measured outcome.

The maximum likelihood estimation algorithm (maxlik) is presented in the following. Let us assume a measurement $\{\hat{\Pi}_j\}$ was measured N times and each outcome j is obtained n_j times, such that $\sum_j n_j = N$. The probability of outcome j is $p_j = \mathrm{Tr}[\hat{\rho}\hat{\Pi}_j]$, of course. The whole task is to maximize the likelihood function, which is simply defined as

$$\mathcal{L}(\hat{\rho}) = \prod_j p_j^{n_j} = \prod_j \left(\mathrm{Tr}[\hat{\rho}\hat{\Pi}_j]\right)^{n_j} \,. \tag{A.75}$$

However, computer programs like sums and product more than exponentials, the task of maximizing Eq. (A.75) is shifted to a maximization of the log-likelihood function

$$\log \mathcal{L}(\hat{\rho}) = \sum_j n_j \log(p_j) \,, \tag{A.76}$$

which is just equivalent as the logarithm is a monotonically increasing function.

During the algorithm the positivity of diagonal elements of the state is ensured by decomposing $\hat{\rho} = \hat{A}^\dagger \hat{A}$ and a Lagrange multiplier λ keeps a unit trace

$$\log \mathcal{L}(\hat{\rho}) = \sum_j \log\left(\mathrm{Tr}[\hat{A}^\dagger \hat{A}\hat{\Pi}_j]\right) - \lambda \mathrm{Tr}[\hat{A}^\dagger \hat{A}] = \mathbf{F} \,. \tag{A.77}$$

Any small variation of $\hat{A} \to \hat{A} + \delta\hat{A}$ leads to a small (i.e. first order) change of $\mathbf{F}$:

$$\begin{aligned} \delta\mathbf{F} &= \sum_j n_j \frac{1}{\mathrm{Tr}[\hat{A}^\dagger \hat{A}\hat{\Pi}_j]} \mathrm{Tr}[\hat{\Pi}_j \hat{A}^\dagger \, \delta\hat{A}] - \lambda \mathrm{Tr}[\hat{\Pi}_j \hat{A}^\dagger \hat{A}] \\ &= \sum_j \frac{n_j}{p_j} \mathrm{Tr}[\hat{\Pi}_j \hat{A}^\dagger \, \delta\hat{A}] - \lambda \mathrm{Tr}[\hat{\Pi}_j \hat{A}^\dagger \, \delta\hat{A}] \end{aligned} \tag{A.78}$$

---

[5] For example, k could represent the number of y-bins of an oscilloscope. Each bin of the oscilloscope is assigned to a POVM element.

As $\hat{\rho}$ is an extremal point, $\delta\mathbf{F}$ must vanish for all $\delta\hat{A}$ and one obtains

$$\begin{aligned} 0 &= \sum_j \frac{n_j}{p_j}\hat{\Pi}_j\hat{A}^\dagger - \lambda\hat{A}^\dagger \\ \lambda\hat{A}^\dagger\hat{A} &= \underbrace{\sum_j \frac{n_j}{p_j}\hat{\Pi}_j}_{\mathbf{R}}\,\hat{A}^\dagger\hat{A}\,, \end{aligned} \tag{A.79}$$

where in the last line $\hat{A}$ was multiplied from the right. We know from construction that $\hat{\rho} = \hat{A}^\dagger\hat{A}$ and the extremal equation reads

$$\hat{\rho} = \frac{1}{\lambda}\mathbf{R}\hat{\rho}\,. \tag{A.80}$$

Note that $\mathbf{R}$ itself depends on the state $\hat{\rho}$, which makes the problem non-trivial. Now one could naively try to iterate while maintaining proper normalization

$$\hat{\rho}^{(n+1)} = \frac{\mathbf{R}(\hat{\rho}^{(n)})\,\hat{\rho}^{(n)}}{\mathrm{Tr}[\mathbf{R}(\hat{\rho}^{(n)})\,\hat{\rho}^{(n)}]}\,. \tag{A.81}$$

This approach does not necessarily give a hermitian or positive semidefinity $\hat{\rho}$. This can be circumvented by the fact that if $\hat{\rho} = \frac{1}{\lambda}\mathbf{R}\hat{\rho}$ holds, also does $(\hat{\rho} = \frac{1}{\lambda}\mathbf{R}\hat{\rho})^\dagger$. It follows with $\hat{\rho}^\dagger = \hat{\rho}$ that $\hat{\rho} = \frac{1}{\lambda^*}\hat{\rho}\mathbf{R}^\dagger$ and inserting this to Eq. (A.80) one finally obtains the positive-semidefinite form of the extremal equation

$$\hat{\rho} = \frac{1}{|\lambda|^2}\mathbf{R}\hat{\rho}\mathbf{R}^\dagger\,. \tag{A.82}$$

In iterative form this reads

$$\hat{\rho}^{(n+1)} = \frac{\mathbf{R}(\hat{\rho}^{(n)})\,\hat{\rho}^{(n)}\mathbf{R}(\hat{\rho}^{(n)})}{\mathrm{Tr}[\mathbf{R}(\hat{\rho}^{(n)})\,\hat{\rho}^{(n)}\mathbf{R}(\hat{\rho}^{(n)})]}\,, \tag{A.83}$$

with

$$\mathbf{R}(\hat{\rho}^{(n)}) = \sum_j \frac{n_j}{p_j^{(n)}}\hat{\Pi}_j \quad \text{and} \quad p_j^{(n)} = \mathrm{Tr}[\hat{\rho}^{(n)}\hat{\Pi}_j]\,. \tag{A.84}$$

The denominator of Eq. (A.83) accounts for the Lagrange multiplier and re-normalizes the state after each iteration step (the numbers can get really large otherwise). In principle, this is the whole maximum likelihood reconstruction algorithm which is not more than five lines of program code. The result is the most likely $\hat{\rho}$ that is cause of the measured outcomes $\{j\}$. The step from a given $\hat{\rho}$ to the corresponding Wigner function is already described in Section 2.1.3 and its numerical implementation is given in the appendix, Section B.4.6.

Application to quadrature values

In the experiment, the reconstruction algorithm is performed on quadrature values obtained via balanced homodyne detection. As a reminder, the generalized quadrature is given by Eq. (2.9)

$$\hat{q}_\theta = \hat{q}\cos\theta + \hat{p}\sin\theta\,. \tag{A.85}$$

However, a convenient basis of the Hilbert space is the Fock basis – especially if one wants to analyze Fock states – so every state is decomposed as

$$\hat{\rho} = \sum_{m,n}^{N} \rho_{mn}|m\rangle\langle n|\,, \tag{A.86}$$

where N truncates the (infinitely large) Hilbert space at some maximum photon number and has to be chosen carefully. If N is chosen too small, information gets lost while a too large Hilbert space may cause artifacts, especially if N approaches the total number of data. However, the main reason to truncate the Hilbert space at some relatively small N ($\lesssim 20$) is to keep the computational costs reasonable.

The probability distribution of the quadrature values given a state $\hat{\rho}$ is

$$P(\hat{q}_\theta|\hat{\rho}) = \langle q_\theta,\theta|\hat{\rho}|q_\theta,\theta\rangle = \mathrm{Tr}\left[\hat{\rho}|q_\theta,\theta\rangle\langle q_\theta,\theta|\right] \tag{A.87}$$

or, for discretized (binned) data,

$$P_{\theta,j} = \int_{q_{j,\min}}^{q_{j,\max}} dq_\theta\, P(\hat{q}_\theta|\hat{\rho}) = \mathrm{Tr}\Big[\hat{\rho}\underbrace{\int_{q_{j,\min}}^{q_{j,\max}} dq_\theta\,|q_\theta,\theta\rangle\langle q_\theta,\theta|}_{\text{POVM element } \hat{\Pi}_{\theta,j}}\Big]\,. \tag{A.88}$$

The POVM elements are decomposed as

$$\hat{\Pi}_{\theta,j} = \sum_{m,n=0}^{N}\left(\hat{\Pi}_{\theta,j}\right)_{mn}|m\rangle\langle n| \tag{A.89}$$

and what is left due is the projection of the POVM elements to the Fock basis:

$$\left(\hat{\Pi}_{\theta,j}\right)_{mn} = \langle m|\hat{\Pi}_{\theta,j}|n\rangle = \int_{q_{j,\min}}^{q_{j,\max}} dq_\theta\,\langle m|q_\theta,\theta\rangle\langle q_\theta,\theta|n\rangle\,, \tag{A.90}$$

where the overlap between a Fock state and a quadrature eigenstate using Hermite polynomials[6] is given by [Leo05]

$$\langle q_\theta,\theta|n\rangle = \mathrm{e}^{in\theta}\frac{1}{\pi^{1/4}\sqrt{2^n n!}}H_n(q)\mathrm{e}^{-q_\theta^2/2}\,. \tag{A.91}$$

---

[6] $H_0(x) = 1$, $H_1(x) = 2x$, $H_n(x) = 2xH_{n-1}(x) - 2(n-1)H_{n-2}(x)$

It follows for the POVM elements

$$\left(\hat{\Pi}_{\theta,j}\right)_{mn} = \mathrm{e}^{\mathrm{i}(n-m)\theta} \frac{1}{\sqrt{\pi\, 2^{m+n} m! n!}} \int_{q_{j,\min}}^{q_{j,\max}} dq_\theta \, H_m(q_\theta) H_n(q_\theta) \mathrm{e}^{-q_\theta^2} \, . \tag{A.92}$$

Note that this formulation is valid for the variance of the vacuum to be $(\Delta\hat{q}_\theta)^2_{\mathrm{vac}} = \frac{1}{2}$ and care has to be taken for other normalizations.

In some situations, and also in the experiment presented in the following, a phase sensitive analysis of the state is not required or even possible. In these cases phase randomized state tomography is applied which simplifies the POVM elements

$$\left(\hat{\Pi}_j\right)_{mn} = \frac{1}{2\pi} \int_0^{2\pi} d\theta \, \langle m|\hat{\Pi}_{\theta,j}|n\rangle = \delta_{mn} \frac{1}{\sqrt{\pi} 2^n n!} \int_{q_{j,\min}}^{q_{j,\max}} dq \, H_n^2(q) \mathrm{e}^{-q^2} \, . \tag{A.93}$$

With these formulae a numerical implementation is straightforward and a python program is given in Section B.4.5.

B. Programs

B.1. Filter cavities

This is the *Finesse*-file for the simulation of the filter cavity in the single photon up-conversion experiment. Note that a second filter cavity is included, which would promise even better filtering. It was not used in the experiment as the complexity for keeping three cavities (SFG, first filter cavity, second filter cavity) on resonance without any bright field was considered to be too complex.

```
l laser 1 0  n0
#maxtem 3
#tem laser 0 1 0.2 0
#tem laser 0 2 0.2 0
#tem laser 0 3 0.2 0

#Cavity Photonenkanone
#Substrate and incoupling mirror
      m ArMenisc1 0 1 0 n0 n1
      s Menisc1 0.0059 1.453 n1 n2
      m2 RMenisc1 .969 0 0 n2 n3
      attr ArMenisc1 Rc -0.02
      attr RMenisc1 Rc -0.025
#spacing, crystal, spacing
      s AirGap1 0.021 n3 n4
      m dummy1 0 1 0 n4 n5
      s Crystal 0.0093 1.8433 n5 n6
      m2 Losses 0 0.029 0 n6 n7     #here, internal losses are included!
      s AirGap2 0.021  n7 n8
#outcoupling mirror and substrate
      m2 RMenisc2 .9985 0 0 n8 n9
      s Menisc2 0.0059 1.453 n9 n10
      m ArMenisc2 0 1 0 n10 n11
      attr RMenisc2 Rc 0.025
      attr ArMenisc2 Rc 0.02

      cav Photonenkanone RMenisc1 n3 RMenisc2 n8
      pd0 afterPhotoncanon n11
```

```
#isolation, required to delete reflection
      s s20 0  n11 n12
      isol isol1 100 n12 n13a
      s s21 0  n13a n13

#filter cavity 1
      m2 Fc1M1 0.99 0 0 n13 n14
      s GapFc1 .0025  n14 n15                       #!!
      m2 Fc1M2 0.99 0 0 n15 n16
      attr Fc1M1 Rc -1
      attr Fc1M2 Rc 1

      cav Filtercavity1 Fc1M1 n14 Fc1M2 n15
      pd0 afterFC1 n16

#isolation, required to delete reflection
      s s13 0  n16 n17
      isol isol3 100 n17 n18a
      s s14 0 n18a n18

#filter cavity 2
      m2 Fc2M1 0.99 0 0 n18 n19
      s GapFc2 0.0032 n19 n20                       #!!
      m2 Fc2M2 0.99 0 0 n20 n21
      attr Fc2M1 Rc -1
      attr Fc2M2 Rc 1

      cav FilterCavity2 Fc2M1 n19 Fc2M2 n20
      pd0 afterFC2 n21



xaxis laser f lin 0 500e9 500000
yaxis log abs
trace 2
pause#
```

B.2. APD power supply

This is the power supply for the APDs used in the experiment. APD-T required a 5V power supply, APD-A and -B required 12V. The electronics are based on an idea and first layout by Aiko Samblowski, which was further optimized by Axel Schönbeck, Andreas Weidner and me.

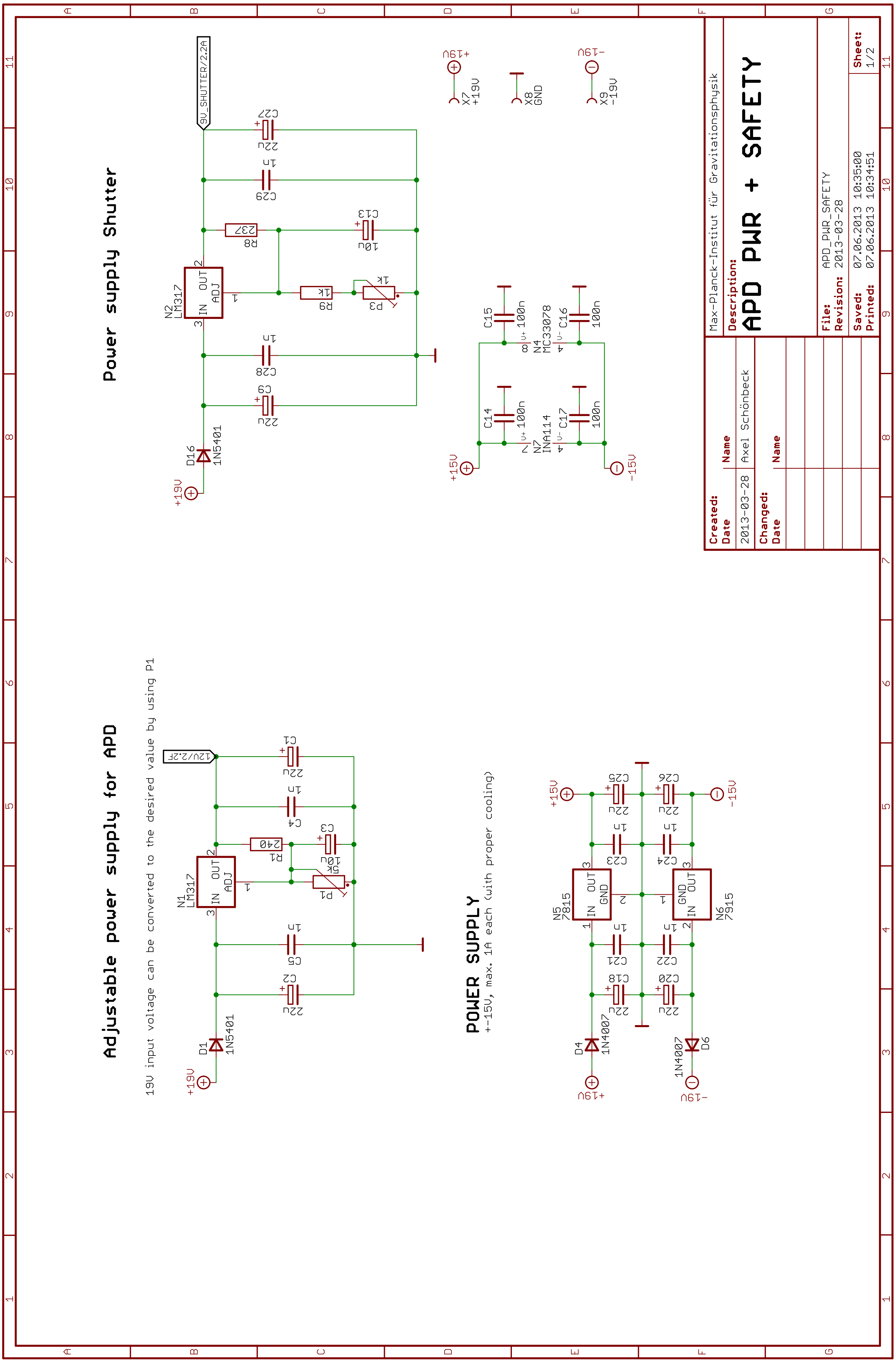
Power supply Shutter
Adjustable power supply for APD
19V input voltage can be converted to the desired value by using P1
POWER SUPPLY
+-15V, max. 1A each (with proper cooling)
N2 LM317
N1 LM317
IN OUT ADJ
9V_SHUTTER/2.2A
12V/2.2A
D16 1N5401
D1 1N5401
+19V
-19V
+15V
-15V
C27 22u
C29 1n
C13 10u
R8 237
R9 1k
P3 1k
C28 1n
C9 22u
C1 22u
C4 1n
C3 10u
R1 240
P1 5k
C5 1n
C2 22u
X7 +19V
X8 GND
X9 -19V
C15 100n
C16 100n
C14 100n
C17 100n
N4 MC33078
N7 INA114
N5 7815
N6 7915
GND
C25 22u
C26 22u
C23 1n
C24 1n
C21 1n
C22 1n
C18 22u
C20 22u
D4 1N4007
D6 1N4007
Max-Planck-Institut für Gravitationsphysik
Description:
APD PWR + SAFETY
File: APD_PWR_SAFETY
Revision: 2013-03-28
Saved: 07.06.2013 10:35:00
Printed: 07.06.2013 10:34:51
Sheet: 1/2
Created: Date 2013-03-28 Name Axel Schönbeck
Changed: Date Name
A B C D E F G
1 2 3 4 5 6 7 8 9 10 11

Figure 1: *Project schematics (sheet 1)*

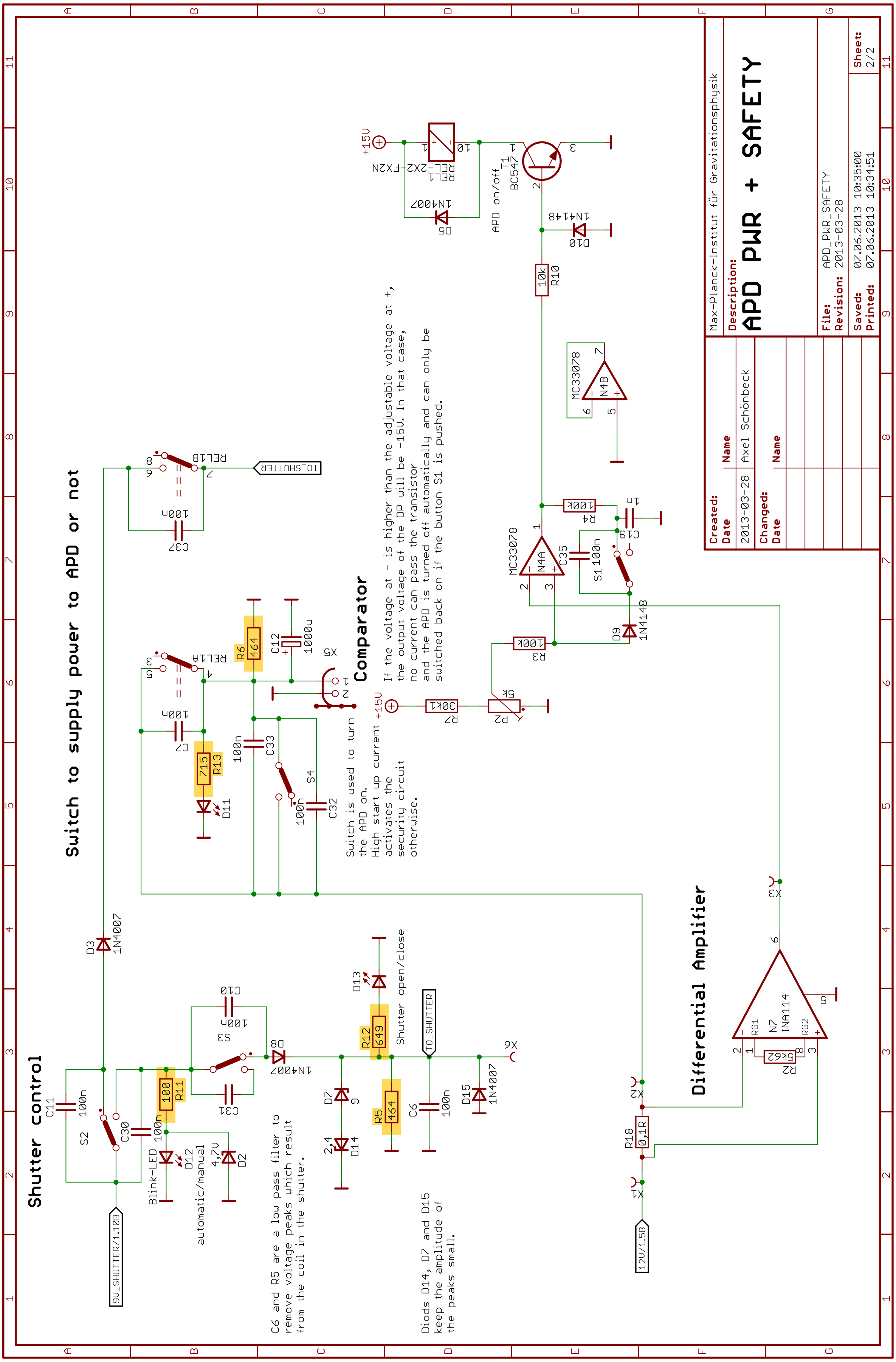
Shutter control
Switch to supply power to APD or not
Comparator
Differential Amplifier
Max-Planck-Institut für Gravitationsphysik
Description:
APD PWR + SAFETY
File: APD_PWR_SAFETY
Revision: 2013-03-28
Saved: 07.06.2013 10:35:00
Printed: 07.06.2013 10:34:51
Sheet: 2/2
Created: Date 2013-03-28 Name Axel Schönbeck
Changed: Date Name
Switch is used to turn the APD on. High start up current activates the security circuit otherwise.
If the voltage at - is higher than the adjustable voltage at +, the output voltage of the OP will be -15V. In that case, no current can pass the transistor and the APD is turned off automatically and can only be switched back on if the button S1 is pushed.
C6 and R5 are a low pass filter to remove voltage peaks which result from the coil in the shutter.
Diods D14, D7 and D15 keep the amplitude of the peaks small.
Shutter open/close
APD on/off
Blink-LED
automatic/manual
9V_SHUTTER/1.10B
12V/1.5B
TO_SHUTTER
REL1 REL-2X2-FX2N
REL1A
REL1B
T1 BC547
N4A MC33078
N4B MC33078
N7 INA114
R2 5k62
R3 100k
R4 100k
R5 464
R6 464
R7 30k1
R10 10k
R11 100
R12 649
R13 715
R18 0,1R
P2 5K
C6 100n
C7 100n
C10 100n
C11 100n
C12 1000u
C19 1n
C30 100n
C31 100n
C32 100n
C33 100n
C35 100n
C37 100n
D2 4,7V
D3 1N4007
D5 1N4007
D6 2,4
D7 6
D8 1N4007
D9 1N4148
D10 1N4148
D11
D12
D13
D14
D15 1N4007
S1
S2
S3
S4
X1
X2
X3
X5
X6
+15V
A B C D E F G
1 2 3 4 5 6 7 8 9 10 11

Figure 2: *Project schematics (sheet 2)*

Parts with more than one population variant are highlighted in *orange*

B.3. Mathematica

Time correlations:
NOPO below threshold

Initialization

```
In[81]:= Clear["Global`*"]
         A[ω_, γ_, e_] = (2 * e * γ) / ((γ - I * ω) ^2 - e^2);
         B[ω_, γ_, e_] = (γ^2 + ω^2 + e^2) / ((γ - I * ω) ^2 - e^2);
         (*AB[ω_,γ_,e_]=FullSimplify[A[-ω,γ,e]*B[ω,γ,e]]*)
         AB[ω_, γ_, e_] = e * γ * (1 / ((γ - e) ^2 + ω^2) + 1 / ((γ + e) ^2 + ω^2))
         (*AA[ω_,γ_,e_]=FullSimplify[A[ω,γ,e]*A[-ω,γ,e]]*)
         AA[ω_, γ_, e_] = e * γ * (1 / ((γ - e) ^2 + ω^2) - 1 / ((γ + e) ^2 + ω^2))
         T[ω_, κ_] = κ / (κ - I * ω)
```

Out[84]= $$e\,\gamma\left(\frac{1}{(-e+\gamma)^2+\omega^2}+\frac{1}{(e+\gamma)^2+\omega^2}\right)$$

Out[85]= $$e\,\gamma\left(\frac{1}{(-e+\gamma)^2+\omega^2}-\frac{1}{(e+\gamma)^2+\omega^2}\right)$$

Out[86]= $$\frac{\kappa}{\kappa-\mathrm{i}\,\omega}$$

```
In[87]:= FourierAB[τ_, γ_, e_] = Integrate[1 / (2 * π) * AB[ω, γ, e] * Exp[-I * τ * ω],
           {ω, -∞, ∞}, Assumptions → {γ, e, τ} ∈ Reals && γ > e && e > 0]
```

Out[87]= $$\frac{1}{2}\,e\,\gamma\left(-\frac{e^{(e-\gamma)\,\mathrm{Abs}[\tau]}}{e-\gamma}+\frac{e^{-(e+\gamma)\,\mathrm{Abs}[\tau]}}{e+\gamma}\right)$$

```
In[88]:= FourierAA[τ_, γ_, e_] = Integrate[1 / (2 * π) * AA[ω, γ, e] * Exp[-I * τ * ω],
           {ω, -∞, ∞}, Assumptions → {γ, e, τ} ∈ Reals && γ > e && e > 0]
```

Out[88]= $$\frac{1}{2}\,e\,\gamma\left(-\frac{e^{(e-\gamma)\,\mathrm{Abs}[\tau]}}{e-\gamma}-\frac{e^{-(e+\gamma)\,\mathrm{Abs}[\tau]}}{e+\gamma}\right)$$

```
In[89]:= AA2[τ_, γ_, e_] = Integrate[1 / (2 * π) * AA[ω, γ, e],
           {ω, -∞, ∞}, Assumptions → {γ, e} ∈ Reals && γ > e && e > 0]
```

Out[89]= $$-\frac{e^2\,\gamma}{e^2-\gamma^2}$$

Validation of the approximation

In[90]:=
```
(*This is the (unfiltered) full correlation function,
without any approximation, compared to the approximation*)
Plot[{FourierAB[t, 1, .2]^2 + FourierAA[t, 1, .2]^2, FourierAB[t, 1, .2]^2},
 {t, -5, 5}, PlotRange → Full]
```

Out[90]=

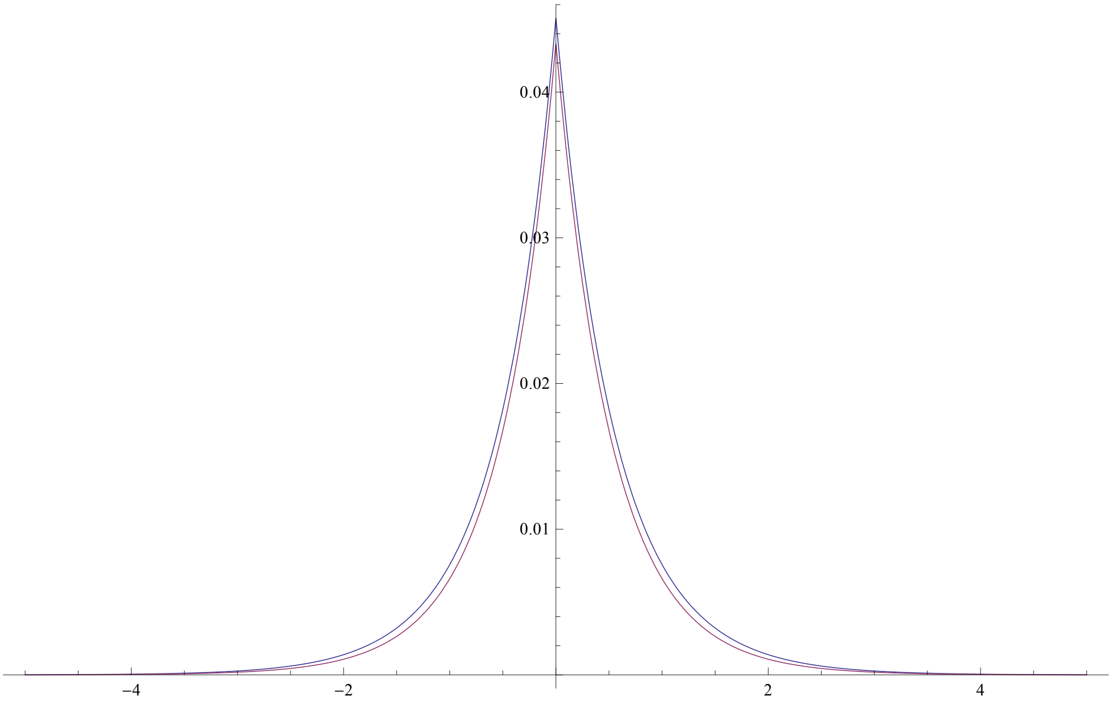

Filtering the trigger mode

In[91]:=
```
(*This is the trigger filtered correlation function without low-
 gain approximation*)
Fil1[τ_, γ_, e_, κ_] = Integrate[1 / (2 * π) * T[ω, κ] * AB[ω, γ, e] * Exp[-I * τ * ω],
     {ω, -∞, ∞}, Assumptions → {γ, e, κ, τ} ∈ Reals && γ > e && e > 0 && κ > 0] ^2;
```

In[92]:=
```
(*First correction term, constant offset*)
Fil2[τ_, γ_, e_, κ_] =
   Integrate[1 / (2 * π) ^2 * T[w, κ] * T[-w, κ] * AA[w, γ, e] * AA[ω, γ, e], {ω, -∞, ∞},
    {w, -∞, ∞}, Assumptions → {γ, e, κ, τ} ∈ Reals && γ > e && e > 0 && κ > 0];
```

In[93]:=
```
(*Second correction term, very small for low gain*)
Fil3[τ_, γ_, e_, κ_] = Integrate[1 / (2 * π) * T[ω, κ] * AA[ω, γ, e] * Exp[-I * τ * ω],
     {ω, -∞, ∞}, Assumptions → {γ, e, κ, τ} ∈ Reals && γ > e && e > 0 && κ > 0] ^2;
```

In[94]:=
```
(*Plot of filtering effect with different filter decay rates,
low-gain approximation*)
Plot[{Fil1[t, 1, .2, .5], Fil1[t, 1, .2, 1], Fil1[t, 1, .2, 2], FourierAB[t, 1, .2] ^2},
 {t, -5, 5}, PlotRange → Full]
```

Out[94]=

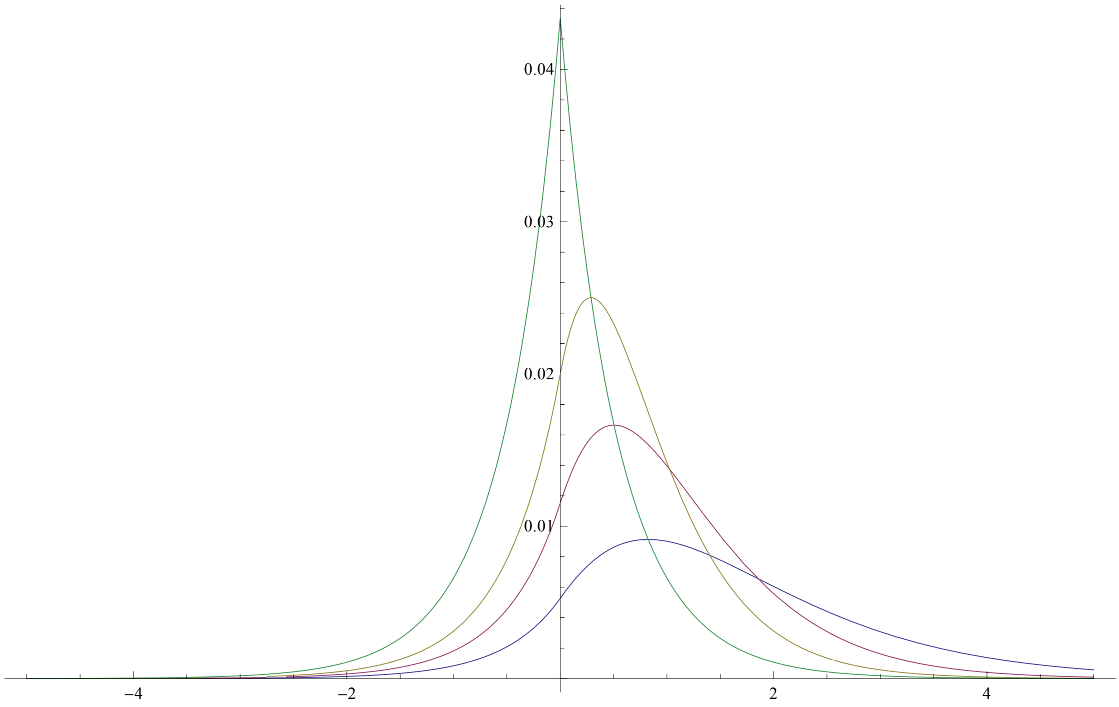

Filtering the trigger mode, w/ and w/o approximation

In[95]:=
```
(*Full filtered correlation function*)
Fil[τ_, γ_, e_, κ_] = Fil1[t, γ, e, κ] + Fil2[t, γ, e, κ] + Fil3[t, γ, e, κ];
```

In[96]:=
```
(*Plot of filtered correlation function compared to filtered approximation*)
Plot[{Fil[t, 1, .2, 1.4] - Fil2[t, 1, .2, 1.4], Fil1[t, 1, .2, 1.4]},
 {t, -5, 5}, PlotRange → Full]
```

Out[96]=

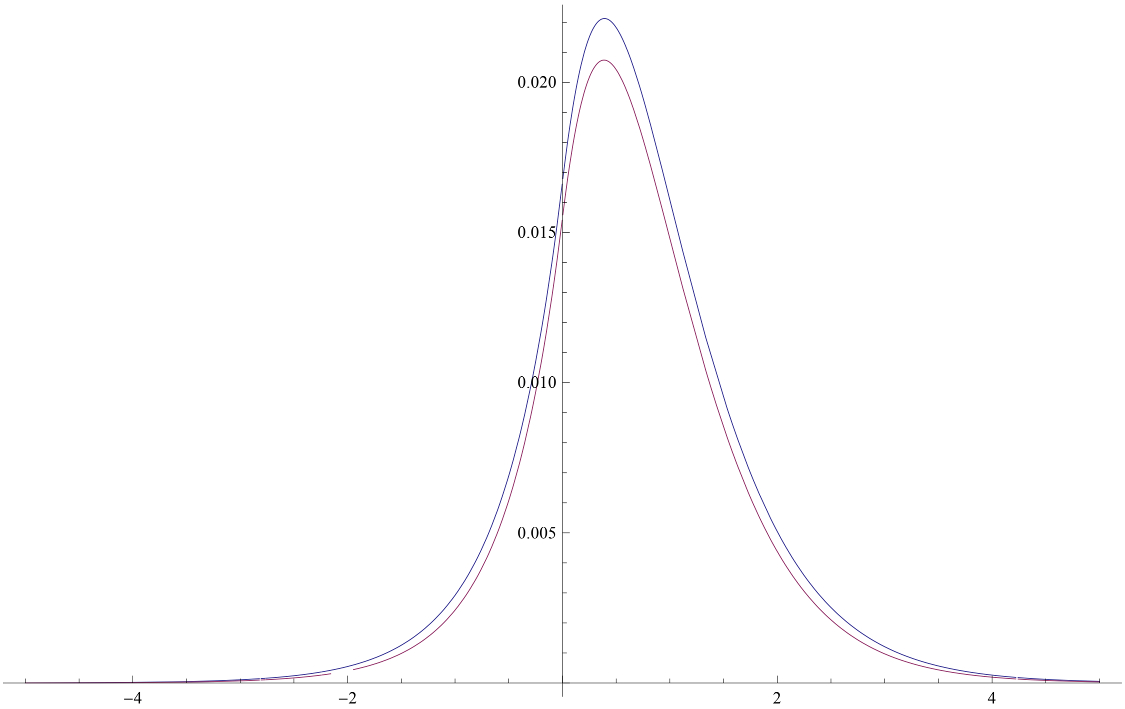

B.4. python programs

B.4.1. Data acquisition with an oscilloscope-PC interface

This program interfaces an oscilloscope to the LAN network via the VISA protocol as it is used in the single photon up-conversion experiment. The commands are taken from a programmer's guide (*InfiniiVision 7000B Series Oscilloscopes Programmer's Guide*, freely accessible on the manufacturer's homepage).

```
# -*- coding: utf-8 -*-
"""
Created on Thu May 30 21:13:12 2013

@author: Christoph Baune
"""


import visa
import time
# Get instrument VISAname
visaInstrList = visa.get_instruments_list()
print(visaInstrList)
#Scope's VISA address
myScope="TCPIP0::10.117.12.2::INSTR"
print(myScope)
scope = visa.instrument(myScope)
# Configuration & Initialisation-------------------------------
#Format specifier: "byte"(binary, 8bit)|"word"(binary, 16bit)|ascii
scope.write(":waveform:format byte")
#Points mode: "normal"|"maximum"|"raw"
scope.write(":waveform:points:mode maximum")
#waveform:type={norm|peak|aver:hres}
scope.write(":waveform:type norm")

#:ACQuire:MODE <mode> ::= {RTIMe | ETIMe | SEGMented}
scope.write(":acquire:mode rtime")

#trigger mode: "norm" (normal)|"auto"
scope.write(":trigger:sweep norm")
#HFReject: 50kHz low-pass filter in trigger path
scope.write(":trigger:hfreject off")
#noise reject: trigger circuit less sensitive to noise
#but may require greater amplitude to trigger
scope.write(":trigger:nreject off")
#holdoff: 60ns to 10 s pause between trigger events
scope.write(":trigger:holdoff 60e-9")
```

```
#trigger source
scope.write(":trigger:source 1")
#trigger level
scope.write(":trigger:level 1")
#:TIMebase:MODE <value> = {MAIN | WINDow | XY | ROLL}
scope.write(":timebase:mode main")
#10Mhz reference clock on rear panel connected? {on|off}
scope.write(":timebase:refclock off")
#:TIMebase:REFerence <reference> ::= {LEFT | CENTer | RIGHt}
scope.write(":timebase:reference center")
#:TIMebase:VERNier <vernier value>:= {{1 | ON} | {0 | OFF}
scope.write(":timebase:vernier off")
#time/division (in seconds)
scope.write(":timebase:main:scale 200e-6")
#delay of trigger event to center of screen (in seconds)
scope.write(":timebase:main:delay 0")
#for position and scale for ZOOM mode
scope.write(":timebase:main:position 0")
#scope.write(":timebase:scale 1")
scope.write(":channel2:probe:skew 50e-9")
scope.write(":channel3:probe:skew 50e-9")
#timeout = time the program waits for a trigger signal for example
scope.timeout=2
channels=3
for i in range(channels):
    print "channel "+format(i+1)+" enabled"
    scope.write(":channel%i:display on"%(i+1))
    scope.write(":channel%i:coupling DC"%(i+1))
    scope.write(":channel%i:units volt"%(i+1))
    scope.write(":channel%i:scale 1"%(i+1))
    #scope.write(":channel%i:offset 1.5"%(i+1))
    scope.write(":channel1:offset .0")
    scope.write(":channel2:offset .0")
    scope.write(":channel3:offset .0")
#number of points{100 | 250 | 500 | 1000 | 2000 | 5000 |
    #10000 | 20000| 50000 | 100000 | 200000 | 500000 |
    #1000000 | 2000000| 4000000 | 8000000 | <points mode>}
points=2000000
scope.write(":WAVeform:POINts %i"%points)
scope.write(":SINGle")
time.sleep(1)
points=int(scope.ask(":waveform:points?"))
print points
lastmeasurement=0
```

```
numberOfShots=2000
binfile="info"
scope.write(":trigger:sweep auto")
scope.write(":SINGle")
scope.write(":trigger:sweep norm")
nPoints=scope.ask(":WAVeform:POINts?")
dt=scope.ask(":WAVeform:XINCrement?")
fullTime=scope.ask("timebase:range?")
#
infofile=open("%s.info"%binfile,'w')
infofile.write("Number of saved channels: %i"%channels+
    "\nNumber of datapoints: "+nPoints+"\ntime increment: "+
dt+"\nFull time range: "+fullTime)
infofile.close()
#
print "\nMeasurement started:"
for j in range(lastmeasurement,numberOfShots+lastmeasurement):
    print "measurement %i"%(j+1)+"/%i"%(numberOfShots+lastmeasurement)
    scope.write(":single")
    for i in range(channels):
        nPoints=scope.ask(":WAVeform:POINts?")
        while nPoints<points:
            #scope necesssarily has to stop to be able to
            #transfer ALL points (<1000 otherwise!):
            time.sleep(.05)
            nPoints=scope.ask(":WAVeform:POINts?")
        time.sleep(.05)
        scope.write(":waveform:source channel%i"%(i+1))
        scope.write(":WAVeform:DATA?")
        raw=scope.read()
        fil=open("ch%i_%i.bin" %(i+1,j+1),'w')
        fil.write(raw)
        fil.close()
```

B.4.2. Data conversion to hdf5

This python program converts stored binary data to hdf5 files, which can be efficiently processed.

```
# -*- coding: utf-8 -*-
"""
Created on Sat Nov 09 09:47:29 2013

@author: Axel Schoenbeck
```

```
"""

import numpy as np
import h5py
def saveToFile3(binfile1,binfile2,binfile3,outfile,
                NumberFiles,PackageSize):

    Datafile=h5py.File("%s.h5"%outfile,"w")
    ch1=np.zeros([1,1],dtype=np.int8)
    ch2=np.zeros([1,1],dtype=np.int8)
    ch3=np.zeros([1,1],dtype=np.int8)
    TimeLength=0

    for m in range (1,NumberFiles+1):
        print "File " + format(m) + " of " + format(NumberFiles)
        file = open("%s_%s.bin"%(binfile1,format(m)), ’rb’)
        Header1 = file.read(10)
        Counts1=int(Header1[2:10])
        file = open("%s_%s.bin"%(binfile2,format(m)), ’rb’)
        Header2 = file.read(10)
        Counts2=int(Header2[2:10])
        file = open("%s_%s.bin"%(binfile3,format(m)), ’rb’)
        Header3 = file.read(10)
        Counts3=int(Header3[2:10])
        TimeLength+=Counts1
        Imp1 = np.fromfile("%s_%s.bin"%(binfile1,format(m)),
                           dtype=np.uint8, count=-1)
        Imp2 = np.fromfile("%s_%s.bin"%(binfile2,format(m)),
                           dtype=np.uint8, count=-1)
        Imp3 = np.fromfile("%s_%s.bin"%(binfile3,format(m)),
                           dtype=np.uint8, count=-1)
        ch1=np.append(ch1,Imp1[10:len(Imp1)])
        ch2=np.append(ch2,Imp2[10:len(Imp2)])
        ch3=np.append(ch3,Imp3[10:len(Imp3)])
        if Counts1!=Counts2 or Counts1!=Counts3 or Counts2!=Counts3:
            print "Length of files is not equal!"
        if len(ch1)!=len(ch2) or len(ch1)!=len(ch2) \
                or len(ch2)!=len(ch3):
            print "Length of files is not equal!"

        if m%PackageSize==0:
            ch1=np.delete(ch1,0)
            ch2=np.delete(ch2,0)
            ch3=np.delete(ch3,0)
            Time=np.arange(1,TimeLength+1,dtype=np.int)
            Data=np.zeros([TimeLength,4],dtype=np.int)
            Data[:,0]=Time
            Data[:,1]=ch1
            Data[:,2]=ch2
            Data[:,3]=ch3
            writeData=Datafile.create_dataset("Package_%s"%\
                format(m/PackageSize),(TimeLength,4),dtype=np.int)
            writeData[...]=Data
            TimeLength=0
            ch1=np.zeros([1,1])
            ch2=np.zeros([1,1])
            ch3=np.zeros([1,1])

    NumberPackages=NumberFiles/PackageSize
    writeData=Datafile.create_dataset("NumberPackages",(1,1),dtype =int)
    writeData[...]=NumberPackages
    Datafile.close()
    file.close()

NumberFiles=2000 #Total number of datafiles
PackageSize=5 #
saveToFile3("ch1","ch2","ch3","Raw_Data",NumberFiles,PackageSize)
```

B.4.3. Data size reduction

This program reduces the amount of data significantly by scanning all data stream, finding events and time-taging them.

```
# -*- coding: utf-8 -*-
"""
Created on Thu Jan 23 16:32:25 2014

@author: Christoph Baune, Axel Schoenbeck
"""

import numpy as np
import h5py
def shrink_three(RawData,trace1,trace2,trace3):
    DataFile=h5py.File("%s.h5"%RawData,"r")
    SaveFile=h5py.File("Shrinked_Data.h5","w")
    #set the threshold of accepting an event as event
    UpperThreshold=150
    LowerThreshold=140
```

```
LoadNumberPackages=DataFile["/NumberPackages"]
NumberPackages=LoadNumberPackages[...]

CounterPeaks=0
for m in range(1,NumberPackages+1):
    ShrinkedData=[]
    Dataset=DataFile["/Package_%s"%format(m)]
    Data=Dataset[...]
    Lastpoint=len(Data[:,0])
    Peakend1=0
    Peakend2=0
    Peakend3=0
    for k in range(Lastpoint):
        Peakfound1=False
        Peakfound2=False
        Peakfound3=False
        if (Data[k,trace1]>UpperThreshold and k>Peakend1):
            Peakfound1=True
            Peakend1=k+1
            if Peakend1==Lastpoint:
                Peakend1=k
            while Data[Peakend1,trace1]>LowerThreshold:
                Data[Peakend1,trace1]=0
                Peakend1+=1
                if Peakend1==Lastpoint:
                    break
        if (Data[k,trace2]>UpperThreshold and k>Peakend2):
            Peakfound2=True
            Peakend2=k+1
            if Peakend2==Lastpoint:
                    Peakend2=k
            while Data[Peakend2,trace2]>LowerThreshold:
                Data[Peakend2,trace2]=0
                Peakend2+=1
                if Peakend2==Lastpoint:
                    break
        if (Data[k,trace3]>UpperThreshold and k>Peakend3):
            Peakfound3=True
            Peakend3=k+1
            if Peakend3==Lastpoint:
                Peakend3=k
            while Data[Peakend3,trace3]>LowerThreshold:
                Data[Peakend3,trace3]=0
```

```
                    Peakend3+=1
                    if Peakend3==Lastpoint:
                        break
            if (Peakfound1==True or Peakfound2==True\
                    or Peakfound3==True):
                ShrinkedData.append(Data[k,:])
                CounterPeaks=CounterPeaks+1

            c=Lastpoint/100.
            if (k/c)%5==0:
                print "Progress: "+format(k/c)+"% of package "\
                    +format(m)+" done."
            elif k==Lastpoint-1:
                print"Progress: 100% of package " + format(m) + " done."
        writeData=SaveFile.create_dataset("Shrinked_%s"%format(m),
            (len(ShrinkedData),4),dtype = int)
        writeData[...]=ShrinkedData
    writeData=SaveFile.create_dataset("NumberPackages",(1,1),dtype =int)
    writeData[...]=NumberPackages
    print "Total number of peaks: "+format(CounterPeaks)
    DataFile.close()
    SaveFile.close()
RawData="Raw_Data"
shrink_three(RawData,1,2,3)
```

B.4.4. Quantum non-Gaussianity verification

This program calculates the quantum non-Gaussianity witness. The standard deviation of the witness is also calculated as follows: The witness of QNG is $W = a\,p_0 + p_1$ and a function of the rates R_0, R_{1A}, R_{1B} and R_2, cf. Section 5.4. (In the following $R_{1A} = R_A$, $R_{1B} = R_B$ for simplicity.) The covariance of W is

$$\begin{aligned}\langle\Delta^2 W\rangle = {} & \left(\frac{\partial W}{\partial R_0}\right)^2 \langle\Delta^2 R_0\rangle + \left(\frac{\partial W}{\partial R_A}\right)^2 \langle\Delta^2 R_A\rangle + \left(\frac{\partial W}{\partial R_B}\right)^2 \langle\Delta^2 R_B\rangle + \left(\frac{\partial W}{\partial R_2}\right)^2 \langle\Delta^2 R_2\rangle \\ & + 2\frac{\partial W}{\partial R_0}\frac{\partial W}{\partial R_A}\langle\Delta R_0 \Delta R_A\rangle + 2\frac{\partial W}{\partial R_0}\frac{\partial W}{\partial R_B}\langle\Delta R_0 \Delta R_B\rangle + 2\frac{\partial W}{\partial R_0}\frac{\partial W}{\partial R_2}\langle\Delta R_0 \Delta R_2\rangle \\ & + 2\frac{\partial W}{\partial R_A}\frac{\partial W}{\partial R_B}\langle\Delta R_A \Delta R_B\rangle + 2\frac{\partial W}{\partial R_A}\frac{\partial W}{\partial R_2}\langle\Delta R_A \Delta R_2\rangle + 2\frac{\partial W}{\partial R_B}\frac{\partial W}{\partial R_2}\langle\Delta R_B \Delta R_2\rangle\,.\end{aligned} \tag{B.1}$$

For all covariances the Cauchy-Schwarz inequality holds:

$$|\langle\Delta R_i \Delta R_j\rangle| \leq \sqrt{\langle\Delta^2 R_i\rangle\langle\Delta^2 R_j\rangle} \tag{B.2}$$

I assume Poissonian statistics of all count rates, meaning $\Delta^2 R_i = R_i$. The error of the witness is then bounded by

$$\begin{aligned}\langle\Delta^2 W\rangle = &\left(\frac{\partial W}{\partial R_0}\right)^2 \langle\Delta^2 R_0\rangle + \left(\frac{\partial W}{\partial R_A}\right)^2 \langle\Delta^2 R_A\rangle + \left(\frac{\partial W}{\partial R_B}\right)^2 \langle\Delta^2 R_B\rangle + \left(\frac{\partial W}{\partial R_2}\right)^2 \langle\Delta^2 R_2\rangle \\ &+ 2\left|\frac{\partial W}{\partial R_0}\frac{\partial W}{\partial R_A}\right|\sqrt{R_0 R_A} + 2\left|\frac{\partial W}{\partial R_0}\frac{\partial W}{\partial R_B}\right|\sqrt{R_0 R_B} + 2\left|\frac{\partial W}{\partial R_0}\frac{\partial W}{\partial R_2}\right|\sqrt{R_0 R_2} \\ &+ 2\left|\frac{\partial W}{\partial R_A}\frac{\partial W}{\partial R_B}\right|\sqrt{R_A R_B} + 2\left|\frac{\partial W}{\partial R_A}\frac{\partial W}{\partial R_2}\right|\sqrt{R_A R_2} + 2\left|\frac{\partial W}{\partial R_B}\frac{\partial W}{\partial R_2}\right|\sqrt{R_B R_2}\,.\end{aligned} \tag{B.3}$$

What is left are the several derivations, here given explicitly:

$$\begin{aligned}\frac{\partial W}{\partial R_0} &= a\frac{R_A + R_B + R_2}{R_0^2} - \frac{R_A + R_B}{R_0^2} + \frac{T^2 + (1-T)^2}{2T(1-T)}\frac{R_2}{R_0^2} \\ \frac{\partial W}{\partial R_A} &= \frac{1-a}{R_0} - \frac{T^2 + (1-T)^2}{2T(1-T)}\frac{R_2}{R_0}\frac{R_B}{R_A + R_B} \\ \frac{\partial W}{\partial R_B} &= \frac{1-a}{R_0} - \frac{T^2 + (1-T)^2}{2T(1-T)}\frac{R_2}{R_0}\frac{R_A}{R_A + R_B} \\ \frac{\partial W}{\partial R_2} &= -\frac{1}{R_0} - \frac{T^2 + (1-T)^2}{2T(1-T)}\frac{1}{R_0}\end{aligned} \tag{B.4}$$

Finally, the standard deviation is of course given by $\Delta W = \sqrt{\langle\Delta^2 W\rangle}$.

```
# -*- coding: utf-8 -*-
"""
Created on Tue Mar 01 18:12:37 2016

@author: chbaun
"""
import numpy as np
x=["low","medium","high"]
for s in x:
    data=np.loadtxt("Rates_%s_long.dat"%s)
    dt=data[:,0] #coincidence window
    R0=data[:,1] #number of triggers
    RA=data[:,2] #number of clicks at APD-A
    RB=data[:,3] #number of clicks at APD-B
    R2=data[:,4] #number or three-fold coincidences
    p0=data[:,5] #vacuum probability
    p1=data[:,6] #single photon probability
    T=data[:,8]  #beam splitter ratio

    #theoretically possible
```

```
#p1=[0.2] #detection efficiency
#p0=[0.8]

from scipy.optimize import fsolve
arr=np.arange(0,1,.01)
W=[]
for i in range(len(p0)):
    wmax=-10000
    for a in arr:
        #find optimal r for given a, [Jezek2011]
        func=lambda r: (1+np.exp(2*r))*a-np.exp(2*r)*(3-np.exp(2*r))
        guess=0.3
        r=fsolve(func,guess)[0]

        #calculate p0 and p1 from r to give a Gaussian state,
        #[Jezek2011]
        d=np.sqrt((np.exp(4*r)-1)/4.)
        P0=np.exp(-d**2*(1-np.tanh(r)))/np.cosh(r)
        P1=d**2*np.exp(-d**2*(1-np.tanh(r)))/np.cosh(r)**3

        #maximum W achievable with Gaussian states
        WG=a*P0+P1

        #Witness of QNG
        w=(a*p0[i]+p1[i]-WG)

        #error of Witness
        dp0dR0=(RA[i]+RB[i]+R2[i])/R0[i]**2
        dp0dRA=-1/R0[i]
        dp0dRB=-1/R0[i]
        dp0dR2=-1/R0[i]
        dp1dR0=-(RA[i]+RB[i])/R0[i]**2+\
            (T[i]**2+(1-T[i])**2)/(2*T[i]*(1-T[i]))*\
            R2[i]/R0[i]**2
        dp1dRA=1/R0[i]-\
            (T[i]**2+(1-T[i])**2)/(2*T[i]*(1-T[i]))*\
            R2[i]/R0[i]*RB[i]/(RA[i]+RB[i])**2
        dp1dRB=1/R0[i]-\
            (T[i]**2+(1-T[i])**2)/(2*T[i]*(1-T[i]))*\
            R2[i]/R0[i]*RA[i]/(RA[i]+RB[i])**2
        dp1dR2=-(T[i]**2+(1-T[i])**2)/(2*T[i]*(1-T[i]))/R0[i]
        dWdR0=a*dp0dR0+dp1dR0
        dWdRA=a*dp0dRA+dp1dRA
        dWdRB=a*dp0dRB+dp1dRB
```

```
            dWdR2=a*dp0dR2+dp1dR2
            dW=np.sqrt(dWdR0**2*R0[i]+dWdRA**2*RA[i]+\
                dWdRB**2*RB[i]+dWdR2**2*R2[i]+\
                2*abs(dWdR0*dWdRA)*np.sqrt(R0[i]*RA[i])+\
                2*abs(dWdR0*dWdRB)*np.sqrt(R0[i]*RB[i])+\
                2*abs(dWdR0*dWdR2)*np.sqrt(R0[i]*R2[i])+\
                2*abs(dWdRA*dWdRB)*np.sqrt(RA[i]*RB[i])+\
                2*abs(dWdRA*dWdR2)*np.sqrt(RA[i]*R2[i])+\
                2*abs(dWdRB*dWdR2)*np.sqrt(RB[i]*R2[i]))

            if w/dW>wmax:
                wmax=w/dW
                dw=dW
        W.append([dt[i],wmax*dw,dw,wmax])
    np.savetxt("W_%s.dat"%s,W)
```

B.4.5. Quantum state estimation

This program is used to reconstruct to most likely density operator $\tilde{\rho}$ from a set of quadrature data. It also requires a dataset with quadrature values of a vacuum state a a reference.

```
# -*- coding: utf-8 -*-
"""
Created on Mon Apr 28 09:51:06 2014

@author: Christoph
"""
import numpy as np
from numpy import trace as tr
I=np.complex(0,1)
np.set_printoptions(precision=5, suppress=True)
def factorial(n):
    sum = 1.0
    for m in range(1, int(n)+1):
        sum = float(m)*sum
    return sum

#Hermite polynomials
def H(n,x):
    if n==0: return 1
    if n==1: return 2*x
    else:
        return 2*x*H(n-1,x)-2*(n-1)*H(n-2,x)
```

```
def reconstruct(vacuumfile,datafile,iterations):
    data=np.loadtxt(datafile)
    dataVac=np.loadtxt(vacuumfile)
    numberOfBins=2000 #set to scope’s y-resolution

    #carefully determine vacuum-variance and offset by
    #evaluation of vacuum noise, v=standard deviation
    v=np.std(dataVac)
    offset=np.mean(dataVac)
    print "Standard deviation of vacuum: "+format(v)
    print np.std(data)
    print "Mean value of vacuum: "+format(offset)
    print np.mean(data)

    #truncation of Hilbert space: maximum number of photons
    maxN=7

    #initialisation of density matrix
    rho=np.eye(maxN+1)
    rho=rho*0.0001
    rho[0,0]=1
    print rho

    #create POVM
    POVM=[]
    for i in range(0,numberOfBins):
        x=(i-numberOfBins/2.)/numberOfBins*20
        #the last factor is the full histogram range!
        #range=(-10,10) => factor=20
        subPOVM=[]
        for n in range(maxN+1):
            subPOVM.append(1./np.sqrt(np.pi)/(2**n)/factorial(n)*\
                H(n,x/v/np.sqrt(2))**2*np.exp(-(x/v/np.sqrt(2))**2))
        tmp=np.diag(subPOVM)
        POVM.append(tmp)

    #build the histograms
    N=np.histogram(data,bins=numberOfBins,range=(-10,10))[0]
    np.savetxt("NFock.dat",(N))
    M=np.histogram(dataVac,bins=numberOfBins,range=(-10,10))[0]
    np.savetxt("NVac.dat",(M))

    for i in range(iterations):
        p=[]
        R=np.zeros((maxN+1,maxN+1))
        for m in range(numberOfBins):
            #calc probability of outcome m
            pm=tr(np.dot(rho,POVM[m]))
            if (pm<1e-12):#numerical stability abort
                pm=1e-12
            p.append(pm)
            R=R+POVM[m]*N[m]/pm

        #iteration step
        tmp=np.dot(R,np.dot(rho,R))

        #re-normalization
        rho=tmp/tr(tmp)

        #likelihood
        if i%9==1:
            L=0
            for m in range(numberOfBins):
                L+=np.log10(p[m])*N[m]
            print L
    return rho
```

B.4.6. Wigner function reconstruction

This program builds a Wigner function from a given density operator in Fock basis $\hat{\rho} = \sum_{mn} \rho_{mn} |m\rangle\langle n|$.

```
# -*- coding: utf-8 -*-
"""
Created on Mon Apr 28 15:47:14 2014

@author: Christoph

This program translates a density matrix in Fock basis
to Wingerfunction values W(q,p)
"""
import numpy as np
I=np.complex(0,1)
def H(n,x):#Hermite polynomials
    if n==0: return 1
    if n==1: return 2*x
    else:
        return 2*x*H(n-1,x)-2*(n-1)*H(n-2,x)
def factorial(n):
    sum = 1.0
    for m in range(1, int(n)+1):
        sum = float(m)*sum
    return sum
def createWignerfile(rho,datfile,xySteps=100):
    def Wigner(q,p,rho):
        def L(n,x):
            if n==0: return 1.
            if n==1: return 1.-x
            else:
                return 1./n*((2*n-1.-x)*L(n-1.,x)-(n-1.)*L(n-2.,x))
        maxN=np.size(rho[0])-1
        def Wmn(q,p,m,n):
            pre=(-1.)**m/np.pi
            alpha=(q+I*p)/np.sqrt(2)
            if m>n:
                val=pre*np.sqrt(1.*factorial(n)/factorial(m))*\
                    np.exp(-2*(np.abs(alpha))**2)*\
                    (-2*np.conj(alpha))**(m-n)*\
                    (L(n,4*(np.abs(alpha))**2))**(m-n)
            if m<n:
                val=pre*np.sqrt(1.*factorial(m)/factorial(n))*\
                    np.exp(-2*(np.abs(alpha))**2)*\
                    (2*(alpha))**(n-m)*\
                    (L(m,4*(np.abs(alpha))**2))**(n-m)
            else:
                val=pre*np.exp(-2*np.abs((alpha))**2)*\
                    L(n,4*np.abs(alpha)**2)
            return val
        W=0
        for m in range(maxN+1):
            for n in range(maxN+1):
                W+=rho[m,n]*Wmn(q,p,m,n)
        return W
    Q=xySteps
    outfile=open(datfile,'w')
    for q in range(Q):
        x=(-Q/2.+q)/(Q/10.)
        for p in range(Q):
            y=(-Q/2.+p)/(Q/10.)
            outfile.write(format(x)+" "+format(y)+" "+\
                format(np.real(Wigner(x,y,rho)))+"\n")
        outfile.write("\n")
    outfile.close()
```

B.5. gnuplot programs

B.5.1. Determine optical loss in squeezing measurements

This simple but useful gnuplot program calculates the overall detection loss for a pair of squeezed and anti-squeezed values and also returns the initial squeezing, i.e. the squeezing beore experiencing optical loss.

```
reset
dbtolin(x)=10**(x/10.)

Sqz=-5.5 #amount of squeezing in dB
ASqz=17.9 #amount of anti-squeezing in dB

eta=(-1+dbtolin(Sqz)+dbtolin(ASqz)-\
    dbtolin(Sqz)*dbtolin(ASqz))/(-2+dbtolin(Sqz)+dbtolin(ASqz))
ISqz=10*log10((dbtolin(ASqz)+eta-1)/eta)

print sprintf("Detection loss = %.2f %",(1-eta)*100)
print sprintf("Initial squeezing = %.2f dB",ISqz)
```

B.5.2. Correlations in two-mode squeezing

This is the program to produce Figure 4.2.

```
reset

set term postscript eps enh color "Helvetica" 18 lw 2

set format x "%.1f{/Symbol p}"
set out "Duan.eps"
#set key out below
set grid
set samples 1000

set xlabel "Phase"
set ylabel "Noise variance [dB]"
lintodb(x)=10.*log10(x)
dbtolin(x)=10**(x/10.)

Vq(r,s,phi)=0.25*((1+cos(phi))**2*exp(-2*r)\
+(1-cos(phi))**2*exp(2*s)+sin(phi)**2*(exp(2*r)+exp(-2*s)))

Vp(r,s,phi)=0.25*(exp(2*r)*(1-cos(phi))**2\
+exp(-2*s)*(1+cos(phi))**2+sin(phi)**2*(exp(-2*r)+exp(2*s)))

r=2.1
s=0
eta=.73 #detection efficiency

set style arrow 1 head filled size screen 0.015,30,45 lw 1
set arrow from 0,9 to 0,0.5 as 1 lw .5   lc rgb "blue"
set label "{/Symbol D}^2[~{/Helvetica-Italic q}{.05\303}_c\
+~{/Helvetica-Italic q}{.05\303}_d]" at -0.35,-7  tc rgb "red"
set label "{/Symbol D}^2[~{/Helvetica-Italic p}{.05\303}_c\
{/Symbol \055}~{/Helvetica-Italic p}{.05\303}_d]" \
at -0.35,+12 tc rgb "blue"
set label "{/Symbol D}^2[~{/Helvetica-Italic q}{.05\303}_c\
{/Symbol \055}~{/Helvetica-Italic q}{.05\303}_d]" \
at -1.35,-2   tc rgb "red"
set label "{/Symbol D}^2[~{/Helvetica-Italic p}{.05\303}_c\
+~{/Helvetica-Italic p}{.05\303}_d]" at -1.35,+19   tc rgb "blue"

set yrange[-10:24]

p [-2:2]  lintodb(eta*(Vq(r,s,x*pi))+(1-eta)) \
t "~{/Helvetica-Italic q}{.05\303}_c locked" lt 1 lw 2 lc rgb "red",\
lintodb((eta*(Vp(r,s,x*pi)))+(1-eta)) \
t "~{/Helvetica-Italic p}{.05\303}_c locked" lt 1 lw 2 lc rgb "blue",\
0 lt 1 lw 2 lc rgb "black" t""#\
lintodb(((Vq(r,s,x*pi))*eta+(Vp(r,s,x*pi))*eta\
+2*(1-eta))/2.) t "Duan"  lt 1 lc rgb "green"
```

C. Contributions

For all experiments presented in this thesis I acknowledge support from my supervisor Roman Schnabel in terms of continuous discussions about progresses and problems. Jaromír Fiurášek from Palacký University Olomouc, Czech Republic, provided valuable theoretical support at all times.

The experiment on the frequency up-conversion of squeezed vacuum from 1550 to 532 nm was initiated during the doctoral studies of Aiko Samblowski and Christina Vollmer, née Laukötter, as well as my master thesis. First results can be found in Christina's doctoral thesis and the related publication in Physical Review Letters **112**. The nonlinear cavities for the improved setup were designed and built by Christina Vollmer and Petrissa Zell, with support from Vitus Händchen and Tobias Gehring. The optical paths were finally build by me, Axel Schönbeck and Jan Gniesmer. The bachelor thesis of Hendrik Weißbrich was also closely related to this experiment.

First results on the up-conversion of part on an entangled state can be found in the master thesis of Petrissa Zell and the doctoral thesis of Christina Vollmer. During the realization of the improved setup, Jan Gniesmer provided help in the laboratory and electronic workshop. I am grateful to Vitus Händchen and Daniela Abdelkhalek for discussions on entanglement resulting in the calculations presented in Section 4.1. I acknowledge Sacha Kocsis' support during preparation of the related publication.

The experiment on single photon up-conversion was mainly performed during the master thesis of Axel Schönbeck. I emphasize his contribution in many aspects of this experiment, especially the data processing and analysis as well as extensive support in the laboratory. Theoretical support on the quantum non-Gaussianity criterion and other aspects were provided by Jaromír Fiurášek.

During the experiment on Fock state tomography I acknowledge specific theoretical support from Jaromír Fiurášek, who taught me the fundamentals on maximum likelihood estimation of quantum states during my two-week research stay in Olomouc in April 2014.

D. Material

All plots in this thesis were generated using gnuplot 4.6. Data analysis was performed using python 2.7 and gnuplot 4.6. All schematics of experimental setups were built with Inkscape 0.91 using the Component Library by Alexander Franzen, which was recently updated by Jan Gniesmer. Wolfram Mathematica 9 was used for various calculations. Simulations of optical cavities were performed using Finesse2 [Fre14]. Mechanical layouts were built with Autodesk Inventor 2014-2016. Electronic circuits were designed with Eagle 5-6. This document was generated using the MiKTeX2.9 distribution and the TeXnicCenter environment.

E. Fundings

During my doctoral studies I acknowledge financial support from the International Max-Planck Research School on Gravitational Wave Astronomy (IMPRS-GW).

This work was supported by the Deutsche Forschungsgemeinschaft (DFG), Project No. SCHN 757/4-1 and by the Centre for Quantum Engineering and Space-Time Research (QUEST). My two-week research stay with Jaromír Fiurášek in Olomouc, Czech Republic, in April 2014 was funded by the ESF “International Centre for Information and Uncertainty”, reg.no. CZ.1.07/2.3.00/20.0060.

F. Acknowledgments

I thank my supervisor Professor Roman Schnabel for continuous support during my doctoral studies in his working group. Within a pleasant working atmosphere he provided me all opportunities to do fruitful research.

I am also thankful to Professor Karsten Danzmann for having created and maintaining this great infrastructure at the Albert Einstein Institute in Hanover which makes it a fantastic place to work. The administrative and IT support as well as the electronic and mechanical workshops are outstanding.

Aiko Samblowski and Christina Vollmer awakened my interest in the topic and taught me the necessary experimental basics. Working with them was always a great pleasure! I furthermore thank Jaromír Fiurášek for his constant support and making theoretical aspects understandable for an experimentalist.

I thank Axel Schönbeck, Vitus Händchen and Jan Gniesmer for their support in the laboratory and also making the lab a fun place to be. Within many discussions with my colleagues I could deepen my understanding of physics and I would like to emphasize those with (in alphabetic order) Daniela Abdelkhalek, Melanie Ast, Stefan Ast, Tobias Gehring, Moritz Mehmet, Sacha Kocsis, Mikhail Korobko, Paolo Piergentili, Henning Vahlbruch and the people I already mentioned earlier. All group members contributed in making the working atmosphere very comfortable and some even became good friends! I thank Axel, Daniela, Jan, Mikhail, Paolo, Roman, Sacha and Vitus for valuable comments and corrections on this thesis.

Ein ganz besonderer Dank gilt meiner Familie und meinen Freunden in und um Mettingen, Hannover und mittlerweile ganz Deutschland. Eure Unterstützung bedeutet mir viel und Ihr erinnert mich an die wichtigen Dinge im Leben!

Danke Marie, Du hast mein Leben so sehr bereichert!

Danke, thanks, grazie, спасибо, děkuji!

G. Gallery

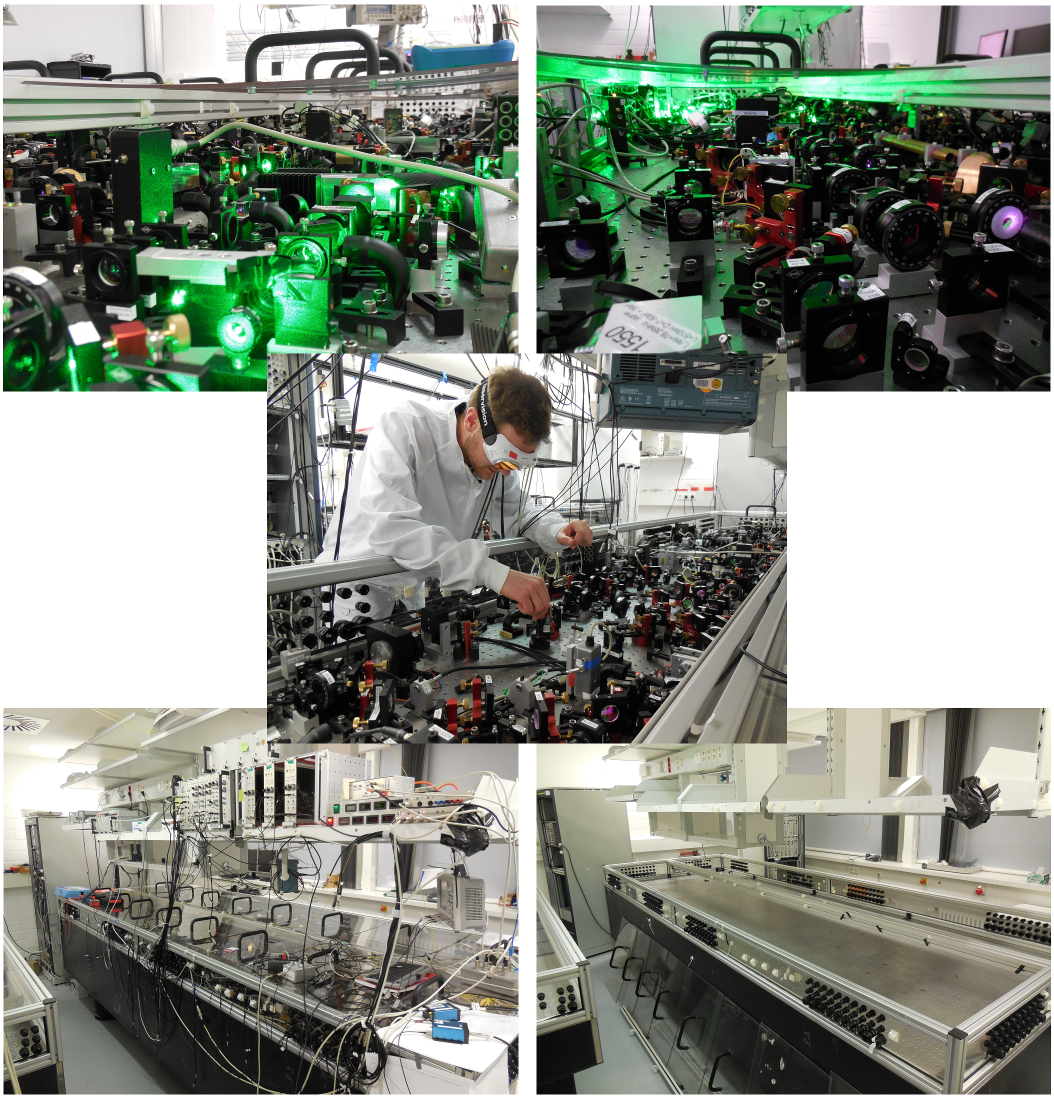

Figure G.1.: Impressions from the laboratory. From top left to bottom right: Photograph of the optical table as seem from the position of the first SHG. Photograph from the other side of the table. Me in the lab working hard. The optical table in his last minutes being fully assembled. The optical table one week later: the working group of Roman Schnabel moved to Hamburg.

Bibliography

[Afz09] M. Afzelius, C. Simon, H. De Riedmatten, and N. Gisin, *Multimode quantum memory based on atomic frequency combs*, Physical Review A **79**, 052329 (2009).

[App08] J. Appel, E. Figueroa, D. Korystov, M. Lobino, and A. I. Lvovsky, *Quantum memory for squeezed light*, Physical Review Letters **100**, 093602 (2008).

[Ast13] S. Ast, M. Mehmet, and R. Schnabel, *High-bandwidth squeezed light at 1550 nm from a compact monolithic PPKTP cavity*, Optics Express **21**, 13572 (2013).

[Ast15] S. Ast, *New approaches in squeezed light generation*, Ph.D. thesis, Leibniz Universität Hannover (2015).

[Bar02] S. D. Bartlett, B. C. Sanders, S. L. Braunstein, and K. Nemoto, *Efficient classical simulation of continuous variable quantum information processes*, Physical Review Letters **88**, 097904 (2002).

[Bau11] C. Baune, *Effiziente Hochkonversion optischer Felder für die Quantenmetrologie*, M.Sc. thesis, Leibniz Universität Hannover (2011).

[Ber91] K. Bergman and H. A. Haus, *Squeezing in fibers with optical pulses*, Optics Letters **16**, 663 (1991).

[Ber13] H. Bernien, B. Hensen, W. Pfaff, G. Koolstra, M. S. Blok, L. Robledo, T. H. Taminiau, M. Markham, D. J. Twitchen, L. Childress, and R. Hanson, *Heralded entanglement between solid-state qubits separated by three metres*, Nature **497**, 86 (2013).

[Bla01] E. D. Black, *An introduction to Pound-Drever-Hall laser frequency stabilization*, American Journal of Physics **69**, 79 (2001).

[Boy03] R. W. Boyd, *Nonlinear Optics*, Academic Press (2003).

[Bra05] S. L. Braunstein and P. van Loock, *Quantum information with continuous variables*, Reviews of Modern Physics **77**, 513 (2005).

[Bri98] H. J. Briegel, W. Dür, J. I. Cirac, and P. Zoller, *Quantum repeaters: The role of imperfect local operations in quantum communication*, Physical Review Letters **81**, 5932 (1998).

[Bro08] I. N. Bronstein, *Taschenbuch der Mathematik*, Verlag Harri Deutsch GmbH, Frankfurt am Main, 6 edition (2008).

[Brü10] F. Brückner, D. Friedrich, T. Clausnitzer, M. Britzger, O. Burmeister, K. Danzmann, E.-B. Kley, A. Tünnermann, and R. Schnabel, *Realization of a monolithic high-reflectivity cavity mirror from a single silicon crystal*, Physical Review Letters **104**, 163903 (2010).

[Dak97] M. Dakna, T. Anhut, T. Opatrný, L. Knöll, and D.-G. Welsch, *Generating Schrödinger-cat-like states by means of conditional measurements on a beam splitter*, Physical Review A **55**, 3184 (1997).

[Die82] D. Dieks, *Communication by EPR devices*, Physics Letters A **92**, 271 (1982).

[DiG07] J. DiGuglielmo, B. Hage, A. Franzen, J. Fiurášek, and R. Schnabel, *Experimental characterization of Gaussian quantum-communication channels*, Physical Review A **76**, 012323 (2007).

[Dru81] P. Drummond, K. McNeil, and D. Walls, *Non-equilibrium transitions in sub/second harmonic generation*, Optica Acta: International Journal of Optics **28**, 211 (1981).

[Dua00] L.-M. Duan, G. Giedke, J. I. Cirac, and P. Zoller, *Inseparability criterion for continuous variable systems*, Physical Review Letters **84**, 2722 (2000).

[Ebe10] T. Eberle, S. Steinlechner, J. Bauchrowitz, V. Händchen, H. Vahlbruch, M. Mehmet, H. Müller-Ebhardt, and R. Schnabel, *Quantum enhancement of the zero-area sagnac interferometer topology for gravitational wave detection*, Physical Review Letters **104**, 251102 (2010).

[Ebe11] T. Eberle, V. Händchen, J. Duhme, T. Franz, R. F. Werner, and R. Schnabel, *Strong Einstein-Podolsky-Rosen entanglement from a single squeezed light source*, Physical Review A **83**, 052329 (2011).

[Ebe13] T. Eberle, V. Händchen, and R. Schnabel, *Stable control of 10 dB two-mode squeezed vacuum states of light*, Optics Express **21**, 11546 (2013).

[Eck91] R. C. Eckardt, C. D. Nabors, W. J. Kozlovsky, and R. L. Byer, *Optical parametric oscillator frequency tuning and control*, Journal of the Optical Society of America B **8**, 646 (1991).

[Ein35] A. Einstein, B. Podolsky, and N. Rosen, *Can quantum-mechanical description of physical reality be considered complete?*, Physical Review **47**, 777 (1935).

[Eke91] A. K. Ekert, *Quantum cryptography based on Bell's theorem* (1991).

[Fil11] R. Filip and L. Mišta, *Detecting quantum states with a positive Wigner function beyond mixtures of Gaussian states*, Physical Review Letters **106**, 200401 (2011).

[Fiu15] J. Fiurášek, C. Baune, A. Schönbeck, and R. Schnabel, *Analysis of counting measurements on narrowband frequency up-converted single photons and the influence of heralding detector dead time*, Physical Review A **91**, 013829 (2015).

[Fre14] A. Freise, *Frequency domain interferometer simulation software: FINESSE* (2014), http://www.gwoptics.org/finesse/.

[Fuj13] K. Fujii, *Introduction to the rotating wave approximation (RWA) : Two coherent oscillations*, arXiv:1301.3585 (2013).

[Gar91] C. W. Gardiner and P. Zoller, *Quantum Noise*, Springer, Berlin (1991).

[Ger05] C. Gerry and P. Knight, *Introductory Quantum Optics*, Cambridge University Press (2005).

[Gis02] N. Gisin, G. Ribordy, W. Tittel, and H. Zbinden, *Quantum cryptography*, Reviews of Modern Physics **74**, 145 (2002).

[Gla63] R. J. Glauber, *Coherent and incoherent states of the radiation field*, Physical Review **131**, 2766 (1963).

[Got99] D. Gottesman, *The Heisenberg representation of quantum computers*, Proceedings of the XXII International Colloquium on Group Theoretical Methods in Physics **1**, 32 (1999).

[Gra86] P. Grangier, G. Roger, and A. Aspect, *Experimental evidence for a photon anticorrelation effect on a beam splitter: A new light on single-photon interferences*, Europhysics Letters (EPL) **1**, 173 (1986).

[Gro08] N. B. Grosse, S. Assad, M. Mehmet, R. Schnabel, T. Symul, and P. K. Lam, *Observation of entanglement between two light beams spanning an octave in optical frequency*, Physical Review Letters **100**, 243601 (2008).

[Gro13] H. Grote, K. Danzmann, K. L. Dooley, R. Schnabel, J. Slutsky, and H. Vahlbruch, *First long-term application of squeezed states of light in a gravitational-wave observatory*, Physical Review Letters **110**, 181101 (2013).

[Had09] R. H. Hadfield, *Single-photon detectors for optical quantum information applications*, Nature Photonics **3**, 696 (2009).

[Hag10] B. Hage, A. Samblowski, and R. Schnabel, *Towards Einstein-Podolsky-Rosen quantum channel multiplexing*, Physical Review A **81**, 062301 (2010).

[Han56] R. Hanbury Brown and R. Q. Twiss, *Correlation between photons in two coherent beams of light*, Nature **177**, 27 (1956).

[Hed10] M. P. Hedges, J. J. Longdell, Y. Li, and M. J. Sellars, *Efficient quantum memory for light*, Nature **465**, 1052 (2010).

[Hes16] K. Heshami, D. G. England, P. C. Humphreys, P. J. Bustard, V. M. Acosta, J. Nunn, and B. J. Sussman, *Quantum memories: emerging applications and recent advances*, Journal of Modern Optics (2016), DOI: 10.1080/09500340.2016.1148212.

[Hon08] K. Honda, D. Akamatsu, M. Arikawa, Y. Yokoi, K. Akiba, S. Nagatsuka, T. Tanimura, A. Furusawa, and M. Kozuma, *Storage and retrieval of a squeezed vacuum*, Physical Review Letters **100**, 093601 (2008).

[Hos11] M. Hosseini, G. Campbell, B. M. Sparkes, P. K. Lam, and B. C. Buchler, *Unconditional room-temperature quantum memory*, Nature Physics **7**, 794 (2011).

[Hua92] J. Huang and P. Kumar, *Observation of quantum frequency conversion*, Physical Review Letters **68**, 2153 (1992).

[Hum14] P. C. Humphreys, W. S. Kolthammer, J. Nunn, M. Barbieri, A. Datta, and I. A. Walmsley, *Continuous-variable quantum computing in optical time-frequency modes using quantum memories*, Physical Review Letters **113**, 130502 (2014).

[Jen11] K. Jensen, W. Wasilewski, H. Krauter, T. Fernholz, B. M. Nielsen, M. Owari, M. B. Plenio, A. Serafini, M. M. Wolf, and E. S. Polzik, *Quantum memory for entangled continuous-variable states*, Nature Physics **7**, 13 (2011).

[Jež11] M. Ježek, I. Straka, M. Mičuda, M. Dušek, J. Fiurášek, and R. Filip, *Experimental test of the quantum non-gaussian character of a heralded single-photon state*, Physical Review Letters **107**, 213602 (2011).

[Jež12] M. Ježek, A. Tipsmark, R. Dong, J. Fiurášek, L. Mišta, R. Filip, and U. L. Andersen, *Experimental test of the strongly nonclassical character of a noisy squeezed single-photon state*, Physical Review A **86**, 043813 (2012).

[Jin15] J. Jin, E. Saglamyurek, M. L. G. Puigibert, V. Verma, F. Marsili, S. W. Nam, D. Oblak, and W. Tittel, *Telecom-wavelength atomic quantum memory in optical fiber for heralded polarization qubits*, Physical Review Letters **115**, 140501 (2015).

[Jul04] B. Julsgaard, J. Sherson, J. I. Cirac, J. Fiurášek, and E. S. Polzik, *Experimental demonstration of quantum memory for light*, Nature **432**, 482 (2004).

[Kaw06] S. Kawamura, T. Nakamura, M. Ando, N. Seto, K. Tsubono, K. Numata, R. Takahashi, S. Nagano, T. Ishikawa, M. Musha, K. Ueda, T. Sato, M. Hosokawa, K. Agatsuma, T. Akutsu, K. Aoyanagi, K. Arai, A. Araya, H. Asada, Y. Aso, T. Chiba, T. Ebisuzaki, Y. Eriguchi, M. Fujimoto, M. Fukushima, T. Futamase, K. Ganzu, T. Harada, T. Hashimoto, K. Hayama, W. Hikida, Y. Himemoto, H. Hirabayashi, T. Hiramatsu, K. Ichiki, T. Ikegami, K. Inoue, K. Ioka, K. Ishidoshiro, Y. Itoh, S. Kamagasako, N. Kanda, N. Kawashima, H. Kirihara, K. Kiuchi, S. Kobayashi, K. Kohri, Y. Kojima,

K. Kokeyama, Y. Kozai, H. Kudoh, H. Kunimori, K. Kuroda, K. Maeda, H. Matsuhara, Y. Mino, O. Miyakawa, S. Miyoki, H. Mizusawa, T. Morisawa, S. Mukohyama, I. Naito, N. Nakagawa, K. Nakamura, H. Nakano, K. Nakao, A. Nishizawa, Y. Niwa, C. Nozawa, M. Ohashi, N. Ohishi, M. Ohkawa, A. Okutomi, K. Oohara, N. Sago, M. Saijo, M. Sakagami, S. Sakata, M. Sasaki, S. Sato, M. Shibata, H. Shinkai, K. Somiya, H. Sotani, N. Sugiyama, H. Tagoshi, T. Takahashi, H. Takahashi, T. Takano, T. Tanaka, K. Taniguchi, A. Taruya, H. Tashiro, M. Tokunari, S. Tsujikawa, Y. Tsunesada, K. Yamamoto, T. Yamazaki, J. Yokoyama, C. Yoo, S. Yoshida, and T. Yoshino, *The Japanese space gravitational wave antenna – DECIGO*, Classical and Quantum Gravity **23**, 125 (2006).

[Kie11] T. Kiesel, W. Vogel, B. Hage, and R. Schnabel, *Direct sampling of negative quasiprobabilities of a squeezed state*, Physical Review Letters **107**, 113604 (2011).

[Kum90] P. Kumar, *Quantum frequency conversion*, Optics Letters **15**, 1476 (1990).

[Kum12] R. Kumar, E. Barrios, A. MacRae, E. Cairns, E. Huntington, and A. Lvovsky, *Versatile wideband balanced detector for quantum optical homodyne tomography*, Optics Communications **285**, 5259 (2012).

[Las07] N. Lastzka and R. Schnabel, *The Gouy phase shift in nonlinear interactions of waves*, Optics express **15**, 7211 (2007).

[Las16] M. Lasota, R. Filip, and V. C. Usenko, *Sufficiency of quantum non-Gaussianity for discrete-variable quantum key distribution*, arXiv:1603.06620 (2016).

[Leo05] U. Leonhardt, *Measuring the Quantum State of Light*, Cambridge University Press (2005).

[LIG16] LIGO Scientific Collaboration and Virgo Collaboration, *Observation of gravitational waves from a binary black hole merger*, Physical Review Letters **116**, 061102 (2016).

[Lou05] B. Lounis and M. Orrit, *Single-photon sources*, Reports on Progress in Physics **68**, 1129 (2005).

[Lu00] Y. J. Lu and Z. Y. Ou, *Optical parametric oscillator far below threshold: Experiment versus theory*, Physical Review A **62**, 033804 (2000).

[Lvo01] A. I. Lvovsky, H. Hansen, T. Aichele, O. Benson, J. Mlynek, and S. Schiller, *Quantum state reconstruction of the single-photon fock state*, Physical Review Letters **87**, 050402 (2001).

[Lvo09] A. I. Lvovsky, *Continuous-variable optical quantum-state tomography*, Reviews of Modern Physics **81**, 299 (2009).

[Mab94] H. Mabuchi, E. S. Polzik, and H. J. Kimble, *Blue-light-induced infrared absorption in KNbO*$_3$, Journal of the Optical Society of America B **11**, 2023 (1994).

[Mar12] A. Mari and J. Eisert, *Positive Wigner functions render classical simulation of quantum computation efficient*, Physical Review Letters **109**, 230503 (2012).

[Mar14] N. Maring, K. Kutluer, J. Cohen, M. Cristiani, M. Mazzera, P. M. Ledingham, and H. de Riedmatten, *Storage of up-converted telecom photons in a doped crystal*, New Journal of Physics **16**, 113021 (2014).

[Meh11] M. Mehmet, S. Ast, T. Eberle, S. Steinlechner, H. Vahlbruch, and R. Schnabel, *Squeezed light at 1550 nm with a quantum noise reduction of 12.3 dB*, Optics Express **19**, 25763 (2011).

[MN10] B. Melholt Nielsen, *A non-classical light source for light-matter interfaces*, Ph.D. thesis, University of Copenhagen (2010).

[Møl06] K. Mølmer, *Non-Gaussian states from continuous-wave Gaussian light sources*, Physical Review A **73**, 063804 (2006).

[NN07] J. S. Neergaard-Nielsen, B. Melholt Nielsen, H. Takahashi, A. I. Vistnes, and E. S. Polzik, *High purity bright single photon source*, Optics Express **15**, 7940 (2007).

[NN08] J. S. Neergaard-Nielsen, *Generation of single photons and Schrödinger kitten states of light*, Ph.D. thesis, University of Copenhagen (2008).

[O'B09] J. L. O'Brien, A. Furusawa, and J. Vučković, *Photonic quantum technologies*, Nature Photonics **3**, 687 (2009).

[Pan12] J. W. Pan, Z. B. Chen, C. Y. Lu, H. Weinfurter, A. Zeilinger, and M. Zukowski, *Multiphoton entanglement and interferometry*, Reviews of Modern Physics **84** (2012).

[Pol92] E. S. Polzik, J. Carri, and H. J. Kimble, *Spectroscopy with squeezed light*, Physical Review Letters **68**, 3020 (1992).

[Pre14] A. Predojević, M. Ježek, T. Huber, H. Jayakumar, T. Kauten, G. S. Solomon, R. Filip, and G. Weihs, *Efficiency vs multi-photon contribution test for quantum dots*, Optics Express **22**, 4789 (2014).

[Rei89] M. D. Reid, *Demonstration of the Einstein-Podolsky-Rosen paradox using non-degenerate parametric amplification*, Physical Review A **40**, 913 (1989).

[Rei11] K. F. Reim, P. Michelberger, K. C. Lee, J. Nunn, N. K. Langford, and I. A. Walmsley, *Single-photon-level quantum memory at room temperature*, Physical Review Letters **107**, 053603 (2011).

[Rit12] S. Ritter, C. Nölleke, C. Hahn, A. Reiserer, A. Neuzner, M. Uphoff, M. Mücke, E. Figueroa, J. Bochmann, and G. Rempe, *An elementary quantum network of single atoms in optical cavities*, Nature **484**, 195 (2012).

[Sag15] E. Saglamyurek, M. l. G. Puigibert, Q. Zhou, L. Giner, F. Marsili, V. B. Verma, S. W. Nam, L. Oesterling, D. Nippa, D. Oblak, and W. Tittel, *A multiplexed light-matter interface for fibre-based quantum networks*, arXiv:1511.01384 (2015).

[Sam12] A. Samblowski, *State preparation for quantum information science and metrology*, Ph.D. thesis, Leibniz Universität Hannover (2012).

[Sam14] A. Samblowski, C. E. Vollmer, C. Baune, J. Fiurášek, and R. Schnabel, *Weak-signal conversion from 1550 to 532 nm with 84% efficiency*, Optics Letters **39**, 2979 (2014).

[San11] N. Sangouard, C. Simon, H. de Riedmatten, and N. Gisin, *Quantum repeaters based on atomic ensembles and linear optics*, Reviews of Modern Physics **83**, 33 (2011).

[Sch26] E. Schrödinger, *Der stetige Übergang von der Mikro- zur Makromechanik*, Naturwissenschaften **14**, 664 (1926).

[Scu97] M. Scully and M. Zubairy, *Quantum Optics*, Cambridge University Press (1997).

[Sim10] C. Simon, M. Afzelius, J. Appel, A. Boyer De La Giroday, S. J. Dewhurst, N. Gisin, C. Y. Hu, F. Jelezko, S. Kröll, J. H. Müller, J. Nunn, E. S. Polzik, J. G. Rarity, H. de Riedmatten, W. Rosenfeld, A. J. Shields, N. Sköld, R. M. Stevenson, R. Thew, I. A. Walmsley, M. C. Weber, H. Weinfurter, J. Wrachtrup, and R. J. Young, *Quantum memories*, European Physical Journal D **58**, 1 (2010).

[Sin14] N. Sinclair, E. Saglamyurek, H. Mallahzadeh, J. A. Slater, M. George, R. Ricken, M. P. Hedges, D. Oblak, C. Simon, W. Sohler, and W. Tittel, *Spectral multiplexing for scalable quantum photonics using an atomic frequency comb quantum memory and feed-forward control*, Physical Review Letters **113**, 053603 (2014).

[Slu85] R. Slusher, L. Hollberg, B. Yurke, J. Mertz, and J. Valley, *Observation of squeezed states generated by four-wave mixing in an optical cavity*, Physical Review Letters **55**, 2409 (1985).

[Str14] I. Straka, A. Predojević, T. Huber, L. Lachman, L. Butschek, M. Miková, M. Mičuda, G. S. Solomon, G. Weihs, M. Ježek, and R. Filip, *Quantum non-gaussian depth of single-photon states*, Physical Review Letters **113**, 223603 (2014).

[Tan05] S. Tanzilli, W. Tittel, M. Halder, O. Alibart, P. Baldi, N. Gisin, and H. Zbinden, *A photonic quantum information interface*, Nature **437**, 116 (2005).

[Tsu95] H. Tsuchida, *Generation of amplitude-squeezed light at 431 nm from a singly resonant frequency doubler*, Optics Letters **20**, 2240 (1995).

[Vol14a] C. E. Vollmer, *Non-classical state engineering for quantum networks*, Ph.D. thesis, Leibniz Universität Hannover (2014).

[Vol14b] C. E. Vollmer, C. Baune, A. Samblowski, T. Eberle, V. Händchen, J. Fiurášek, and R. Schnabel, *Quantum up-conversion of squeezed vacuum states from 1550 to 532 nm*, Physical Review Letters **112**, 073602 (2014).

[Wag14] K. Wagner, J. Janousek, S. Armstrong, J.-F. Morizur, P. K. Lam, and H.-A. Bachor, *Asymmetric EPR entanglement in continuous variable systems*, Journal of Physics B: Atomic, Molecular and Optical Physics **47**, 225502 (2014).

[Wal94] D. F. Walls and G. J. Milburn, *Quantum Optics*, Springer-Verlag, Berlin, Heidelberg, New York, 1st edition (1994).

[Wee12] C. Weedbrook, S. Pirandola, R. García-Patrón, N. J. Cerf, T. C. Ralph, J. H. Shapiro, and S. Lloyd, *Gaussian quantum information*, Reviews of Modern Physics **84**, 621 (2012).

[Wei14] H. Weißbrich, *Charakterisierung von Photodioden für die effiziente Homodyndetektion bei 532 nm*, B.Sc. thesis, Leibniz Universität Hannover (2014).

[Woo82] W. K. Wootters and W. H. Zurek, *A single quantum cannot be cloned*, Nature **299**, 802 (1982).

[Yur87] B. Yurke and M. Potasek, *Obtainment of thermal noise from a pure quantum state*, Physical Review A **36**, 3464 (1987).

[Zel14] P. Zell, *Verschränkung zwischen sichtbarem und nah-infrarotem Licht durch Frequenzkonversion*, M.Sc. thesis, Leibniz Universität Hannover (2014).

[Zho15] M. Zhong, M. P. Hedges, R. L. Ahlefeldt, J. G. Bartholomew, S. E. Beavan, S. M. Wittig, J. J. Longdell, and M. J. Sellars, *Optically addressable nuclear spins in a solid with a six-hour coherence time*, Nature **517**, 177 (2015).

Christoph Baune

Address

Ahlemer Straße 7
30451 Hannover
Germany

Phone: +49 160 2032 944
chrbaune@web.de

Born on January 9th, 1986 in Mettingen, Germany

Academic history

- 04/2015-now
  Doctoral studies at Leibniz Universität Hannover, employed as research fellow at Universität Hamburg
- 02/2013-03/2015
  Doctoral studies at Leibniz Universität Hannover, employed as research fellow at Leibniz Universität Hannover
- 11/2011-02/2013
  Doctoral studies at Leibniz Universität Hannover, funded by a scholarship of the *International Max-Planck Research School on Gravitational Wave Astronomy* (IMPRS)
- 10/2009-10/2011
  Master studies in physics at Leibniz Universität Hannover
  Master of Science (1.2, very good)
- 10/2007-10/2009
  Bachelor studies in physics at Leibniz Universität Hannover
  Bachelor of Science (1.7, good)
- 10/2006-9/2007
  Interdisciplinary Bachelor studies in math and physics at Leibniz Universität Hannover

School and civil service

- 08/2005-04/2006
  Civil service at Altenheim Maria Frieden (retirement home), Mettingen
- 09/1996-06/2005
  Kardinal-von-Galen Gymnasium Mettingen
  Abitur (1.7)

List of publications

1. Christoph Baune, Jan Gniesmer, Sacha Kocsis, Christina E. Vollmer, Petrissa Zell, Jaromír Fiurášek, and Roman Schnabel
Unconditional entanglement interface for quantum networks
Physical Review A **93**, 010302(R) (2016)

2. Christoph Baune, Jan Gniesmer, Axel Schönbeck, Christina E. Vollmer, Jaromír Fiurášek, and Roman Schnabel
Strongly squeezed states at 532 nm based on frequency up-conversion
Optics Express **23**, 16035 (2015)

3. Jaromír Fiurášek, Christoph Baune, Axel Schönbeck, and Roman Schnabel
Analysis of counting measurements on narrowband frequency up-converted single photons and the influence of heralding detector dead time
Physical Review A **91**, 013829 (2015)

4. Christoph Baune, Axel Schönbeck, Aiko Samblowski, Jaromír Fiurášek, and Roman Schnabel
Quantum non-Gaussianity of frequency up-converted single photons
Optics Express **22**, 22808 (2014)

5. Aiko Samblowski, Christina E. Vollmer, Christoph Baune, Jaromír Fiurášek, and Roman Schnabel
Weak signal conversion from 1550 nm to 532 nm with 84% efficiency
Optics Letters **39**, 2979 (2014)

6. Christina E. Vollmer, Christoph Baune, Aiko Samblowski, Tobias Eberle, Vitus Händchen, Jaromír Fiurášek, and Roman Schnabel
Quantum up-conversion of squeezed vacuum states from 1550 nm to 532 nm
Physical Review Letters **112**, 073602 (2014)

Publications as a member of the Ligo/Virgo Science Collaboration

(more than 1000 co-authors)

7. B. P. Abbott, …, C. Baune, …, J. Zweisig
GW151226: Observation of gravitational waves from a 22-solar-mass binary black hole coalescence
Physical Review Letters **116**, 241103 (2016)

8. B. P. Abbott, …, C. Baune, …, J. Zweisig
GW150914: First results from the search for binary black hole coalescence with Advanced LIGO
Physical Review D **93**, 122003 (2016)

9. B. P. Abbott, …, C. Baune, …, J. Zweisig
Observing gravitational-wave transient GW150914 with minimal assumptions
Physical Review D **93**, 122004 (2016)

10. B. P. Abbott, …, C. Baune, …, J. Zweisig
Directly comparing GW150914 with numerical solutions of Einstein's equations for binary black hole coalescence
arXiv:1606.01262

11. B. P. Abbott, …, C. Baune, …, J. Zweisig
An improved analysis of GW150914 using a fully spin-precessing waveform model
arXiv:1606.01210

12. B. P. Abbott, …, C. Baune, …, J. Zweisig
Tests of general relativity with GW150914
Physical Review Letters **116**, 221101 (2016)

13. B. P. Abbott, …, C. Baune, …, J. Zweisig
Comprehensive all-sky search for periodic gravitational waves in the sixth science run LIGO data
arXiv:1605.03233

14. B. P. Abbott, …, C. Baune, …, J. Zweisig
A first targeted search for gravitational-wave bursts from core-collapse supernovae in data of first-generation laser interferometer detectors
arXiv:1605.01785

15. B. P. Abbott, …, C. Baune, …, J. Zweisig
Search for transient gravitational waves in coincidence with short duration radio transients during 2007-2013
arXiv:1605.01707

16. D.V. Martynov, …, C. Baune, …, J. Zweisig
S*ensitivity of the Advanced LIGO detectors at the beginning of gravitational wave astronomy*
Physical Review Letters D **93**, 112004 (2016)

17. B. P. Abbott, …, C. Baune, …, J. Zweisig
GW150914: The Advanced LIGO detectors in the era of first discoveries
Physical Review Letters **116**, 131103 (2016)

18. B. P. Abbott, …, C. Baune, …, J. Zweisig
GW150914: Implications for the stochastic gravitational-wave background from binary black holes
Physical Review Letters **116**, 131102 (2016)

19. B. P. Abbott, …, C. Baune, …, J. Zweisig
Localization and broadband follow-up of the gravitational-wave transient GW150914
arXiv:1602.08492

20. J. Aasi, …, C. Baune, …, J. Zweizig
First low frequency all-sky search for continuous gravitational wave signals’
Physical Review D **93**, 042007 (2016)

21. J. Aasi, …, C. Baune, …, J. Zweizig
Search of the Orion spur for continuous gravitational waves using a loosely coherent algorithm on data from LIGO
Physical Review D **93**, 042006 (2016)

22. B. P. Abbott, …, C. Baune, …, J. Zweisig
Characterization of transient noise in Advanced LIGO relevant to gravitational wave signal GW150914
Classical and Quantum Gravity **33**, 134001 (2016)

23. B.P. Abbott, …, C. Baune, …, J. Zweisig
All-sky search for long-duration gravitational wave transients with initial LIGO
Physical Review D **93**, 042005 (2016)

24. B. P. Abbott, …, C. Baune, …, J. Zweisig
The rate of binary black hole mergers inferred from Advanced LIGO observations surrounding GW150914
arXiv:1602.03842

25. B. P. Abbott, …, C. Baune, …, J. Zweisig
Observation of gravitational waves from a binary black hole merger
Physical Review Letters **116**, 061102 (2016)

26. B. P. Abbott, …, C. Baune, …, J. Zweisig
Astrophysical implications of the binary black hole merger GW150914
The Astrophysical Journal Letters **818**, L22 (2016)

27. B. P. Abbott, …, C. Baune, …, J. Zweisig
Prospects for observing and localizing gravitational-wave transients with Advanced LIGO and Advanced Virgo
Living Reviews in Releativity **19**, 1 (2016)

28. J. Aasi, …, C. Baune, ..., J. Zweizig
Directed search for gravitational waves from Scorpius X-1 with initial LIGO data
Physical Review D **91**, 062008 (2015)

29. J. Aasi, …, C. Baune, …, J. Zweizig
Advanced LIGO
Classical and Quantum Gravity **32**, 1 (2015)

30. J. Aasi, …, C. Baune, …, J. Zweizig
Narrow-band search of continuous gravitational-wave signals from Crab and Vela pulsars in Virgo VSR4 data
Physical Review D **91**, 022004 (2015)

31. J. Aasi, …, *C. Baune*, …, J. Zweizig
Searches for continuous gravitational waves from nine young supernova remnants
The Astrophysical Journal **813**, 39 (2015)

32. M. G. Aartsen, …, C. Baune, …, J. Zweizig
Multimessenger search for sources of gravitational waves and high-energy neutrinos: Initial results for LIGO-Virgo and IceCube
Physical Review D **90**, 102002 (2014)

33. J. Aasi, …, C. Baune, ..., A. von Kienlin
Search for gravitational waves associated with gamma-ray bursts detected by the interplanetary network
Physical Review Letters **113**, 011102 (2014)

34. J. Aasi, …, C. Baune, …, J. Zweizig
Methods and results of a search for gravitational waves associated with γ-ray bursts using the GEO 600, LIGO, and Virgo detectors
Physical Review D **89**, 12204 (2014)